



THÈSE DE DOCTORAT

Observation géodésique et modélisation de la déformation des failles dans le Plateau Tibétain

Yanchuan Li

Géoazur

**Présentée en vue de l'obtention
du grade de docteur** en Sciences
de la Terre et de l'Univers
d'Université Côte d'Azur
Dirigée par Jean-Mathieu Nocquet
co-dirigée par Xinjian Shan
Soutenue le 18.02.2020

Devant le jury, composé de
Cécile Lasserre, Professeur de Université de Lyon
Philippe Vernant, Professeur Agrégé au Université Montpellier II
Mathilde Vergnolle, Chargée de Recherche au CNRS
Jean-Mathieu Nocquet, Directeur de Recherche IRD
Xinjian Shan, Professeur de IGCEA
Chunyan Qu, Professeur de IGCEA

Geodetic observation and modelling of fault deformation in the Tibetan Plateau

Thèse présentée devant le jury composé de

Rapporteurs:

Cécile Lasserre, Professeur de Université de Lyon

Philippe Vernant, Professeur Agrégé au Université Montpellier II

Examineurs:

Mathilde Vergnolle, Chargée de Recherche au CNRS

Chunyan Qu, Professeur de Institute of Geology, China Earthquake Administration

Directeurs de these:

Jean-Mathieu Nocquet, Directeur de recherche IRD

Xinjian Shan, Professeur de Institute of Geology, China Earthquake Administration

Résumé

La convergence continue des plaques entre l'Inde et l'Eurasie au cours des ~40 millions d'années a créé le plateau tibétain, une région avec une altitude moyenne de ~4500 m, une superficie de plus de 600×1000 km², et des failles actives et une déformation crustale s'étendent sur plus de 2000 km Asie centrale. Environ la moitié des 36 à 40 mm/a de l'Inde vers le nord se répartit dans le plateau tibétain, ce qui entraîne un épaississement, un raccourcissement, des plis et des systèmes de failles complexes. La déformation crustale active provoque divers styles d'accumulation et de libération de déformation sur les failles crustales, exprimées sous la forme de comportements de failles ou de cycles sismiques distincts. L'étude de la déformation des failles crustales et des cycles sismiques sur le plateau tibétain à l'aide de la géodésie spatiale, c'est-à-dire le système de positionnement global (GPS) et l'interférométrie radar à ouverture synthétique (InSAR), a commencé il y a 30 ans. Actuellement, la géodésie à haute résolution spatio-temporelle nous fournit des données abondantes et une résolution suffisante pour étudier la déformation de la surface du sol associée aux processus du cycle sismique.

Dans cette dissertation, je me concentre sur la déformation intersismique le long de trois grands systèmes de failles de glissement du plateau tibétain, la faille Altyn Tagh, le système de failles Haiyuan et le système de failles Xianshuihe-Anninghe-Zemuhe-Xiaojiang (XAZX). J'utilise les observations géodésiques GPS (1999–2018) et InSAR (2003–2016), ainsi que les modèles de dislocations 2D et de blocs 3D, pour inverser les taux de glissement et le couplage des failles intersismiques, évaluer le risque sismique et étudier les cycles sismiques le long de ces failles; étudier en outre la cinématique de la déformation à travers le plateau tibétain. Mes résultats montrent des taux de glissement allant de ~2 à ~12 mm/a, un couplage de failles intersismiques très hétérogène (coexistant complètement verrouillé avec un fluage total), un potentiel sismique distinct et différents cycles de tremblement de terre le long de ces failles. En particulier, j'identifie deux et un nouveaux segments rampants asismiques le long du système de faille Haiyuan et de la faille Xianshuihe respectivement. Mes résultats d'observation et de modélisation géodésiques démontrent la diversité spatio-temporelle et la complexité de la déformation intersismique des failles dans le plateau tibétain, mettent en évidence l'importance de considérer la déformation verticale dans InSAR et permettent une compréhension nouvelle et approfondie des cycles sismiques le long des trois failles ci-dessus systèmes.

Mots clés: Plateau Tibétain, Déformation intersismique, Faille Altyn Tagh, Faille Haiyuan, Système de failles Xianshuihe-Xiaojiang, GPS et InSAR, Cycle sismique

Abstract

Ongoing plate convergence between India and Eurasia during the past ~40 million years has created the Tibetan Plateau, a region with average elevation of ~4500 m, area of over 600×1000 km², and active faulting and crustal deformation extends more than 2000 km into central Asia. Approximately one-half of India's 36–40 mm/a northward motion is partitioned in the Tibetan Plateau, resulting in crustal thickening, shortening, folds, and complex fault systems. The active crustal deformation cause diverse styles of strain accumulation and release on crustal faults, expressed as distinct faulting behavior or earthquake cycles. Investigating into crustal fault deformation and earthquake cycles in the Tibetan Plateau using space-based geodesy, i.e., Global Positioning System (GPS) and Synthetic Aperture Radar Interferometry (InSAR), has started 30 years ago. Currently, high spatial-temporal resolution geodesy provides us with abundant data and sufficient resolution to study the ground deformation associated with earthquake cycle processes.

In this dissertation, I focus on the interseismic deformation along three boundary large strike-slip fault systems of the Tibetan Plateau, the Altyn Tagh fault, the Haiyuan fault system and the Xianshuihe-Anninghe-Zemuhe-Xiaojiang fault system (XAZX). I use GPS (1999-2018) and InSAR (2003-2016) geodetic observations, along with 2D dislocation and 3D block models, to invert for slip rates and interseismic fault coupling, assess seismic hazard and investigate earthquake cycles along these faults; moreover, study the kinematics of deformation across the Tibetan Plateau. My results show slip rates ranging from ~2 to ~12 mm/a, highly heterogeneous interseismic fault coupling (fully locked coexist with fully creeping), distinct seismic potential and different earthquake cycles along these faults. In particular, I identify two and one new aseismic creeping segments along the Haiyuan fault system and the Xianshuihe fault respectively. My geodetic observation and modeling results demonstrate the spatio-temporal diversity and complexity of interseismic fault deformation in the Tibetan Plateau, highlight the significance of considering vertical deformation in InSAR, and allow a new and in-depth understanding of earthquake cycles along the above three fault systems.

Key words: Tibetan Plateau, Interseismic fault deformation, Altyn Tagh fault, Haiyuan fault, Xianshuihe-Xiaojiang fault system, GPS and InSAR, Earthquake cycle

Acknowledgements/Merci

‘A journey of a thousand miles begins with a single step’. I learn the proverb or ancient poetry when I was in primary school. Although I did not fully understand the meaning behind the proverb when I was young, I was lucky to follow it on my way during the school-time in the past 24 years. I remember one night I watched a documentary about China's college entrance examination, I was deeply moved; not only for their stories, but because I was one of them. I have been from a poor rural family in China to now studying in France and receiving a PhD, which is the best reward for me and my family. On the eve of my doctoral thesis, I'd like to show my thanks to those who helped and accompanied me all the way.

First, and foremost, thanks to my supervisor Jean-Mathieu Nocquet, for receiving me to study in Geoazur, for teaching me many new things and ongoing patience in each discussion, for teaching me what qualities a scientist should have. Also, you helped me to revise my ugly manuscripts, and reminded me of the details of my works. Stay with you for the one and a half years will be one beautiful memory and the wealth of my life. I am grateful to my Chinese advisor Xinjian Shan, who not only offered me with opportunity and funding to study in France, but also supported me with everything I need in my research. Professor Shan is more like my father who gave me a lot of advice, thank you. Also, my thanks to all team colleagues in China, Chunyan Qu, Guohong Zhang, Xiaogang Song, Yunhua Liu, et al. I am happy to work with you, to work in the field, and to talk in daily lives.

I show my thanks to my friends and teachers in France, Zoe Candaux, Huihui Weng, Junchao Chen, Chen Luo, Sandrine Bertetic, Valérie Mercier-Valéro, Youling Wang, Paul Jarrin, Maria Jose Hernandez Salazar, Jenny Trevisan, Shanhong Liu, and all others who helped me and worked with me. Without you, I could not adapt to life in France so easy. My Chinese friends and colleagues, Chuanhua Zhu, Yingfeng Zhang, Dezheng Zhao, Hao Yin, Xin Qiao, Xiaodong Liu, Zicheng Huang, Shaoyan Wen, Liyan Hou, Zhishen Zhang, Pengcheng Sha, Lei Zhao, Anming Liu, Ronghu Zuo, Nana Han, Zhiyu Gao, and all others who I do not mention here, thank you for working and enjoying with me.

I am also grateful to the China Scholarship Council and China Earthquake Administration for funding me to study in France. Especially, I show my thanks to Simon Daout and his co-workers for sharing the interseismic InSAR results across the Altyn Tagh fault. I am grateful to Jiankun He, in Institute of Tibetan Plateau Research, Chinese Academy of Sciences, who shared the GPS data acquired in 2009–2011 across the western Altyn Tagh fault. I thank Cavalie Olivier for his help in revising my manuscript. I also show my gratitude to Yann Klinger for his comments on my

Xianshuihe manuscript. Moreover, the Crustal Movement Observation Network Of China (CMONOC) GPS data were provided by the National Earthquake Infrastructure Service, China Earthquake Administration, I show my thanks to all people who participated in the GPS fieldwork. Besides, Wei Zhan from the First Crust Deformation Monitoring and Application Center, China Earthquake Administration, helped me a lot with GPS data processing.

My gratitude and love to my parents and sisters. Although my family was not rich, my parents supported me and my sisters to study without any slack and complaints. We are lucky to complete our college education. Without the fully support from my parents and sisters, I may have dropped out early. I would apologize to my younger sisters for not being able to attend your weddings. I also show my love to my elder sister for taking care of our parents. My nephew and niece, I love you.

And finally to my girlfriend Huizi Jian, who is lovely, kind and considerate. She is now a PhD candidate, I hope you will also enjoy the journey. I am really happy to talk with you about our researches. It was my luck to meet you and love you. You have always encouraged me during the hardest part of my dissertation writing. Go back to the dormitory with you, eat together on weekends, watch movies, go to the gym, and go for a walk and so on, every moment will be our romantic memories. I love you.

新的旅途已经开启，愿岁月厚待，生活如花。

Yanchuan, in Nice, France
December 2019

Table of Contents

Chapter 1· Introduction.....	1
1.1. Seismic hazard in the Tibetan Plateau.....	2
1.2. Earthquake cycle	6
1.2.1. Interseismic deformation.....	7
1.2.2. Coseismic deformation.....	9
1.2.3. Postseismic deformation	10
1.3. Previous geodetic observation and modelling of crustal deformation in the Tibetan Plateau	12
1.4. The aims of this thesis.....	18
1.5. References.....	19
Chapter 2· Geodetic datasets and data processing.....	28
2.1. GPS measurements and data processing	29
2.1.1. GPS measurement	29
2.1.2. GPS data processing.....	31
2.2. InSAR dataset	35
2.2.1. The Altyn Tagh fault.....	35
2.2.2. The Haiyuan fault.....	35
2.2.3. The Xianshuihe fault	36
2.3. Geodetic data integration	38
2.3.1. How to consider vertical deformation	38
2.3.2. Methodology and data integration.....	39
2.3.3. Minor comments	44
2.4. References.....	45
Chapter 3· Measuring the crustal deformation along the Altyn Tagh fault using GPS and InSAR.....	48
3.1. Abstract	67
3.2. Introduction.....	68
3.3. Geodetic data and analysis	69
3.3.1. GPS measurements and data processing	69
3.3.2. Comparison of GPS and InSAR.....	71
3.4. Results.....	72
3.4.1. GPS velocity field	72
3.4.2. Corrections of the geodetic data for block-rotation.....	73
3.4.3. Modeling results.....	75

3.5. Discussion	77
3.5.1. Slow strain accumulation rate along the western Altyn Tagh fault	77
3.5.2. Do asymmetric patterns of interseismic velocity exist across the western Altyn Tagh fault?	77
3.5.3. High spatial resolution crustal deformation in the northwestern Tibet	79
3.6. Conclusions.....	82
3.7. References.....	83
Chapter 4• Surface creep on the Haiyuan fault system, northeastern Tibet, constrained from GPS and InSAR	87
4.1. Abstract	88
4.2. Introduction.....	89
4.3. Geodetic data.....	93
4.3.1. GPS data and processing.....	93
4.3.2. InSAR data.....	94
4.3.3. Geodetic data comparison and combination	95
4.4. Modeling strategy	98
4.4.1. Interseismic horizontal GPS velocities	98
4.4.2. Combined GPS-InSAR inversion.....	98
4.5. Results.....	100
4.5.1. GPS velocity profile fitting	100
4.5.2. Fault creep from the restored InSAR	101
4.5.3. Block modeling of the GPS and restored InSAR.....	101
4.6. Discussions.....	103
4.6.1. Shallow creep segments along the Laohushan fault.....	103
4.6.2. Mechanism of shallow fault creep along the Laohushan fault	103
4.6.3. The correlation between fault creep and the M~8 1920 Haiyuan earthquake	104
4.6.4. Earthquake scenarios along the Haiyuan fault system	106
4.7. Conclusions.....	108
4.8. References.....	109
Chapter 5• Heterogeneous interseismic coupling along the Xianshuihe-Xiaojiang fault system, eastern Tibet.....	115
5.1. Abstract	116
5.2. Introduction.....	117
5.3. Data and model	119
5.3.1. GPS data processing.....	119
5.3.2. GPS data modeling.....	120
5.3.3. InSAR data and processing	121
5.4. Interseismic coupling results.....	123
5.5. Discussion	125
5.5.1. Fault behavior and moment budget along the XXFS	125
5.5.1.1. Overall characteristics	125
5.5.1.2. Northern Xianshuihe fault.....	126

5.5.1.3. Southern Xianshuihe fault.....	128
5.5.1.3. Anninghe-Zemuhe fault.....	130
5.5.1.4. Xiaojiang fault.....	131
5.5.1.5. Seismic potential along XXFS	131
5.5.2. Shallow creep along the Xianshuihe fault.....	131
5.5.3. Temporal variation in creep rate along the Xianshuihe fault (~30.2°N–30.4°N)	135
5.6. Conclusions.....	138
5.7. References.....	139
Chapter 6• Discussions and conclusions.....	143
6.1. Fault coupling and seismic potential.....	144
6.2. What we learn about the shallow fault creep in Tibet	146
6.2.1. Interseismic fault creep on crustal faults in Tibet.....	146
6.2.2. Very long-term creep/afterslip on crustal faults in Tibet.....	150
6.2.3. The role of shallow creeping in seismic behavior	151
6.3. What we learn about the geodetic data.....	154
6.4. Future work.....	157
6.5. References.....	159
Appendix A-Appendix for Chapter 3	163
Appendix B-Appendix for Chapter 4	168
Appendix C-Appendix for Chapter 5.....	173

Chapter 1· Introduction

In this chapter, I first present brief introductions about the seismic hazards in the Tibetan Plateau. In this section, I address the significance of using geodetic measurements to study interseismic fault deformation. Subsequently, I present general introductions on earthquake cycle, and the crustal fault deformation characters in each phase of the cycle. Then, I summarize the geodetic observations in the Tibetan Plateau over the last 30 years, and studies of the interseismic crustal deformation in the Tibetan Plateau. In the last, I present the aims of this dissertation, and the main contents of each chapter are also briefly introduced.

1.1. Seismic hazard in the Tibetan Plateau

The Tibetan Plateau is known as the roof of the world for its extremely high altitude. The formation of the Tibetan Plateau is one of the greatest events in the earth history that started ~55 millions of years ago, with complex dynamics and kinematic processes (e.g., [Tapponnier et al., 1986](#)). It is generally interpreted as the result of long-term collision of the Indian plate and the Eurasian plate. The collision not only caused intense crustal deformation extending thousands of kilometers northward from the Himalayan mountain range to the Mongolian platform (Figure 1.1), but also had large impacts on climate, environment, and ecology of Asia (e.g., [Molnar and Tapponnier, 1975](#); [Rowley, 1996](#)). Probing the mechanism of lithospheric deformation of Tibet has been one key question of geodynamics and tectonics. (e.g., [Avouac and Tapponnier, 1993](#); [Shen et al., 2001](#); [Tapponnier et al., 2001](#); [Wright et al., 2004](#); [Thatcher, 2007](#); [Zhang, 2013](#); [Li et al., 2018a, 2018b](#)).

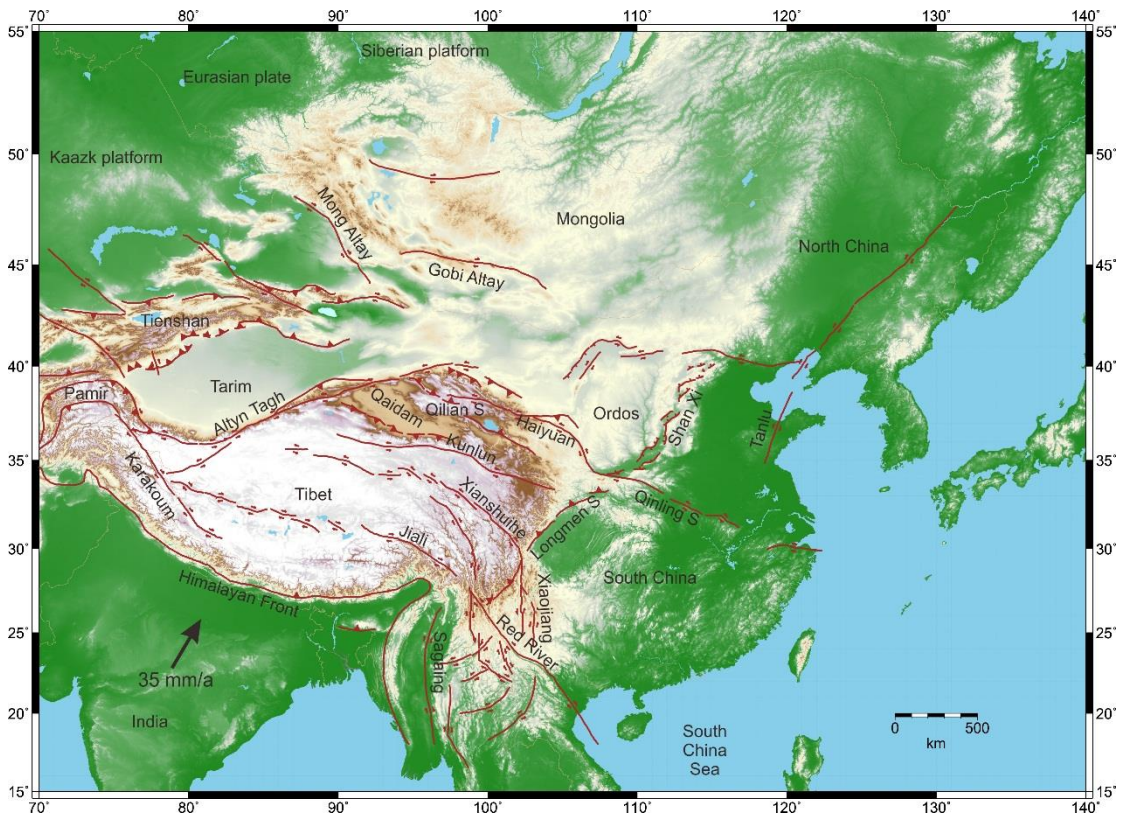


Figure 1.1. Tectonic map of the Tibetan Plateau. Dark red lines indicate active faults ([Deng et al., 2003](#)).

During the last century, several kinematic models have been proposed to explain the crustal lithospheric deformation mechanism of the Tibetan Plateau. These models include the ‘northward underthrusting of the Indian plate beneath Tibet’ model proposed by Argand (1924), the ‘intracrustal shortening within a hot ductile Asia’ (e.g., [Dewey and Burke, 1973](#)), the ‘successive collision of small continental blocks with the leading edge of Asia’ (e.g., [Chang and Cheng, 1973](#)), the ‘lithosphere extrusion model’ (e.g., [Tapponnier and Molnar, 1975](#)), the ‘continuum model’ (e.g.,

England and Houseman, 1986, 1988), the ‘subduction of Asian lithospheric mantle beneath Tibet’ (e.g., Willett and Beaumont, 1994), the ‘mantle diapir model’ (Xu et al., 1996), the ‘south underthrusting plus north melting’ (Owens and Zandt, 1997), and the ‘eastward flow of a channel of viscous crustal rocks’ (e.g., Royden et al., 1997; Clark and Royden, 2000). Among them, two end-number models, i.e., the ‘lithosphere extrusion model’ and the ‘continuum model’, has become a matter of debates. The ‘lithosphere extrusion model’ proposes the India-Eurasia collision to be accommodated laterally along large-scale narrow bounding fault zones by lithosphere extrusion (e.g., Tapponnier and Molnar, 1975; Meade, 2007), whereas the ‘continuum model’ stresses that the collision is partitioned by numerous, isolated fault structures, that is, the deformation is continuous throughout the entire lithosphere and dominated by broadly distributed crustal shortening and thickening (e.g., England and Houseman, 1986, 1988; Shen et al., 2001). Regardless of the deformation model of the Tibetan Plateau, one thing is certain: the active deformation has resulted in the occurrence of large crustal earthquakes inside and around the Tibet (Figure 1.2). Thus, understanding the faulting behaviors of crustal faults in Tibet are not only crucial for unraveling the mechanisms driving deformation, but also to provide insights into earthquake physics, seismic potential and hazards.

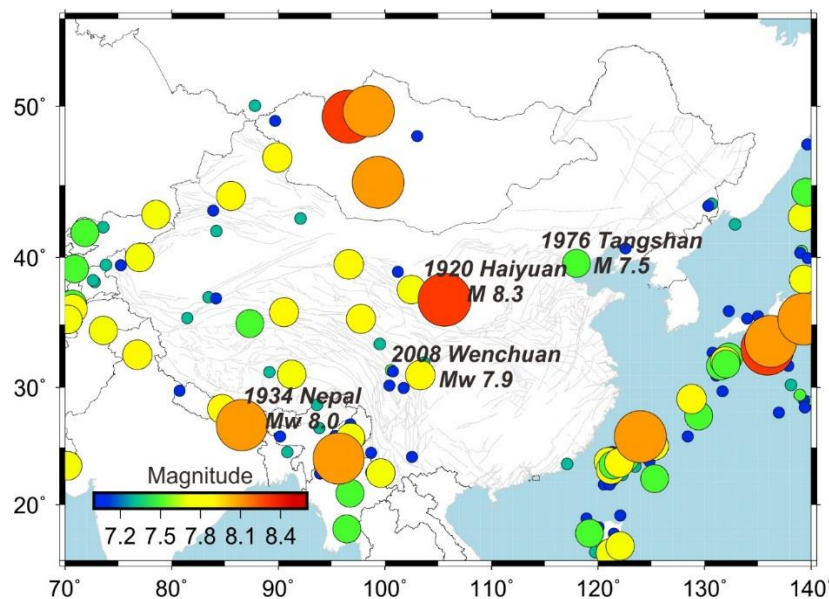


Figure 1.2. Large earthquakes (M7+, 1900-2019) in and around mainland China. Circles are coloured by earthquake magnitude. Earthquake data from U.S. Geological Survey (USGS).

The classical view of earthquake faulting portrays large earthquakes as sudden slip events that dynamically propagate along a fault, releasing years of accumulated strain (e.g., Davison, 1901; Reid, 1910, 1911). In Tibet, the subduction of the Indian plate under the Eurasian plate results in different movement of rigid or deforming blocks, which in turn lead to strain accumulation along bounding faults, leading to a variety of faulting style (e.g., Zhang et al., 2004). Since earthquakes have started to be recorded several centuries ago, as many as 18 large earthquakes with magnitude

estimated larger than 8.0 and more than 100 earthquakes with magnitudes in 7.0-8.0 have been documented in and around the Tibet (Deng et al., 2016). As a result, China is the country with the highest recorded large continental earthquakes (Zhang et al., 2002). Figure 1.2 shows the large earthquakes ($M7+$) in the China mainland during the last century. Almost all continental earthquakes occurred in and around Tibet. Some of them have been very destructive. The 1920 Haiyuan M 8.3 earthquake caused 237,114 casualties, produced a surface rupture length of 220 km, and a maximum displacement of 10 m (e.g., Deng et al., 1986; Zhang et al., 1987); the 2008 Wenchuan M_w 7.9 earthquake had a total surface rupture length of 312 km along the Longmenshan fault zone, with maximum vertical and horizontal offsets of 6.5 m and 4.9 m respectively. It caused the destruction of buildings and the death of more than 80,000 people (e.g., Xu et al., 2009; Zhang, 2013; Figure 1.3). The frequent occurrence of destructive earthquakes inside and around Tibet calls for investigating the physical mechanisms behind earthquakes to better anticipate them.



Figure 1.3. Beichuan County, Sichuan Province, China. Picture taken about half an hour after the M_w 7.9 2008 Wenchuan earthquake, from Zhang (2013).

In the recent years, seismic potential assessment in Tibet benefited from various disciplines, such as paleoearthquake research (e.g., Liu-Zeng et al., 2007; Wen et al., 2008; Li et al., 2009; Yao et al., 2019), geomorphology (e.g., Gaudemer et al., 1995; Kirby et al., 2008), numerical simulations (e.g., Toda et al., 2008; Xiong et al., 2010; Li et al., 2014), crustal structure imaging (e.g., Wang et al., 2015), geodetic study (e.g., Cavalié et al., 2008; Shen et al., 2009; Jolivet et al., 2012, 2013, 2015a; Daout et al., 2016; Li et al., 2017, 2018a, 2018b, 2019; Rui and Stamps, 2019a). Despite fundamental differences in data and methods, most studies agree that several crustal faults inside and around the Tibet show a high potential of rupture in the near future, such as the ‘Tianzhu seismic gap’ along the Haiyuan fault, the Altyn Tagh fault, the eastern Kunlun fault and the Anninghe-Zemuhe fault system (seismotectonic settings for each of these faults are present in the following chapters; Figure 1.1). As an example, Figure 1.4 shows the logarithm of the tectonic forecast of seismicity, which was calculated from geodetic strain rates and reveals the seismic potential in one

region, of mainland China and its surroundings at large scale (Rui and Stamps, 2019b). The Himalaya, the Xianshuihe-Xiaojiang fault system, the eastern Kunlun fault system, and the western Tien Shan are the regions showing the highest forecasted seismicity rate. I recommend readers to Rui and Stamps (2019b) for more details of the calculation method.

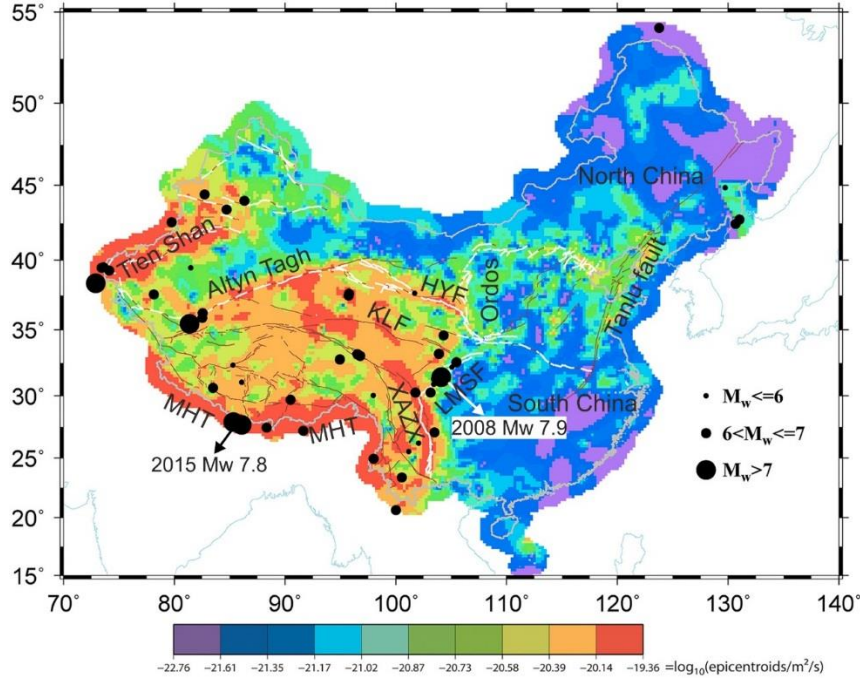


Figure 1.4. Common logarithm of the tectonic forecast of seismicity in mainland China and its surroundings. Update from Rui and Stamps (2019b). HYF: Haiyuan fault; XAXX: Xianshuihe-Anninghe-Zemuhe-Xiaojiang fault system; KLF: Kunlun fault; LMSF: Longmenshan fault; MHT: Main Himalayan Thrust.

As one developing technology, modern geodetic measurements, i.e., Global Positioning System (GPS) and Synthetic Aperture Radar Interferometry (InSAR), reveal that slip along crustal faults is composed of aseismic and seismic slip (e.g., Bürgmann et al., 2000; Kaneko et al., 2013; Jolivet et al., 2015b; Stevens and Avouac, 2015). At depths greater than about 30-40 km, steady aseismic slip becomes dominant, whereas great continental earthquakes result from rupture of heterogeneous patches or asperities at shallower depths. In order for elastic strain to build up and be released during large earthquakes, the fault must be wholly or partially locked during the interseismic phase so that a slip deficit accumulates. With sufficient geodetic observations, it is now possible to measure surface displacements associated with interseismic strain build up or release along continental faults in great detail, thus leading to higher resolution in identifying locked/creeping patches, characterizing their temporal evolution, providing insight into interseismic behaviors and earthquake cycle physics. These are the general issues that will be addressed in the thesis, which focuses on the Haiyuan fault system, Altyn Tagh fault and the Xianshuihe-Anninghe-Zemuhe-Xiaojiang (XAXX) fault system that bounding the Tibet (Figure 1.1).

1.2. Earthquake cycle

Crustal displacements have been observed since the late 1800s in Japan by geodetic leveling and coastal uplift (Nagata and Okada, 1947; Fitch and Scholz, 1971). These observations lead to recognize that earthquakes were cyclic, and that the cycle of earthquake could be divided into the interseismic, coseismic, and postseismic phases. The interseismic and coseismic phases could be quantitatively related when the concept of the elastic rebound was formulated (Reid, 1911). The theory assumes elastic rheology: tectonic movements result in a steady, slow, buildup of elastic strain within certain portions of the crust. When these strains reach the maximum supportable level, an elastic rebound (an earthquake) occurs in such a way as to release the stored strain energy, accompanied by a shear dislocation on the fault plane. The quantitative relationship is: the notion that interseismic and coseismic deformation are equal in magnitude but opposite in sign so that they cancel. The elastic rebound theory explains remarkably well the overall nature of major earthquakes. However, it has been confirmed that the strain release by actual earthquakes takes place in a variety of ways. For example, most major earthquakes are followed by aftershocks and, in most cases, by creep-like postseismic deformations. This variety results from the difference in the nature of the crust (visco-elastic of the mantle) and the stress field in the respective epicentral area. This usually be termed as postseismic deformation.

I show the conceptual cartoon of deformation in the crust and uppermost mantle in Figure 1.5a, which represents the earthquake cycle deformation along one strike-slip fault. In the following, I introduce the detailed crustal deformation in each stage of an earthquake cycle, along with typical examples of surface deformation mapped by geodetic measurements.

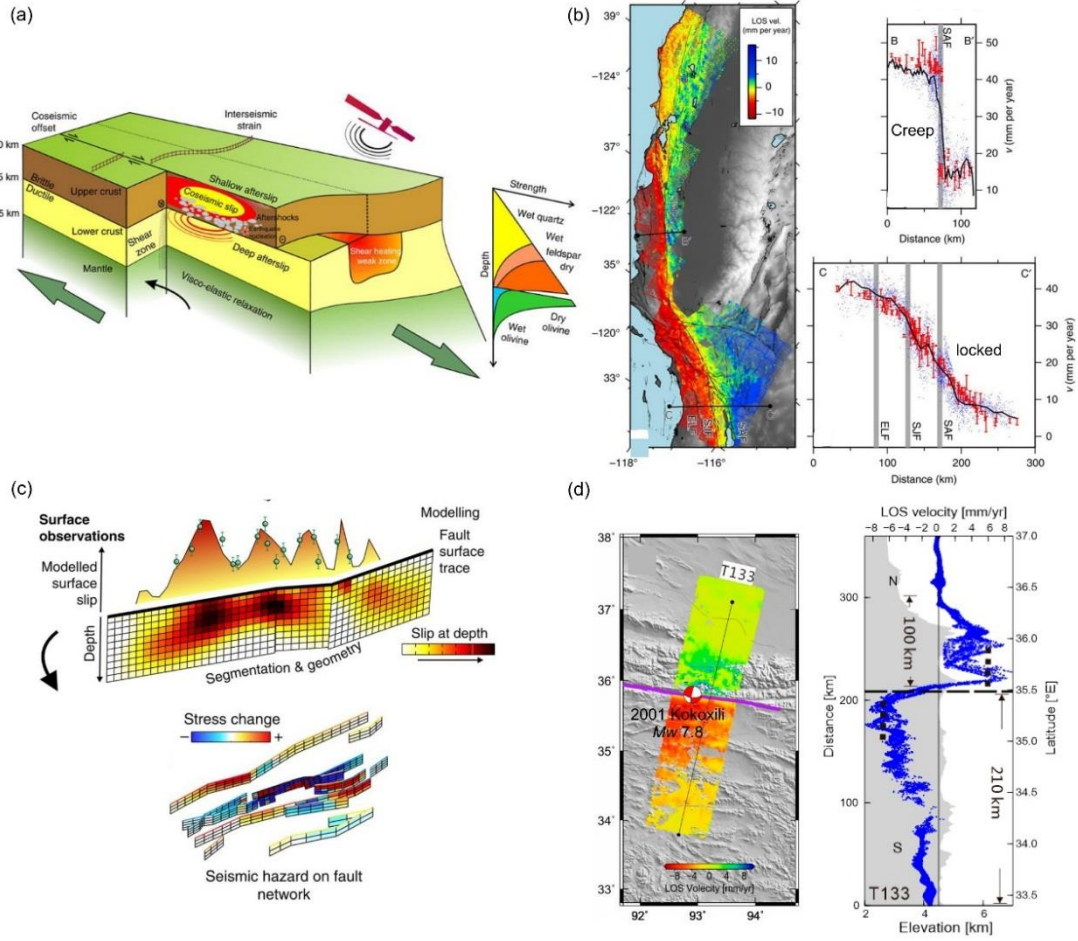


Figure 1.5. Crustal deformation during the earthquake cycle. (a) Conceptual cartoon of deformation in the crust and uppermost mantle. (b) Interseismic phase. InSAR interseismic crustal velocities along the San Andreas Fault Zone (SAF), California; corresponding InSAR displacements profiles are shown. (c) Coseismic phase. The complex slip distribution of an earthquake, and the occurrence of an earthquake increases and decreases the Coulomb failure stresses on nearby faults. (d) Postseismic phase. The InSAR Light of Sight (LOS) velocity across the Kunlun fault and corresponding LOS rate profile. Figure updated from Tong et al. (2013), Elliott et al. (2016) and Zhao et al. (2018).

1.2.1. Interseismic deformation

(1) Locked faults

Interseismic refers to the time between earthquakes (Harris, 2017). Reid (1910) made the first geodetic observation of interseismic deformation across the San Andreas Fault (SAF) in the 1860s and 1880s by triangulation. Since this pioneering work, similar measurements have been made across active deformation regions worldwide using modern geodetic technology, such as GPS and InSAR (e.g., Wang et al., 2001; Wright et al., 2004).

Savage and Burford (1973) first proposed the elastic screw dislocation model (equation 1.1) to analyze the triangulation data across the SAF:

$$V(x) = (V_0/\pi) * \arctan(x/D) \quad (1.1)$$

This approach models the fault as a buried infinite screw dislocation in homogeneous elastic half-space, where the interseismic aseismic slip occurs at a rate of V_0 below a locking depth of D , $V(x)$ is the displacement at a perpendicular distance x from the fault trace. In this model, no transition zone at depth is assumed, which is unphysical for strike-slip faults in nature. Nevertheless, it has been widely adopted to invert for fault slip rates and locking depths owing to its simplicity. There are geodetic data showing asymmetric patterns of interseismic velocities across strike-slip faults, which could result from varying elastic thickness (e.g., Chéry, 2008), lateral variations in the elastic strength, or a shift in the position of dislocation at depth relative to the fault trace (Le Pichon et al., 2005; He et al., 2013); modeling the asymmetry geodetic data needs more complex equation, and I will present in Chapter 3.

Savage (1983) proposed the ‘back slip’ model for strain accumulation and release at subduction zones. The model was originally motivated by the recognition that the overriding plate apparently experiences little permanent inelastic deformation on the timescales relevant to the seismic cycle (several hundred years). The back slip model accomplishes this zero net strain in the overriding plate by parameterizing interseismic fault slip as normal slip, i.e., back slip, on the same patch that also slips in the reverse sense during great earthquakes (see Savage, 1983). Along with the establishment of dislocation analytical solution (Okada, 1985), spatially variable coupling models were proposed (e.g., McCaffrey, 1995; Savage et al., 2000; Wallace et al., 2004), which characterize the interseismic fault slip on the fault plane using a unitless parameter (between 0 and 1), locking coefficient or the interseismic fault coupling. The locking coefficient is equal to the back-slip rate divided by fault loading rate. Under such a frame, both fully locked (coupled) patches and fully slipping (creeping) patches might co-exist on the same fault plane. This idea has continued to this day, and inverting for the interseismic fault coupling both along subduction zones (e.g., Nocquet et al., 2014) and continental faults (e.g., Stevens and Avouac, 2015), using GPS and InSAR, has become an important tool in assessing the seismic potential and investigating the fault physical mechanism.

(2) Aseismic slipping faults

Aseismic refers to the situation where neither earthquakes nor earthquake waves are generated. Aseismic fault slip occurs when there is gradual movement on a fault without generating seismic energy or fast-moving waves in the Earth’s crust (Harris, 2017). Both interseismic shallow fault creep and slow-slip events (SSEs) are aseismic processes.

Whereas most continental faults do appear to be interseismically locked, at least within the resolution of geodetic measurements, it was discovered more than 50 years ago (e.g., Louderback, 1942) that some continental faults at specific locations exhibit significant motion during the interseismic phase. Such phenomenon was named as shallow fault creep, and has been observed along several crustal faults, such as along the Haiyuan fault in China (e.g., Cavalié et al., 2008), the central San Andreas Fault in USA (e.g., Ryder and Bürgmann, 2008) and the North Anatolian Fault

(e.g., Cakir et al., 2005) among others. Shallow fault creep is a prominent behavior in earthquake cycle, I will present some mean observation of the process in Chapter 4 and 5.

In Figure 1.5b, I present one example to show the differences between locked and creeping segments. If the fault segment is creeping up to the surface, contrary to the locked segment that produces relatively smooth geodetic velocity gradient across the fault, fault-crossing geodetic velocity show sharp gradient or offset.

SSEs (also referred to as silent earthquakes) release strain on tectonic faults at slip rates faster than plate rates but slowly enough that seismic shaking is not generated. SSEs do not induce seismic waves but could produce surface deformation. SSEs have been measured along several subduction zones (e.g., Lowry et al., 2001; Radiguet et al., 2016; Voss et al., 2018) and the southern San Andreas Fault (e.g., Tymofyeyeva et al., 2019). SSEs often occur on adjacent regions of large earthquakes on the fault interface (Rolandone et al., 2018), which could last for weeks to months, releasing energy of similar magnitude to earthquakes. Previous studies along the Mexico subduction zone have suggested that SSEs are triggering factors for large earthquakes (e.g., Kostoglodov et al., 2003; Graham et al., 2014; Radiguet et al., 2016; Voss et al., 2018); however, there is also evidence that earthquakes can trigger SSEs (e.g., Zigone et al., 2012; Villegas-Lanza et al., 2016).

1.2.2. Coseismic deformation

Earthquakes are the result of sudden slip that dynamically propagate along a fault and release the accumulated strain during the interseismic phase (e.g., Davison, 1901; Reid, 1910, 1911). Earthquakes produce seismic waves, cause permanent displacements of the ground around the fault rupture, and induce Coulomb Failure Stress (CFS) perturbations along adjacent faults (Figure 1.5c). The seismic waves, with high resolution temporal information, for medium-large earthquakes could be recorded globally, and can be analyzed to investigate the rupture process (e.g., Ammon et al., 2005; Grandin et al., 2015). The coseismic ground static displacements could be recorded by triangulation, GPS, InSAR, Leveling and other geodetic measurements, which provide high spatial resolution. Over the last 30 years, GPS and InSAR were widely adopted to invert for the coseismic slip on the fault plane (e.g., Shen et al., 2009; Figure 1.6). To this date, despite the widely use of modern geodetic data in earthquake source inversions, it is still difficult to capture the ground deformation for medium-small earthquakes (M6-) owing to the low signal to noise ratio (Funning and Garcia, 2018). An earthquake could alter the shear and normal stress on surrounding faults, often integrated as Coulomb Failure Stress changes (ΔCFS). Positive ΔCFS could bring the fault closer to failure in the short term, thus increasing the seismic potential. Negative ΔCFS reduces the seismic hazard on the fault. Besides, the CFS is commonly used to interpret the occurrence of aftershocks and afterslips following an earthquake (e.g., Stein, 1999; Perfettini and Avouac, 2004).

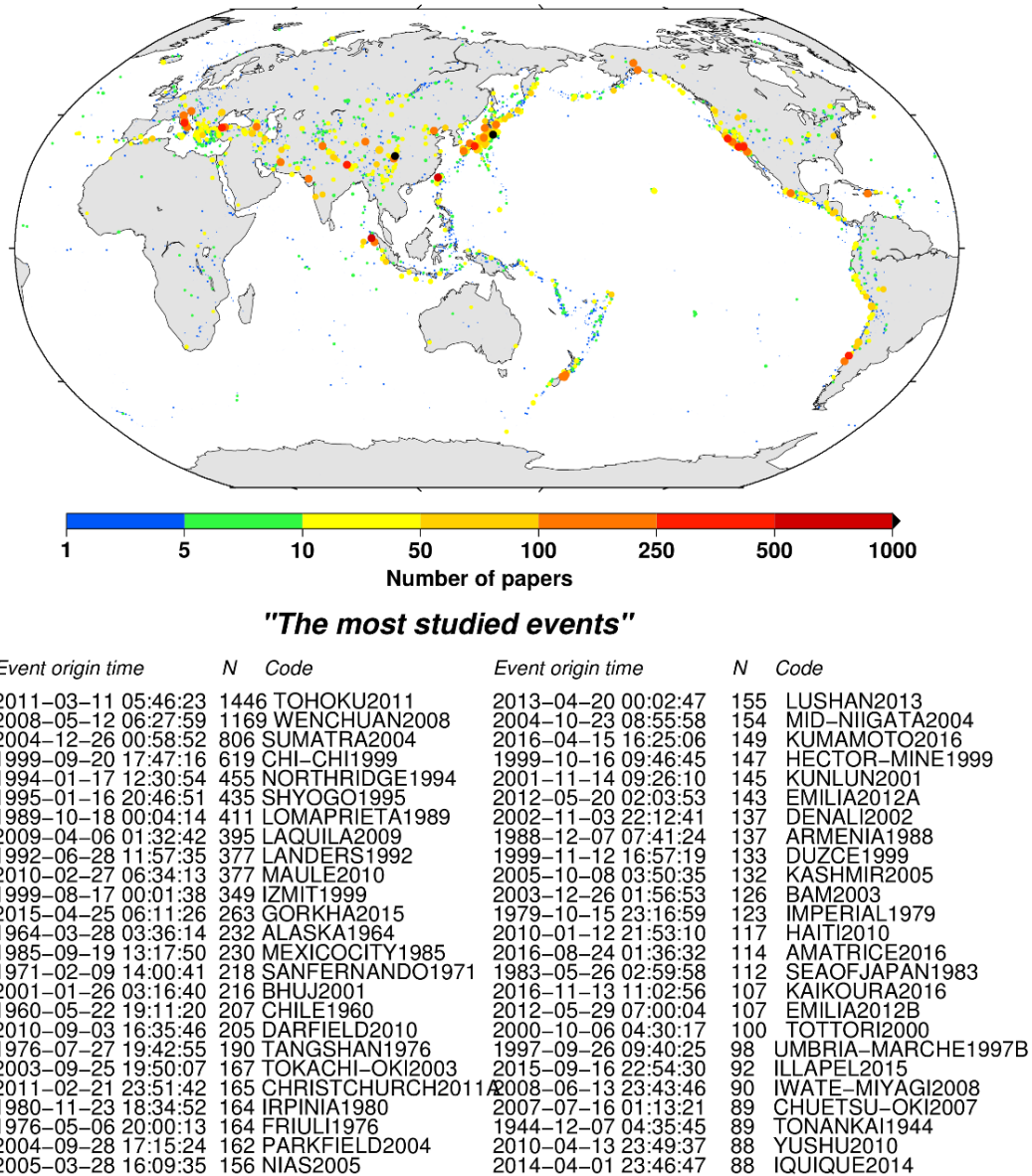


Figure 1.6. The map of seismic events color-coded by the number of associated scientific publications (top) and list of the top 50 earthquakes with the largest number of associated publications. Figure come from http://www.isc.ac.uk/event_bibliography/overview.php.

1.2.3. Postseismic deformation

Postseismic deformation was first measured by Okada and Nagata (1953) following the 1946 Mw 8.1 Nankaido, Japan, earthquake. Postseismic deformation typically occurs in hours to years following an earthquake, and provide constraints on the rheology of the lithosphere (Figure 1.5d). Three different mechanisms have been proposed to interpret the postseismic deformation following large earthquakes: aseismic afterslip (e.g. Bürgmann et al., 2002), poroelastic rebound (e.g., Peltzer et al., 1998) and viscoelastic relaxation (e.g., Nur and Mavko, 1974). Afterslip is attributed to the interaction of a velocity-weakening region at depth (within which earthquakes nucleate) with an upper region of velocity-strengthening frictional behavior (Marone et al., 1991); that is, coseismic

stress changes drive aseismic afterslip. Commonly, afterslip decay rapidly following a large earthquake and last for days to years. Poroelastic rebound is related to coseismic pressure changes, which drive fluid flow within the upper crust; poroelastic rebound often affect regions around the fault. Viscoelastic relaxation, where coseismic stress changes imparted to the hot lower crust and upper mantle cannot be sustained and drive viscoelastic flow, could last for tens of years and to more wide spread. After a large earthquake, these different mechanisms may not always operate separately, and distinguishing between them is often difficult.

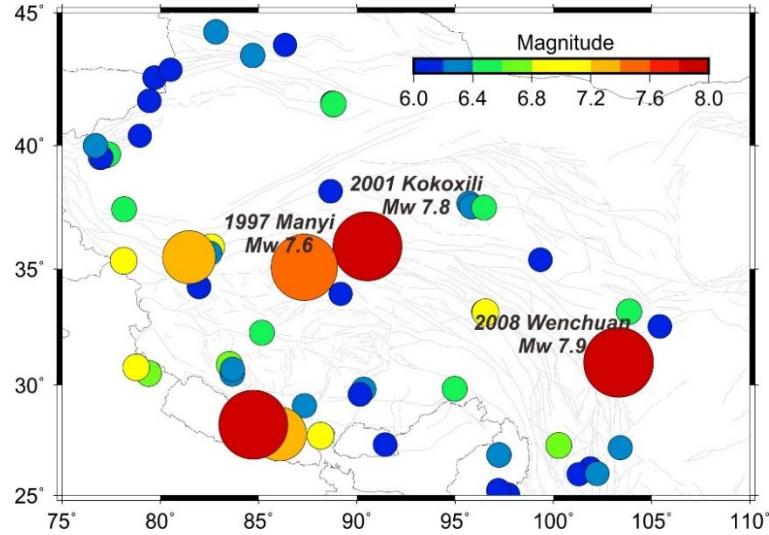


Figure 1.7. Map showing earthquakes with magnitudes larger than 6.0 occurred in and around the **Tibetan Plateau in 1990-2019**. Labels show the three earthquakes with significant postseismic deformation that have been studied using GPS and/or InSAR.

Within Tibet, several earthquakes with significant postseismic deformation have been documented using GPS and/or InSAR (Figure 1.7), such as the 1997 Manyi Mw 7.6 earthquake (e.g., [Ryder et al., 2007](#)), the 2001 Kokoxili Mw 7.8 earthquake (e.g., [Wen et al., 2012](#); [Zhao et al., 2018](#); [Liu et al., 2019](#)), and the 2008 Wenchuan Mw 7.9 earthquake (e.g., [Huang et al., 2014](#); [Diao et al., 2018](#)). Note that, despite these large earthquakes have occurred 10-20 years ago, the post-earthquake geodetic velocity solutions in Tibet are still be contaminated by slow ongoing postseismic deformation ([Li et al., 2019](#)).

1.3. Previous geodetic observation and modelling of crustal deformation in the Tibetan Plateau

Modern geodetic measurements using GPS in Tibet date back to the early 1990s when different international research projects and institutes established several regional GPS networks for crustal deformation studies in China and neighboring regions (e.g., King et al., 1997; Bendick et al., 2000; Zhu et al., 2000; Chen et al., 2000; 2004; Wang et al., 2001). By 1999, a nationwide GPS network, the Crustal Movement Observation Network of China (CMONOC-I), had been established. The CMONOC-I network included 27 continuously operating GPS stations and 1056 campaign-mode GPS stations (Niu et al., 2005). In 2009, the Tectonic and Environmental Observation Network of Mainland China (CMONOC-II) was established, adding 233 continuous stations and 1000 campaign-mode stations to the CMONOC I network (Gan et al., 2012; Figure 1.8, 1.9). To this date, campaign-mode GPS stations have been observed regularly in 1999, 2001, 2004, 2007, 2009, 2011, 2013, 2015, 2017 and 2019, with at least four days (30 s sampling rate) of continuously record. Moreover, campaign-mode observations were undertaken in Sichuan, Ordos, North China, Sichuan, Yunnan, and the Tianshan area in 2012, 2014, and 2016.

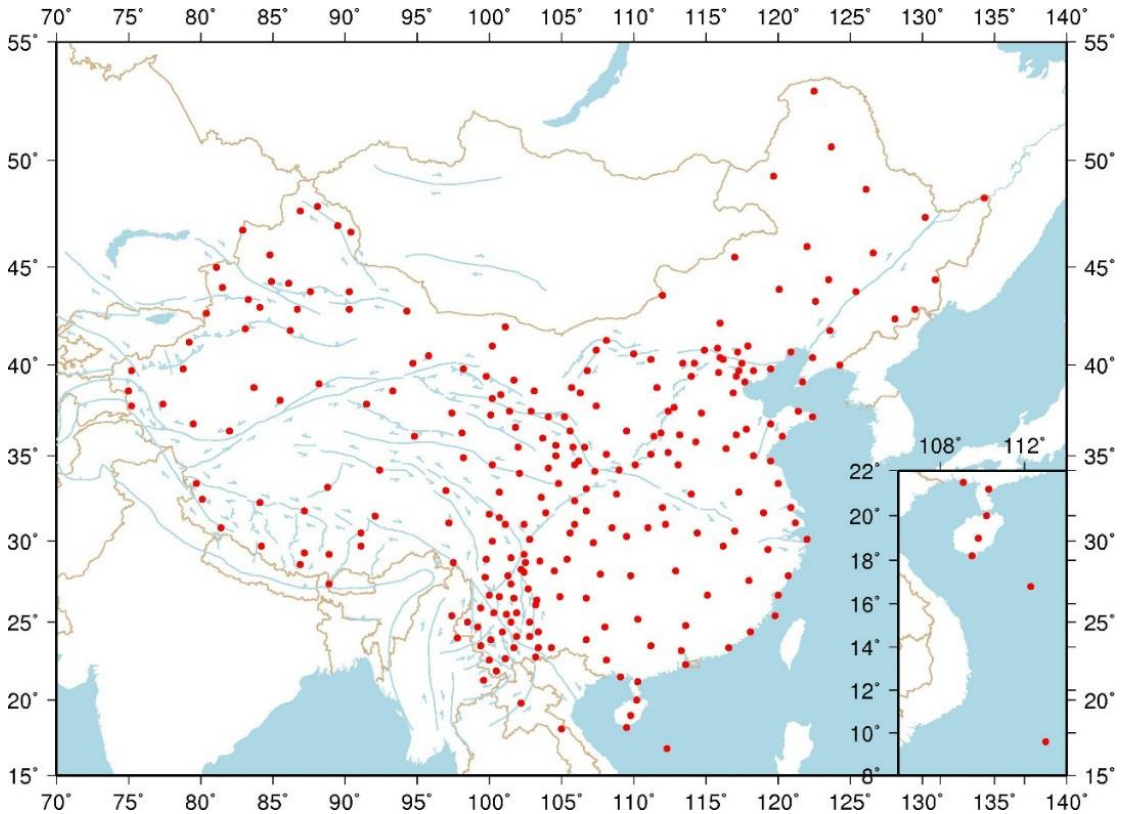


Figure 1.8. Continuous GPS stations in mainland China (<http://www.cgps.ac.cn/>).

Over the last 20 years, GPS data from CMONOC has been extensively used in earthquake cycle deformation studies, including interseismic deformation (e.g., Wang et al., 2001; Zhang et al.,

2004; Gan et al., 2007; Liang et al., 2013), coseismic deformation (e.g., Shen et al., 2009; Wang et al., 2011; Jiang et al., 2014), and postseismic deformation (e.g., Diao et al., 2018; Li et al., 2019; Figure 1.7). Here in my thesis, I focus on the interseismic deformation along the Haiyuan fault system, Altyn Tagh fault and the Xianshuihe-Anninghe-Zemuhe-Xiaojiang (XAZX) fault system (Figure 1.1). In the following, I introduce only previous studies about interseismic GPS velocity field.

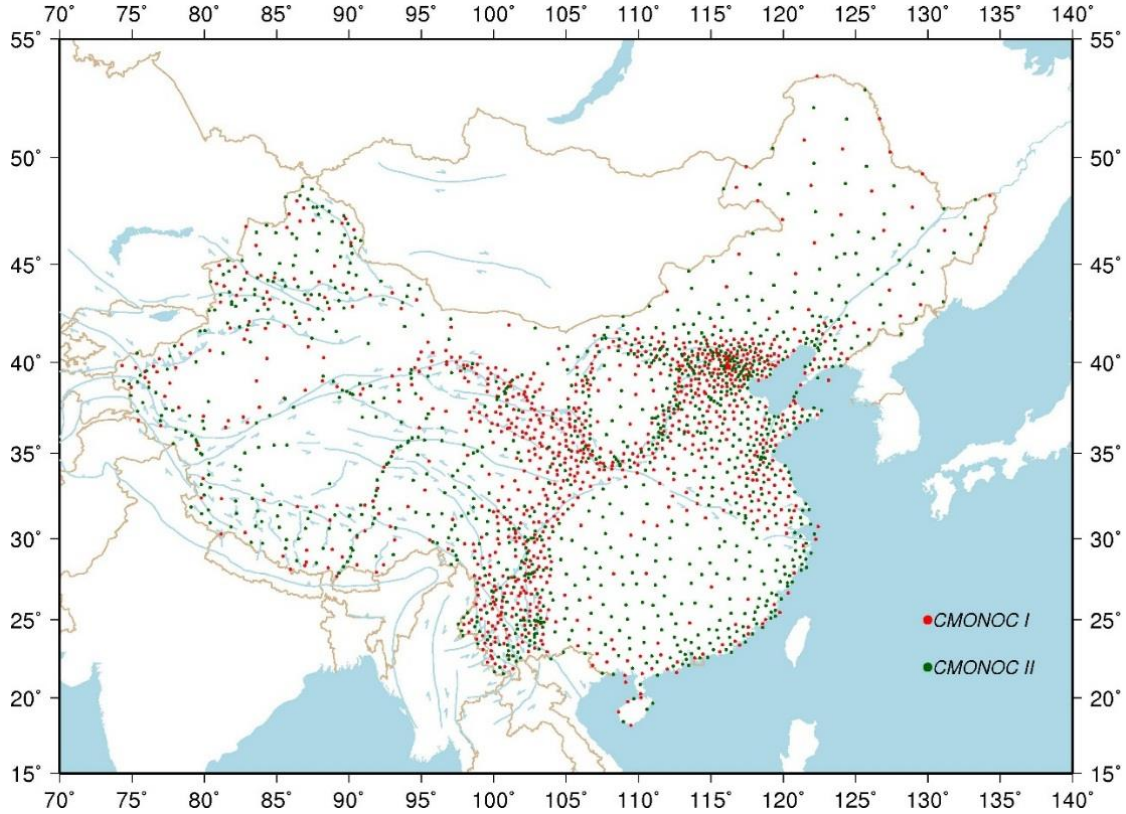


Figure 1.9. Campaign-mode GPS stations in mainland China (<http://www.cgps.ac.cn/>).

Wang et al. (2001) derived the first nationwide interseismic GPS horizontal velocity field (354 stations in total) using the GPS data measured between 1991 and 2001. The velocity map depicts the general crustal deformation of the Tibetan Plateau and provides constraints for several deformation areas or faults. At the large scale, they argued that deformation within the Tibet and its margins, the Himalaya, the Altyn Tagh, and the Qilian Shan, absorbs more than 90% of the relative motion between the Indian and Eurasian plates; internal shortening of the Tibetan plateau itself accounts for more than one-third of the total convergence. Subsequently, Zhang et al. (2004) included more GPS stations (553) with longer time span (1998-2004) and derived an enlarged interseismic GPS velocity map of Tibet. By conducting and analyzing GPS velocity profiles, they argued that the present-day tectonics in the plateau could be best described as deformation of a continuous medium, at least when averaged over distances larger than 100 km. Gan et al. (2007) updated the GPS velocity solution by including 726 GPS stations in and around the Tibetan Plateau. Although the spatial resolution of these above velocity solutions are limited compared to subsequent

published results (e.g., Liang et al., 2013; Ge et al., 2015; Wang et al., 2017; Zheng et al., 2017), they represent the secular interseismic crustal deformation of Tibet (Figure 1.10). As in the above velocity solutions, data of GPS stations that along the Kunlun fault, where the 2001 Kokoxili Mw 7.8 earthquake occurred, were excluded. Here, I use the ‘secular’ to refer to the velocity solution is not contaminated by postseismic deformation. After that, Liang et al. (2013), Ge et al. (2015), Wang et al. (2017) and Zheng et al. (2017) published their own GPS velocity solution of the Tibet or mainland China, however, an important factor was ignored, that is, the postseismic deformation of the 2001 Kokoxili Mw 7.8 earthquake was ignored, despite they all excluded the GPS stations (measured after the 2008 Wenchuan Mw 7.9 earthquake) in eastern Tibet (Liu et al., 2019). The readers are recommend to refer Wen et al. (2012) and Zhao et al. (2018) for detailed knowledge of postseismic deformation of the 2001 Kokoxili Mw 7.8 earthquake. Note that in Liang et al.’s solution, they also derived the vertical velocity field of the Tibetan Plateau. I discuss their reliability in Chapter 4 for northeastern Tibet.

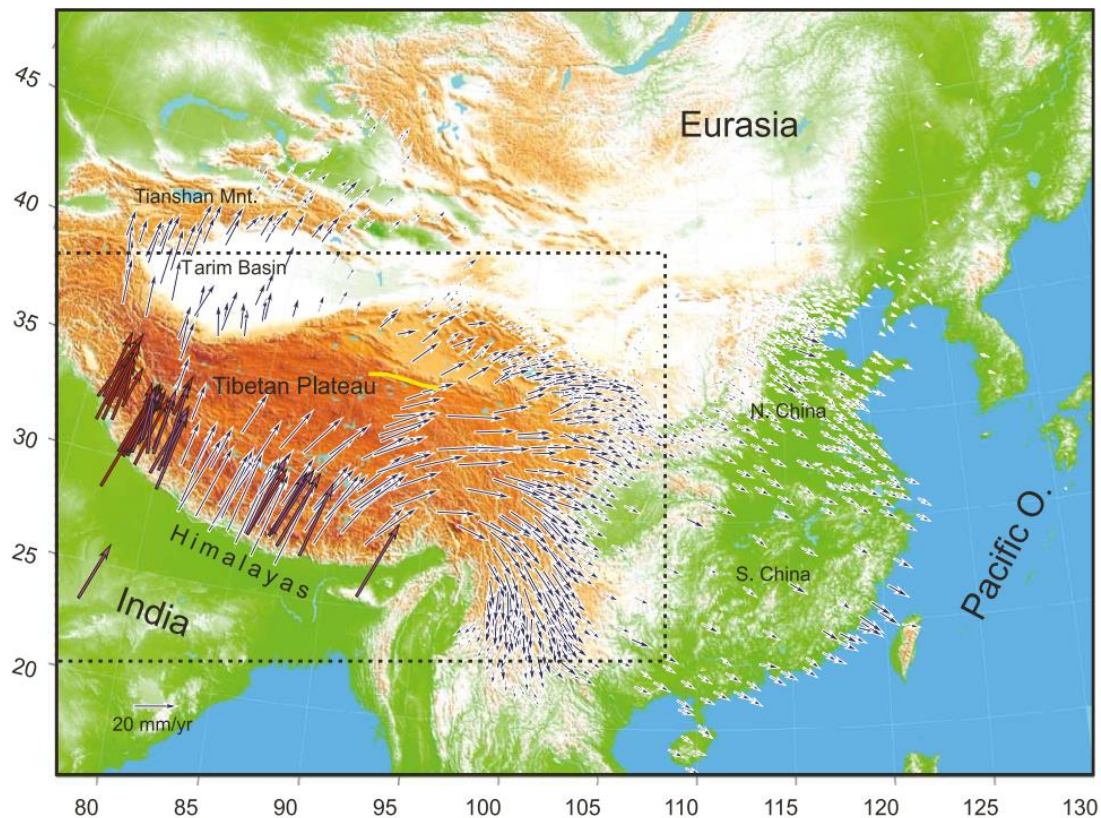


Figure 1.10. GPS velocity field of crustal motion in central Asia relative to the stable Eurasia. Figure come from Gan et al. (2007).

With the publication of GPS velocity solutions, geodesists focused on interpreting the velocity results. Wang et al. (2001), Zhang et al. (2004), Gan et al. (2007) and Ge et al. (2015) proposed the horizontal GPS velocities could explained by the ‘continuum model’, in spite of different methods or interpretations/arguments. Meanwhile, some other geodesists argued that the horizontal GPS velocities could be modeled by (elastic) block models. For instance, Shen et al. (2005) modeled the

GPS velocities in southeastern Tibet using block models and obtained a satisfactory data fitting. They proposed that the crustal deformation of southeastern Tibet could be described by rotating blocks, bounded by crustal faults, of different scales. Subsequently, Meade and Hager (2005), Thatcher (2007), Loveless and Meade (2011) and Wang et al. (2017) developed microplate or block models for Tibet. Despite differences in the scale and number of blocks, their block model predictions agree well with observations. The debate of ‘continuum model’ and ‘block model’ is not well resolved so far. Thatcher (2007) argued that as the size of the blocks decreases and tends towards the thickness of the seismogenic layer, the block model approaches a continuum and will be indistinguishable from surface velocities.

Over the last 30 years, many studies, using interseismic GPS velocities, focused on regional areas or specific faults, such as the northeastern Tibetan Plateau (e.g., Li et al., 2017), the Altyn Tagh fault (e.g., Li et al., 2018a), and the Xianshuihe-Xiaojiang fault system (e.g., Jiang et al., 2015). To avoid repeating, I will introduce previous work of each of the fault system in the following chapters.

Table 1.1. Summary of previous InSAR Studies

Location	Study	Location	Study
A	Wright et al., 2004	M	Bell et al., 2011
B	Taylor and Peltzer, 2006	N	Grandin et al., 2012
C	Taylor and Peltzer, 2006	O	Qiao et al., 2017
D	Taylor and Peltzer, 2006	P	Liu et al., 2011
E	Lasserre et al., 2007	Q	Garthwaite et al., 2013
F	Lasserre et al., 2007	R	Wen et al., 2012
	Jolivet et al., 2008		Zhao et al., 2018
	Elliott et al., 2008		
G	Daout et al., 2018	S	Song et al., 2019
	Cavalié et al., 2008		
H	Daout et al., 2016	T	Zhu et al., 2016
J	Wang et al., 2009	U	Wang et al., 2019
K	Wang and Wright, 2012	V	Huang et al., 2014
L	Jolivet et al., 2012		

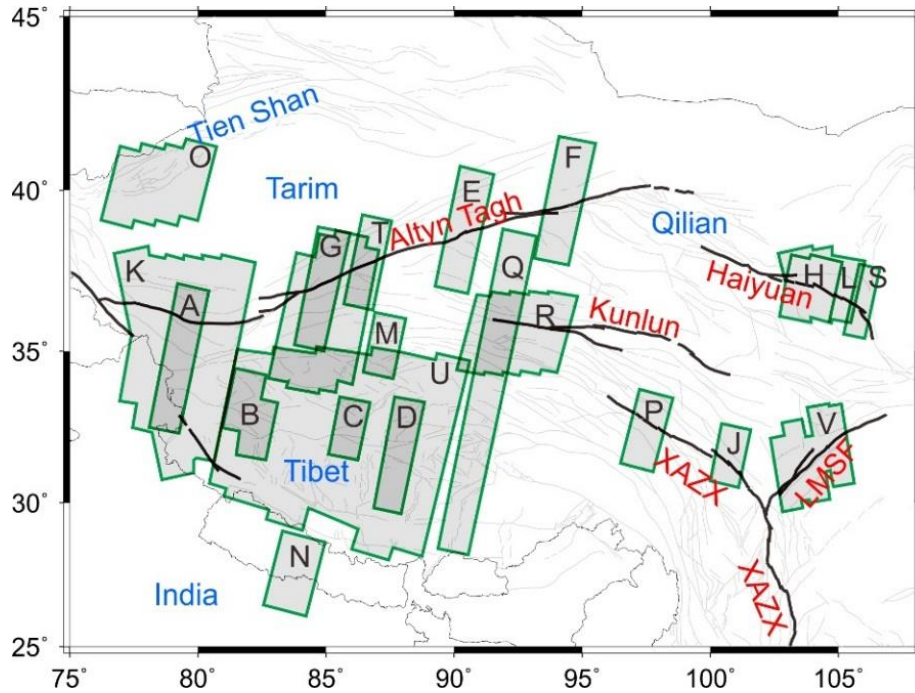


Figure 1.11. Map showing the distribution of published InSAR studies of interseismic deformation in Tibet. Grey polygons with green outlines show the spatial extent of Synthetic Aperture Radar (SAR) data used in each study. See Table 1.1 for the citations relating to each lettered polygon.

The interseismic InSAR studies in Tibet date back to Wright et al. (2004), who used the European Remote Sensing Satellite (ERS) data spanning 1992-1999 to constrain the slip rates on the Karakoram and Altn Tagh faults. Their results show that slip rates on the Karakoram and Altn Tagh faults are lower than what would be expected from the extrusion model and suggest a significant amount of internal deformation in Tibet. Subsequently, Lasserre et al. (2007), Elliott et al. (2008), Jolivet et al. (2008), Wang and Wright (2012), Zhu et al. (2016), Daout et al. (2018), and Xu and Zhu. (2019) processed different sources/time-spans SAR data covering different segments of the Altn Tagh fault, aiming at either estimating its slip rate/locking depth or investigating the strain partitioning between several crustal faults in northwestern Tibet. Also, the crustal deformation along the Haiyuan fault attracted attention of geodesists. Cavalié et al. (2008) first introduced SAR data to map the left-lateral motion along the Laohushan segment. They identified a shallow creeping section along the Laohushan segment, which was later confirmed by Jolivet et al. (2012) and further studied by Jolivet et al. (2013) and Daout et al. (2015). Other faults in Tibet have also been investigated by InSAR, such as the Xianshuihe fault (Wang et al., 2009; Liu et al., 2011) and the Main Himalayan Thrust (Grandin et al., 2012). Moreover, with the accumulation of SAR data and improvement of data processing methods, large-scaled crustal deformation monitoring using InSAR becomes now possible, as the work done by Wang et al. (2019) (Figure 1.11). Furthermore, the monitoring of postseismic deformation using InSAR has been conducted along the Manyi fault (e.g., Bell et al., 2011), Kunlun fault (e.g., Wen et al., 2012; Zhao et al., 2018) and the Longmenshan fault (Huang et al., 2014). I show in Figure 1.11 the distribution of published InSAR studies of

interseismic deformation in Tibet. Although many areas of the Tibetan Plateau have been studied using InSAR, there are still large unmapped areas, especially in the southeastern Tibet, where dense vegetation cover causes a loss of coherence.

1.4. The aims of this thesis

The thesis focuses on three large strike-slip faults which pose a significant seismic hazard in Tibet, the Altyn Tagh fault, the Haiyuan fault system and the XAZX fault system (Figure 1.1). These faults have slip rates ranging from 2-12 mm/a, intensive historical earthquakes, different interseismic deformation characteristics (locked and shallow creeping segments), and distinct earthquake cycles. Benefiting from the geodetic observations (GPS and InSAR) across these faults, we could investigate into the interseismic fault coupling and lateral variation of coupling along faults distance. The thesis seeks to answer the following general questions: what's the interseismic fault coupling along these faults and the seismic potential implications? The existence and distribution of shallow aseismic creep and their temporal/spatial behaviors? What we could learn about the earthquake cycle from the present-day fault deformation? For each crustal fault I studied, I emphasize its specific scientific issues in the following chapters. I will use GPS and InSAR to measure the interseismic velocities across these faults, interpret the geodetic data in detail, model the geodetic data using both two dimensional and three dimensional kinematic models, and finally interpret the results and their implications.

The rest of this thesis is organized as follows:

Chapter 2 describes, in general, the geodetic data (GPS and InSAR) and processing methods. It presents methods for GPS and InSAR comparison and integration, and shows the GPS/InSAR integration result in northeastern Tibet.

Chapter 3 consists of two part. The first is adapted from my paper ([Li et al., 2018a](#)), which investigates the fault coupling along the Altyn Tagh fault. The remaining describes the interseismic GPS/InSAR velocity solution across the western Altyn Tagh fault (86°E), and inverts for the slip rate and locking depth on the fault.

Chapter 4 is a paper in preparation. It describes newly identified shallow creeping along the Haiyuan fault system, presents the elastic block modeling of GPS/InSAR data around the Haiyuan fault system, and describes the interseismic fault coupling and earthquake cycle along the Haiyuan fault system.

Chapter 5 is a paper submitted to Earth and Planetary Science Letters. It describes the interseismic locking and creeping on the Xianshuihe-Xiaojiang fault system, based on GPS and InSAR. Seismic potential and earthquake cycle behavior along the fault system are also discussed.

Chapter 6 summarizes the findings of the previous chapters, discusses the implications of these findings, and explores future works.

1.5. References

- Ammon, C. J., Ji, C., Thio, H. K., Robinson, D., Ni, S., Hjorleifsdottir, V., ... & Ichinose, G. (2005). Rupture process of the 2004 Sumatra-Andaman earthquake. *Science*, 308(5725), 1133-1139.
- Argand, E. (1924), La Tectonique de l'Asie, in *Compte-rendu du 13e congrès Géologique International* (in French), pp. 171-372, Int. Geol. Congr., Brussels.
- Avouac, J. P., & Tapponnier, P. (1993). Kinematic model of active deformation in central Asia. *Geophysical Research Letters*, 20(10), 895-898.
- Bell, M. A., Elliott, J. R., & Parsons, B. E. (2011). Interseismic strain accumulation across the Manyi fault (Tibet) prior to the 1997 Mw 7.6 earthquake. *Geophysical Research Letters*, 38(24).
- Bendick, R., Bilham, R., Freymueller, J., Larson, K., & Yin, G. (2000). Geodetic evidence for a low slip rate in the Altyn Tagh fault system. *Nature*, 404(6773), 69.
- Bürgmann, R., Ergintav, S., Segall, P., Hearn, E. H., McClusky, S., Reilinger, R. E., ... & Zschau, J. (2002). Time-dependent distributed afterslip on and deep below the Izmit earthquake rupture. *Bulletin of the Seismological Society of America*, 92(1), 126-137.
- Bürgmann, R., Schmidt, D., Nadeau, R. M., d'Alessio, M., Fielding, E., Manaker, D., ... & Murray, M. H. (2000). Earthquake potential along the northern Hayward fault, California. *Science*, 289(5482), 1178-1182.
- Cakir, Z., Akoglu, A. M., Belabbes, S., Ergintav, S., & Meghraoui, M. (2005). Creeping along the Ismetpasa section of the North Anatolian fault (Western Turkey): Rate and extent from InSAR. *Earth and Planetary Science Letters*, 238(1-2), 225-234.
- Cavalié, O., Lasserre, C., Doin, M. P., Peltzer, G., Sun, J., Xu, X., & Shen, Z. K. (2008). Measurement of interseismic strain across the Haiyuan fault (Gansu, China), by InSAR. *Earth and Planetary Science Letters*, 275(3-4), 246-257.
- Chen, Q., Freymueller, J. T., Yang, Z., Xu, C., Jiang, W., Wang, Q., & Liu, J. (2004). Spatially variable extension in southern Tibet based on GPS measurements. *Journal of Geophysical Research: Solid Earth*, 109(B9).
- Chen, Z. H., Burchfiel, B. C., Liu, Y., King, R. W., Royden, L. H., Tang, W., ... & Zhang, X. (2000). Global Positioning System measurements from eastern Tibet and their implications for India/Eurasia intercontinental deformation. *Journal of Geophysical Research: Solid Earth*, 105(B7), 16215-16227.
- Cheng-Fa, C., & Chang, Hsi-Lan. (1973). Some tectonic features of the Mt. Jolmo Lungma area, southern Tibet, China. *Scientia Sinica*, 16(2), 257-265.
- Chéry, J. (2008). Geodetic strain across the San Andreas Fault reflects elastic plate thickness variations (rather than fault slip rate). *Earth and Planetary Science Letters*, 269(3-4), 352-365.
- Clark, M. K., & Royden, L. H. (2000). Topographic ooze: Building the eastern margin of Tibet by lower crustal flow. *Geology*, 28(8), 703-706.
- Daout, S., Doin, M. P., Peltzer, G., Lasserre, C., Socquet, A., Volat, M., & Sudhaus, H. (2018). Strain partitioning and present-day fault kinematics in NW Tibet from Envisat SAR interferometry. *Journal of Geophysical Research: Solid Earth*, 123(3), 2462-2483.
- Daout, S., Jolivet, R., Lasserre, C., Doin, M. P., Barbot, S., Tapponnier, P., ... & Sun, J. (2016). Along-strike variations of the partitioning of convergence across the Haiyuan fault system detected by InSAR. *Geophysical Journal International*, 205(1), 536-547.

- Davison, C. (1901). The Great Japanese Earthquake of October 28, 1891. *The Geographical Journal*, 17(6), 635-655.
- Deng, Q., Chen, S., Song, F., Zhu, S., Wang, Y., Zhang, W., ... & Zhang, P. (1986). Variations in the geometry and amount of slip on the Haiyuan (Nanxihaushan) fault zone, China, and the surface rupture of the 1920 Haiyuan earthquake. *Earthquake Source Mechanics, Geophys. Monogr. Ser.*, 37, 169-182.
- Deng, Q., Cheng, S., Ma, J., & Peng, D. (2014). Seismic activities and earthquake potential in the Tibetan Plateau. *Chinese Journal of Geophysics*, 57(5), 678-697.
- Deng, Q., Zhang, P., Ran, Y., Yang, X., Min, W., & Chu, Q. (2003). Basic characteristics of active tectonics of China. *Science in China Series D: Earth Sciences*, 46(4), 356-372.
- Dewey, J. F., & Burke, K. C. (1973). Tibetan, Variscan, and Precambrian basement reactivation: products of continental collision. *The Journal of Geology*, 81(6), 683-692.
- Diao, F., Wang, R., Wang, Y., Xiong, X., & Walter, T. R. (2018). Fault behavior and lower crustal rheology inferred from the first seven years of postseismic GPS data after the 2008 Wenchuan earthquake. *Earth and Planetary Science Letters*, 495, 202-212.
- Elliott, J. R., Biggs, J., Parsons, B., & Wright, T. J. (2008). InSAR slip rate determination on the Altyn Tagh Fault, northern Tibet, in the presence of topographically correlated atmospheric delays. *Geophysical Research Letters*, 35(12).
- Elliott, J. R., Walters, R. J., & Wright, T. J. (2016). The role of space-based observation in understanding and responding to active tectonics and earthquakes. *Nature Communications*, 7, 13844.
- England, P. C., & Houseman, G. A. (1988). The mechanics of the Tibetan Plateau. *Philosophical Transactions of the Royal Society of London. Series A, Mathematical and Physical Sciences*, 326(1589), 301-320.
- England, P., & Houseman, G. (1986). Finite strain calculations of continental deformation: 2. Comparison with the India-Asia collision zone. *Journal of Geophysical Research: Solid Earth*, 91(B3), 3664-3676.
- Fitch, T. J., & Scholz, C. H. (1971). Mechanism of underthrusting in southwest Japan: A model of convergent plate interactions. *Journal of Geophysical Research*, 76(29), 7260-7292.
- Funning, G. J., & Garcia, A. (2018). A systematic study of earthquake detectability using Sentinel-1 Interferometric Wide-Swath data. *Geophysical Journal International*, 216(1), 332-349.
- Gan, W., Li, Q., Zhang, R., & Shi, H. B. (2012). Construction and application of tectonics and environmental observation network of mainland China. *J. Eng. Stud.*, 4(4), 324-331.
- Gan, W., Zhang, P., Shen, Z. K., Niu, Z., Wang, M., Wan, Y., ... & Cheng, J. (2007). Present-day crustal motion within the Tibetan Plateau inferred from GPS measurements. *Journal of Geophysical Research: Solid Earth*, 112(B8).
- Gaudemer, Y., Tapponnier, P., Meyer, B., Peltzer, G., Shunmin, G., Zhitai, C., ... & Cifuentes, I. (1995). Partitioning of crustal slip between linked, active faults in the eastern Qilian Shan, and evidence for a major seismic gap, the 'Tianzhu gap', on the western Haiyuan Fault, Gansu (China). *Geophysical Journal International*, 120(3), 599-645.
- Ge, W. P., Molnar, P., Shen, Z. K., & Li, Q. (2015). Present-day crustal thinning in the southern and northern Tibetan plateau revealed by GPS measurements. *Geophysical Research Letters*, 42(13), 5227-5235.
- Graham, S. E., DeMets, C., Cabral-Cano, E., Kostoglodov, V., Walpersdorf, A., Cotte, N., ... &

- Salazar-Tlaczani, L. (2014). GPS constraints on the 2011–2012 Oaxaca slow slip event that preceded the 2012 March 20 Ometepe earthquake, southern Mexico. *Geophysical Journal International*, 197(3), 1593-1607.
- Grandin, R., Doin, M. P., Bollinger, L., Pinel-Puyssegur, B., Ducret, G., Jolivet, R., & Sapkota, S. N. (2012). Long-term growth of the Himalaya inferred from interseismic InSAR measurement. *Geology*, 40(12), 1059-1062.
- Grandin, R., Vallée, M., Satriano, C., Lacassin, R., Klinger, Y., Simoes, M., & Bollinger, L. (2015). Rupture process of the Mw= 7.9 2015 Gorkha earthquake (Nepal): Insights into Himalayan megathrust segmentation. *Geophysical Research Letters*, 42(20), 8373-8382.
- Harris, R. A. (2017). Large earthquakes and creeping faults. *Reviews of Geophysics*, 55(1), 169-198.
- He, J., Vernant, P., Chéry, J., Wang, W., Lu, S., Ku, W., ... & Bilham, R. (2013). Nailing down the slip rate of the Altyn Tagh fault. *Geophysical Research Letters*, 40(20), 5382-5386.
- Huang, M. H., Bürgmann, R., & Freed, A. M. (2014). Probing the lithospheric rheology across the eastern margin of the Tibetan Plateau. *Earth and Planetary Science Letters*, 396, 88-96.
- Jiang, G., Xu, X., Chen, G., Liu, Y., Fukahata, Y., Wang, H., ... & Xu, C. (2015). Geodetic imaging of potential seismogenic asperities on the Xianshuihe-Anninghe-Zemuhe fault system, southwest China, with a new 3-D viscoelastic interseismic coupling model. *Journal of Geophysical Research: Solid Earth*, 120(3), 1855-1873.
- Jiang, Z., Wang, M., Wang, Y., Wu, Y., Che, S., Shen, Z. K., ... & Li, Q. (2014). GPS constrained coseismic source and slip distribution of the 2013 Mw6. 6 Lushan, China, earthquake and its tectonic implications. *Geophysical Research Letters*, 41(2), 407-413.
- Jolivet, R., Candela, T., Lasserre, C., Renard, F., Klinger, Y., & Doin, M. P. (2015a). The Burst-Like Behavior of Aseismic Slip on a Rough Fault: The Creeping Section of the Haiyuan Fault, China Short Note. *Bulletin of the Seismological Society of America*, 105(1), 480-488.
- Jolivet, R., Cattin, R., Chamot-Rooke, N., Lasserre, C., & Peltzer, G. (2008). Thin-plate modeling of interseismic deformation and asymmetry across the Altyn Tagh fault zone. *Geophysical Research Letters*, 35(2).
- Jolivet, R., Lasserre, C., Doin, M. P., Guillaso, S., Peltzer, G., Dailu, R., ... & Xu, X. (2012). Shallow creep on the Haiyuan fault (Gansu, China) revealed by SAR interferometry. *Journal of Geophysical Research: Solid Earth*, 117(B6).
- Jolivet, R., Lasserre, C., Doin, M. P., Peltzer, G., Avouac, J. P., Sun, J., & Dailu, R. (2013). Spatio-temporal evolution of aseismic slip along the Haiyuan fault, China: Implications for fault frictional properties. *Earth and Planetary Science Letters*, 377, 23-33.
- Jolivet, R., Simons, M., Agram, P. S., Duputel, Z., & Shen, Z. K. (2015b). Aseismic slip and seismogenic coupling along the central San Andreas Fault. *Geophysical Research Letters*, 42(2), 297-306.
- Kaneko, Y., Fialko, Y., Sandwell, D. T., Tong, X., & Furuya, M. (2013). Interseismic deformation and creep along the central section of the North Anatolian fault (Turkey): InSAR observations and implications for rate-and-state friction properties. *Journal of Geophysical Research: Solid Earth*, 118(1), 316-331.
- King, R. W., Shen, F., Clark Burchfiel, B., Royden, L. H., Wang, E., Chen, Z., ... & Li, Y. (1997). Geodetic measurement of crustal motion in southwest China. *Geology*, 25(2), 179-182.
- Kirby, E., Whipple, K., & Harkins, N. (2008). Topography reveals seismic hazard. *Nature*

- Geoscience, 1(8), 485.
- Kostoglodov, V., Singh, S. K., Santiago, J. A., Franco, S. I., Larson, K. M., Lowry, A. R., & Bilham, R. (2003). A large silent earthquake in the Guerrero seismic gap, Mexico. *Geophysical Research Letters*, 30(15).
- Lasserre, C., Cavalié, O., Peltzer, G., Socquet, A., Doin, M. P., Sun, J., ... & Gaudemer, Y. (2007). Interseismic strain across the Altyn Tagh and Haiyuan faults at the northern edge of the Tibetan plateau, measured by space geodesy. *EGU General Assembly*.
- Le Pichon, X., Kreemer, C., & Chamot-Rooke, N. (2005). Asymmetry in elastic properties and the evolution of large continental strike-slip faults. *Journal of Geophysical Research: Solid Earth*, 110(B3).
- Li, C., Zhang, P. Z., Yin, J., & Min, W. (2009). Late Quaternary left-lateral slip rate of the Haiyuan fault, northeastern margin of the Tibetan Plateau. *Tectonics*, 28(5).
- Li, Y., Jia, D., Wang, M., Shaw, J. H., He, J., Lin, A., ... & Rao, G. (2014). Structural geometry of the source region for the 2013 Mw 6.6 Lushan earthquake: Implication for earthquake hazard assessment along the Longmen Shan. *Earth and Planetary Science Letters*, 390, 275-286.
- Li, Y., Shan, X., & Qu, C. (2019). Geodetic Constraints on the Crustal Deformation along the Kunlun Fault and Its Tectonic Implications. *Remote Sensing*, 11(15), 1775.
- Li, Y., Shan, X., Qu, C., Liu, Y., & Han, N. (2018a). Crustal deformation of the Altyn Tagh fault based on GPS. *Journal of Geophysical Research: Solid Earth*, 123(11), 10309-10322.
- Li, Y., Shan, X., Qu, C., Zhang, Y., Song, X., Jiang, Y., ... & Wang, C. (2017). Elastic block and strain modeling of GPS data around the Haiyuan-Liupanshan fault, northeastern Tibetan Plateau. *Journal of Asian Earth Sciences*, 150, 87-97.
- Li, Y., Zhang, G., Shan, X., Liu, Y., Wu, Y., Liang, H., ... & Song, X. (2018b). GPS-derived fault coupling of the Longmenshan fault associated with the 2008 Mw Wenchuan 7.9 earthquake and its tectonic implications. *Remote Sensing*, 10(5), 753.
- Liang, S., Gan, W., Shen, C., Xiao, G., Liu, J., Chen, W., ... & Zhou, D. (2013). Three-dimensional velocity field of present-day crustal motion of the Tibetan Plateau derived from GPS measurements. *Journal of Geophysical Research: Solid Earth*, 118(10), 5722-5732.
- Liu, S., Xu, X., Klinger, Y., Nocquet, J.-M., Chen, G., Yu, G., & Jónsson, S. (2019). Lower crustal heterogeneity beneath the northern Tibetan Plateau constrained by GPS measurements following the 2001 Mw 7.8 Kokoxili earthquake. *Journal of Geophysical Research: Solid Earth*, 124.
- Liu, Y., Xu, C., Li, Z., Wen, Y., & Forrest, D. (2011). Interseismic slip rate of the Garze–Yushu fault belt in the Tibetan Plateau from C-band InSAR observations between 2003 and 2010. *Advances in Space Research*, 48(12), 2005-2015.
- Liu-Zeng, J., Klinger, Y., Xu, X., Lasserre, C., Chen, G., Chen, W., ... & Zhang, B. (2007). Millennial recurrence of large earthquakes on the Haiyuan fault near Songshan, Gansu Province, China. *Bulletin of the Seismological Society of America*, 97(1B), 14-34.
- Louderback, G. D. (1942). Faults and earthquakes. *Bulletin of the Seismological Society of America*, 32(4), 305-330.
- Loveless, J. P., & Meade, B. J. (2011). Partitioning of localized and diffuse deformation in the Tibetan Plateau from joint inversions of geologic and geodetic observations. *Earth and Planetary Science Letters*, 303(1-2), 11-24.
- Lowry, A. R., Larson, K. M., Kostoglodov, V., & Bilham, R. (2001). Transient fault slip in Guerrero,

- southern Mexico. *Geophysical Research Letters*, 28(19), 3753-3756.
- Marone, C. J., Scholtz, C. H., & Bilham, R. (1991). On the mechanics of earthquake afterslip. *Journal of Geophysical Research: Solid Earth*, 96(B5), 8441-8452.
- McCaffrey, R. (1995). *DEFNODE users guide*. Rensselaer Polytechnic Institute, Troy, New York.
- Meade, B. J. (2007). Present-day kinematics at the India-Asia collision zone. *Geology*, 35(1), 81-84.
- Meade, B. J., & Hager, B. H. (2005). Block models of crustal motion in southern California constrained by GPS measurements. *Journal of Geophysical Research: Solid Earth*, 110(B3).
- Molnar, P., & Tapponnier, P. (1975). Cenozoic tectonics of Asia: effects of a continental collision. *Science*, 189(4201), 419-426.
- Nagata, T., and A. Okada (1947). Land deformation of the Muroto Point before and after the Nankai great earthquake on December 21, 1946. *Bull. Earthq. Res. Inst.* 25, 85-89.
- Niu, Z., Min, W., Hanrong, S., Jianzhong, S., Xinzhaoy, Y., Weijun, G., ... & Yongxiang, W. (2005). Contemporary velocity field of crustal movement of Chinese mainland from Global Positioning System measurements. *Chinese Science Bulletin*, 50(9), 939-941.
- Nocquet, J. M., Villegas-Lanza, J. C., Chlieh, M., Mothes, P. A., Rolandone, F., Jarrin, P., ... & Martin, X. (2014). Motion of continental slivers and creeping subduction in the northern Andes. *Nature Geoscience*, 7(4), 287.
- Nur, A., & Mavko, G. (1974). Postseismic viscoelastic rebound. *Science*, 183(4121), 204-206.
- Okada, A., and T. Nagata (1953). Land deformation of the neighborhood of Muroto Point after the Nankaido great earthquake in 1946. *Bull. Earthquake Res. Inst. Univ. Tokyo*, 31, 169-177.
- Okada, Y. (1985). Surface deformation due to shear and tensile faults in a half-space. *Bulletin of the Seismological Society of America*, 75(4), 1135-1154.
- Owens, T. J., & Zandt, G. (1997). Implications of crustal property variations for models of Tibetan plateau evolution. *Nature*, 387(6628), 37.
- Peltzer, G., Rosen, P., Rogez, F., & Hudnut, K. (1998). Poroelastic rebound along the Landers 1992 earthquake surface rupture. *Journal of Geophysical Research: Solid Earth*, 103(B12), 30131-30145.
- Perfettini, H., & Avouac, J. P. (2004). Postseismic relaxation driven by brittle creep: A possible mechanism to reconcile geodetic measurements and the decay rate of aftershocks, application to the Chi-Chi earthquake, Taiwan. *Journal of Geophysical Research: Solid Earth*, 109(B2).
- Qiao, X., Yu, P., Nie, Z., Li, J., Wang, X., Kuzikov, S. I., ... & Yang, S. (2017). The crustal deformation revealed by GPS and InSAR in the northwest corner of the Tarim Basin, northwestern China. *Pure and Applied Geophysics*, 174(3), 1405-1423.
- Radiguet, M., Perfettini, H., Cotte, N., Gualandi, A., Valette, B., Kostoglodov, V., ... & Campillo, M. (2016). Triggering of the 2014 M_w 7.3 Papanao earthquake by a slow slip event in Guerrero, Mexico. *Nature Geoscience*, 9(11), 829.
- Reid, H. F. (1910). On mass movements in tectonic earthquakes and the depth of the focus. *Beitragen Geophys.*, 10, 318-351.
- Reid, H. F. (1911). The elastic-rebound theory of earthquakes. *Univ. Calif. Publ. Bull. Dept. Geol.*, 6(19), 413-444.
- Rolandone, F., Nocquet, J. M., Mothes, P. A., Jarrin, P., Vallée, M., Cubas, N., ... & Font, Y. (2018). Areas prone to slow slip events impede earthquake rupture propagation and promote afterslip. *Science Advances*, 4(1), eaao6596.

- Rowley, D. B. (1996). Age of initiation of collision between India and Asia: A review of stratigraphic data. *Earth and Planetary Science Letters*, 145(1-4), 1-13.
- Royden, L. H., Burchfiel, B. C., King, R. W., Wang, E., Chen, Z., Shen, F., & Liu, Y. (1997). Surface deformation and lower crustal flow in eastern Tibet. *Science*, 276(5313), 788-790.
- Rui, X., & Stamps, D. S. (2019a). Strain accommodation in the Daliangshan Mountain area, southeastern margin of the Tibetan Plateau. *Journal of Geophysical Research: Solid Earth*, 124
- Rui, X., & Stamps, D. S. (2019b). A geodetic strain rate and tectonic velocity model for China. *Geochemistry, Geophysics, Geosystems*, 20(3), 1280-1297.
- Ryder, I., & Bürgmann, R. (2008). Spatial variations in slip deficit on the central San Andreas fault from InSAR. *Geophysical Journal International*, 175(3), 837-852.
- Ryder, I., Parsons, B., Wright, T. J., & Funning, G. J. (2007). Post-seismic motion following the 1997 Manyi (Tibet) earthquake: InSAR observations and modelling. *Geophysical Journal International*, 169(3), 1009-1027.
- Savage, J. C. (1983). A dislocation model of strain accumulation and release at a subduction zone. *Journal of Geophysical Research: Solid Earth*, 88(B6), 4984-4996.
- Savage, J. C., & Burford, R. O. (1973). Geodetic determination of relative plate motion in central California. *Journal of Geophysical Research*, 78(5), 832-845.
- Savage, J. C., Svarc, J. L., Prescott, W. H., & Murray, M. H. (2000). Deformation across the forearc of the Cascadia subduction zone at Cape Blanco, Oregon. *Journal of Geophysical Research: Solid Earth*, 105(B2), 3095-3102.
- Shen, Z. K., Lü, J., Wang, M., & Bürgmann, R. (2005). Contemporary crustal deformation around the southeast borderland of the Tibetan Plateau. *Journal of Geophysical Research: Solid Earth*, 110(B11).
- Shen, Z. K., Sun, J., Zhang, P., Wan, Y., Wang, M., Bürgmann, R., ... & Wang, Q. (2009). Slip maxima at fault junctions and rupturing of barriers during the 2008 Wenchuan earthquake. *Nature Geoscience*, 2(10), 718.
- Shen, Z. K., Wang, M., Li, Y., Jackson, D. D., Yin, A., Dong, D., & Fang, P. (2001). Crustal deformation along the Altyn Tagh fault system, western China, from GPS. *Journal of Geophysical Research: Solid Earth*, 106(B12), 30607-30621.
- Song, X., Jiang, Y., Shan, X., Gong, W., & Qu, C. (2019). A Fine Velocity and Strain Rate Field of Present-Day Crustal Motion of the Northeastern Tibetan Plateau Inverted Jointly by InSAR and GPS. *Remote Sensing*, 11(4), 435.
- Stein, R. S. (1999). The role of stress transfer in earthquake occurrence. *Nature*, 402(6762), 605.
- Stevens, V. L., & Avouac, J. P. (2015). Interseismic coupling on the main Himalayan thrust. *Geophysical Research Letters*, 42(14), 5828-5837.
- Tapponnier, P., Peltzer, G., & Armijo, R. (1986). On the mechanics of the collision between India and Asia. *Geological Society, London, Special Publications*, 19(1), 113-157.
- Tapponnier, P., Zhiqin, X., Roger, F., Meyer, B., Arnaud, N., Wittlinger, G., & Jingsui, Y. (2001). Oblique stepwise rise and growth of the Tibet Plateau. *Science*, 294(5547), 1671-1677.
- Taylor, M., & Peltzer, G. (2006). Current slip rates on conjugate strike-slip faults in central Tibet using synthetic aperture radar interferometry. *Journal of Geophysical Research: Solid Earth*, 111(B12).
- Thatcher, W. (2007). Microplate model for the present-day deformation of Tibet. *Journal of Geophysical Research: Solid Earth*, 112(B1).

- Toda, S., Lin, J., Meghraoui, M., & Stein, R. S. (2008). 12 May 2008 $M=7.9$ Wenchuan, China, earthquake calculated to increase failure stress and seismicity rate on three major fault systems. *Geophysical Research Letters*, 35(17).
- Tong, X., Sandwell, D. T., & Smith-Konter, B. (2013). High-resolution interseismic velocity data along the San Andreas fault from GPS and InSAR. *Journal of Geophysical Research: Solid Earth*, 118(1), 369-389.
- Tymofeyeva, E., Fialko, Y., Jiang, J., Xu, X., Sandwell, D., Bilham, R., ... & Moa'fipoo, S. Slow slip event on the southern San Andreas fault triggered by the 2017 $Mw8.2$ Chiapas (Mexico) earthquake. *Journal of Geophysical Research: Solid Earth*.
- Villegas-Lanza, J. C., Nocquet, J. M., Rolandone, F., Vallée, M., Tavera, H., Bondoux, F., ... & Chlieh, M. (2016). A mixed seismic–aseismic stress release episode in the Andean subduction zone. *Nature Geoscience*, 9(2), 150-154.
- Voss, N., Dixon, T. H., Liu, Z., Malservisi, R., Protti, M., & Schwartz, S. (2018). Do slow slip events trigger large and great megathrust earthquakes?. *Science Advances*, 4(10), eaat8472.
- Wallace, L. M., Stevens, C., Silver, E., McCaffrey, R., Lorantung, W., Hasiata, S., ... & Taugaloidi, J. (2004). GPS and seismological constraints on active tectonics and arc-continent collision in Papua New Guinea: Implications for mechanics of microplate rotations in a plate boundary zone. *Journal of Geophysical Research: Solid Earth*, 109(B5).
- Wang, H., Wright, T. J., & Biggs, J. (2009). Interseismic slip rate of the northwestern Xianshuihe fault from InSAR data. *Geophysical Research Letters*, 36(3).
- Wang, H., Wright, T. J., Liu-Zeng, J., & Peng, L. (2019). Strain Rate Distribution in South-Central Tibet from Two Decades of InSAR and GPS. *Geophysical Research Letters*, 46(10), 5170-5179.
- Wang, H., Wright, T. J., Yu, Y., Lin, H., Jiang, L., Li, C., & Qiu, G. (2012). InSAR reveals coastal subsidence in the Pearl River Delta, China. *Geophysical Journal International*, 191(3), 1119-1128.
- Wang, Q., Xuejun, Q., Qigui, L., Freymueller, J., Shaomin, Y., Caijun, X., ... & Gang, C. (2011). Rupture of deep faults in the 2008 Wenchuan earthquake and uplift of the Longmen Shan. *Nature Geoscience*, 4(9), 634.
- Wang, Q., Zhang, P. Z., Freymueller, J. T., Bilham, R., Larson, K. M., Lai, X. A., ... & Liu, J. (2001). Present-day crustal deformation in China constrained by global positioning system measurements. *Science*, 294(5542), 574-577.
- Wang, W., Qiao, X., Yang, S., & Wang, D. (2017). Present-day velocity field and block kinematics of Tibetan Plateau from GPS measurements. *Geophysical Journal International*, 208(2), 1088-1102.
- Wang, Z., Su, J., Liu, C., & Cai, X. (2015). New insights into the generation of the 2013 Lushan Earthquake ($M_s 7.0$), China. *Journal of Geophysical Research: Solid Earth*, 120(5), 3507-3526.
- Wen, X., Ma, S., Xu, X., & He, Y. (2008). Historical pattern and behavior of earthquake ruptures along the eastern boundary of the Sichuan-Yunnan faulted-block, southwestern China. *Physics of the Earth and Planetary Interiors*, 168(1-2), 16-36.
- Wen, Y., Li, Z., Xu, C., Ryder, I., & Bürgmann, R. (2012). Postseismic motion after the 2001 $Mw 7.8$ Kokoxili earthquake in Tibet observed by InSAR time series. *Journal of Geophysical Research: Solid Earth*, 117(B8).
- Willett, S. D., & Beaumont, C. (1994). Subduction of Asian lithospheric mantle beneath Tibet

- inferred from models of continental collision. *Nature*, 369(6482), 642.
- Wright, T. J., Parsons, B., England, P. C., & Fielding, E. J. (2004). InSAR observations of low slip rates on the major faults of western Tibet. *Science*, 305(5681), 236-239.
- Xiong, X., Shan, B., Zheng, Y., & Wang, R. (2010). Stress transfer and its implication for earthquake hazard on the Kunlun Fault, Tibet. *Tectonophysics*, 482(1-4), 216-225.
- Xu, C., & Zhu, S. (2019). Temporal and spatial movement characteristics of the Altyn Tagh fault inferred from 21 years of InSAR observations. *Journal of Geodesy*, 1-14.
- Xu, X., Wen, X., Yu, G., Chen, G., Klinger, Y., Hubbard, J., & Shaw, J. (2009). Coseismic reverse- and oblique-slip surface faulting generated by the 2008 Mw 7.9 Wenchuan earthquake, China. *Geology*, 37(6), 515-518.
- Xu, Z., Jiang, M., & Yang, J. (1996). Tectonophysical process at depth for the uplift of the northern part of the Qinghai-Tibet plateau- Illustrated by the geological and geophysical comprehensive profile from Golmud to the Tanggula Mountains, Qinghai Province, China. *Acta Geologica Sinica*, 70(3), 195-206.
- Yao, W., Liu-Zeng, J., Oskin, M. E., Wang, W., Li, Z., Prush, V., ... & Klinger, Y. (2019). Reevaluation of the Late Pleistocene Slip Rate of the Haiyuan Fault near Songshan, Gansu Province, China. *Journal of Geophysical Research: Solid Earth*, 124(5), 5217-5240.
- Zhang, G., Wang, S., Li, L., Zhang, X., & Ma, H. (2002). Focal depth research of earthquakes in Mainland China: Implication for tectonics. *Chinese Science Bulletin*, 47(12), 969-974.
- Zhang, P. Z. (2013). Beware of slowly slipping faults. *Nature Geoscience*, 6(5), 323.
- Zhang, P. Z., Shen, Z., Wang, M., Gan, W., Bürgmann, R., Molnar, P., ... & Hanrong, S. (2004). Continuous deformation of the Tibetan Plateau from global positioning system data. *Geology*, 32(9), 809-812.
- Zhang, W., Decheng, J., Peizhen, Z., Molnar, P., Burchfield, B. C., Qidong, D., ... & Fangmin, S. (1987). Displacement along the Haiyuan fault associated with the great 1920 Haiyuan, China, earthquake. *Bulletin of the Seismological Society of America*, 77(1), 117-131.
- Zhao, D., Qu, C., Shan, X., Bürgmann, R., Gong, W., & Zhang, G. (2018). Spatiotemporal Evolution of Postseismic Deformation Following the 2001 Mw7. 8 Kokoxili, China, Earthquake from 7 Years of InSAR Observations. *Remote Sensing*, 10(12), 1988.
- Zheng, G., Wang, H., Wright, T. J., Lou, Y., Zhang, R., Zhang, W., ... & Wei, N. (2017). Crustal deformation in the India-Eurasia collision zone from 25 years of GPS measurements. *Journal of Geophysical Research: Solid Earth*, 122(11), 9290-9312.
- Zhu, S., Xu, C., Wen, Y., & Liu, Y. (2016). Interseismic deformation of the Altyn Tagh fault determined by Interferometric Synthetic Aperture Radar (INSAR) measurements. *Remote Sensing*, 8(3), 233.
- Zhu, W., Wang, X., Cheng, Z., Xiong, Y., Zhang, Q., Ye, S., ... & Lai, X. A. (2000). Crustal motion of Chinese mainland monitored by GPS. *Science in China Series D: Earth Sciences*, 43(4), 394.
- Zigone, D., Rivet, D., Radiguet, M., Campillo, M., Voisin, C., Cotte, N., ... & Kostoglodov, V. (2012). Triggering of tremors and slow slip event in Guerrero, Mexico, by the 2010 Mw 8.8 Maule, Chile, earthquake. *Journal of Geophysical Research: Solid Earth*, 117(B9).

Chapter 2· Geodetic datasets and data processing

GPS and InSAR have been intensively used in Tibet to map the interseismic crustal deformation, as I described in Chapter 1. To date, processing of GPS data is relatively mature, whereas many challenges remain for the interseismic InSAR data processing. In this Chapter, I will first briefly outline the GPS data processing. I introduce the newly deployed and re-measured GPS stations by the Institute of Geology, China Earthquake Administration across the Haiyuan fault and the western Altyn Tagh fault (86°E) respectively. In section 2.2, I briefly introduce the InSAR datasets used in the dissertation. In the last part, I describe the crustal deformation signals in the observed GPS and InSAR, methods of GPS/InSAR integration, and show the integration results in the northeastern Tibet.

2.1. GPS measurements and data processing

2.1.1. GPS measurement

In Chapter 1, I have introduced the network architecture of the CMONOC and the GPS data collection. Here, I describe the GPS measurements along the Altyn Tagh fault and the Haiyuan fault carried out by our group in the Institute of Geology, China Earthquake Administration. The locations of GPS stations are shown in Figure 2.1.

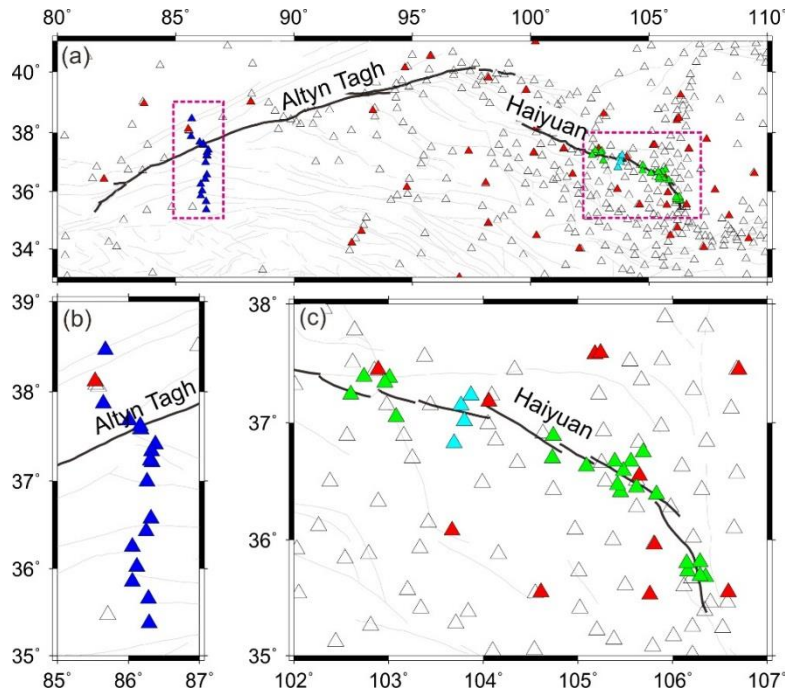


Figure 2.1. GPS sites distribution. (a) Distribution of GPS stations in northern Tibet. (b) and (c) show GPS stations along the Altyn Tagh fault and the Haiyuan fault system. White and red triangles show the location of campaign-mode and continuous GPS stations of CMONOC respectively. Blue triangles represent the campaign-mode stations that we re-measured in 2017 across the Altyn Tagh fault. Green and Cyan triangles indicate the location of campaign-mode and continuous GPS stations that we deployed across the Haiyuan fault.

Our team revisited the same 17 benchmarks used by He et al. (2013) in October 2017. These benchmarks were measured 2–3 times in the period 2009–2011, across the western segment of the Altyn Tagh fault (86°E). These GPS stations were deployed roughly perpendicular to the Altyn Tagh fault, extending about a 400 km long profile across the fault. These GPS benchmarks were installed with forced centering system (Figure 2.2a). Of the 17 stations, 16 are well preserved; only one station near Qimo County (north of the Altyn Tagh fault) was damaged. We used Trimble NetR9 receiver with Trimble GNSS Choke Ring Geodetic Antenna and collected continuous observations for 72 to 240 hours at the GPS sites at a 30s sampling rate. The collected GPS data, together with CMONOC GPS data in 1999–2017, constitute the dataset that I am going to use in Chapter 3.

Along the Haiyuan fault, our team started to deploy campaign-mode GPS sites since 2013. In 2015, 21 new stations were established in order to compensate the low spatial resolution of CMONOC in the near field of Haiyuan fault (Figure 2.1). The construction of GPS station follows the standard of CMONOC. The base of GPS stations has a depth of at least 70 cm on the bedrock and a depth of at least 2 m in soil layer. Each station was equipped with forced centering system. We measured these GPS stations annually during the summer in order to reduce the effect of annual and semiannual components when estimating velocities. We used Trimble NetR9 and Topcon NetG5 receivers with choke ring antennas to perform continuous observations at 30s sampling rate, with at least 72 hours per site during each campaign. As of September 2019, we accumulated 5–7 campaigns of GPS data. In my work, I only used the GPS data spanning the 2013–2017 period.

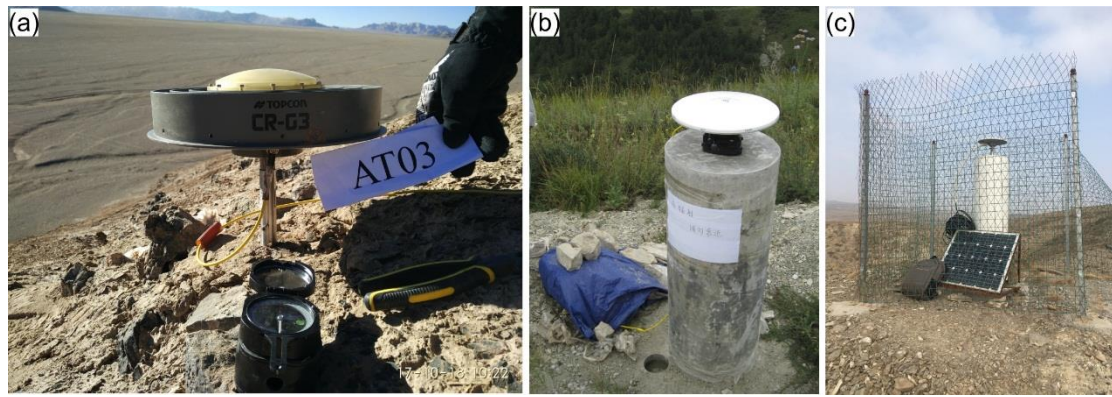


Figure 2.2. Pictures of GPS stations. (a) The typical campaign-mode GPS station across the Altyn Tagh fault. (b) The typical campaign-mode GPS station across the Haiyuan fault. (c) The continuous GPS station across the Haiyuan fault.

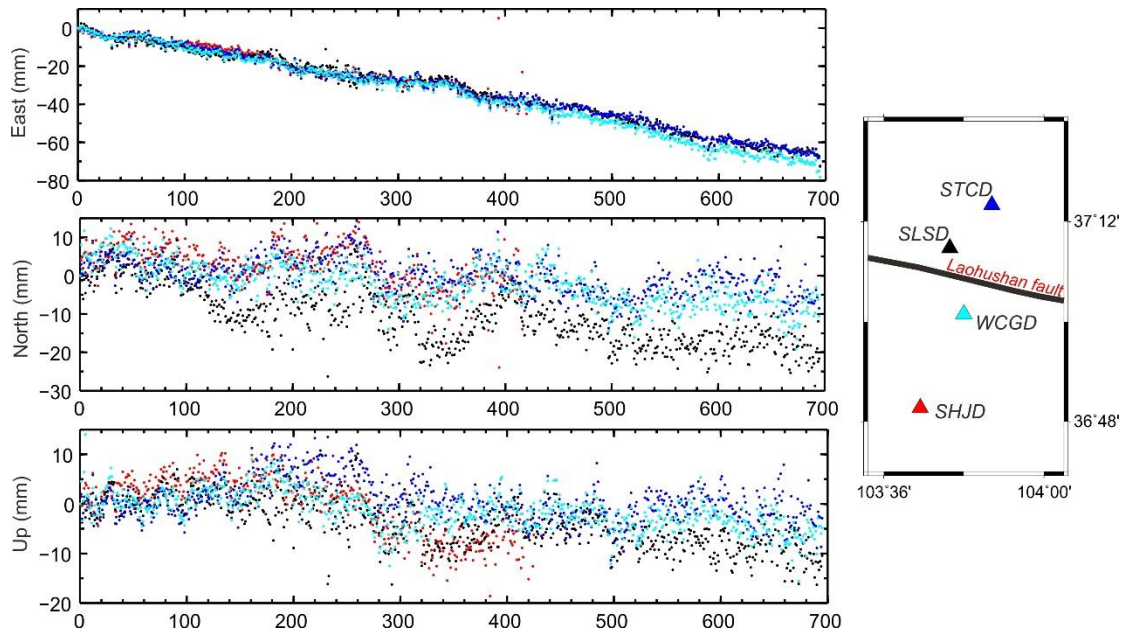


Figure 2.3. Example of GPS position time series of the four continuous GPS sites along the Laohushan fault. The x-axis indicates the number of days from October 5, 2017.

Cavalié et al. (2008) first identified a shallow creeping segment along the Laohushan segment ($\sim 103.8^\circ\text{E}$), Haiyuan fault, using the ERS InSAR spanning 1993–1998, which was later confirmed by Jolivet et al. (2012) using the Envisat InSAR spanning the 2003–2009 period. Furthermore, Jolivet et al. (2012, 2013) found that the shallow creep extend a 35 km-long segment, with transient slipping behaviors. However, there have been no GPS measurements across the segment. Consequently, our group deployed four continuous GPS stations in the near-field of the fault and normal to the fault in September 2017 (Figure 2.1, 2.3). These GPS stations were constructed on bedrock, equipped with Trimble NetR9 receiver and Trimble GNSS Choke Ring Geodetic Antenna (Figure 2.2c). The GPS sites started to operate around October 2017, and at the time of my PhD, since only a year of data were available, I did not include these GPS stations to the work presented in Chapter 4. Now, we have accumulated around two years of data, and I show the position time series of the four GPS stations in Figure 2.3. It is obvious that across the Laohushan fault, GPS sites velocities show variation, both in horizontal and vertical. I leave the interpretations of those four GPS sites for future work.

2.1.2. GPS data processing

Here, I take the GPS data surveyed across the western Altyn Tagh fault (86°E) as example to illustrate data processing. In the following Chapters, I will also introduce briefly the GPS data used in each study, the data sources, and corresponding data processing or integration.

I processed the campaign-mode GPS data measured in 2017 together with those data collected between 2009 and 2011, and with seven regional CMONOC continuous sites using the GAMIT/GLOBK 10.6 software (Herring et al., 2016), which consist of three steps:

(1) **Loosely constrained daily solutions from GAMIT.** Raw phase observations are first processed together with 40 globally distributed sites from the International Global Navigation Satellite System Service (IGS, <http://www.igs.org/>) to obtain loosely constrained daily station coordinates and satellite orbit parameters. The processing includes IGS precise orbits and Earth orientation parameters, absolute antenna phase center calibrations, and the Finite Element Solution 2004 ocean tide loading model during the daily data processing (Lyard et al., 2006).

(2) **Position time series.** Loosely constrained daily solutions are then expressed in the International Terrestrial Reference System 2008 (ITRF2008) by estimating seven parameters transformation (orientation, translation, and scale) using the 40 globally distributed IGS stations. The time series for each station is carefully examined to exclude outliers. I set 3-sigma from the mean as the threshold for outlier selection. I show one example of position time series in Figure 2.3.

(3) **GPS site velocity and its uncertainty.** Currently, there are two methods to estimate the GPS site velocity and its uncertainty. The first one uses position time series to simultaneously estimate linear terms (including offsets and slopes), nonlinear terms (annual and semiannual), and

the amplitude and spectral index of a time-correlated (or power law) noise model, such as the Maximum Likelihood Estimation implemented in the CATS software (Williams, 2008). Such method fits flicker and white noises to all time series to estimate the slope (velocities) and their realistic uncertainties. This method works well with continuous and clean time series but has drawbacks (Saria et al., 2013). First, it requires at least 4 years of continuous data collection to provide reliable spectral index estimates. Second, episodic time series or sites with abundant observation gaps lead to unrealistic velocity and uncertainties estimates.

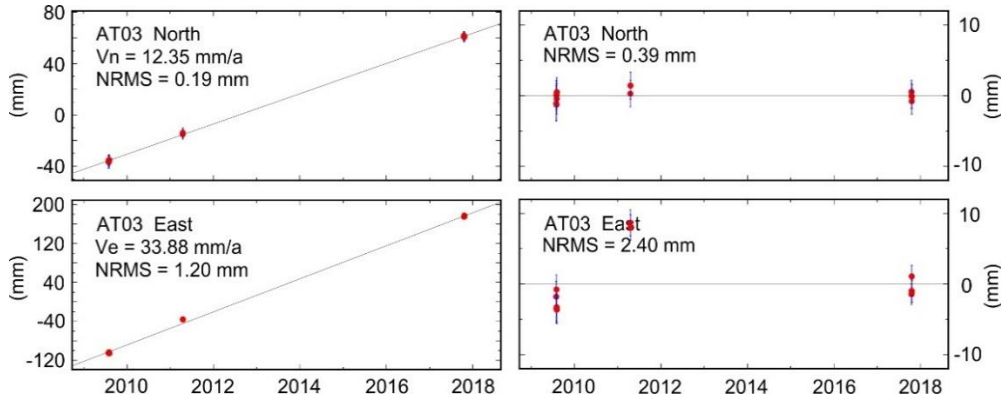


Figure 2.3. One example of (left panel) campaign-mode GPS position time series (AT03 station), and (right panel) residuals after removing a linear detrend. The GPS station is located along the western Altyn Tagh fault.

The alternative method is to use the GLOBK package, which estimate the point coordinates and velocities from a combined solution comprising the daily loosely constrained estimates, earth orientation parameters (EOP) values, orbit data, and their covariance through Kalman filtering. This method usually requires to enlarge regional GPS network further with more globally scattered and loosely constrained IGS stations (e.g., <ftp://garner.ucsd.edu/pub/hfiles>). Velocity uncertainties are estimated using the ‘realistic sigma’ algorithm (e.g., Herring, 2003; Reilinger et al., 2006). The method fits the increase in χ^2 with successively longer averaging times to an exponential function, then evaluates the exponential function at infinite averaging time to get the velocity uncertainty. This method can handle time series with outliers and data gaps.

Considering that most of the GPS sites were measured episodically, I used the ‘realistic sigma’ algorithm (GLOBK package) to calculate the velocity uncertainties (e.g., Herring, 2003; Reilinger et al., 2006). I used a random-walk value of $1.0 \text{ mm}/\sqrt{a}$ for the horizontal component, which is the average value of correlated noise model and is determined from 320 globally distributed continuous GPS stations with time series spans ranging from 2.5 to 17 years (He et al., 2013; Reilinger et al., 2006).

(4) Reference frame. Finally, I transform the velocities into a Eurasia-fixed frame of reference using the Euler vector for Eurasia with respect to the ITRF 2008 provided by Altamimi et al. (2011). In order to highlight the deformation of the Altyn Tagh fault, I express the velocity field in a Tarim-

fixed reference frame, which is determined by minimizing the horizontal velocities at GPS sites north of the fault. Because most of the GPS sites were measured in campaign-mode, I do not estimate their vertical velocities owing to the large uncertainties. I show the GPS velocity solution in Figure 2.4. The interpretation and modeling are present in Chapter 3.

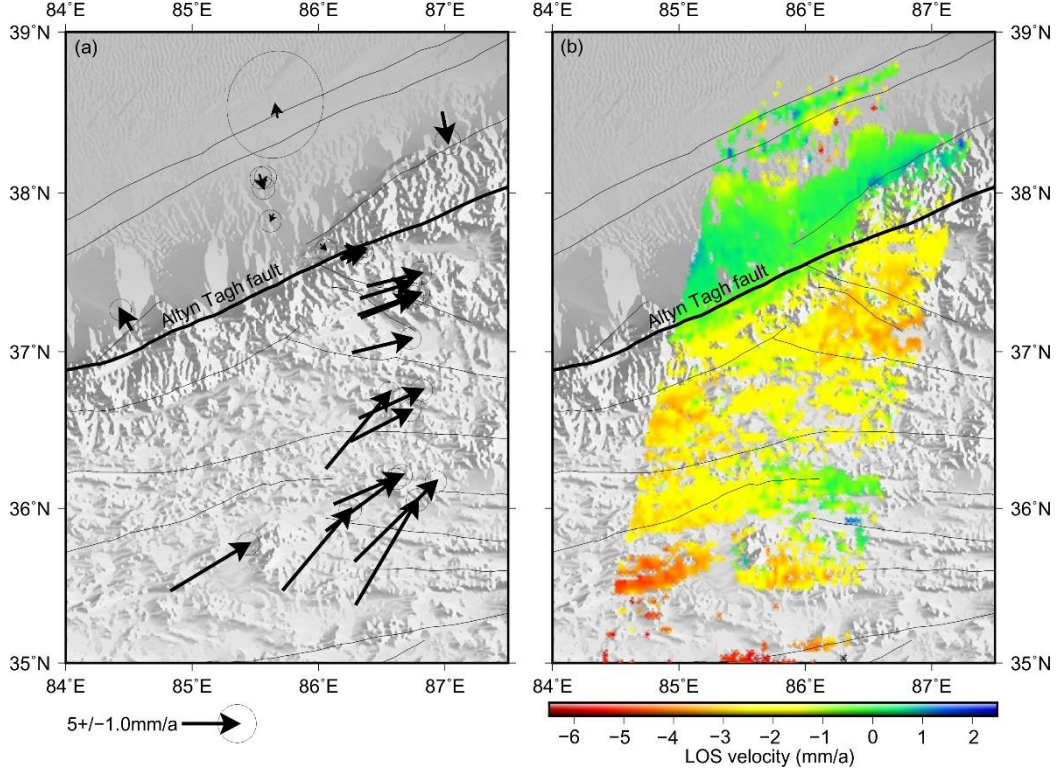


Figure 2.4. (a) Obtained GPS velocities from 2009–2017 in the Tarim-fixed reference frame. All GPS velocities have uncertainties at the 95% confidence. (b) Line-of-sight (LOS) velocity map of the two tracks 119 and 348.

(5) Co- and post- seismic deformation. In the GPS data processing, it's important to consider the impact of coseismic and postseismic deformation. Here, I also describe how I deal with the issue. No earthquake with magnitude larger than 6 occurred between 2009 and 2017 in the northern Tibet, corresponding to the time span of observation across the Altyn Tagh fault. Of the 16 campaign-mode GPS sites, the southernmost station (Figure 2.1), which is ~ 100 km from the epicenter of the 1997 Mw 7.5 Manyi earthquake, is most likely to be affected by the postseismic deformation following the earthquake. However, surface deformation derived from the InSAR data, which were acquired between November 1997 and September 2001, shows that the postseismic deformation of the 1997 Mw 7.5 Manyi earthquake only affected a region of ~ 20 km from the surface rupture and the surface displacement following the earthquake obeys an exponential decay with time (e.g., [Ryder et al., 2007](#); [Yamasaki and Houseman, 2012](#)). Hence, the 1997 Mw 7.5 Manyi earthquake postseismic signal contributes scarcely to my velocity solution. In conclusion, I regard the above GPS solutions as secular interseismic velocities. Note that, here the secular also refers to the GPS velocity solution is not contaminated by postseismic deformation.

For the GPS data (1999–2018) across the Haiyuan fault, I adopt similar data processing strategies. During our GPS data time span (1999–2018), several destructive earthquakes occurred in the China mainland and its surrounding, of which the 2001 Kokoxili Mw 7.8 earthquake, the 2004 Sumatra Mw 9.3 earthquake, the 2008 Wenchuan Mw 7.9 earthquake and the 2011 Tohoku (Japan) Mw 9.0 were the ones generated minor yet obvious coseismic deformation in the northeastern Tibet (e.g., Wang et al., 2011). As a consequence, I add offsets parameters in the GPS position time series to be estimated simultaneously to get velocity. Despite both the 2001 Kokoxili Mw 7.8 earthquake and the 2008 Wenchuan Mw 7.9 earthquake induced significant postseismic deformation (e.g., Wen et al., 2012; Huang et al., 2014; Diao et al., 2018), they have scarcely impact in northeastern Tibet. In summary, I regard the GPS solution as secular interseismic velocities. I also show the GPS velocity here (Figure 2.5), and the interpretation and modeling are present in Chapter 4.

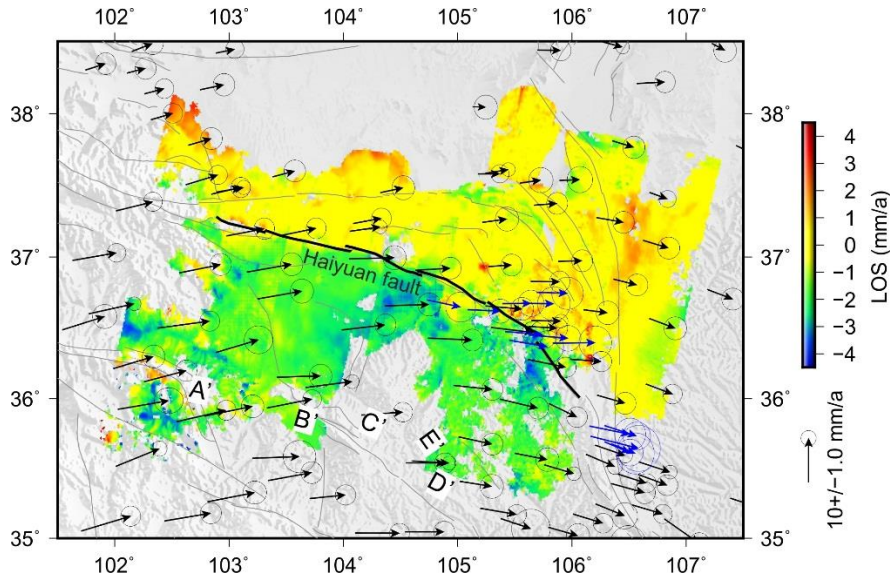


Figure 2.5. InSAR displacements and GPS velocity field in the northeastern Tibet. GPS velocities with respect to the stable Eurasian plate. Arrows in blue represent newly-built station velocities. Error ellipses indicate the 95% confidence levels. Background color represent the observed InSAR displacements.

For the GPS data (2015-2018) across the Xianshuihe-Xiaojiang fault system, I also used the same data processing strategies. Note that in August 8, 2017, an Mw 6.5 earthquake struck the Jiuzhaigou County (epicenter 103.861° E, 33.198° N; U.S. Geological Survey [USGS]), about 350 km away from Xianshuihe-Xiaojiang fault system. During the data processing, I corrected the coseismic offsets for GPS stations located within 150 km from the epicenter. Considering that the magnitude of the earthquake is relatively small and that there were no continuous GPS stations near the epicenter (within 50 km), we ignored the postseismic transients in our GPS velocity solution.

2.2. InSAR dataset

The interseismic InSAR displacement data that I used in the thesis were provided by Simon Daout from the publication of Daout et al. (2018) (covering the western Altyn Tagh fault, Chapter 3); provided by Xiaogang Song from the publication of Song et al. (2019) (covering the Haiyuan fault, Chapter 4); and provided by Lei Zhang from the publication of Zhang et al. (2018a) (covering the Xianshuihe fault, Chapter 5). The readers are recommended these papers for details on the InSAR data processing. Here, I introduce briefly the SAR data time span, spatial coverage of data, and some basic technical points.

2.2.1. The Altyn Tagh fault

Daout et al. (2018) processed the complete Envisat descending archive along four 500 km long and 100 km wide Envisat overlapping tracks (162, 391, 119, and 348) between 2003 and 2011 (Figure 2.6). The InSAR track encompasses our GPS profile. They constructed 484 small baseline differential interferograms with the New Small Baselines Subset chain (NSBAS) based on the ROI_PAC software. In their data processing, they applied a series of corrections for atmospheric delays, separation of the effects of hydrology and permafrost seasonal changes in the high plateau and corrections for the orbital residuals. The resulting LOS rate map is shown in Figure 2.4.

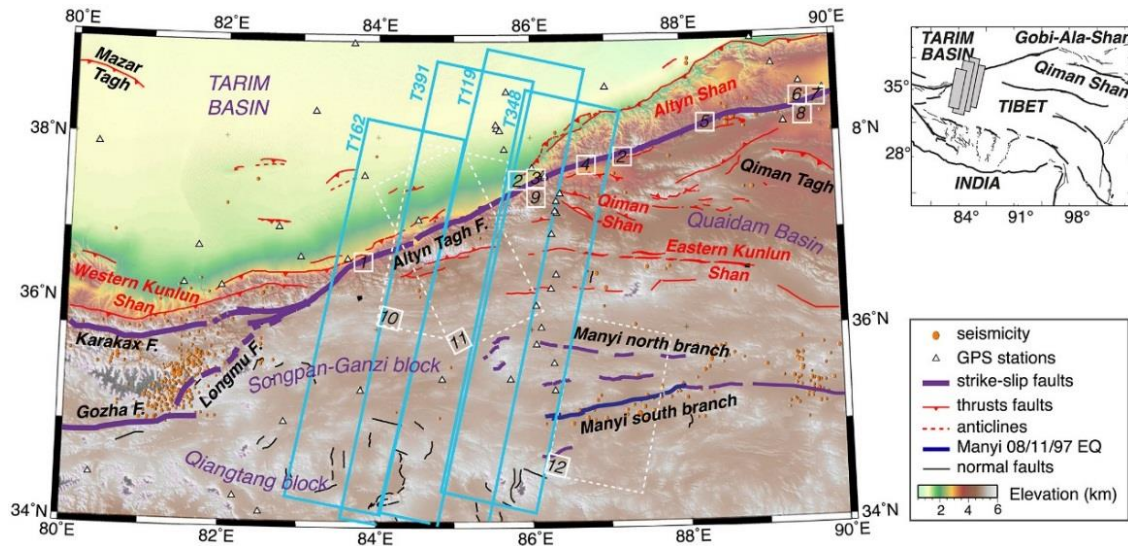


Figure 2.6. InSAR data convergence across the Altyn Tagh fault. Cyan rectangles show the Envisat descending tracks. White triangles show the location of GPS stations. Figure adopted from Daout et al. (2018). The readers are referred to the origin paper for more detailed description of each elements.

2.2.2. The Haiyuan fault

Song et al. (2019) processed the InSAR data from 6 Envisat ASAR descending tracks, spanning the

2003–2010 period, covering the most part of the northeastern margin of the Tibetan Plateau (Figure 2.7). Interferograms with baselines of less than 200 m were produced for each track by using ROI_PAC software. Shuttle Radar Topography Mission (SRTM) DEM was used to remove the topographic contribution to the interferometric phase changes. Interferograms were unwrapped using the branch-cut method (Goldstein et al., 1988). The resulting unwrapped interferograms were selected to construct a chain for stacking in the InSAR rate map estimation. They introduced the MEdium Resolution Imaging Spectrometer (MERIS) data to correct for the atmospheric delays. The resulting LOS rate map is shown in Figure 2.5.

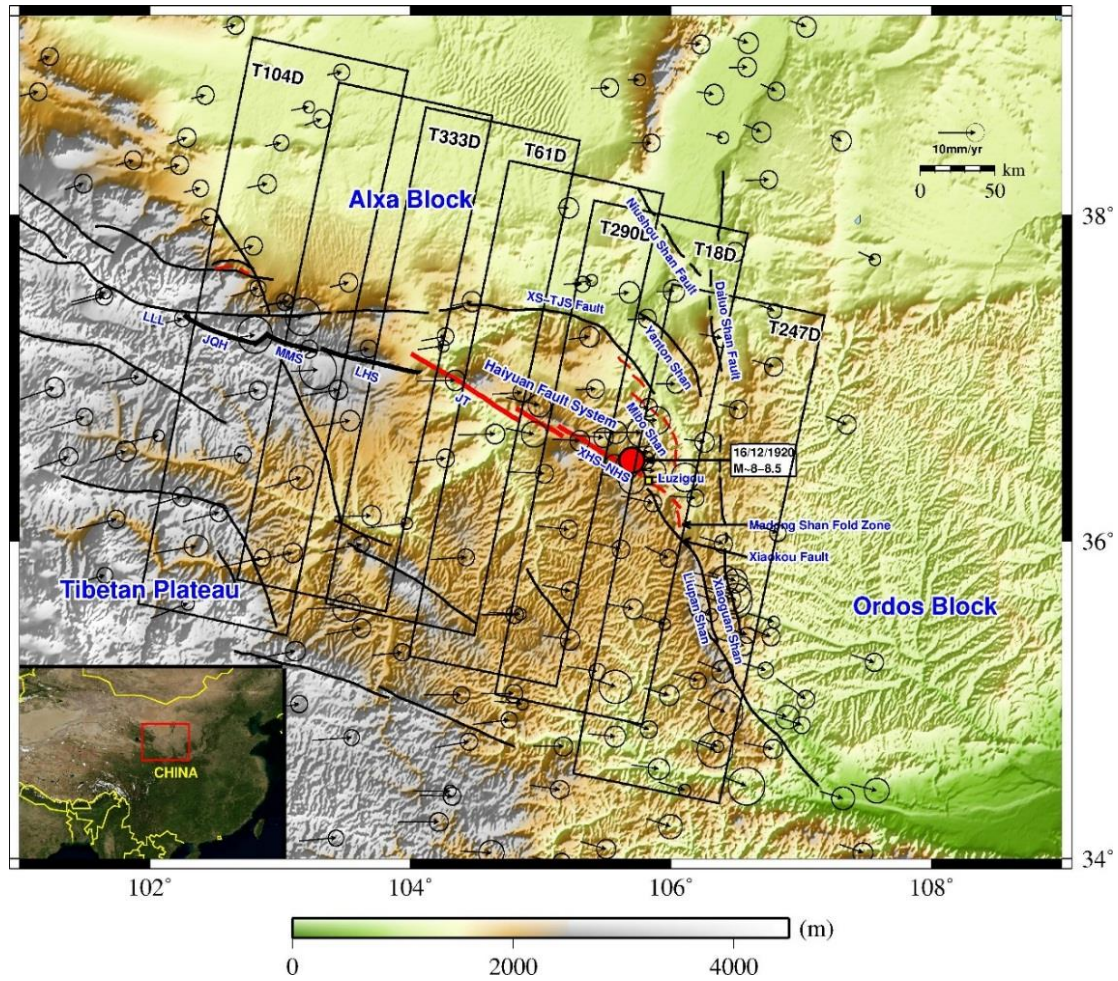


Figure 2.7. InSAR data convergence across the Haiyuan fault. Black rectangles show the coverage of Envisat ASAR data, with track numbers indicated. Figure adopted from Song et al. (2019). The readers are recommended to the origin paper for more detailed description of each elements.

2.2.3. The Xianshuihe fault

Zhang et al. (2018a) processed 21 Sentinel-1 Single Look Complex (SLC) SAR images from December 2014 to November 2016 covering the Xianshuihe fault, where were proposed to be creeping (e.g., Allen et al., 1991; Zhang et al., 2018b; Figure 2.8). They also used the ROI_PAC software for the data processing, the topographic phase was removed using a simulated phase from

the 1-arc (~30 m) DEM from SRTM. Atmospheric and elevation correction were conducted using the standard SBAS processing and a network approach (Li et al., 2016). The resulting LOS rate map is shown in Figure 2.8.

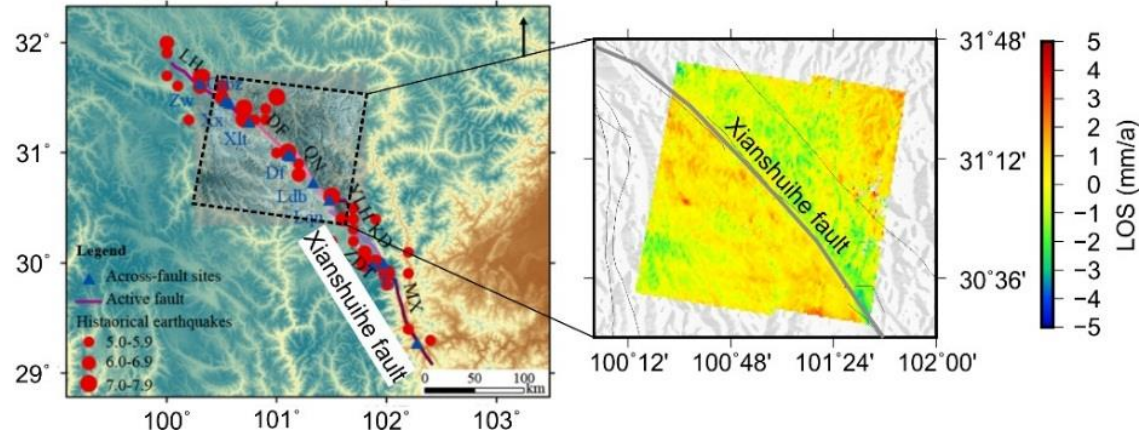


Figure 2.8. InSAR data convergence and LOS rate across the Xianshuihe fault. Figure updated from Zhang et al. (2018a).

Note that in previous studies (e.g., Daout et al., 2018; Zhang et al., 2018a; Song et al., 2019), models all assumed that the InSAR-derived displacements are due to horizontal only displacements. They neglected the potential vertical crustal deformation contribution in the InSAR LOS. Such an assumption is practical if there is no/negligible vertical deformation. However, the assumption is not appropriate when there is vertical deformation across the fault. Actually, the long-term leveling measurements have reported ~1-2 mm/a and ~1 mm/a vertical velocity differences across the Haiyuan fault and the Xianshuihe fault respectively (Hao et al., 2014; Figure 2.9), which, if not corrected from the LOS, would undoubtedly bias the InSAR data interpretations. As a consequence, I revisited the poor-processing of InSAR LOS displacements data, aiming at isolating the potential long wavelength vertical deformation signals from LOS and integrating horizontal GPS velocities with InSAR. I show the methods and results in section 2.3.

2.3. Geodetic data integration

2.3.1. How to consider vertical deformation

InSAR displacements are typically most sensitive to vertical deformation than horizontal deformation (Wright et al., 2004). To highlight the effects of vertical deformation in data interpretation, I use the Envisat descending satellite as an example to illustrate the sensitivity of LOS to east, north and vertical displacements. Here, I take the average incidence angle to be 23° , azimuth to be 193° , then the LOS could be decomposed:

$$V_{LOS} = [V_N, V_E, V_U] \cdot [-0.094, 0.391, 0.916]^T \quad (2.1)$$

in this case, LOS is more sensitive to vertical than horizontal by a factor of 2.5. Here, I take the creeping fault as an example to illustrate how vertical deformation might bias our interpretation. Assuming there is 1 mm/a vertical deformation across one E-W orientation strike-slip fault, such as the case for the Haiyuan fault, which has a shallow creep rate of 5 mm/a; then, theoretically, the observed LOS rate difference should be 2.871 mm/a across the fault. Should we neglect the vertical deformation across the fault and use the observed LOS displacement to invert for the fault creep rate, we could obtain a creep rate of 7.34 mm/a, which is overestimated almost 50%. The simple calculation highlights the importance of accounting for the vertical deformation in the InSAR LOS when horizontal deformation only to modeled.

In the following, I explain how to consider vertical deformation. Let's write the observed horizontal GPS velocity as:

$$V_{GPS} = V_{h-long} + F_{GPS} + \varepsilon_{GPS} \quad (2-1)$$

where V_{h-long} represents the ground true horizontal deformation, F_{GPS} is the reference frame of GPS (for instance, the Eurasian plate reference frame), and ε_{GPS} is the random errors. Note that in the following, unless otherwise specified, GPS corresponds to horizontal crustal deformation.

The observed InSAR displacement is written as:

$$V_{InSAR} = G_h \cdot V_h + G_u \cdot V_u + F_{InSAR} + \varepsilon_{InSAR} \quad (2-2)$$

where V_h and V_u represent the ground true horizontal and vertical deformation respectively, G_h and G_u are the projection vectors for horizontal and vertical respectively, F_{InSAR} is the reference frame of InSAR (for instance, referenced to the unwrapping point), and ε_{InSAR} is the errors, which includes random error and long wavelength error.

Under specific assumptions, we could do the comparison and combination/integration between GPS and InSAR. The assumptions of my methodology are: (1) the long wavelength error, e.g., orbit residual error, in InSAR is random and small (compared to the random errors, such as atmospheric error); (2) the variation of the frame difference values, between InSAR and GPS, could be estimated as a constant or modeled as a plane. Then, the relationship between GPS and InSAR could be written as:

$$V_{InSAR} = G_h \cdot V_{GPS} + G_u \cdot V_u + F_{GPS \rightarrow InSAR} + \varepsilon_{GPS \& InSAR} \quad (2-3)$$

where G_h and G_u are the projection vectors, $F_{GPS \rightarrow InSAR}$ is the frame difference value (constant or plane) between InSAR and GPS, and $\varepsilon_{GPS \& InSAR}$ is the random errors.

Thanks to the geodesy observations in the Tibetan Plateau in the past few decades, now we have horizontal GPS velocity solution (my case), three-dimensional GPS velocity solution (e.g., Liang et al., 2013; Pan et al., 2018; Su et al., 2019), and long-term leveling velocity solution (Hao et al., 2014). Thus, we could use external vertical deformation to combine horizontal GPS and InSAR data. Before that, evaluating the consistency of the data sets is necessary.

2.3.2. Methodology and data integration

In my thesis, I have the interseismic horizontal GPS velocities, the interseismic InSAR LOS displacements, and the long-term leveling results (Hao et al., 2014). I tried three methods to integrate GPS and InSAR:

(1) External vertical data from leveling. The method assumes that the vertical crustal deformation is time-invariant. That is, we could use the leveling-derived vertical rate to simulate the vertical velocity of GPS site when the two benchmarks are co-located or within a certain distance. If the GPS+Leveling projection (to LOS) reconcile with InSAR LOS, then we could remove the interpolated vertical values (at InSAR points) from InSAR LOS. The remaining LOS values represent horizontal crustal deformation. Besides, the leveling vertical velocity could be adopted as constraints for kinematic models.

(2) Three dimensional GPS velocities. In my GPS data processing, I did not estimate the vertical velocity due to its large uncertainties. Therefore, I used the 3D velocity field from Liang et al. (2013) to test this method. The scheme is similar to the case of leveling except well distributed GPS site would help the interpolation.

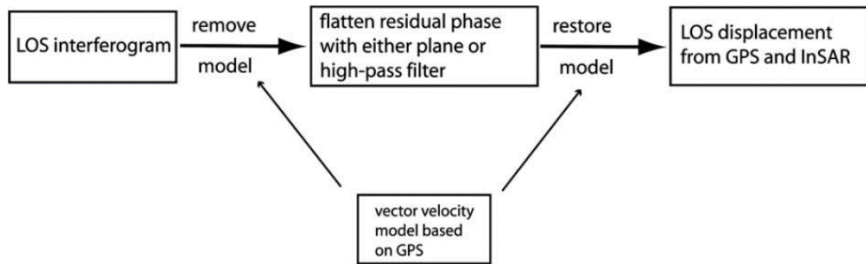


Figure 2.9. Flow chart for combining InSAR and GPS using the remove/filter/restore method. From Wei et al. (2010).

(3) The remove-filter-restore method proposed by Wei et al. (2010). I show the basic idea of this method in Figure 2.9. The method assumes that GPS-derived velocity field is dominated by the long wavelength horizontal crustal deformation, while the InSAR-derived LOS rate field is

composed of both the long and short wavelength 3-D information. The first step is to remove the GPS-interpolated horizontal velocity (projected to LOS) from LOS, then high-pass filter the LOS residuals using a Gaussian filter, and finally add the high-pass filtered results back to the GPS velocity map (interpolation expressed in LOS). Such procedure ensures that the InSAR velocities agree with the GPS at the longest wavelengths, while preserving the short wavelength features that make the InSAR contribution valuable in the near field of fault.

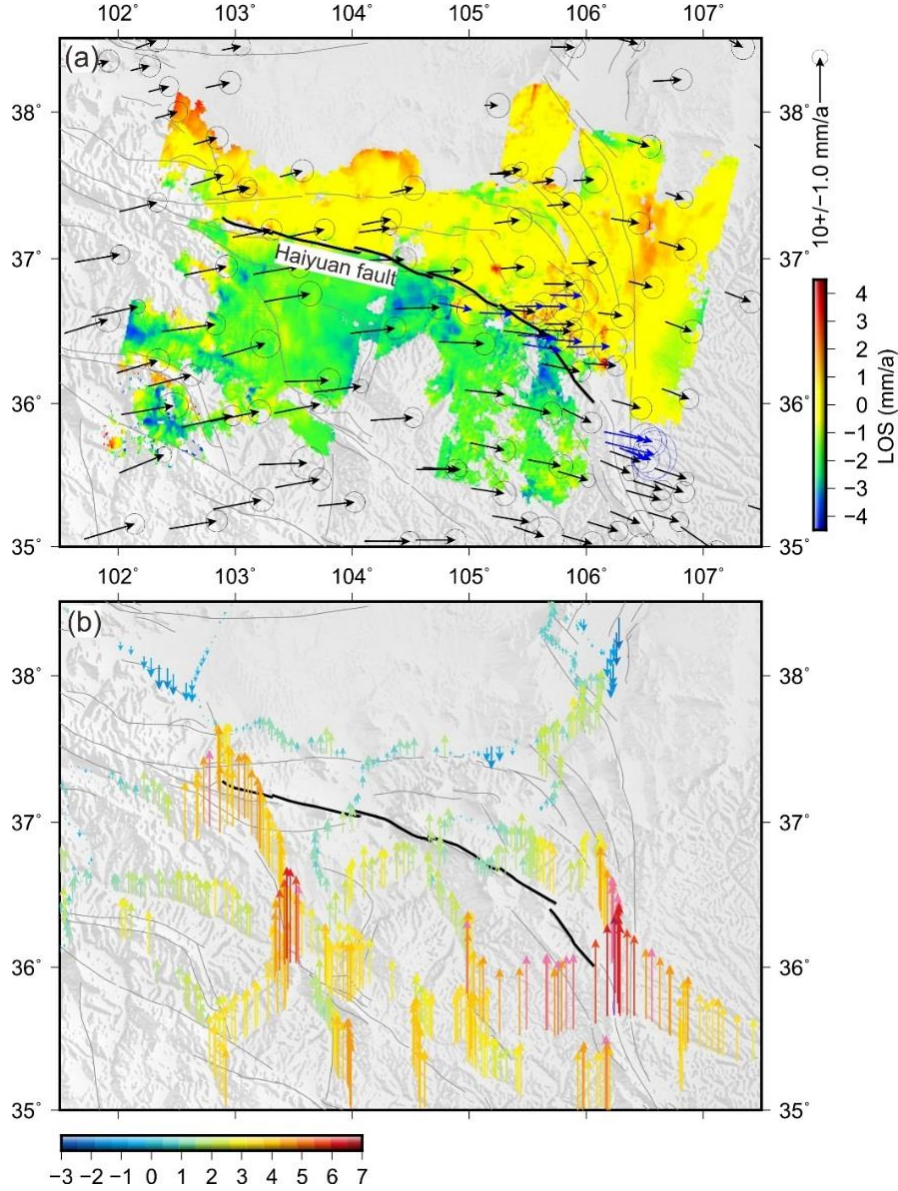


Figure 2.10. (a) Observed InSAR displacements and GPS velocity field in the northeastern Tibet. (b) Vertical velocity field from leveling measurements (Hao et al., 2014).

In order to confirm which method could be used to integrate GPS and InSAR, here, I take the geodetic dataset in the northeastern Tibet as example. I did three kinds of comparisons, details as follows:

- (1) The long-term (1970-2012) interseismic leveling data were used (Figure 2.10; Hao et al.,

2014). I first selected the leveling stations within 5 km from GPS stations, and use the leveling value to simulate the vertical velocity of the GPS site. Then projected the 3D velocity to LOS according to the local incidence angles. The InSAR data, which are located within a circle radius of 1 km of the GPS sites, were averaged and used for comparison with the GPS+Leveling projection.

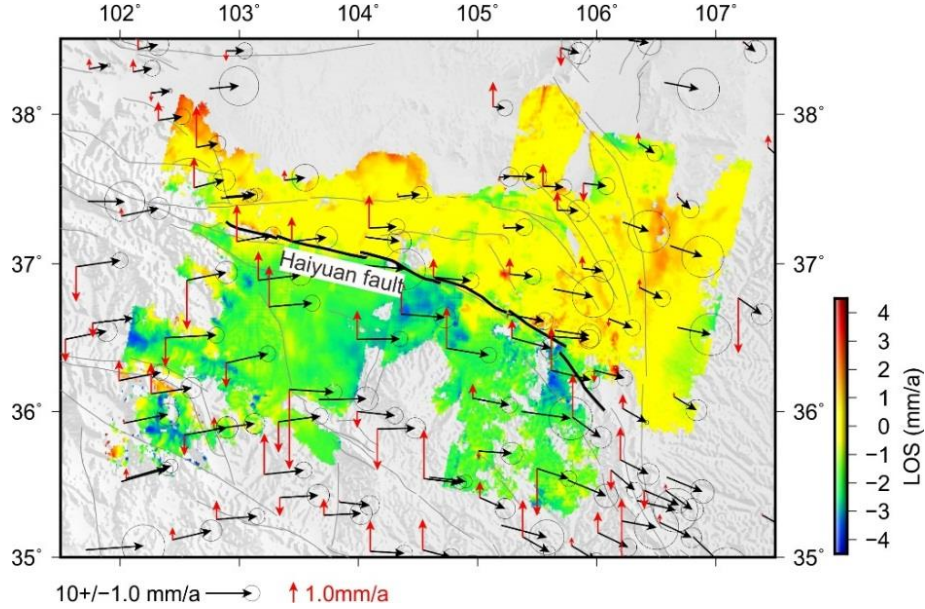


Figure 2.11. Observed InSAR displacements and three dimensional GPS velocity field in the northeastern Tibet (Liang et al., 2013).

(2) I used the 3D GPS velocity solution of Liang et al. (2013) (Figure 2.11). Similar to the above procedure, I projected the 3D GPS velocity to LOS according to the local incidence angles, and then compare with the observed InSAR LOS values.

(3) I used the remove-filter-restore method. First, I removed an interpolated map of the horizontal GPS velocities from the observed InSAR data, then high-pass filtered the residual at 50 km wavelength (determined by the average spacing of GPS sites; Figure 2.12), and finally added the result back to the GPS velocity map. The final restored LOS velocity map is under the same reference frame with GPS horizontal velocity. Note that the restored LOS velocity map is dominated by horizontal crustal deformation (from GPS and InSAR), but there still exists the potential short wavelength vertical deformation (from InSAR), for instance, small scale local subsidence.

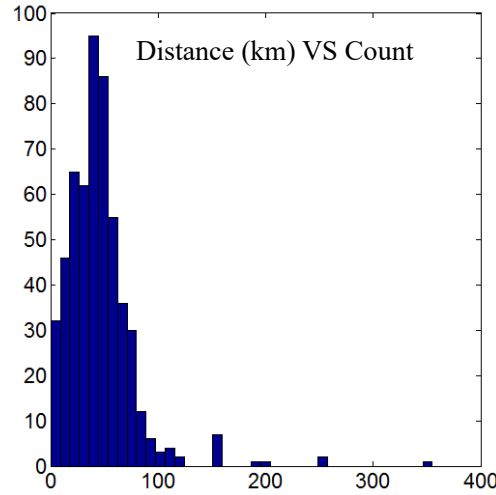


Figure 2.12. Histogram of relative distance between GPS stations in the northeastern Tibetan Plateau. The mean value is 0.46° , corresponds to 45.7 km.

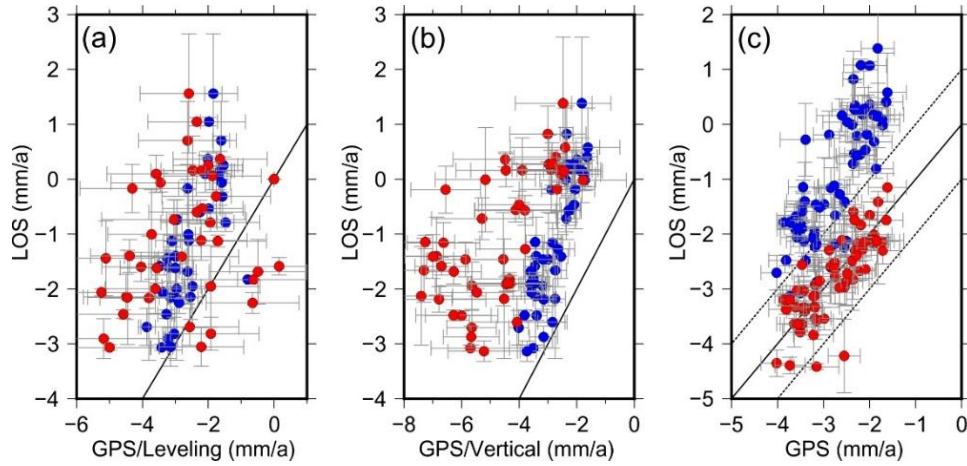


Figure 2.13. Comparisons between different geodetic dataset. (a) Observed InSAR LOS values versus observed GPS horizontal velocities projected to LOS (blue error bars). Observed InSAR LOS values versus the ‘GPS horizontal + leveling vertical’ projected to LOS (red error bars). (b) Blue error bars represent observed InSAR LOS values versus GPS horizontal velocities projected to LOS (Liang et al., 2013). Red error bars represent the observed InSAR LOS values versus ‘GPS horizontal + GPS vertical’ projected to LOS (Liang et al., 2013). (c) Blue error bars indicate observed InSAR LOS values versus observed GPS horizontal velocities projected to LOS. Red error bars represent the restored InSAR LOS values versus observed GPS horizontal velocities projected to LOS.

The geodetic data comparison results are shown in Figure 2.13. First, we see that the LOS projection of horizontal GPS velocities deviate significantly from observed InSAR LOS by the 1:1 line. This indicates that systematic vertical deformation or orbital residuals exist in the InSAR LOS displacements, where the former is most likely the dominant factor. Besides, it is noteworthy that adding the leveling-derived vertical velocities leads to higher dispersion between GPS and InSAR (Figure 2.13a), implying that 3D deformation (GPS+leveling) are not consistent at 1-2 mm/a level with InSAR LOS. The discrepancy might relates to several factors: orbital residuals in InSAR, or

leveling measurements could not represent the present-day vertical deformation in the northeastern Tibet, or temporal variations in vertical deformation over the past few decades as GPS (1998-2017), leveling (1970-2012) and InSAR (2003-2010) covers different periods, or combinations of the above factors. Furthermore, 3D GPS velocities could also not be made consistent with InSAR (Figure 2.13b). The above factors also apply here; as an possibility, the inconsistence might indicates that the conventional nontectonic deformation corrections (especially for campaign-mode GPS sites) in GPS vertical velocity estimation, such as atmospheric loading and surface water loading (Liang et al., 2013), are insufficient to derive a reliable tectonic vertical velocity solution. Finally, the remove-filter-restore method produced a LOS ratemap that reconciles InSAR with the 2D GPS velocity (Figure 2.13c), despite short wavelength vertical crustal deformation might be still preserved. The above results indicate complicated vertical crustal deformation in the northeastern Tibet, and highlight the significance to consider the vertical deformation signals in the observed InSAR LOS map.

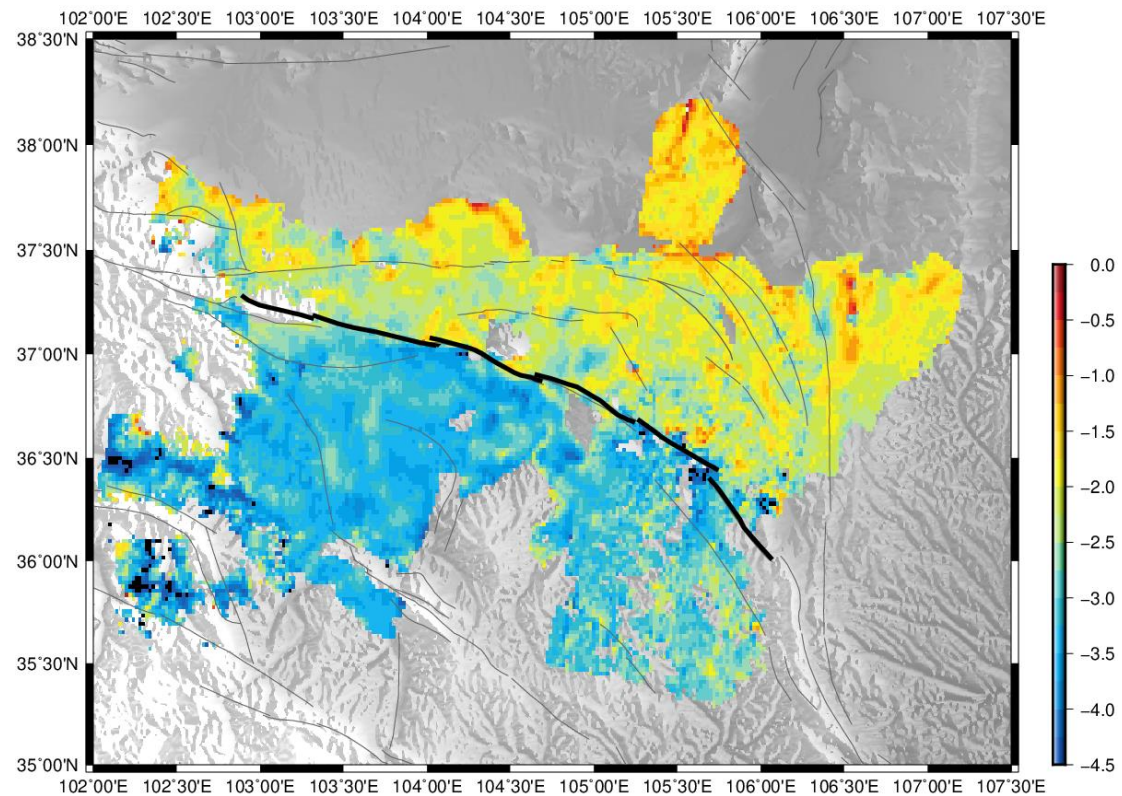


Figure 2.12. The InSAR displacements from the remove-filter-restore method.

Considering the above results, the restored LOS ratemap is thus used in my following models. That is, along the Haiyuan fault system and the Xianshuihe fault in the following Chapters. As for the Altyn Tagh fault, due to the sparse distribution of GPS stations across the fault, I chose to compare the GPS and InSAR directly and masked InSAR points that located in regions with subsidence or uplift. I will describe in detail the geodetic interpretations and modeling in each Chapter.

2.3.3. Minor comments

In the above contents, I introduced three methods to integrate horizontal GPS, Leveling and InSAR; despite I did careful works, for example, assess different weights datasets (2D-GPS vs Leveling, 2D-GPS vs GPS-vertical) and select co-located points (GPS vs Leveling, GPS vs InSAR) at different distances, the results show GPS+Leveling and 3D-GPS do not consistent with observed InSAR at 1-2 mm/a level. Several factors can cause irreconciliation between the geodetic datasets, as I present in the previous section. In Chapter 6, I will present further arguments on the geodetic datasets. Here, I argue that, despite the remove-filter-restore method produced a LOS ratemap consistent with horizontal GPS, the restored LOS displacements lose the long wavelength vertical crustal deformation (from InSAR) but preserve short wavelength vertical crustal deformation (from InSAR). As a result, I propose that the remove-filter-restore method is not the ultimate but a trade-off choice to combine GPS with InSAR. I expect more efforts to solve this issue.

2.4. References

- Allen, C. R., Zhuoli, L., Hong, Q., Xueze, W., Huawei, Z., & Weishi, H. (1991). Field study of a highly active fault zone: The Xianshuihe fault of southwestern China. *Geological Society of America Bulletin*, 103(9), 1178-1199.
- Altamimi, Z., Collilieux, X., & Métivier, L. (2011). ITRF2008: an improved solution of the international terrestrial reference frame. *Journal of Geodesy*, 85(8), 457-473.
- Cavalié, O., Lasserre, C., Doin, M. P., Peltzer, G., Sun, J., Xu, X., & Shen, Z. K. (2008). Measurement of interseismic strain across the Haiyuan fault (Gansu, China), by InSAR. *Earth and Planetary Science Letters*, 275(3-4), 246-257.
- Daout, S., Doin, M. P., Peltzer, G., Lasserre, C., Socquet, A., Volat, M., & Sudhaus, H. (2018). Strain partitioning and present-day fault kinematics in NW Tibet from Envisat SAR interferometry. *Journal of Geophysical Research: Solid Earth*, 123(3), 2462-2483.
- Diao, F., Wang, R., Wang, Y., Xiong, X., & Walter, T. R. (2018). Fault behavior and lower crustal rheology inferred from the first seven years of postseismic GPS data after the 2008 Wenchuan earthquake. *Earth and Planetary Science Letters*, 495, 202-212.
- Goldstein, R. M., Zebker, H. A., & Werner, C. L. (1988). Satellite radar interferometry: Two-dimensional phase unwrapping. *Radio Science*, 23(4), 713-720.
- Hao, M., Wang, Q., Shen, Z., Cui, D., Ji, L., Li, Y., & Qin, S. (2014). Present day crustal vertical movement inferred from precise leveling data in eastern margin of Tibetan Plateau. *Tectonophysics*, 632, 281-292.
- He, J., Vernant, P., Chéry, J., Wang, W., Lu, S., Ku, W., ... & Bilham, R. (2013). Nailing down the slip rate of the Altyn Tagh fault. *Geophysical Research Letters*, 40(20), 5382-5386.
- Herring, T. (2003). MATLAB Tools for viewing GPS velocities and time series. *GPS Solutions*, 7(3), 194-199.
- Herring, T. A., R. W. King, M. A. Floyd, S. C. McCluskey. (2016). Introduction to GAMIT/GLOBK, Release 10.6, Massachusetts Institute of Technology.
- Huang, M. H., Bürgmann, R., & Freed, A. M. (2014). Probing the lithospheric rheology across the eastern margin of the Tibetan Plateau. *Earth and Planetary Science Letters*, 396, 88-96.
- Jolivet, R., Lasserre, C., Doin, M. P., Guillaso, S., Peltzer, G., Dailu, R., ... & Xu, X. (2012). Shallow creep on the Haiyuan fault (Gansu, China) revealed by SAR interferometry. *Journal of Geophysical Research: Solid Earth*, 117(B6).
- Jolivet, R., Lasserre, C., Doin, M. P., Peltzer, G., Avouac, J. P., Sun, J., & Dailu, R. (2013). Spatio-temporal evolution of aseismic slip along the Haiyuan fault, China: Implications for fault frictional properties. *Earth and Planetary Science Letters*, 377, 23-33.
- Li, Y., Zhang, J., Li, Z., Luo, Y., Jiang, W., & Tian, Y. (2016). Measurement of subsidence in the Yangbajing geothermal fields, Tibet, from TerraSAR-X InSAR time series analysis. *International Journal of Digital Earth*, 9(7), 697-709.
- Liang, S., Gan, W., Shen, C., Xiao, G., Liu, J., Chen, W., ... & Zhou, D. (2013). Three-dimensional velocity field of present-day crustal motion of the Tibetan Plateau derived from GPS measurements. *Journal of Geophysical Research: Solid Earth*, 118(10), 5722-5732.
- Lyard, F., Lefevre, F., Letellier, T., & Francis, O. (2006). Modelling the global ocean tides: modern insights from FES2004. *Ocean Dynamics*, 56(5-6), 394-415.

- Pan, Y., Shen, W. B., Shum, C. K., & Chen, R. (2018). Spatially varying surface seasonal oscillations and 3-D crustal deformation of the Tibetan Plateau derived from GPS and GRACE data. *Earth and Planetary Science Letters*, 502, 12-22.
- Reilinger, R., McClusky, S., Vernant, P., Lawrence, S., Ergintav, S., Cakmak, R., ... & Nadariya, M. (2006). GPS constraints on continental deformation in the Africa-Arabia-Eurasia continental collision zone and implications for the dynamics of plate interactions. *Journal of Geophysical Research: Solid Earth*, 111(B5).
- Ryder, I., Parsons, B., Wright, T. J., & Funning, G. J. (2007). Post-seismic motion following the 1997 Manyi (Tibet) earthquake: InSAR observations and modelling. *Geophysical Journal International*, 169(3), 1009-1027.
- Saria, E., Calais, E., Altamimi, Z., Willis, P., & Farah, H. (2013). A new velocity field for Africa from combined GPS and DORIS space geodetic Solutions: Contribution to the definition of the African reference frame (AFREF). *Journal of Geophysical Research: Solid Earth*, 118(4), 1677-1697.
- Song, X., Jiang, Y., Shan, X., Gong, W., & Qu, C. (2019). A Fine Velocity and Strain Rate Field of Present-Day Crustal Motion of the Northeastern Tibetan Plateau Inverted Jointly by InSAR and GPS. *Remote Sensing*, 11(4), 435.
- Su, X., Yao, L., Wu, W., Meng, G., Su, L., Xiong, R., & Hong, S. (2019). Crustal deformation on the northeastern margin of the Tibetan plateau from continuous GPS observations. *Remote Sensing*, 11(1), 34.
- Wang, M., Li, Q., Wang, F., Zhang, R., Wang, Y., Shi, H., ... & Shen, Z. (2011). Far-field coseismic displacements associated with the 2011 Tohoku-oki earthquake in Japan observed by Global Positioning System. *Chinese Science Bulletin*, 56(23), 2419-2424.
- Wei, M., Sandwell, D., & Smith-Konter, B. (2010). Optimal combination of InSAR and GPS for measuring interseismic crustal deformation. *Advances in Space Research*, 46(2), 236-249.
- Wen, Y., Li, Z., Xu, C., Ryder, I., & Bürgmann, R. (2012). Postseismic motion after the 2001 Mw 7.8 Kokoxili earthquake in Tibet observed by InSAR time series. *Journal of Geophysical Research: Solid Earth*, 117(B8).
- Williams, S. D. (2008). CATS: GPS coordinate time series analysis software. *GPS solutions*, 12(2), 147-153.
- Wright, T. J., Parsons, B. E., & Lu, Z. (2004). Toward mapping surface deformation in three dimensions using InSAR. *Geophysical Research Letters*, 31(1).
- Yamasaki, T., & Houseman, G. A. (2012). The crustal viscosity gradient measured from post-seismic deformation: A case study of the 1997 Manyi (Tibet) earthquake. *Earth and Planetary Science Letters*, 351, 105-114.
- Zhang, J., Wen, X. Z., Cao, J. L., Yan, W., Yang, Y. L., & Su, Q. (2018b). Surface creep and slip-behavior segmentation along the northwestern Xianshuihe fault zone of southwestern China determined from decades of fault-crossing short-baseline and short-level surveys. *Tectonophysics*, 722, 356-372.
- Zhang, L., Cao, D., Zhang, J., & Sui, L. (2018a). Interseismic Fault Movement of Xianshuihe Fault Zone Based on Across-Fault Deformation Data and InSAR. *Pure and Applied Geophysics*, 176(2), 649-667.

Chapter 3· Measuring the crustal deformation along the Altyn Tagh fault using GPS and InSAR

The work in this chapter consists of two parts, the first part focuses on using 3D block model, only with GPS data, to invert the fault coupling along the Altyn Tagh fault. I discuss the seismic potential along the Altyn Tagh fault, and implications for the kinematic crustal deformation mechanism of the Tibetan Plateau. This work has been published as: *Li, Y., Shan, X., Qu, C., Liu, Y., & Han, N. (2018). Crustal deformation of the Altyn Tagh fault based on GPS. Journal of Geophysical Research: Solid Earth, 123(11), 10309-10322.*

The second part mainly focuses on using GPS and InSAR to measure the crustal deformation across the western Altyn Tagh fault (longitude 86°E). First, I present the GPS and InSAR data that are used. Then, using the 2D buried infinite screw dislocation model, the fault locking depth and slip rate of the western Altyn Tagh fault are inverted. In the last, I discuss the interseismic faulting behavior of the western Altyn Tagh fault.

The first part of the above was done while I was in China in 2017, and was published in November 2018. After one month when I arrived in France in December 2017, the InSAR result from Daout et al. (2018) was published. So, I continued the study on the Altyn Tagh fault by simultaneously using GPS and InSAR, within the framework of Bayesian method.

First part

Crustal deformation of the Altyn Tagh fault system based on GPS

This work has been published as: *Li, Y., Shan, X., Qu, C., Liu, Y., & Han, N. (2018). Crustal deformation of the Altyn Tagh fault based on GPS. Journal of Geophysical Research: Solid Earth, 123(11), 10309-10322.* Therefore, I present in the following as the published version.

Journal of Geophysical Research: Solid Earth

RESEARCH ARTICLE

10.1029/2018JB015814

Crustal Deformation of the Altyn Tagh Fault Based on GPS

Yanchuan Li¹ , Xinjian Shan¹ , Chunyan Qu¹, Yunhua Liu¹ , and Nana Han¹¹State Key Laboratory of Earthquake Dynamics, Institute of Geology, China Earthquake Administration, Beijing, China

Key Points:

- Altyn Tagh fault slip rate and coupling inverted using new, dense interseismic GPS velocities
- The three fault segments between Sulamu Tagh and Aksay bends have the potential to rupture in *Mw* 7.7, *Mw* 7.6, and *Mw* 7.8 earthquakes
- A hybrid kinematic model is needed to delineate the crustal deformation of the Tibetan Plateau

Supporting Information:

- Supporting Information S1
- Data Set S1

Correspondence to:

X. Shan,
xjshan@ies.ac.cn

Citation:

Li, Y., Shan, X., Qu, C., Liu, Y., & Han, N. (2018). Crustal deformation of the Altyn Tagh fault based on GPS. *Journal of Geophysical Research: Solid Earth*, 123. <https://doi.org/10.1029/2018JB015814>

Received 22 MAR 2018

Accepted 10 NOV 2018

Accepted article online 15 NOV 2018

Abstract Knowledge of the slip behavior of the Altyn Tagh fault (ATF) has significant implications for our understanding of the tectonic deformation of the Tibetan Plateau. In this study, we process Global Positioning System (GPS) data spanning 2009–2017 across the western ATF, merge the solution with recently published GPS velocities, and obtain a dense GPS velocity field for northern Tibet. We introduce an elastic block model and estimate the fault slip rate, interseismic fault coupling (ISC), and seismic moment accumulation rate along the ATF. The estimated left-lateral strike-slip rate of the ATF decreases eastward from 12.8 ± 0.4 mm/a to 0.1 ± 0.2 mm/a. Results show a heterogeneous distribution of ISC along the fault, with the fault locking depth varying from 5 to 20 km. The seismic moment accumulation rate is $2.16\text{--}2.37 \times 10^{18}$ N m/km along three segments between Sulamu Tagh and Aksay bends, where the accumulated seismic moment over the last five centuries could be balanced by earthquakes with magnitudes of *Mw* 7.7, *Mw* 7.6, and *Mw* 7.8, respectively. We calculate the ratio of the Indo-Eurasia convergence accommodated by the ATF and find that 10.3% of the convergence is accommodated along the fault by lateral extrusion; quantitative analysis of the strain rate, however, shows that a large part of the northern Tibet is not well described by elastic block rotation. Consequently, we suggest that a hybrid kinematic model that includes both block-like and continuous deformation is needed to better delineate the crustal deformation of the Tibetan Plateau.

1. Introduction

The northern edge of the Tibetan Plateau is defined by the, ~1,500-km-long, active left-lateral Altyn Tagh fault (Figure 1), which separates the active Tibetan Plateau and the stable Tarim platform (Molnar & Tapponnier, 1975; Shen et al., 2001; Yin et al., 2002). The kinematic behavior of the Altyn Tagh fault is of great significance for understanding the present-day crustal deformation in the northern Tibetan Plateau and the collisional tectonics in Asia (Mériaux et al., 2012). For instance, the fault slip rate provides key constraints for testing whether the crustal deformation of Tibet is dominated by lateral extrusion (e.g., Avouac & Tapponnier, 1993; Tapponnier et al., 2001) or by distributed crustal shortening (e.g., England & Molnar, 1997; Houseman & England, 1993). Both millennial and present-day slip rates of the Altyn Tagh fault have been well constrained from postglacial offsets (e.g., Cowgill, 2007; Peltzer et al., 1989), morphochronologic investigations (e.g., Gold et al., 2009; Mériaux et al., 2004, 2005, 2012; Zhang et al., 2007), Global Positioning System (GPS) measurements (e.g., Bendick et al., 2000; He et al., 2013; Shen et al., 2001), and Interferometric Synthetic Aperture Radar (InSAR) observations (e.g., Elliott et al., 2008; Wright et al., 2004). The previous results provide a slip rate of ~10 mm/a along the central segment of the Altyn Tagh fault. However, interseismic fault coupling along the length of the Altyn Tagh fault, which acts as a quantitative characteristic of fault kinematics and provides insight into the fault physical mechanisms, remains poorly known (e.g., Jolivet et al., 2015).

Two *M* 7.2 earthquakes occurred along the continental Altyn Tagh fault in 1924, west of Qiemo county, and another *M* 6.7 earthquake occurred along the fault south of Qiemo county in 1933 (Shen et al., 2001; Figure 1). Only a minor level of seismicity has been detected by instrumental recordings along the entire fault over the last several decades. In contrast, other continental strike-slip faults have hosted numerous catastrophic earthquakes, such as the 1906 *M* 8.3 San Francisco earthquake along the San Andreas fault (e.g., Thatcher, 1975), a sequence of eight *M* > 7 earthquakes along the North Anatolian fault from 1939 to 1999 (e.g., Cakir et al., 2005), and the 2001 *Mw* 7.8 Kokoxili earthquake along the Kunlun fault (e.g., Xu et al., 2006, Figure 1). As a consequence, questions remain about the level of seismic risk along the active strike-slip Altyn Tagh fault, highlighting the need for better quantification of the seismic potential of the fault. Modern space geodetic techniques enable investigations of the heterogeneous fault coupling along the Altyn Tagh fault. Such exploration leads to the identification of regions where faults are locked, or coupled, accumulating elastic

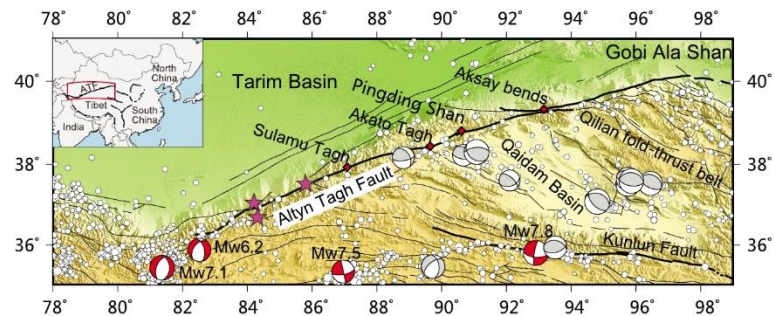


Figure 1. Tectonic setting of the northern Tibetan plateau. Bold black lines represent the surface trace of the Altyn Tagh fault (ATF) and the Kunlun fault. Thin black lines show regional active faults. White circles are earthquakes with magnitudes of smaller than 6.0 from 1986 to 2017, as reported by the U.S. Geological Survey. The gray focal mechanism solutions have magnitudes of equal to or greater than 6.0 and are based on the global centroid moment tensor. Red focal mechanisms correspond to the 1997 Mw 7.5 Manyi earthquake, 2001 Mw 7.8 Kokoxili earthquake, 2008 Mw 7.1 Yutian earthquake, and 2012 Mw 6.2 Yutian earthquake, respectively. Pink stars correspond to $M > 6$ historical earthquakes along the ATF (Shen et al., 2001). Red diamonds show locations of the four major restraining bends. The inset map in the upper left shows the location of the study area.

strain that can provide information for building scenarios of future large earthquakes (e.g., Jolivet et al., 2015; Li et al., 2017).

In this study, we revisit the same locations used for campaign-mode GPS benchmarks across the western segment of the Altyn Tagh fault (86°E) by He et al. (2013). We first process the GPS data and combine the derived velocity solution with recently published velocity solutions from the surrounding area and obtain a dense GPS velocity field for the northern Tibetan Plateau. Using the DEFNODE elastic block modeling approach (McCaffrey et al., 2007), we estimate the fault slip rate, interseismic fault coupling (ISC), and seismic accumulation rate along the Altyn Tagh fault. Then we explore the elastic strain accumulation and evaluate the seismic hazard along the fault. Finally, combined with the second invariant of the strain rate tensor field around the Altyn Tagh fault, which gives new insights that are not available from the block model, implications for the crustal deformation of the Tibetan Plateau are considered. We find heterogeneous interseismic fault coupling and strain concentration along the Altyn Tagh fault and suggest a hybrid kinematic model that includes both block-like and continuous deformation be applied to investigate the crustal deformation of the Tibetan Plateau.

2. GPS Data and Block Modeling

2.1. GPS Data Processing

Our GPS velocity solution consists of three parts: (1) the Crustal Movement Observation Network of China and the Tectonic and Environmental Observation Network of Mainland China (CMONOC I/II). CMONOC GPS data acquired between 1999 and 2014, including those from both campaign and continuous stations (a total of 968 sites in the study area), were processed/compiled by Wang et al. (2017). (2) We also compile the velocities of eight GPS sites from Ge et al. (2015), including five continuous and three campaign-mode sites. The continuous stations were installed in 2011, span the southern Tarim Basin, the central Altyn Tagh fault (90°E), and a region of west-northwest trending fold and thrust faults. Ge et al. (2015) used GPS data spanning from 2011 to 2016 to obtain a regional velocity solution under a Eurasia-fixed frame. (3) We revisit the same 16 locations used by He et al. (2013) as campaign-mode GPS benchmarks in October 2017; these were measured 2–3 times in the period 2009–2011, across the western segment of the Altyn Tagh fault (86°E).

We then process the campaign-mode GPS data together with those data collected between 2009 and 2011, and with seven regional CMONOC continuous sites using the GAMIT/GLOBK 10.6 software (Herring et al., 2016). Raw phase observations are first processed together with 40 globally distributed International Global Navigation Satellite System Service (IGS, <http://www.igs.org/>) sites to obtain loosely constrained daily station coordinates and satellite orbit parameters. We employ IGS precise orbits and Earth orientation parameters, absolute antenna phase center calibrations, and the Finite Element Solution 2004 ocean tide loading model during the daily data processing (Lyard et al., 2006). The time series for each station is carefully

Table 1
The Number of Colocated Sites and the Root-Mean-Square (RMS) of Velocity Residuals

Source	Source	Number of common sites	RMS (mm/a)
Wang et al., 2017	This study	16	0.75
	Ge et al., 2015	6	0.71

examined to exclude outliers, where we set 3-sigma from the mean as the threshold for outlier detection. Loosely constrained daily solutions are then expressed in the International Terrestrial Reference System 2008 (ITRF2008) by estimating seven transformation parameters (orientation, translation, and scale) using the 40 globally distributed IGS stations. Finally, we obtain a new unified, consistent, and robust geodetic velocity field across the western Altyn Tagh fault in a Eurasia-fixed reference frame (Altamimi et al., 2011).

Although the previously published velocity solutions (i.e., Ge et al., 2015; Wang et al., 2017) that we used are all referenced to the *Eurasia-fixed reference frame*, deviations still occur due to different processing strategies in data trade-off, frame choice, and a priori constraints; to combine them, we solve for the Euler vector between two solutions by minimizing the velocity residuals within common sites (Li et al., 2017). We choose the Wang et al. (2017) solution as the master solution and translated our solutions and those of Ge et al. (2015) into the frame of Wang et al. (2017). We average the velocities for the colocated sites. The number of colocated sites and the root-mean-square of the velocity residuals are listed in Table 1. The final Eurasia-fixed GPS sites velocities are shown in Figure 2.

During our GPS data time span (1999–2017), several destructive earthquakes occurred in the China mainland, of which the 2001 *Mw* 7.8 Kokoxili earthquake and the 2008 *Mw* 7.9 Wenchuan earthquake are the ones most likely to generate significant postseismic deformation (e.g., Rui & Stamps, 2016). For the two earthquakes, Wang et al. (2017) state that they removed the postearthquake data of the near-field stations. Due to sparse GPS sites converged near the epicenter of the 2001 *Mw* 7.8 Kokoxili earthquake, there have been no published papers using GPS to study the postseismic deformation. However, several studies (e.g., Garthwaite et al., 2013; Zhao et al., 2018) reported that significant postseismic deformation occurs near the epicenter by using InSAR. It remains a scientific issue as whether the GPS sites velocities near the epicenter are affected by the postseismic deformation of the 2001 *Mw* 7.8 Kokoxili earthquake. Along the central Altyn Tagh fault (90°E), no earthquake with magnitude larger than 6 occurred between 2011 and 2016, when Ge et al. (2015) occupied the measurements of GPS stations. Of the 16 campaign-mode GPS sites (2009–2017) across the western Altyn Tagh fault (86°E), the southernmost station, which is ~100 km from the epicenter of the 1997 *Mw* 7.5 Manyi earthquake (Figure 1), is most likely to be affected by the postseismic deformation following the earthquake. However, surface deformation derived from the InSAR data, which were acquired between November 1997 and September 2001, show the postseismic deformation of the 1997 *Mw* 7.5 Manyi earthquake only affected a region of ~20 km from the surface rupture and the surface displacement

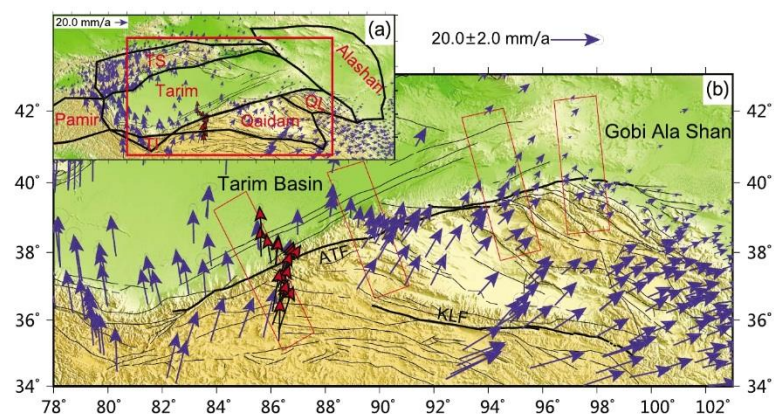


Figure 2. (a) Global Positioning System (GPS) velocity field in the northern Tibetan plateau and block boundaries (bold black lines) of the northern Tibetan plateau. GPS velocities with respect to the stable Eurasian plate. Blue arrows that correspond to horizontal GPS velocities are compiled from Wang et al. (2017) and Ge et al. (2015). Red arrows represent horizontal GPS velocities obtained by processing data spanning 2009–2017. Bold red rectangle marks the location of b. (b) Enlarged map to show the GPS velocities across the Altyn Tagh fault. Red rectangles show the locations of GPS velocity profiles in Figure 5. Error ellipses indicate the 95% confidence levels. Abbreviations: QL, Qilian block; TS, Tien Shan block; TI, Tianshuihai block; ATF, Altyn Tagh fault; KLF, Kunlun fault.

following the earthquake obeys an exponential decay with time (e.g., Ryder et al., 2007; Yamasaki & Houseman, 2012). Hence, the 1997 M_w 7.5 Manyi earthquake postseismic signal contributes scarcely to our velocity solution. In conclusion, we regard the above GPS solutions as secular interseismic velocities (Table S1 in the supporting information).

2.2. Elastic Block Modeling

GPS stations are scarce and unevenly distributed in northern Tibet, especially across the Altyn Tagh fault. To utilize available velocities, we introduce a DEFNODE elastic block model, which simultaneously solves for angular velocities of coherent rotating blocks, permanent strain rate within the blocks, and ISC on the bounding faults (McCaffrey et al., 2007). The interseismic backslip method is applied in the model to get the fault coupling coefficient, namely, the ISC (Savage, 1983). The ISC is unitless, with 1.0 indicating where the fault surface is fully locked, and 0.0 indicating where the fault surface is fully creeping. The faults are specified by three-dimensional nodes (longitude, latitude, and depth, forming an irregular grid of points) on the fault plane. The ISC for each node is estimated during the inversion. To get the linear change in ISC values between adjacent nodes, a bilinear interpolation is used to estimate values on small rectangular fault patches (25 km along the strike and 2 km along the down-dip in our model) between the nodes. Data misfit is defined by the reduced chi-square statistic (χ_r^2):

$$\chi_r^2 = \sum_1^n \left(r_i / \sigma_i \right)^2 / (n - m) \quad (1)$$

where n is the number of observations, m is the number of free parameters, r_i is the residuals (observed minus calculated velocities), and σ_i is the data uncertainty.

Our model construction is as follows. (1) With reference to Loveless and Meade (2011) and Wang et al. (2017), we divide northern Tibet into seven blocks (Figure 2a), namely, the Alashan block, the Tien Shan block (TS), the Pamir block, the Qaidam block, the Tarim block, the Qilian block (QL), and the Tianshuihai block (TI). The Alashan and Tarim blocks are assumed to undergo block motion and elastic deformation from the locked faults, and an additional uniform internal strain rate is added for the Tien Shan block, Pamir block, Qaidam block, Qilian block, and Tianshuihai block (e.g., Zhang et al., 2004). (2) DEFNODE has numerical problems if the fault dip is set to exactly 90° , consequently, the dip angle for the Altyn Tagh fault is set to 89° , in accordance with the fault structure from magnetotelluric data (e.g., Xiao et al., 2017). The dip angle of the southern Tien Shan fault is set to 30° , as determined by a grid search (between 5° and 85°) to minimize the misfit between the observed and modeled GPS velocities. Other block-bounding faults, such as the Kunlun fault and the Haiyuan fault, are set to be vertical (89°). The optimal mean fault locking depth (locking depth = 20 km) is also estimated using a grid search (between 0.1 and 35 km). During the inversion, a uniform fault locking depth (20 km) for the block-bounding faults is used, except for the Altyn Tagh fault, which is the focus of the study. Considering the sparse distribution of GPS sites in the near field of the Altyn Tagh fault and no shallow fault creeping reported along the fault, ISC is constrained to decrease with depth to avoid unrealistic fault-coupling results. (3) We perform an iterative procedure to estimate the block rotation parameters. We obtain the initial block rotation parameter values by assuming rigid blocks, and then in all further iterations the internal strain parameters are estimated. We execute the program for more than 1,000 times and find that the prior ISC values have little effect on the inversion results. The final rotation and strain rate parameters are provided in the supporting information (Table S2).

We conduct several resolution tests (the *zebra test*; e.g., Li et al., 2017; McCaffrey et al., 2007) to determine what wavelengths of variations in ISC our GPS network could resolve. We first set the mean spacing between two adjacent nodes to increase from ~ 60 to ~ 300 km along the Altyn Tagh fault with an increment of 5 km. Second, we calculate the predicted GPS velocities at all of our sites under a given ISC distribution (defined as the forward model), as shown in Figure 3. Third, we add the white noise characteristics of the estimated uncertainties to the predicted velocities. Under the constraints of those *noisy* velocities, we conduct an inversion to estimate the ISC distributions (defined as the backward model). Resolution tests (only two test results are shown; Figures 3a and 3b) show that the ISC distribution could be well recovered when the mean spacing of the fault nodes is ~ 300 km; the existing GPS velocities are not sufficient to distinguish variations of ISC along strike when the mean spacing of fault nodes is ~ 60 km. As shown in Figure 2, GPS sites are relatively densely distributed across the eastern Altyn Tagh fault and sparse across the western Altyn Tagh fault. To

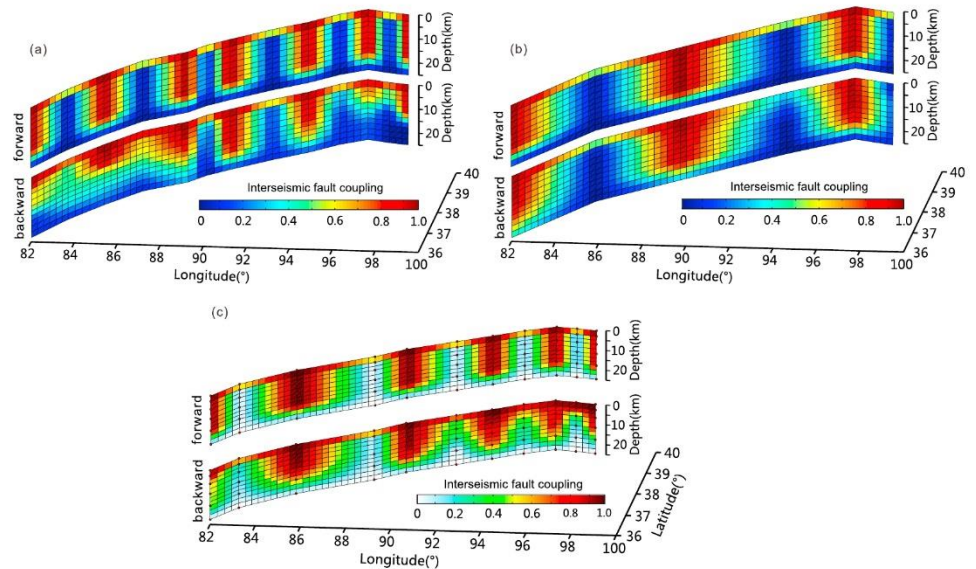


Figure 3. Resolution test for interseismic fault coupling on the Altyn Tagh fault. (a) The spacing of adjacent nodes on the Altyn Tagh fault plane with an average of 60 km. Forward represents the assumed interseismic fault coupling, and backward is the interseismic fault coupling recovered by inversion of *noisy* data generated by the forward model. (b) The forward model and recovered results when the spacing of adjacent nodes on the Altyn Tagh fault has an average of 300 km. (c) The forward model and recovered results when the location of fault nodes is set according to Global Positioning System site distribution.

reconcile the density of GPS stations and the resolution of the inversion, the location of fault nodes is set according to the GPS site distribution, with the spacing between two adjacent nodes between 60 and 300 km. Resolution results with this model (Figure 3c) show that our GPS data can detect ISC variations along the strike of the Altyn Tagh fault above a depth of ~20 km.

3. Results

We obtain the angular velocities and strain rate parameters of each block in our best fitting model ($\chi^2=3.6$). The angular velocities are then used to calculate the fault slip rates of the Altyn Tagh fault (Figure 4), which we interpret to be comparable to long-term fault slip rates (e.g., Li et al., 2017; Zhang et al., 2004). Our results show that the Altyn Tagh fault is dominated by left-lateral strike-slip movements, accompanied by small thrusting motions. The eastward decreasing strike-slip rates (~13–0 mm/a) are consistent with other previously published geodetic results (e.g., Shen et al., 2001; Zhang et al., 2004); however, the thrust component increases from west to east (~1–3 mm/a).

As an alternative approach to elastic block modeling, we also construct four cross-fault profiles based on the distribution of GPS stations and use the 2-D screw dislocation model (Savage & Burford, 1973) to invert the fault-parallel slip rate and locking depth. We use a Monte Carlo simulation approach to account for the uncertainties of GPS velocities. In each Monte Carlo simulation, the fault-parallel velocities are perturbed up to a value of 1σ uncertainties of the data using a normal distribution of noise. Then a simulated annealing method is used to get the best curve-fitting solution. A total of 2,000 Monte Carlo simulations were implemented for each profile, where fault slip rate, locking depth, and their uncertainties are derived. The fault strike-slip rates estimated by velocity profile fitting also decrease eastward (8.5–1.3 mm/a, Figure 5), in accordance with the results from the elastic block model.

Interseismic fault coupling along the Altyn Tagh fault is also calculated in the inversion (Figure 5). Our results show a heterogeneous distribution of ISC along the Altyn Tagh fault. The western segments (82–87°E) of the Altyn Tagh fault are only coupled to ~5–15 km in depth, whereas the middle segments (87–97°E) have deeper fault locking depths (~15–20 km). On the eastern segments (97–100°E), the fault locking depth is estimated at

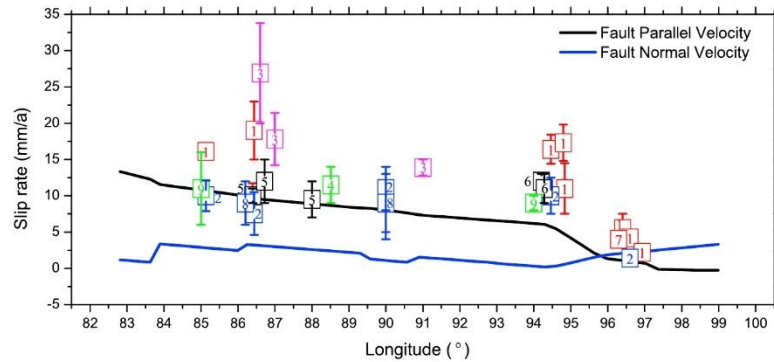


Figure 4. Slip rates of the Altyn Tagh fault derived from the elastic block model. Rectangles with error bars represent published strike-slip rates for the Altyn Tagh fault. Data are from (1) Xu et al. (2005); (2) Zhang et al. (2007); (3) Mériaux et al. (2004, 2005, 2012); (4) Cowgill, (2007), Cowgill et al. (2009); (5) Gold et al. (2009); (6) Chen et al. (2012, 2013); (7) Global Positioning System results from Bendick et al. (2000), Wallace et al. (2004), and He et al. (2013); (8) Interferometric Synthetic Aperture Radar results from Elliott et al. (2008) and Jolivet et al. (2008).

~5 km, shallower than that along the western middle segments. Fault-locking depth estimated from the screw dislocation model (Figure 5) are also in agreement with that obtained from the elastic block model. Our fault-coupling result does not show lateral variation across the major restraining bends, that is, the Sulamu Tagh, Akato Tagh, Pingding Shan, and Aksay, which most likely serve as barriers to earthquake

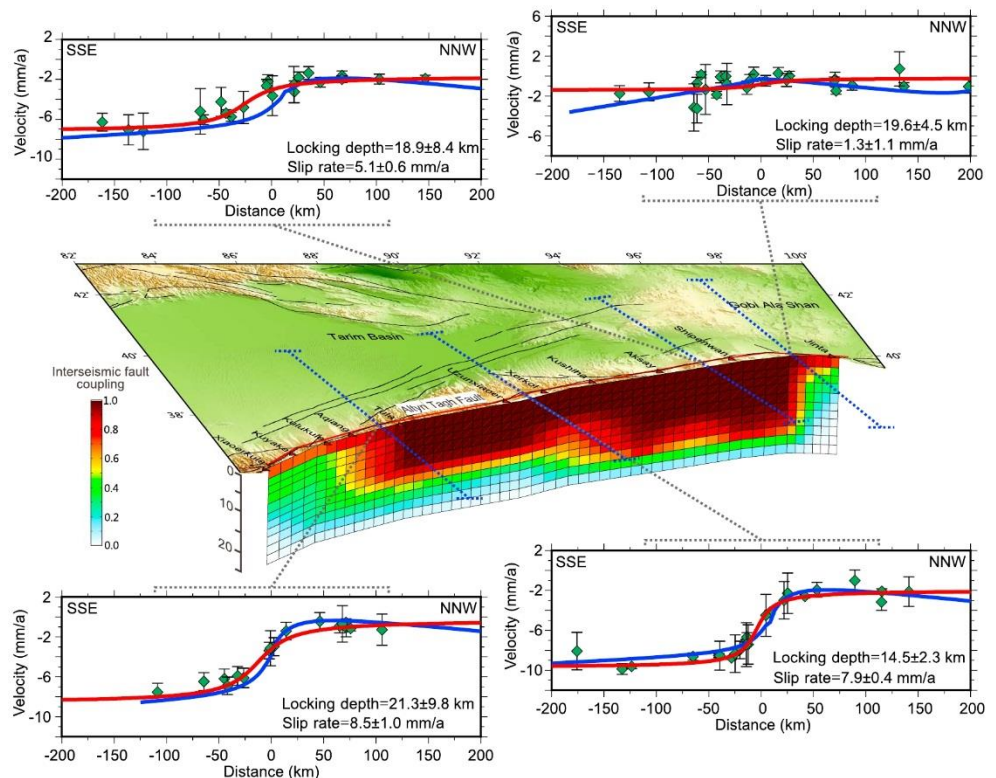


Figure 5. Interseismic fault coupling along the Altyn Tagh fault and the fault-parallel Global Positioning System velocities (green diamonds) with 1σ uncertainty error bars. Red lines correspond to the best fit model using the 2-D screw dislocation model (Savage & Burford, 1973), with values of locking depth and slip rate labeled. Blue lines represent the elastic block model predictions.

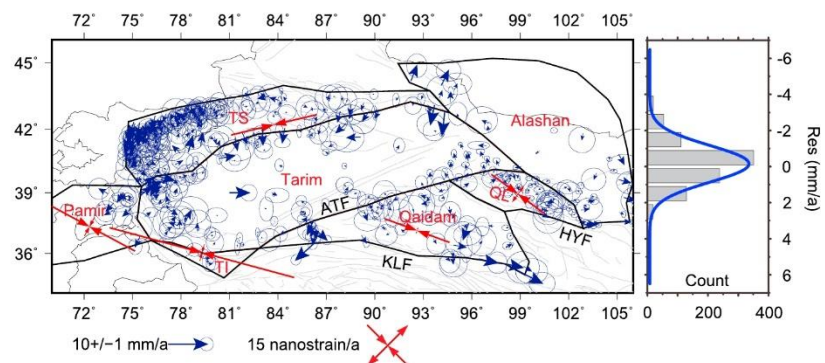


Figure 6. Global Positioning System velocity residuals associated with the block kinematic model and their statistical histogram. Error ellipses indicate the 95% confidence levels. Red arrows show the principle strain rates from the block model. ATF = Altyn Tagh fault; KLF = Kunlun Fault; QL = Qilian block; TI = Tianshuihai block; HYF = Haiyuan fault.

ruptures (e.g., Shao et al., 2018). This is due to the simplified fault geometry in our model and the spatial resolution of GPS sites. Estimated block internal strain rates are dominated by extrusion and in the order of 20–40 nanostrain/a, highlighting nonnegligible block internal deformation (Figure 6).

Observations and block model predictions fit well, as shown by the GPS velocity profiles (Figure 5). GPS velocity residuals associated with the block kinematic model and their statistical histogram are shown (Figure 6). Velocity residuals are randomly distributed without systematic misfits and are within uncertainties. The residual distribution is also consistent with a Gaussian distribution, suggesting no significant signal has been left out by the model and a reasonable consistency between observations and model. The relatively large residuals of the northeasternmost stations might be due to the effect of the Kunlun fault, as uniform fault locking depth (20 km) was set in our model without accounting for its along-strike variations. Note also the discrepancies between the block model predictions and the screw dislocation model predictions (Figure 5), which imply differences between 3-D and 2-D models.

4. Discussion

4.1. Deformation Characteristics of the Altyn Tagh Fault

The fault slip rate of the Altyn Tagh fault has been debated for decades. Early geological results (e.g., Gold et al., 2009; Mériaux et al., 2004) differed from geodetic results (e.g., Bendick et al., 2000; Elliott et al., 2008; He et al., 2013; Shen et al., 2001; Wright et al., 2004) by up to a factor of 3 (Figure 4). The disagreements were often interpreted to result from the changes in slip rate on multimillennial and decadal timescales (e.g., Cowgill et al., 2009; He et al., 2013), or due to systematic errors in interpretations of the age and offset of geological markers (e.g., Cowgill et al., 2009). Early geological results showed that a slip rate of the Altyn Tagh fault is as high as 20–30 mm/a (e.g., Mériaux et al., 2004; Peltzer et al., 1989). With improved interpretations of the ages and offsets of Quaternary geomorphic features (e.g., Zhang et al., 2007), both geodetic measurements (GPS and InSAR) and studies of Late Quaternary faulting (e.g., Mériaux et al., 2012) became consistent, giving a slip rate of ~10 mm/a along the central segment of the Altyn Tagh Fault. The fault slip rates derived from our elastic block model (Figure 4) are consistent with those from recent geological interpretations (e.g., Mériaux et al., 2012).

With regard to previous geodetic results, Elliott et al. (2008) obtained the interseismic velocities across the Altyn Tagh Fault at 85°E by processing Envisat SAR data for the period 1993–2000. By assuming a 15-km fault locking depth, the left-lateral strike-slip motion of the Altyn Tagh fault was estimated to be 11 ± 5 mm/a, which is consistent with our elastic block model result of 11.0 ± 0.7 mm/a. Jolivet et al. (2008) applied a thin-plate model to interpret the interseismic InSAR data (Lasserre et al., 2007) across the eastern segment of the Altyn Tagh fault (94°E). Their results imply a slip rate of 8–10 mm/a, overlapping the 6.2 ± 1.8 mm/a from our elastic block model (Figure 4); however, the estimated fault locking depth (~15 km) from our block model differs with that estimated by Jolivet et al. (2008) by a factor

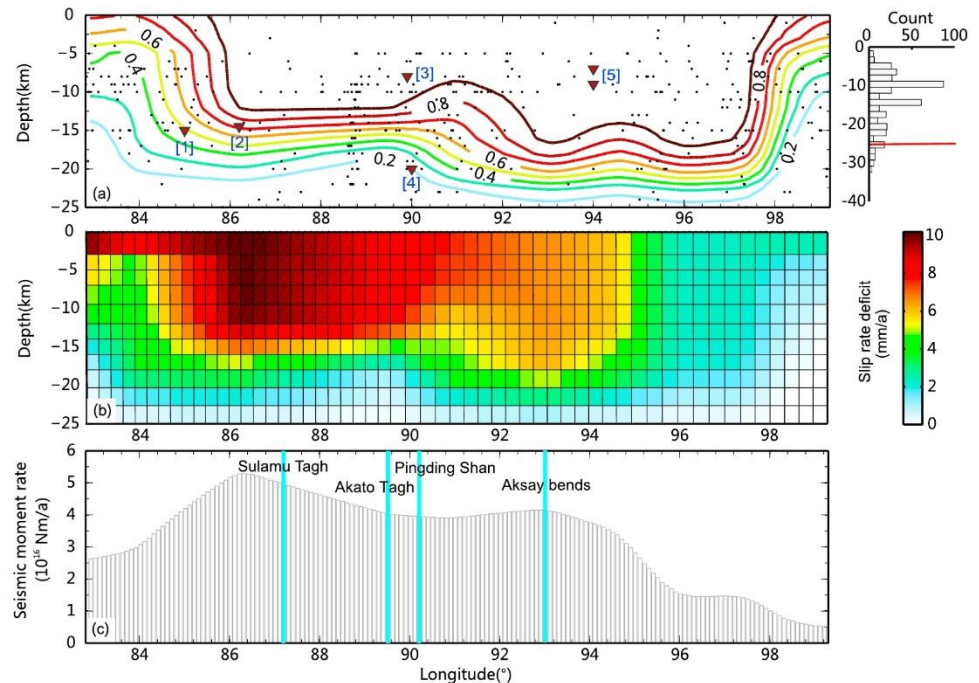


Figure 7. (a) Comparison between inverted interseismic fault coupling and fault locking from published studies and focal depth of microseisms (black dots). Data are from (1) Elliott et al. (2008); (2) He et al. (2013); (3) Bendick et al. (2000); (4) Wallace et al. (2004); (5) Jolivet et al. (2008). Microseisms are from China earthquake datacenter, spanning between 1980 and 2017. (b) Slip rate deficit on the Altyn Tagh fault plane. (c) Seismic moment accumulation rate along the Altyn Tagh fault. Bold cyan lines show the locations of the four major restraining bends.

of 2 (Figure 7a). The inconsistency might be related to different data sets, as the InSAR line of sight displacements across the Altyn Tagh fault were assumed to be purely horizontal and fault-parallel without considering the vertical deformation. He et al. (2013) established 17 GPS benchmarks across the Altyn Tagh fault at $\sim 86.2^\circ\text{E}$ and occupied those sites 2–3 times between 2009 and 2011. The resulting campaign-mode GPS velocities indicated a velocity of 9.0 ± 4.0 mm/a across the western ATF, and the best arctangent curve fitting indicates a fault locking depth of 14.5 km (Figure 7a). Compared to He et al. (2013), we construct the same cross-fault GPS velocity profile (Figures 2 and 5). However, our best curve-fitting results, such as the strike-slip fault slip rate (8.5 ± 1.0 mm/a) and the fault locking depth (21.3 ± 9.8 km), differ with those of He et al. (2013). The discrepancies may reflect the different data sets, as we revisited these sites in 2017 and obtain an improved GPS velocity field, and we also include the CMONOC sites for the cross-fault profile. Our new GPS velocity solution differs with He et al. (2013) by up to 4 mm/a under the same reference frame; the analysis of this geodetic profile and its tectonic implications are beyond the scope of this paper and have been discussed in our other literature (*Slip rate along the western Altyn Tagh fault from GPS and InSAR*, submitted to *GJI*).

We also compare the fault coupling inferred from block model with the focal depth of microearthquakes (Figure 7a). Regional earthquakes are selected within the 50-km width region on either side of the Altyn Tagh fault. Most of those minor earthquakes occurred above the depth of 25 km, implying that the seismogenic depth along the Altyn Tagh fault matches our geodetic fault coupling. However, note that such a comparison depends highly upon the quality of the earthquake locations. In summary, the fault slip rate and fault locking depth of the Altyn Tagh fault derived from the elastic block model are in general agreement with the results obtained by previous geological and geodetic measures. Moreover, our results show continuous estimates of slip rate and interseismic fault coupling along the fault, which are essential for characterizing the deformation and seismic behaviors of the fault.

4.2. Role of the Fault Coupling in Seismic Hazard Analyses Along the Altyn Tagh Fault

We obtain the slip rate deficit at each rectangular fault patch by multiplying the slip rate and ISC coefficient (Figure 7a). The slip rate deficit on the fault plane shows a clearly heterogeneous distribution (Figure 7b). The eastwards decreasing rate of slip deficit implies that the rate of elastic strain accumulation on the fault plane decreases. Note that we constrain the ISC value on the fault interface to decrease with depth, so the high slip rate deficit on the shallow part of the fault is a product of this constraint. Whether or not there are low slip rate deficit segments along the fault probably related to shallow fault creeping is unresolvable with our data set and model.

Assuming a constant shear modulus of $\mu = 30$ GPa and adopting the slip rate deficit on the fault plane, we calculate the seismic moment accumulation rate at each rectangular fault patch; these could be utilized to assess the seismic hazard on the fault. By integrating the seismic moment accumulation rate for each patch along downdip, we obtain the seismic moment accumulation rate variations along the Altyn Tagh fault (Figure 7c). The seismic moment accumulation rate also shows a heterogeneous distribution, with the highest rate occurring along the western segment ($\sim 86^\circ\text{E}$), where fault locking depths are moderately deep (~ 15 km) and the slip rates are high (~ 10 mm/a). The lowest rate is along the easternmost segment, where the fault slip rates ($1\text{--}3$ mm/a) are low and wide strain partitioning occurs across the Qilian fold-thrust belt (e.g., Zheng et al., 2013).

A quantitative calculation of the seismic moment accumulated on the Altyn Tagh fault requires the time interval from the last major earthquake. However, no major pretwentieth century earthquakes have been documented along the Altyn Tagh fault. Paleoseismologic investigations have revealed the rupture histories along the fault (e.g., Shao et al., 2018). Morphometric evidence showed relatively fresh, no more than 1,000 years old ($\sim 250\text{--}730$ years), ruptures along the central Altyn Tagh fault (e.g., Mériaux et al., 2005; Washburn et al., 2001). Recently, Elliott et al. (2015) reported the most recent event, which are a pair of adjacent events that occurred between 1215 and 1775 CE (Common Era) along the central Altyn Tagh fault; Shao et al. (2018) identified four paleo-earthquakes after 3650 before CE and reported an average interval of $1,433 \pm 57$ to $1,326 \pm 179$ years for large earthquakes along the central Altyn Tagh fault.

Here we use a time span of 500 years to calculate the accumulated seismic moment on the fault plane. Four major restraining bends along the fault, Sulamu Tagh, Akato Tagh, Pingding Shan, and Aksay, could act as barriers to earthquake ruptures (e.g., Shao et al., 2018). Therefore, we calculate the accumulated seismic moment for each single segment divided by these four-restraining bends. We define them as the West-Sulamu segment, Sulamu-Akato segment, Akato-Pingding Shan segment, Pingding Shan-Aksay segment, and East-Aksay segment (Figure 1). We obtain a total seismic moment of 8.75×10^{20} , 4.15×10^{20} , 3.03×10^{20} , 5.03×10^{20} , and 6.65×10^{20} N m for the fault segments from west to east. Note that several large earthquakes (e.g., two M 7.2 earthquakes in 1924 and the M 6.7 earthquake in 1933) have ruptured the West-Sulamu segment in the last century; as a consequence, we estimate that the above moment deficit along the five segments could be balanced by earthquakes with magnitudes of M_w 7.9, M_w 7.7, M_w 7.6, M_w 7.8, and M_w 7.9, respectively. The above calculation assumes that both the locked and partially locked patches on the fault segments rupture completely during one event. To quantitatively compare the seismic potential of each segment, we divide the total accumulated seismic moment by the length of each fault segment and get an estimate of seismic moment per unit length of the faults. We obtain the values of 1.83×10^{18} , 2.37×10^{18} , 2.16×10^{18} , 2.22×10^{18} , and 1.19×10^{18} N m/km for the fault segments from west to east, highlighting a relatively high seismic potential along the Sulamu-Akato, Akato-Pingding Shan, and Pingding Shan-Aksay segments. Compared with other ruptured continental strike-slip faults (such as the San Andreas fault, the North Anatolian fault, and the Kunlun fault; e.g., Cakir et al., 2005; Thatcher, 1975; Xu et al., 2006), the Altyn Tagh fault has a high strain rate concentration, yet remains unruptured. Consequently, we suggest high seismic potential along the Altyn Tagh fault, especially for the fault segments between the Sulamu Tagh and the Aksay bends. More detailed studies are needed to investigate the multisegment rupture behaviors along the Altyn Tagh fault, and our results will provide the necessary data for more accurate assessment of the seismic hazard along the fault.

4.3. Implications for Crustal Deformation of the Tibetan Plateau

Quantitatively assessing how Indo-Eurasia convergence is accommodated along the Altyn Tagh fault has been a key constraint in studies of the mode of crustal deformation of the Tibetan Plateau, representing a subject of considerable debate. For instance, by investigating the Quaternary slip rate of the Altyn Tagh fault, Peltzer et al. (1989), Avouac and Tapponnier (1993), and Mériaux et al. (2004, 2005) proposed that as much as 30–50% of the Indo-Eurasia convergence is accommodated by eastward extrusion of the Tibetan plateau along the Altyn Tagh fault, suggesting that the crustal deformation of Tibet is dominated by lateral extrusion. Whereas low ratio values imply broadly distributed crustal shortening across the Tibet. For instance, England and Houseman (1986) and Zhang et al. (2004) estimated the ratio to be <20% using numerical simulations and GPS velocity profile analysis, respectively, to support the continuous deformation model of the Tibetan Plateau. The ratio obtained by geodesy, however, is different. Bendick et al. (2000) proposed a ratio of ~10% for the accommodation of Indo-Eurasia convergence along the Altyn Tagh fault by investigating geodetic data (campaign-model GPS velocities and leveling data) across the Altyn Tagh fault. However, Shen et al. (2001) estimated the ratio to be 23% by interpreting sparse GPS velocities spanning the northern Tibetan Plateau; Zhang et al. (2004) obtained a ratio of ~15–17% by introducing more GPS velocities.

We used the same method as Shen et al. (2001) to estimate the ratio of Indo-Eurasia convergence accommodated along the Altyn Tagh fault. Assuming that the Indo-Tibet plate boundary is ~2,400-km long and that the average convergence rate is ~38 mm/a (e.g., Shen et al., 2001), the total reduction in area between the two plates would be ~0.091 km²/a projected at the Himalaya. We integrate the slip rate along the Altyn Tagh fault and obtain an area reduction of 0.0096 km²/a accommodated by lateral extrusion, accounting for 10.6% of the Indo-Asia convergence (Figure 8a). We also take into account the Haiyuan-Liupanshan fault on the northeastern boundary of the Tibetan Plateau. Using the same method, our previous results (Li et al., 2017) show that 3% of Indo-Asia convergence is accommodated by the lateral extrusion along the Haiyuan-Liupanshan fault. The above results indicate that a total of 13.6% of the Indo-Asia convergence is accommodated along the northern-northeastern boundary faults of the Tibetan Plateau, consistent with the results of Bendick et al. (2000) and Zhang et al. (2004), and do not support the lateral extrusion model (e.g., Mériaux et al., 2005) as the primary crustal deformation mode of the Tibetan Plateau.

The above analysis is based on the elastic block modeling results, but it does not necessarily mean the present-day crustal deformation of the Tibetan Plateau is completely described by elastic block-like motions. An alternative approach is to calculate horizontal strain rates over the study area, which give new insights that are not available from the block model. To avoid unrealistic calculation results induced by interpolation functions, which apply smoothing factors in gridding (e.g., the method of Wang & Wright, 2012), we discretize the study area using a Delaunay triangulation. The vertices of each triangle coincide with the GPS sites. For each triangle, the strain rate tensor ($\epsilon_{\phi\phi}, \epsilon_{\lambda\lambda}, \epsilon_{\lambda\phi}$) is calculated using the equation between velocity and strain rate on the sphere (Appendix A of Savage et al., 2001). The strain rate tensor is then used to calculate the second invariant of the strain rate tensor ($\sqrt{\epsilon_{\lambda\phi}^2 - \epsilon_{\lambda\lambda}\epsilon_{\phi\phi}}$, Walters et al., 2014). In addition to using the observed GPS velocities to calculate the strain rate field (Figure 8b), we also used the GPS velocity residuals from the elastic block model (Figure 8c). We conduct a quantitative comparison, given by $\text{Reduction} = \frac{(\text{Strain}_{\text{obs}} - \text{Strain}_{\text{res}})}{\text{Strain}_{\text{obs}}}$, between the results from observations (termed as $\text{Strain}_{\text{obs}}$) and those from residuals ($\text{Strain}_{\text{res}}$). The resulting maps show an overall reduction of strain rates values from $\text{Strain}_{\text{obs}}$ (Figure 8b) to $\text{Strain}_{\text{res}}$ (Figure 8c), especially along block boundaries (e.g., the Kunlun fault and the Qilian thrust, Reduction > 60%, Figure 8d), indicating that the elastic block-like motion fit at least 60% of the crustal deformation in those regions. However, the improvements (Reduction < 60%, Figure 8d) for broad regions, that is, the Qaidam block, the Qilian block and across the Altyn Tagh fault, where the strain rates show smooth gradients (Figure 8b), are minor. These regions show strain rates between 3×10^{-9} /a and 8×10^{-9} /a, which are within the precision level of the GPS data set (1×10^{-9} /a, average triangle dimension of ~100 km, velocity precision ~1 mm/a), implying continuous broadly distributed crustal deformation (e.g., England & Molnar, 1997; Houseman & England, 1993). Note that the strain rate calculation and analysis are dependent on the sparsely distributed GPS sites, and more GPS sites in the future will help to refine the above interpretations.

Integrating the above analysis and results, we demonstrate that the lateral extrusion (e.g., Mériaux et al., 2005) is not the primary crustal deformation mode of the Tibetan Plateau, which is also supported by the

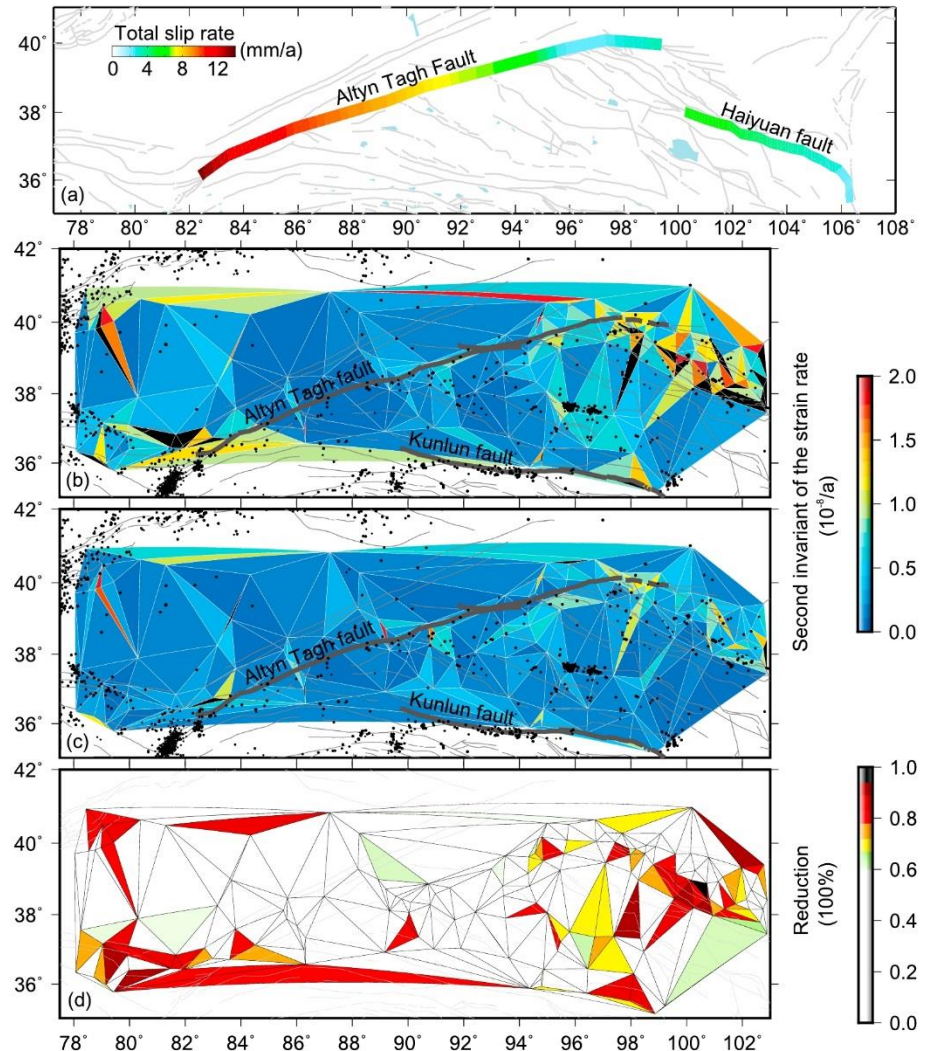


Figure 8. (a) Total magnitude of slip rate along the Altyn Tagh fault and the Haiyuan-Liupanshan fault. Thin gray lines correspond to active faults. (b) The second invariant of the strain rate tensor field derived from the observed Global Positioning System velocities. Black dots represent earthquakes with magnitudes of smaller than 6.0 from 1986 to 2017 (U.S. Geological Survey). (c) The second invariant of the strain rate tensor field derived from the block model velocity residuals. (d) Ratio of the second invariant of the strain rate tensor reduction.

interpretations of the interseismic deformation result from InSAR (e.g., Daout et al., 2018). Nevertheless, the (elastic) block model still provides an effective kinematic description of surface deformation of the Tibetan Plateau, as demonstrated by this study and previous works (e.g., Loveless & Meade, 2011; Meade & Hager, 2005; Thatcher, 2007; Wang et al., 2017). Admittedly, both the block modeling results and the strain rate fields presented here do not resolve, by themselves, the debate on the mode of crustal deformation of the Tibetan Plateau, but we propose a hybrid kinematic model that includes both block-like and continuous deformation to better model the crustal deformation of the Tibetan Plateau, supporting the view reported by previous studies (e.g., Chen et al., 2004; Loveless & Meade, 2011; Zhang, 2013).

5. Conclusions

We calculate an updated GPS velocity solution across the western Altyn Tagh fault and merge it with published GPS velocity solutions to obtain a dense GPS velocity field for the northern Tibetan Plateau. The

fault slip rate, interseismic fault coupling, and seismic moment accumulation rate along the Altyn Tagh fault are then inverted using an elastic block approach. Our results show a heterogeneous distribution of interseismic fault coupling along the fault. We also calculate the seismic moment along the Altyn Tagh fault and suggest high seismic potential along three fault segments between the Sulamu Tagh and the Aksay bends, where the accumulated seismic moment over the past 500 years could be balanced by M_w 7.6–7.8 earthquakes. In addition, from a calculation of the ratio (10.3%) of Indo-Eurasia convergence that is accommodated along the Altyn Tagh fault, and by investigating the strain rate field in the northern Tibetan Plateau, we suggest that the lateral extrusion is not the primary crustal deformation mode of the Tibetan Plateau, a hybrid kinematic model that includes both block-like and continuous deformation should be introduced to better delineate the crustal deformation of the Tibetan Plateau.

Acknowledgments

The authors thank Editor Paul Tregoning, Jeff Freymueller, and an anonymous reviewer for their thorough and constructive reviews, which greatly improved the quality of this manuscript. We are grateful to all the colleagues who constructed the CMONOC network and collected the GPS measurements. We also show our gratitude to colleagues who conducted the GPS measurements across the western Altyn Tagh fault. Particular thanks go to Jiankun He, in Institute of Tibetan Plateau Research, Chinese Academy of Sciences, who shared the GPS data acquired in 2009–2011 across the western Altyn Tagh fault. The program for the elastic block model was shared by Robert McCaffrey. This work was supported by the National Natural Science Foundation of China (grants 41631073 and 41461164002). Some figures and maps were generated using the Generic Mapping Tools (GMT) software (Wessel et al., 2013). The GPS velocity solution and some block modeling results can be accessed in the supporting information files. The block modeling input files could be accessed by contacting the corresponding author.

References

- Altamimi, Z., Collilieux, X., & Métivier, L. (2011). ITRF2008: An improved solution of the international terrestrial reference frame. *Journal of Geodesy*, 85(8), 457–473. <https://doi.org/10.1007/s00190-011-0444-4>
- Avouac, J. P., & Tapponnier, P. (1993). Kinematic model of active deformation in Central Asia. *Geophysical Research Letters*, 20(10), 895–898. <https://doi.org/10.1029/93GL00128>
- Bendick, R., Bilham, R., Freymueller, J., Larson, K., & Yin, G. (2000). Geodetic evidence for a low slip rate in the Altyn Tagh fault system. *Nature*, 404(6773), 69–72. <https://doi.org/10.1038/35003555>
- Cakir, Z., Akoglu, A. M., Belabbes, S., Ergintav, S., & Meghraoui, M. (2005). Creeping along the Ismetpasa section of the north Anatolian fault (Western Turkey): Rate and extent from InSAR. *Earth and Planetary Science Letters*, 238(1–2), 225–234. <https://doi.org/10.1016/j.epsl.2005.06.044>
- Chen, Q., Freymueller, J. T., Wang, Q., Yang, Z., Xu, C., & Liu, J. (2004). A deforming block model for the present-day tectonics of Tibet. *Journal of Geophysical Research*, 109, B09401. <https://doi.org/10.1029/2002JB002151>
- Chen, Y., Li, S. H., & Li, B. (2012). Slip rate of the Aksay segment of Altyn Tagh fault revealed by OSL dating of river terraces. *Quaternary Geochronology*, 10, 291–299. <https://doi.org/10.1016/j.quageo.2012.04.012>
- Chen, Y., Li, S. H., Sun, J., & Fu, B. (2013). OSL dating of offset streams across the Altyn Tagh fault: Channel deflection, loess deposition and implication for the slip rate. *Tectonophysics*, 594, 182–194. <https://doi.org/10.1016/j.tecto.2013.04.002>
- Cowgill, E. (2007). Impact of riser reconstructions on estimation of secular variation in rates of strike-slip faulting: Revisiting the Cherchen River site along the Altyn Tagh fault, NW China. *Earth and Planetary Science Letters*, 254(3–4), 239–255. <https://doi.org/10.1016/j.epsl.2006.09.015>
- Cowgill, E., Gold, R. D., Chen, X., Wang, X., Arrowsmith, J. R., & Southon, J. (2009). Low quaternary slip rate reconciles geodetic and geologic rates along the Altyn Tagh fault, northwestern Tibet. *Geology*, 37(7), 647–650. <https://doi.org/10.1130/G25623A.1>
- Daout, S., Doin, M. P., Peltzer, G., Lasserre, C., Socquet, A., Volat, M., & Sudhaus, H. (2018). Strain partitioning and present-day fault kinematics in NW Tibet from Envisat SAR interferometry. *Journal of Geophysical Research: Solid Earth*, 123, 2462–2483. <https://doi.org/10.1002/2017JB015020>
- Elliott, A. J., Oskin, M. E., Liu-Zeng, J., & Shao, Y. (2015). Rupture termination at restraining bends: The last great earthquake on the Altyn Tagh fault. *Geophysical Research Letters*, 42, 2164–2170. <https://doi.org/10.1002/2015GL063107>
- Elliott, J. R., Biggs, J., Parsons, B., & Wright, T. J. (2008). InSAR slip rate determination on the Altyn Tagh fault, northern Tibet, in the presence of topographically correlated atmospheric delays. *Geophysical Research Letters*, 35, L12309. <https://doi.org/10.1029/2008GL033659>
- England, P., & Houseman, G. (1986). Finite strain calculations of continental deformation: 2. Comparison with the India-Asia collision zone. *Journal of Geophysical Research*, 91(B3), 3664–3676. <https://doi.org/10.1029/JB091iB03p03664>
- England, P., & Molnar, P. (1997). The field of crustal velocity in Asia calculated from quaternary rates of slip on faults. *Geophysical Journal International*, 130(3), 551–582. <https://doi.org/10.1111/j.1365-246X.1997.tb01853.x>
- Garthwaite, M. C., Wang, H., & Wright, T. J. (2013). Broad-scale interseismic deformation and fault slip rates in the central Tibetan plateau observed using InSAR. *Journal of Geophysical Research: Solid Earth*, 118, 5071–5083. <https://doi.org/10.1002/jgrb.50348>
- Ge, W. P., Molnar, P., Shen, Z. K., & Li, Q. (2015). Present-day crustal thinning in the southern and northern Tibetan plateau revealed by GPS measurements. *Geophysical Research Letters*, 42, 5227–5235. <https://doi.org/10.1002/2015GL064347>
- Gold, R. D., Cowgill, E., Arrowsmith, J. R., Gosse, J., Chen, X., & Wang, X. (2009). Riser diachroneity, lateral erosion, and uncertainty in rates of strike-slip faulting: A case study from Tuzidun along the Altyn Tagh fault, NW China. *Journal of Geophysical Research*, 114, B04401. <https://doi.org/10.1029/2008JB005913>
- He, J., Vernant, P., Chéry, J., Wang, W., Lu, S., Ku, W., Xia, X., et al. (2013). Nailing down the slip rate of the Altyn Tagh fault. *Geophysical Research Letters*, 40, 5382–5386. <https://doi.org/10.1002/2013GL057497>
- Herring, T. A., King, R. W., Floyd, M. A., & McCluskey, S. C. (2016). Introduction to GAMIT/GLOBK, release 10.6, Massachusetts Institute of Technology. http://geoweb.mit.edu/~simon/gtg/Intro_GG.pdf
- Houseman, G., & England, P. (1993). Crustal thickening versus lateral expulsion in the Indian-Asian continental collision. *Journal of Geophysical Research*, 98(B7), 12,233–12,249. <https://doi.org/10.1029/93JB00443>
- Jolivet, R., Cattin, R., Chamot-Rooke, N., Lasserre, C., & Peltzer, G. (2008). Thin-plate modeling of interseismic deformation and asymmetry across the Altyn Tagh fault zone. *Geophysical Research Letters*, 35, L02309. <https://doi.org/10.1029/2007GL031511>
- Jolivet, R., Simons, M., Agram, P. S., Duputel, Z., & Shen, Z. K. (2015). Aseismic slip and seismogenic coupling along the Central San Andreas fault. *Geophysical Research Letters*, 42, 297–306. <https://doi.org/10.1002/2014GL062222>
- Lasserre, C., Cavalié, O., Peltzer, G., Socquet, A., Doin, M.-P., Sun, J., Xu, X., et al. (2007). Interseismic deformation across the Altyn Tagh and Haiyuan faults at the northern edge of the Tibetan plateau, measured by space geodesy. *Geophysical Research Abstracts*, 9(10), 102.
- Li, Y., Shan, X., Qu, C., Zhang, Y., Song, X., Jiang, Y., Zhang, G., et al. (2017). Elastic block and strain modeling of GPS data around the Haiyuan-Liupanshan fault, northeastern Tibetan plateau. *Journal of Asian Earth Sciences*, 150, 87–97. <https://doi.org/10.1016/j.jseas.2017.10.010>
- Loveless, J. P., & Meade, B. J. (2011). Partitioning of localized and diffuse deformation in the Tibetan plateau from joint inversions of geologic and geodetic observations. *Earth and Planetary Science Letters*, 303(1–2), 11–24. <https://doi.org/10.1016/j.epsl.2010.12.014>

- Lyard, F., Lefevre, F., Letellier, T., & Francis, O. (2006). Modelling the global ocean tides: Modern insights from FES2004. *Ocean Dynamics*, 56(5-6), 394–415. <https://doi.org/10.1007/s10236-006-0086-x>
- McCaffrey, R., Qamar, A. I., King, R. W., Wells, R., Khazaradze, G., Williams, C. A., Stevens, C. W., et al. (2007). Fault locking, block rotation and crustal deformation in the Pacific northwest. *Geophysical Journal International*, 169(3), 1315–1340. <https://doi.org/10.1111/j.1365-246X.2007.03371.x>
- Meade, B. J., & Hager, B. H. (2005). Block models of crustal motion in southern California constrained by GPS measurements. *Journal of Geophysical Research*, 110, B03403. <https://doi.org/10.1029/2004JB003209>
- Mériaux, A. S., Ryerson, F. J., Tapponnier, P., Van der Woerd, J., Finkel, R. C., Xu, X., Xu, Z., et al. (2004). Rapid slip along the central Altyn Tagh fault: Morphochronologic evidence from Cherchen He and Sulamu Tagh. *Journal of Geophysical Research*, 109, B06401. <https://doi.org/10.1029/2003JB002558>
- Mériaux, A. S., Tapponnier, P., Ryerson, F. J., Xu, X., King, G., Van der Woerd, J., Finkel, R. C., et al. (2005). The Aksay segment of the northern Altyn Tagh fault: Tectonic geomorphology, landscape evolution, and Holocene slip rate. *Journal of Geophysical Research*, 110, B04404. <https://doi.org/10.1029/2004JB003210>
- Mériaux, A. S., Van Der Woerd, J., Tapponnier, P., Ryerson, F. J., Finkel, R. C., Lasserre, C., & Xu, X. (2012). The Pingding segment of the Altyn Tagh fault (91°E): Holocene slip-rate determination from cosmogenic radionuclide dating of offset fluvial terraces. *Journal of Geophysical Research*, 117, B09406. <https://doi.org/10.1029/2012JB009289>
- Molnar, P., & Tapponnier, P. (1975). Cenozoic tectonics of Asia: Effects of a continental collision. *Science*, 189(4201), 419–426. <http://www.jstor.org/stable/1740465>. <https://doi.org/10.1126/science.189.4201.419>
- Peltzer, G., Tapponnier, P., & Armijo, R. (1989). Magnitude of late Quaternary left-lateral displacements along the north edge of Tibet. *Science*, 246(4935), 1285. <https://doi.org/10.1126/science.246.4935.1285-1289>
- Rui, X., & Stamps, D. S. (2016). Present-day kinematics of the eastern Tibetan plateau and Sichuan Basin: Implications for lower crustal rheology. *Journal of Geophysical Research: Solid Earth*, 121, 3846–3866. <https://doi.org/10.1002/2016JB012839>
- Ryder, I., Parsons, B., Wright, T. J., & Funning, G. J. (2007). Post-seismic motion following the 1997 Manyi (Tibet) earthquake: InSAR observations and modelling. *Geophysical Journal International*, 169(3), 1009–1027. <https://doi.org/10.1111/j.1365-246X.2006.03312.x>
- Savage, J. C. (1983). A dislocation model of strain accumulation and release at a subduction zone. *Journal of Geophysical Research*, 88(B6), 4984–4996. <https://doi.org/10.1029/JB088iB06p04984>
- Savage, J. C., & Burford, R. O. (1973). Geodetic determination of relative plate motion in Central California. *Journal of Geophysical Research*, 78(5), 832–845. <https://doi.org/10.1029/JB078i005p0832>
- Savage, J. C., Gan, W., & Svarc, J. L. (2001). Strain accumulation and rotation in the eastern California shear zone. *Journal of Geophysical Research*, 106(B10), 21,995–22,007. <https://doi.org/10.1029/2000JB000127>
- Shao, Y., Liu-Zeng, J., Oskin, M. E., Elliott, A. J., Wang, P., Zhang, J., Yuan, Z., et al. (2018). Paleoseismic investigation of the Aksay restraining double-bend, Altyn Tagh fault, and its implication for barrier-breaching ruptures. *Journal of Geophysical Research: Solid Earth*, 123, 4307–4330. <https://doi.org/10.1029/2017JB015397>
- Shen, Z. K., Wang, M., Li, Y., Jackson, D. D., Yin, A., Dong, D., & Fang, P. (2001). Crustal deformation along the Altyn Tagh fault system, western China, from GPS. *Journal of Geophysical Research*, 106(B12), 30,607–30,621. <https://doi.org/10.1029/2001JB000349>
- Tapponnier, P., Zhiqin, X., Roger, F., Meyer, B., Arnaud, N., Wittlinger, G., & Jingsui, Y. (2001). Oblique stepwise rise and growth of the Tibet plateau. *Science*, 294(5547), 1671–1677. <https://doi.org/10.1126/science.105978>
- Thatcher, W. (1975). Strain accumulation and release mechanism of the 1906 San Francisco earthquake. *Journal of Geophysical Research*, 80(35), 4862–4872. <https://doi.org/10.1029/JB080i035p04862>
- Thatcher, W. (2007). Microplate model for the present-day deformation of Tibet. *Journal of Geophysical Research*, 112, B01401. <https://doi.org/10.1029/2005JB004244>
- Wallace, K., Yin, G., & Bilham, R. (2004). Inescapable slow slip on the Altyn Tagh fault. *Geophysical Research Letters*, 31, L09613. <https://doi.org/10.1029/2004GL019724>
- Walters, R. J., Parsons, B., & Wright, T. J. (2014). Constraining crustal velocity fields with InSAR for eastern Turkey: Limits to the block-like behavior of eastern Anatolia. *Journal of Geophysical Research: Solid Earth*, 119, 5215–5234. <https://doi.org/10.1002/2013JB010909>
- Wang, H., & Wright, T. J. (2012). Satellite geodetic imaging reveals internal deformation of western Tibet. *Geophysical Research Letters*, 39, L07303. <https://doi.org/10.1029/2012GL015122>
- Wang, W., Qiao, X., Yang, S., & Wang, D. (2017). Present-day velocity field and block kinematics of Tibetan plateau from GPS measurements. *Geophysical Journal International*, 208(2), 1088–1102. <https://doi.org/10.1093/gji/ggw445>
- Washburn, Z., Arrowsmith, J. R., Forman, S. L., Cowgill, E., Wang, X., Zhang, Y., & Chen, Z. (2001). Late Holocene earthquake history of the central Altyn Tagh fault, China. *Geology*, 29, 1051–1054. <https://pubs.geoscienceworld.org/gsa/geology/article-abstract/29/11/1051/197885/late-holocene-earthquake-history-of-the-central?redirectedFrom=fulltext>. [https://doi.org/10.1130/0091-7613\(2001\)029<1051:LHEHOT>2.0.CO;2](https://doi.org/10.1130/0091-7613(2001)029<1051:LHEHOT>2.0.CO;2)
- Wessel, P., Smith, W. H., Scharroo, R., Luis, J., & Wobbe, F. (2013). Generic mapping tools: Improved version released. *Eos Transactions American Geophysical Union*, 94(45), 409–410. <https://doi.org/10.1002/2013EO450001>
- Wright, T. J., Parsons, B., England, P. C., & Fielding, E. J. (2004). InSAR observations of low slip rates on the major faults of western Tibet. *Science*, 305(5681), 236–239. <https://doi.org/10.1126/science.1096388>
- Xiao, Q., Yu, G., Liu-Zeng, J., Oskin, M. E., & Shao, G. (2017). Structure and geometry of the Aksay restraining double bend along the Altyn Tagh fault, northern Tibet, imaged using magnetotelluric method. *Geophysical Research Letters*, 44, 4090–4097. <https://doi.org/10.1002/2017GL072581>
- Xu, X., Wang, F., Zheng, R., Chen, W., Ma, W., Yu, G., Chen, G., et al. (2005). Late Quaternary sinistral slip rate along the Altyn Tagh fault and its structural transformation model. *Science China Earth Sciences*, 48(3), 384–397. <https://doi.org/10.1360/02yd0436>
- Xu, X., Yu, G., Klinger, Y., Tapponnier, P., & Van Der Woerd, J. (2006). Reevaluation of surface rupture parameters and faulting segmentation of the 2001 Kunlunshan earthquake (Mw 7.8), northern Tibetan plateau, China. *Journal of Geophysical Research*, 111, B05316. <https://doi.org/10.1029/2004JB003488>
- Yamasaki, T., & Houseman, G. A. (2012). The crustal viscosity gradient measured from post-seismic deformation: A case study of the 1997 Manyi (Tibet) earthquake. *Earth and Planetary Science Letters*, 351–352, 105–114. <https://doi.org/10.1016/j.epsl.2012.07.030>
- Yin, A., Rumelhart, P. E., Butler, R., Cowgill, E., Harrison, T. M., Foster, D. A., Ingersoll, R. V., et al. (2002). Tectonic history of the Altyn Tagh fault system in northern Tibet inferred from Cenozoic sedimentation. *GSA Bulletin*, 114(10), 1257–1295. [https://doi.org/10.1130/0016-7606\(2002\)114<1257:THOTAT>2.0.CO;2](https://doi.org/10.1130/0016-7606(2002)114<1257:THOTAT>2.0.CO;2)
- Zhang, P. Z. (2013). A review on active tectonics and deep crustal processes of the Western Sichuan region, eastern margin of the Tibetan plateau. *Tectonophysics*, 584, 7–22. <https://doi.org/10.1016/j.tecto.2012.02.021>

- Zhang, P. Z., Molnar, P., & Xu, X. (2007). Late Quaternary and present-day rates of slip along the Altyn Tagh fault, northern margin of the Tibetan plateau. *Tectonics*, 26, TC5010. <https://doi.org/10.1029/2006TC002014>
- Zhang, P. Z., Shen, Z., Wang, M., Gan, W., Bürgmann, R., Molnar, P., Wang, Q., et al. (2004). Continuous deformation of the Tibetan plateau from global positioning system data. *Geology*, 32(9), 809–812. <https://doi.org/10.1130/G20554.1>
- Zhao, D., Qu, C., Shan, X., Zuo, R., Liu, Y., Gong, W., & Zhang, G. (2018). Broad-scale postseismic deformation and lower crustal relaxation in the central Bayankala block (central Tibetan plateau) observed using InSAR data. *Journal of Asian Earth Sciences*, 154, 26–41. <https://doi.org/10.1016/j.jseas.2017.12.016>
- Zheng, W. J., Zhang, P. Z., He, W. G., Yuan, D. Y., Shao, Y. X., Zheng, D. W., Ge, W. P., et al. (2013). Transformation of displacement between strike-slip and crustal shortening in the northern margin of the Tibetan plateau: Evidence from decadal GPS measurements and late Quaternary slip rates on faults. *Tectonophysics*, 584, 267–280. <https://doi.org/10.1016/j.tecto.2012.01.006>

Second part

Measuring the crustal deformation across western Altyn Tagh fault (longitude 86°E) using GPS and InSAR

Motivations:

In the first part, I used elastic block model to invert for the slip rate and interseismic fault coupling along the Altyn Tagh fault (Li et al., 2018). Modeling results show a slip rate of ~10-11 mm/a across the western Altyn Tagh fault (longitude 86°E). Even though we used the updated GPS velocity solution, a low spatial resolution of GPS stations might bring uncertainties. Moreover, my results lack detail discussions of the crustal deformation across the western Altyn Tagh fault (longitude 86°E).

Daout et al. (2018) published the InSAR velocity solution across the western Altyn Tagh fault. They adopted a fault model consisting of a vertical fault plane under the Altyn Tagh fault and a shallow flat décollement ending in a steeper ramp on the Tarim side. Their Bayesian inversion results, using GPS and InSAR, show 10.5 mm/a of left-lateral strike-slip movement on the Altyn Tagh fault, below a 17 km locking depth. There are two imperfections: the first is they used the GPS velocity solution from He et al. (2013), which suffers from a short time span (2009-2011); the second is they did not consider the potential vertical deformation across the Altyn Tagh fault in the InSAR LOS.

Considering the above works, we decided to further study the crustal deformation across the western Altyn Tagh fault (longitude 86°E) by combining the updated GPS

velocity solution ([Li et al., 2018](#)) and InSAR velocity solution ([Daout et al., 2018](#)). To consider the potential vertical deformation in InSAR and to fully consider the observation data uncertainties, we started with comparing and integrating GPS and InSAR, then using a Bayesian approach to conduct kinematic inversions. We seek to conduct a fine study of the crustal deformation in northwestern Tibet and across the western Altyn Tagh fault (longitude 86°E). Furthermore, we seek any new information, perspectives, and understanding that might be learned from the study.

3.1. Abstract

We combine the Global Positioning System (GPS) velocity field from Li et al. (2018) with Interferometric Synthetic Aperture Radar (InSAR) from Daout et al. (2018) to study the interseismic deformation across the western Altyn Tagh fault (longitude 86°E). GPS and InSAR data are consistent after correcting for contributions from the localized deformation, this has enabled us to robustly estimate the slip rate and locking depth for the western Altyn Tagh fault using a simple 2-D elastic dislocation model. Results indicate a strike slip rate of 8.1 ± 0.4 mm/a and locking depth of 15.1 ± 3.4 km for the fault. Our estimated slip rate is 11-36% lower than some previous geodetic estimates, with implications for both seismic hazards and regional tectonic, implying a relative slow strain accumulation rate along the western Altyn Tagh fault. Results also show two regions with apparent uplift and one with subsidence, highlighting the importance of accounting for the vertical deformation during the interseismic InSAR data interpretations. Moreover, our results indicate no apparent asymmetric interseismic velocities across the western Altyn Tagh fault, ruling out the requirement of lateral variations in elastic strength and/or dislocation shift with respect to the fault trace. A quantitative analysis of the GPS and InSAR data suggests the crustal deformation in the northwestern Tibetan Plateau is a combination of strike-slip faulting, localized crustal shearing, shortening, subsidence and uplift.

3.2. Introduction

The ~1600 km long Altyn Tagh fault (Figure 3.1) separating the Tibetan Plateau from the undeformed Tarim basin (Molnar and Tapponnier, 1977; Burchfiel et al., 1989; Yin and Harrison, 2000; Yin et al., 2002) and defines a major boundary accommodating the eastward motion of the Tibetan Plateau (e.g., Molnar and Tapponnier, 1975).

The present-day slip rate of the Altyn Tagh fault has been considered as a key-parameter to discriminate among models on active continental deformation in Asia (e.g., Molnar and Tapponnier, 1975; Avouac and Tapponnier, 1993; Houseman and England, 1993; England and Molnar, 1997; Tapponnier et al., 2001). During the last 20 years, Global Positioning System (GPS) measurements (e.g., Bendick et al., 2000; Shen et al., 2001; Wallace et al., 2004; Zhang et al., 2004; Zhang et al., 2007; He et al., 2013; Li et al., 2018) and Interferometric Synthetic Aperture Radar (InSAR) observations (e.g., Wright et al., 2004a; Elliott et al., 2008; Jolivet et al., 2008; Zhu et al., 2016; Daout et al., 2018) have provided constraints on the Altyn Tagh fault slip rate from the present-day interseismic surface motion (Figure 4 of Li et al., 2018). Although we present an improved GPS velocity field across the Altyn Tagh fault (86°E; Li et al., 2018), GPS stations are still too sparse to investigate the localized crustal deformation. InSAR observations have higher spatial resolution, however, the sharp topography gradient of up to 4 km over 20 km across the Altyn Tagh fault results in an elevation-dependent atmospheric perturbation, particularly from tropospheric water vapor, which may impact on InSAR interseismic velocity estimates (e.g., Puysségur et al., 2007). Furthermore, previous studies (e.g., Wright et al., 2004a; Elliott et al., 2008; Jolivet et al., 2008; Zhu et al., 2016; Daout et al., 2018) usually assume all the InSAR-derived displacements are horizontal and parallel to the fault. Neglecting the vertical deformation could lead to overestimation of the fault slip rate or underestimation of the fault locking depth, as the line-of-sight (LOS) displacements are more sensitive to vertical deformation than horizontal deformation (Wright et al., 2004b). It is thus critical to effectively combine GPS with InSAR, which corrected for the vertical deformation, to estimate the slip rate of the Altyn Tagh fault.

Previous geodetic profiles across the Altyn Tagh fault also suggested asymmetric interseismic strain accumulation (e.g., Jolivet et al., 2008; He et al., 2013), implying a rigidity contrast within the upper crust between the blocks on either side of the fault (e.g., Elliott et al., 2008; Vernant, 2015). In order to account for the apparent asymmetry of the GPS velocities relative to the surface fault (86°E) in their screw dislocation model (Savage and Burford, 1973; Savage, 2006), He et al. (2013), Vernant (2015), and Zheng et al. (2017) shifted the position of the dislocation at depth to the south relative to the fault trace by distances of 13 km, 12.5 km, and ~20 km. Their models therefore imply a fault dip angle of ~45 ° in the upper crust, a result at odds with the high dip angle structure of the Altyn Tagh fault inferred from magnetotelluric data (e.g., Zhang et al., 2015; Xiao et al., 2017) and geomorphic observation (e.g., Molnar et al., 1987).

In this study, we focus on a segment of the western Altyn Tagh fault located at longitude 86°E. The work is motivated by several scientific questions, which are not resolved in our recent paper (Li et al., 2018): (1) Could we obtain a high spatial resolution interseismic geodetic velocity field by effectively combining GPS with InSAR? (2) What is the high spatial resolution crustal deformation across the western Altyn Tagh fault? (3) Could we use simple 2-D elastic dislocation models to delineate the faulting behaviors of the Altyn Tagh fault? In the following sections, we compare our recently published GPS horizontal velocity result (Li et al., 2018) with the InSAR LOS rate map result recently published by Daout et al. (2018). The combined velocity field not only show that vertical deformation likely occurs in the northern Tibet, but also enables us to robustly estimate the slip rate, locking depth and re-assess the possible asymmetry of the velocity field across the Altyn Tagh fault using a simple 2-D model.

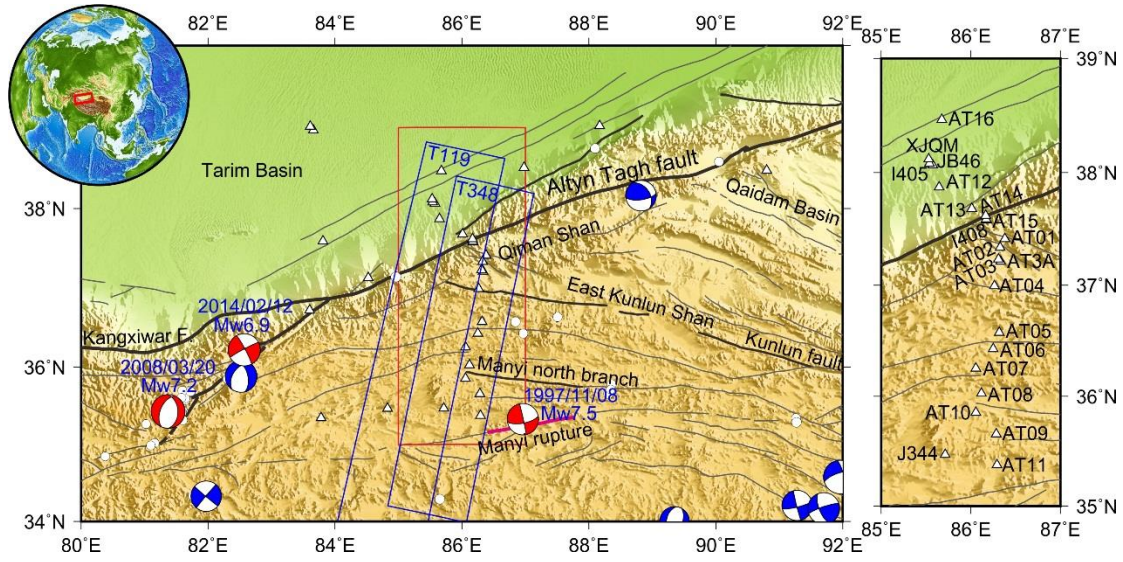


Figure 3.1. Active tectonic map of the northwestern Tibetan Plateau. (a) White triangles indicate the location of Global Positioning System (GPS) sites used in this study. Black and grey solid lines indicate major and secondary faults respectively. Blue focal mechanism solutions (Global Centroid Moment Tensor, GCMT) are earthquakes with moment magnitudes of greater than 6 from 1976 to 2017. Red focal mechanism solutions correspond to the 1997 Mw 7.5 Manyi earthquake and the Yutian earthquakes in 2008 (Mw 7.2) and 2014 (Mw 6.9). Thin white circles represent earthquakes with magnitudes between 5 and 6 from 2009 to 2017 (U.S. Geological Survey, USGS). The red solid line represents the surface rupture of the 1997 Mw 7.5 Manyi earthquake (Ryder et al., 2007). The blue rectangles show the InSAR frame for T348 and T119 Envisat descending tracks used by Daout et al. (2018). The red rectangle corresponds to the area shown in Figure 1b. (b) Enlarged view of GPS sites locations together with their names.

3.3. Geodetic data and analysis

3.3.1. GPS measurements and data processing

I have introduced the GPS measurements and data processing across the western Altyn Tagh fault in Chapter 2. To avoid excessive duplication, I present several main points here.

A total of 17 GPS stations was deployed across the western Altyn Tagh fault by He et al. (2013) (Figure 3.1). They measured the GPS stations 2–3 times in the period 2009–2011. In October 2017, we remeasured 16 GPS sites that are well preserved. We used Trimble NetR9 receiver with Trimble GNSS Choke Ring Geodetic Antenna and collected continuous observations for 72 to 240 hours at the GPS sites (30s sampling rate).

We processed the campaign-mode GPS data measured in 2017 together with those data collected between 2009 and 2011, and with seven regional CMONOC sites (continuous+campaign-mode) using the GAMIT/GLOBK 10.6 software. Firstly, the GPS network was enlarged to include 40 globally distributed International Global Navigation Satellite System Service (IGS, <http://www.igs.org/>) sites. IGS precise orbits and Earth orientation parameters, absolute antenna phase center calibrations, and the Finite Element Solution 2004 ocean tide loading model were employed during the processing. Secondly, we conducted carefully examinations for the GPS position time series for each station to exclude outliers, where we set 3-sigma from the mean as the threshold for outlier detection. Thirdly, we estimated the GPS sites velocities and uncertainties using the ‘realistic sigma’ algorithm embedded in the GLOBK package. Finally, we transformed the velocity field in a Tarim-fixed reference frame, which is determined by minimizing the horizontal velocities at GPS sites north of the fault (Figure 3.2a).

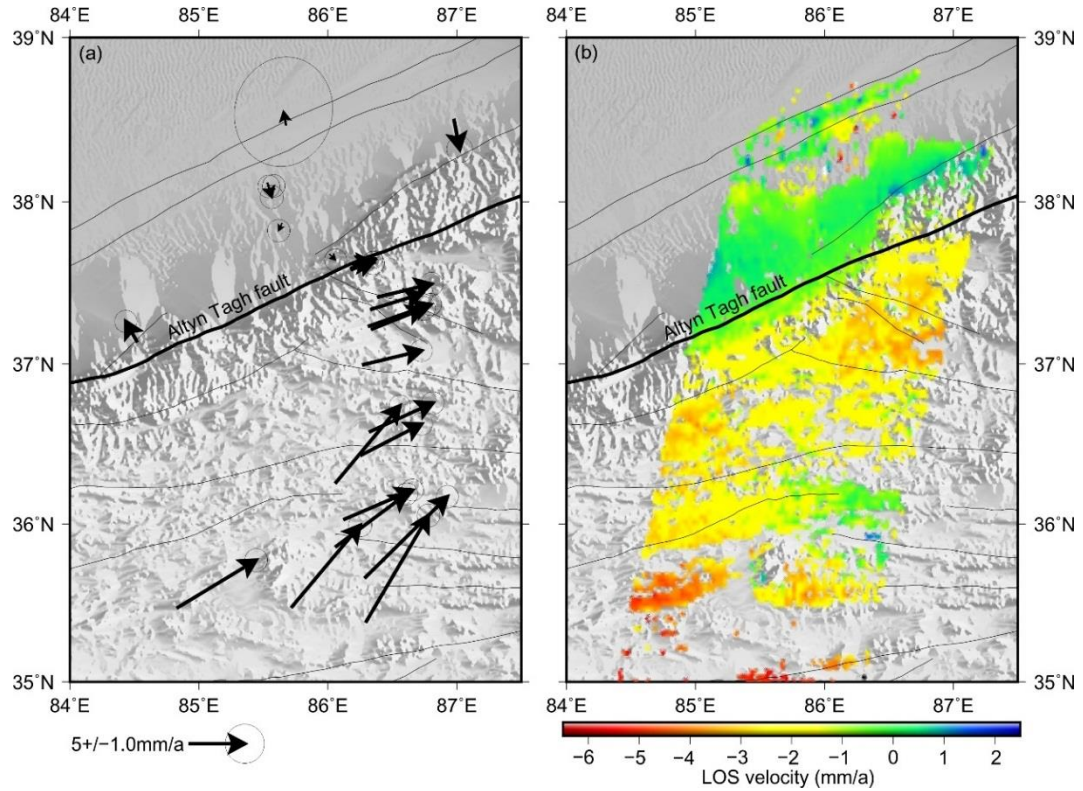


Figure 3.2. (a) Obtained GPS velocities from 2009–2017 in the Tarim-fixed reference frame. All GPS velocities have uncertainties at the 95% confidence. (b) Line-of-sight (LOS) velocity map of the two

tracks 119 and 348. Black solid lines indicate major faults.

3.3.2. Comparison of GPS and InSAR

Daout et al. (2018) processed Environmental Satellite (Envisat) descending tracks covering the northwestern Tibetan Plateau between 2003 and 2011. They used the ROI_PAC software (Rosen et al., 2004) and applied a series of corrections for atmospheric delays, separation of the effects of hydrology and permafrost seasonal changes in the high plateau and corrections for the orbital residuals. Here, we compare our GPS horizontal velocity field with LOS rate map from Daout et al. (2018) for tracks 348 and 119 which overlap our GPS network (Figure 3.2b).

As the GPS and InSAR data are referenced to different frames, to compare them, we align them to the same reference frame. For each GPS site, we first calculate the dispersion of the InSAR LOS values for pixels located within a circle radius of 1 to 10 km (Figure A.1). Three GPS stations (AT13, AT14 and AT15), where the dispersion of the co-located InSAR LOS values is stable and small, are chosen as reference sites to align the two datasets. Horizontal GPS velocities are projected to LOS according to the local incidence angles. We estimate a mean InSAR LOS rate inside a circle of radius 1 km. An averaged value of offsets between the LOS_{GPS} (GPS velocity in LOS) and the LOS_{InSAR} (InSAR LOS velocity) is calculated and added to the LOS_{InSAR} . The comparison allows us to quantify the contribution of vertical deformation to InSAR. The procedure used assumes negligible relative vertical deformation for the 3 reference GPS sites. Consequently, all the vertical deformation discussed in the following are referenced to the 3 GPS sites.

3.4. Results

3.4.1. GPS velocity field

We compare the GPS velocity solution between 2009 and 2011 from He et al. (2013; Figure 3.3a) with the results for the 2009-2017 period (Figure 3.3b; Li et al., 2018). In overall, the two velocity solutions show a good agreement in magnitude and direction. However, the 2009-2017 velocity field shows a better consistency, especially for velocity magnitudes, for example, between AT03 & AT3A (3 km apart) and AT05 & AT06 (17 km apart). These results are more reasonable for crustal deformation within a small area, implying an improvement in the GPS velocity quality using longer observation time span. The largest velocity difference reaches up to ~ 5 mm/a (Figure 3.3c). Furthermore, the velocity residuals (velocity solution of 2009-2017 minus velocity solution of 2009-2011) show a systematic east-west trend near the fault. As the occupation of the GPS benchmarks was in September 2009 and April 2011, an interval of 1.7 years, the data could be perturbed by annual errors in the GPS data time series (Blewitt and Lavallée, 2002). As a result, the longer-period GPS velocity solution (2009-2017) provides a more consistent and robust GPS velocity field across the western Altyn Tagh fault.

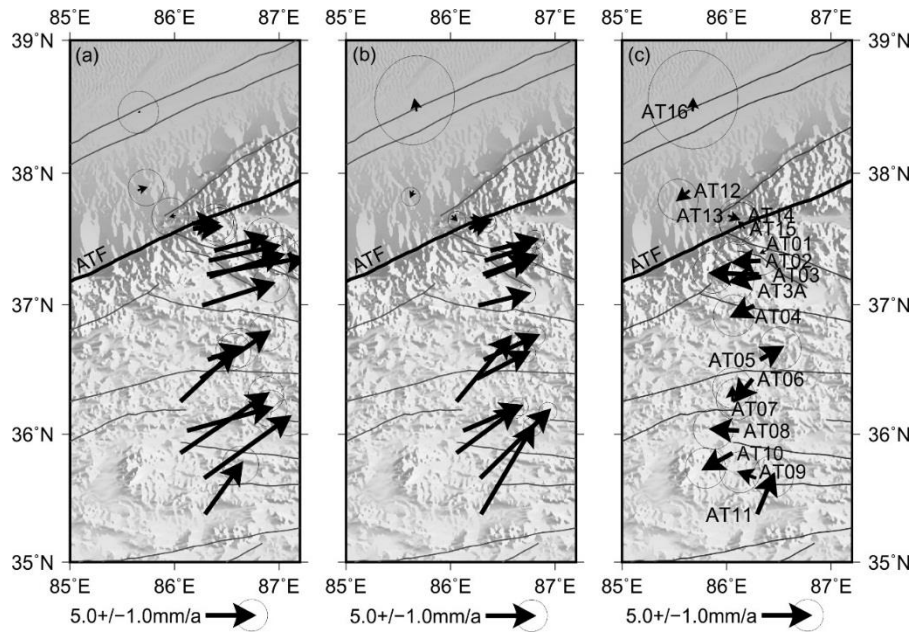


Figure 3.3. GPS velocities for sites across the western Altyn Tagh fault from (a) 2009-2011 (He et al., 2013) and (b) 2009-2017. (c) Velocity differences between the two solutions (velocity solution of 2009-2017 minus the velocity solution of 2009-2011). All GPS velocities are under the Tarim-fixed reference frame, with uncertainties at the 95% confidence level.

The GPS velocities (2009-2017) across the Altyn Tagh fault shows a clear decrease in the fault-parallel velocities from south to north, consistent with the left-lateral motion of the Altyn Tagh fault

(Figure 3.2a). A simple reference frame translation relative to the AT15, which is located ~200 m south of the fault trace, highlights the velocity gradient across the fault (Figure 3.4a, 3.4b). While gradual changes in site velocities are observed south of AT01, a sharp change in velocities is observed between AT01 and I408 (30 km apart), giving rise to an upper limit of the fault zone width in the region where most interseismic gradient is accommodated. The fault-perpendicular velocities show ~0.3 mm/a motion across the fault in the 250 km width region (AT08-XJQM; Figure 3.4c), less than the velocity uncertainties and only accounting for ~4% of the strike-slip rate, implying negligible thrusting movement across the fault and a reasonable assumption of pure strike-slip motion across the western Altyn Tagh fault. A ~3 mm/a fault-parallel shear deformation rate and ~6 mm/a fault-perpendicular crustal shortening rate is found between 150 km and 250 km south of the fault (AT11-AT08, Figure 3.4b, 3.4c). We do not have an explanation for such a motion, which may either be related to secondary faults or other unknown factors, such as unstable benchmark. Therefore, we remove those sites from our model in the following. We also note that the velocity for site AT07 is inconsistent with adjacent stations (AT06 and AT08), and we discard it in our model. The northernmost site (AT16) exhibits like an outlier especially for the fault-perpendicular component, this may be due to its short time span (only two epochs, in 2009 and 2011).

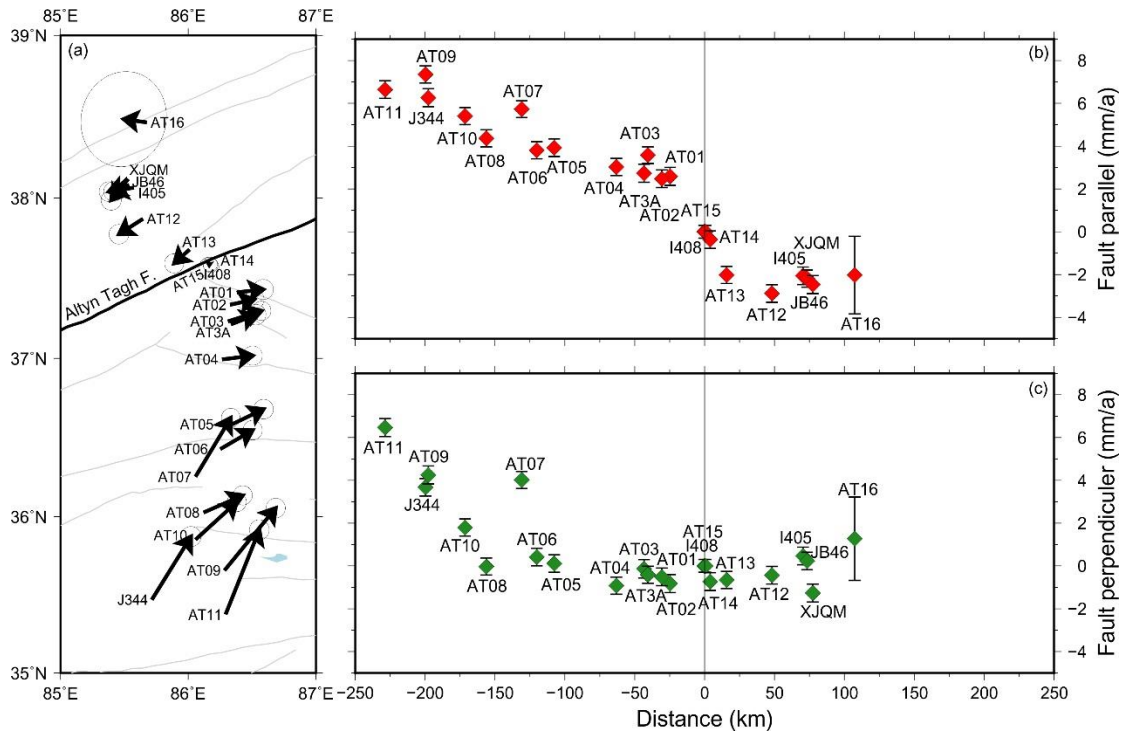


Figure 3.4. (a) GPS velocities for sites across the western Altyn Tagh fault referenced to the AT15 site. (b) Fault-parallel and (c) fault-perpendicular components.

3.4.2. Corrections of the geodetic data for block-rotation

The fault-parallel velocity profiles are shown in Figure 3.4b. We notice that the fault-parallel component north of the Altyn Tagh fault shows a systematic trend away from the fault. We suspect

that this trend, which is seen far away from the Altyn Tagh fault, might be related to the block rotation on a profile rather than a consequence of actual strain rate. In order to test this hypothesis, we use the Euler poles from Wang et al. (2017), which introduced a wider range of GPS data, especially to the south of the Altyn Tagh fault, for the Tarim and Qaidam blocks to calculate the fault-parallel and fault-perpendicular components induced by block rotations (Figure A.2). Results show that to the south of the Altyn Tagh fault, the rotation south of the Altyn Tagh fault contributes ~ 0.3 mm/a to the fault-parallel and ~ 0.1 mm/a to the fault-perpendicular velocities along the ~ 160 -km-long profile (Figure A.2a, A.2b), which are negligible compared with the GPS velocity errors (0.4 mm/a). However, north of the Altyn Tagh fault, the rotating Tarim block results in ~ 1.3 mm/a fault-parallel gradient and < 0.1 mm/a to the fault-perpendicular velocities over the ~ 100 -km-long profile, which would bias the Altyn Tagh fault slip rate estimate (Figure A.2c, A.2d). Consequently, we correct the Tarim block rotation from the GPS velocities north of the Altyn Tagh fault and obtain a corrected fault-parallel velocity profile (Figure 3.5a, 3.5b). The corrected fault-parallel velocity profile shows better consistency and trend. We suggest that such a simple test should be performed for all across-fault geodetic profile before using the data as input for 2-D models.

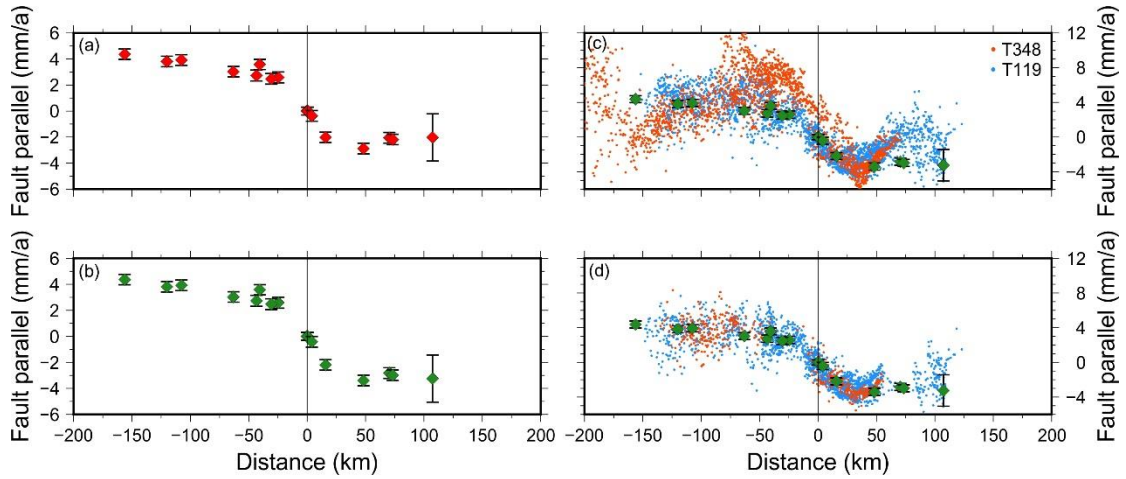


Figure 3.5. Fault-parallel components of GPS velocities across the western Altyn Tagh fault (a) before and (b) after the correction for the contribution from the Tarim block rotation. Comparison between GPS and InSAR (c) before and (d) after masking out the InSAR data points in the localized uplift and subsidence regions. The InSAR data have been projected to the fault-parallel direction.

For the NEE strike-slip Altyn Tagh fault, InSAR LOS displacement is more sensitive to the vertical signal than the horizontal signal (Wright et al., 2004b). It is, therefore, critical to correct the vertical velocity from the InSAR LOS. No leveling measurements has been implemented across the western Altyn Tagh fault, and only the descending InSAR data is available for the moment. Thus, we quantify the vertical deformation from a direct comparison of GPS and InSAR. We first use the 2-D model (presented in section 3.3; Savage and Burford, 1973) to fit the fault-parallel GPS velocities and obtain the optimal fault parameters (slip rate, locking depth and dislocation shift) for the western Altyn Tagh fault; then using the GPS derived fault parameters, we calculate the fault-

parallel velocities at each InSAR point; finally, we project the fault-parallel velocities to LOS and compare with the observed InSAR data (Figure 3.5). The differences between the GPS predicted LOS rates and the observed InSAR LOS rates should mainly related to vertical motion. Note that only fault-parallel components contribute to the predicted LOS rates, and we assume that long-wave length errors, such as orbit errors, are small compared with the vertical signals in the observed InSAR data. The resulting vertical velocity field (Figure 3.5c, 3.5f) show two regions with noticeable uplift and one region with subsidence, where the deformation rates are larger than the uncertainties (~ 1.0 mm/a). Consequently, we suggest that those three areas with apparent, localized vertical deformation, and the InSAR data located in those regions should be masked out when used to model the horizontal Altyn Tagh faulting behaviors. Following the procedures of block rotation correction for GPS site velocities, we also correct the block rotation contributions for the InSAR data. GPS and InSAR data show better consistency after correcting the block rotation and masking the data in the localized deformation regions (Figure 3.4c, 3.4d), highlighting the importance of accounting for the vertical deformation during the InSAR data interpretations. More analyses of the vertical deformation as well as its contribution to the fault parameter inversions are given in the discussion section.

3.4.3. Modeling results

The fault-perpendicular GPS velocities (Figure 3.4c) show ~ 0.3 mm/a relative motion across the western Altyn Tagh fault, accounting for $\sim 4\%$ of the strike-slip rate, implying negligible thrusting movement across the fault and a reasonable assumption of pure strike-slip motion across the fault. Therefore, we model the western Altyn Tagh fault as a buried infinite screw dislocation in an elastic half-space, where the interseismic left-lateral aseismic slip occurs at a rate of V_0 below a locking depth of D . A dislocation shift (d) from the fault trace is introduced to account the possible geodetic data asymmetry across the fault. For a displacement $V(x)$ at a perpendicular distance x from the fault, $V(x) = (V_0/\pi) * \arctan((x - d)/D)$ (Savage and Burford, 1973). We use a Bayesian approach to derive the posterior probability density function (PDF) of the model parameters (Minson et al., 2013), $p(\mathbf{m}|\mathbf{d})$ is defined as: $p(\mathbf{m}|\mathbf{d}) \sim p(\mathbf{m}) \exp [(\mathbf{d} - \mathbf{p})^T C^{-1} (\mathbf{d} - \mathbf{p})]$, with \mathbf{d} and \mathbf{p} vectors containing the observations and model predictions, C^{-1} the inverse of the covariance matrix of the data, and $p(\mathbf{m})$ the prior PDF of the model parameters. We use uniform prior distributions and construct the covariance matrix as diagonal matrix using the GPS and InSAR data uncertainties. Results presented below are derived from a total of 10,000 sampling from the Markov chain.

For the GPS only fitting solution, results show a strike-slip rate of 8.6 ± 0.9 mm/a and a locking depth of 21.9 ± 7.4 km along the western Altyn Tagh fault (Figure 3.6a). The results obtained by only using the InSAR data show discrepancies (Figure 3.6b), with the fault slip rate and locking depth estimated to be 8.0 ± 0.6 mm/a and 13.5 ± 4.1 km, respectively. Joint inversion of GPS and

InSAR data shows a better estimation of locking depth and slip rate (Figure 3.6c). The slip rate estimate is 8.1 ± 0.4 mm/a with a fault locking depth of 15.1 ± 3.4 km. Integrating the fault locking depth and the dislocation offset (0.6 km to the south), the dip angle of the Altyn Tagh fault is estimated to be $\sim 87^\circ$ above the locking crust and agrees with fault structure from magnetotelluric data interpretations (e.g., Zhang et al., 2015; Xiao et al., 2017). Note that as the GPS sites are relatively sparsely distributed (0–25 km) in the near-field of the western Altyn Tagh fault, the improvement for joint inversion is significant over the GPS-only model. Our inversion parameters show overall consistency with previous geodetic results (e.g., Elliott et al., 2008; He et al., 2013; Vernant, 2015; Daout et al., 2018; Li et al., 2018), yet with some discrepancies, which are discussed below.

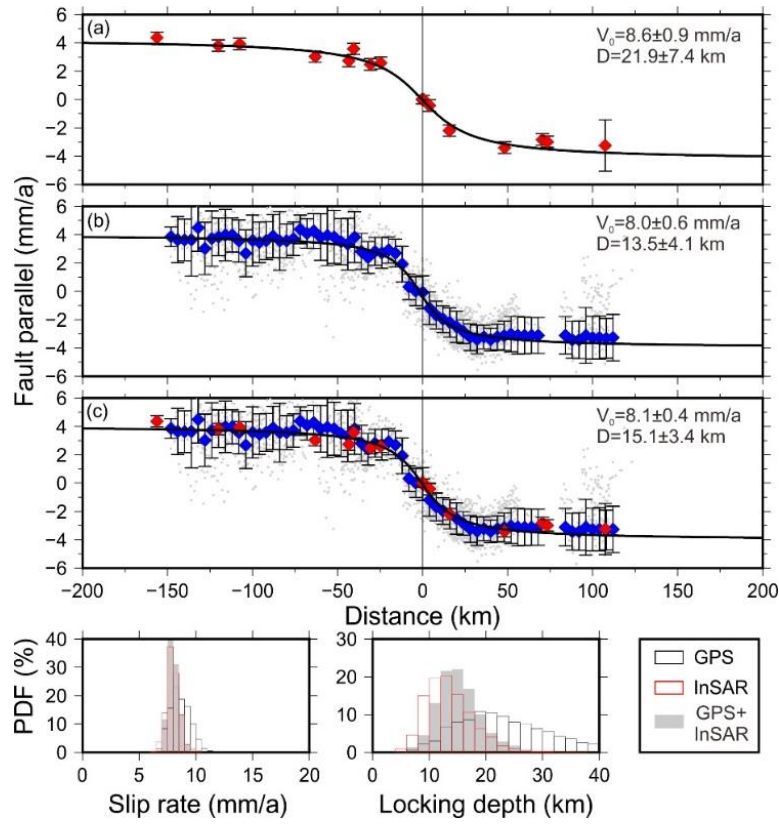


Figure 3.6. Observed and calculated fault-parallel velocities across the western Altyn Tagh fault. Red and blue diamonds with 1σ uncertainty error bars show the fault-parallel velocity component of the GPS and InSAR respectively. Black solid lines represent best fitting curves for (a) GPS data only, (b) InSAR data only, and (c) joint inversion of GPS and InSAR. The velocity of each InSAR data point is calculated using the median rates and their standard deviation of all the pixels (gray dots) within a 4-km-wide bin along the profile. The bottom panels show posterior marginal Probability Density Functions (PDFs) using GPS data only, InSAR data only and GPS+InSAR data. The parameters of the best-fit results are shown in each sub graph.

3.5. Discussion

3.5.1. Slow strain accumulation rate along the western Altyn Tagh fault

The slip rate of the Altyn Tagh fault has long been studied. Early geological results (e.g., Peltzer et al., 1989; Mériaux et al., 2004) reported as high as 20-30 mm/a long-term slip rate along the fault, implying fast strain accumulation rate on the fault plane. Over the last 20 years, with improved interpretations of the ages and offsets of Quaternary geomorphic features, geologists (e.g., Mériaux et al., 2005, 2012; Cowgill, 2007; Cowgill et al., 2009; Zhang et al., 2007; Gold et al., 2009) revised the multi-millennial slip rate of the Altyn Tagh fault to be ~ 10 mm/a along the central segment, which is consistent with the geodetic results (e.g., Bendick et al., 2000; Shen et al., 2001; Wallace et al., 2004; Wright et al., 2004a; Elliott et al., 2008; He et al., 2013; Daout et al., 2018; Li et al., 2018).

Using the relatively short time-span (2009-2011) GPS sites velocities, He et al. (2013) reported a slip rate of 9.0 ± 4.0 mm/a, a fault locking depth of 14.5 km and a dislocation offset of 13 km for the western Altyn Tagh fault. Our GPS+InSAR results (Figure 3.6c), especially the fault slip rate (11% lower) and dislocation offset, show discrepancies with that of He et al. (2013) and Vernant (2015), which are due to different dataset. Moreover, the geodetic data selection matters. If the southernmost GPS sites (AT11, AT09, J344 and AT10, Figure 3.4), which located in localized crustal shearing and shortening deformation regions, are included in our model, the fault slip rate (10.8 ± 1.3 mm/a) and fault locking depth (24.7 ± 9.8 km) will be overestimated by 33% and 64% respectively (Figure A.3a). Consequently, the resulting strain accumulation rate as well as the seismic potential on the western Altyn Tagh fault would be overestimated. We also conduct the inversion without masking out the InSAR data located in the localized uplift and subsidence regions. The results infer a fault slip rate of 7.5 ± 0.9 mm/a and fault locking depth of 7.6 ± 6.7 km (Figure A.3b), biased from our preferred model results (Figure 3.6c) and show asymmetry with an offset of 5.8 km northwards of the fault, contradictory to what is expected for a more rigid Tarim basin and high dip angle of the Altyn Tagh fault (e.g., Zhang et al., 2015; Xiao et al., 2017). Also note that although we use the same InSAR data with Daout et al. (2018), the resulting fault slip rate and locking depth of the western Altyn Tagh fault are different (slip rate of 10.5 mm/a and locking depth of 17 km in Daout et al. 2018), the discrepancies may either be related to the model or the GPS velocity dataset. Discrepancies also exist between 2-D and 3-D model results, as 3-D block model show a slip rate of 11.0 ± 0.7 mm/a (Li et al., 2018). In conclusion, quantitative comparisons show that previous geodetic results (2-D model results) have overestimated the slip rate of the western Altyn Tagh fault up to 36% (e.g., 11 ± 5 mm/a of Elliott et al. 2008), implying a relatively slow strain accumulation rate (~ 8 mm/a) than expected along the fault.

3.5.2. Do asymmetric patterns of interseismic velocity exist across the western

Altyn Tagh fault?

Asymmetric patterns of interseismic geodetic velocities across the strike-slip fault could result from varied elastic thickness (e.g., Chéry, 2008), lateral variations in the elastic strength, or a shift in the position of dislocation at depth relative to the fault trace (Le Pichon et al., 2005; He et al., 2013). Asymmetry in the interseismic strain across the San Andreas Fault (e.g., Savage et al., 2004; Fialko, 2006) and the North Anatolian Fault (e.g., Meade et al., 2002) have been reported by interpreting GPS velocities. Along the strike-slip Altyn Tagh fault, Lasserre et al. (2007) processed 15 interferograms of European Remote Sensing (ERS) and Envisat radar data and obtained a fault-parallel velocity map in the Aksay region (94°E). Clear asymmetry with respect to the northern Altyn Tagh fault was identified and suggests the Tarim Basin behaves as a rigid block (Zhang et al., 2004). Subsequently, Elliott et al. (2008) processed 26 ERS-1/2 SAR data for the period 1993-2000 across the western Altyn Tagh fault (85°E, ~150 km west of our GPS profile). Their derived rate map also shows asymmetry with an offset in the maximum deformation gradient ~10 km northwards of the fault. However, the sense of asymmetry is in the opposite direction to what is expected for a more rigid Tarim Basin. A shift in the freely slipping dislocation at depth relative to the surface fault trace to the south would also give the opposite sense of asymmetry. These results remain unexplained. Moreover, owing to the loss of coherence in InSAR interference, the InSAR deformation signal is missing to the south of the fault, as a result, the existence of asymmetrical interseismic velocities to the south of the Altyn Tagh fault (85°E) is unresolved. Jolivet et al. (2008) applied a thin-plate model sheared at its base to interpret the asymmetric InSAR data of Lasserre et al. (2007) across the Altyn Tagh fault (94°E). They proposed that the asymmetric patterns of interseismic velocities reflected the joint effects of a rigidity decrease from Tarim to Qaidam and a southward offset of 5-7 km from the northern Altyn Tagh fault to the southern Altyn Tagh fault. He et al. (2013) also reported apparent asymmetry of the shear strain across the Altyn Tagh fault (86°E) by interpreting cross-fault GPS velocities. Their best fault-parallel velocity fitting solution was obtained by shifting the position of the dislocation at depth to the south relative to the fault trace by 13 km, implying that a position shift of the dislocation at depth was responsible for asymmetric velocities. However, the resulting dip angle (~48°) for the Altyn Tagh fault is inconsistent with magnetotelluric data interpretations (e.g., Zhang et al., 2015; Xiao et al., 2017).

To test how such a rigidity contrast could impact our results, we invert the data profile again for slip rate, locking depth, and rigidity ratio K according to the equations (e.g., Jolivet et al., 2008):

$$V(x) = \begin{cases} \frac{2KV_0}{\pi} \arctan\left(\frac{x-d}{D}\right), & \text{if } x > d \\ \frac{2(1-K)V_0}{\pi} \arctan\left(\frac{x-d}{D}\right), & \text{if } x < d \end{cases}$$

where K is the asymmetry coefficient, ranging from 0 to 1. This coefficient also represents the rigidity ratio between the upper crust on each side of the fault. A value of $K = 0.5$ indicates no

rigidity contrast between two sides of the fault.

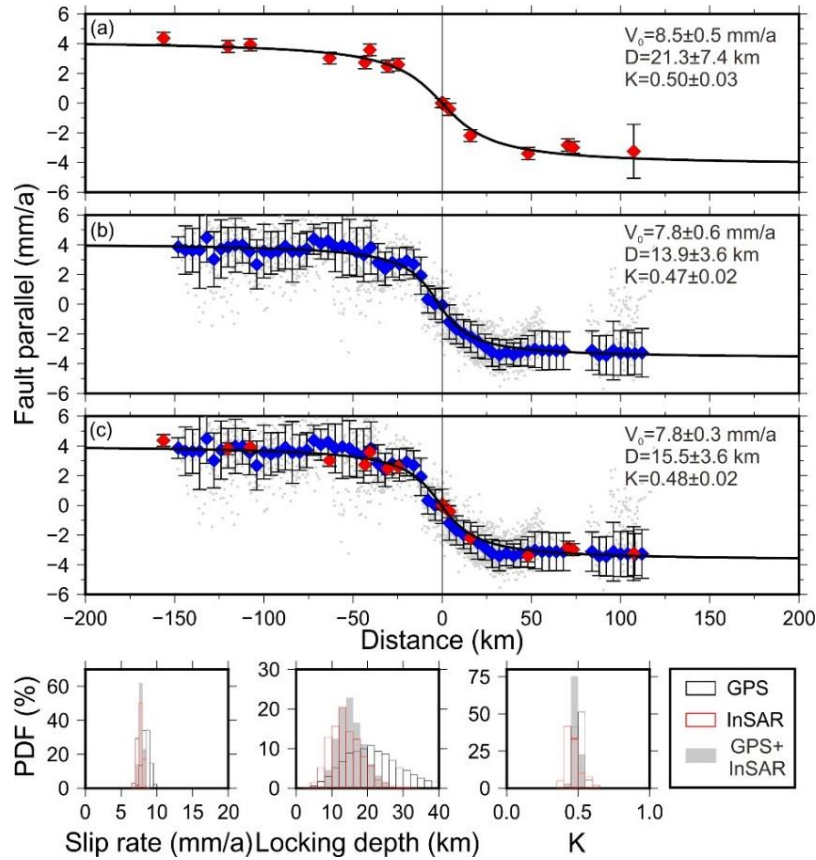


Figure 3.7. Observed and calculated fault-parallel velocities across the western Altyn Tagh fault. Red and blue diamonds with 1σ uncertainty error bars show the fault-parallel velocity component of the GPS and InSAR respectively. Black solid lines represent best fitting curves for (a) GPS data only, (b) InSAR data only, and (c) joint inversion of GPS and InSAR. The velocity of each InSAR data point is calculated using the median rates and their standard deviation of all the pixels (gray dots) within a 4-km-wide bin along the profile. The bottom panels show posterior marginal Probability Density Functions (PDFs) using GPS data only, InSAR data only and GPS+InSAR data. The parameters of the best-fit results are shown in each sub graph.

The rigidity contrast between the northern Tibetan Plateau and the southern Tarim Basin is estimated to be 0.47 ± 0.02 - 0.50 ± 0.03 from the different datasets (Figure 3.7), implying the north side of the fault (the Tarim Basin) roughly 0-11% more rigid than the south side (the northern Tibetan Plateau). Including a rigidity contrast in our model gives values for fault slip rates, fault locking depths and dislocation offsets that are within the error bounds (Figure 3.6c). Consequently, we propose that no apparent asymmetric interseismic velocities across the western Altyn Tagh fault (86°E), ruling out both a lateral variation in the elastic strength and a dislocation shift across the fault.

3.5.3. High spatial resolution crustal deformation in the northwestern Tibet

A three-dimensional velocity field is obtained by quantitative comparison of the GPS and InSAR across the western Altyn Tagh fault (Figure 3.8). The first-order features of the horizontal velocity field are the steep gradient across the western Altyn Tagh fault both for GPS and InSAR, showing the strike-slip faulting behavior of the Altyn Tagh fault. The relatively low slip rate (8.1 ± 0.4 mm/a) along the Altyn Tagh fault do not support the lateral extrusion (e.g., Avouac and Tapponnier, 1993; Tapponnier et al., 2001; Mériaux et al., 2005) as the primary crustal deformation mode of the Tibetan Plateau. Our proposed separation for vertical motion highlights three regions with localized vertical deformation (Figure 3.8d, 3.8i). It's intriguing that a subsidence region located 150 km south of the Altyn Tagh fault, bracketed by the tail of the Kunlun fault and the Manyi fault (Manyi north branch, Figure 3.1). The localized subsidence may be either related to the seasonal deformation due to the freeze and thaw cycles of the permafrost active layer or the complex interactions of secondary faults. To the south of the subsidence region, between AT08 and AT11, a localized 6 mm/a crustal shortening and 3 mm/a left-lateral shear deformation (Figure 3.4b, 3.4c) may either reflect the faulting behaviors of the Manyi fault or the distributed deformation. The interaction and influence between the two localized regions are still unknown, a larger range of 3-dimensional deformation fields, especially extends to the east, will help to decipher the origin of such signal.

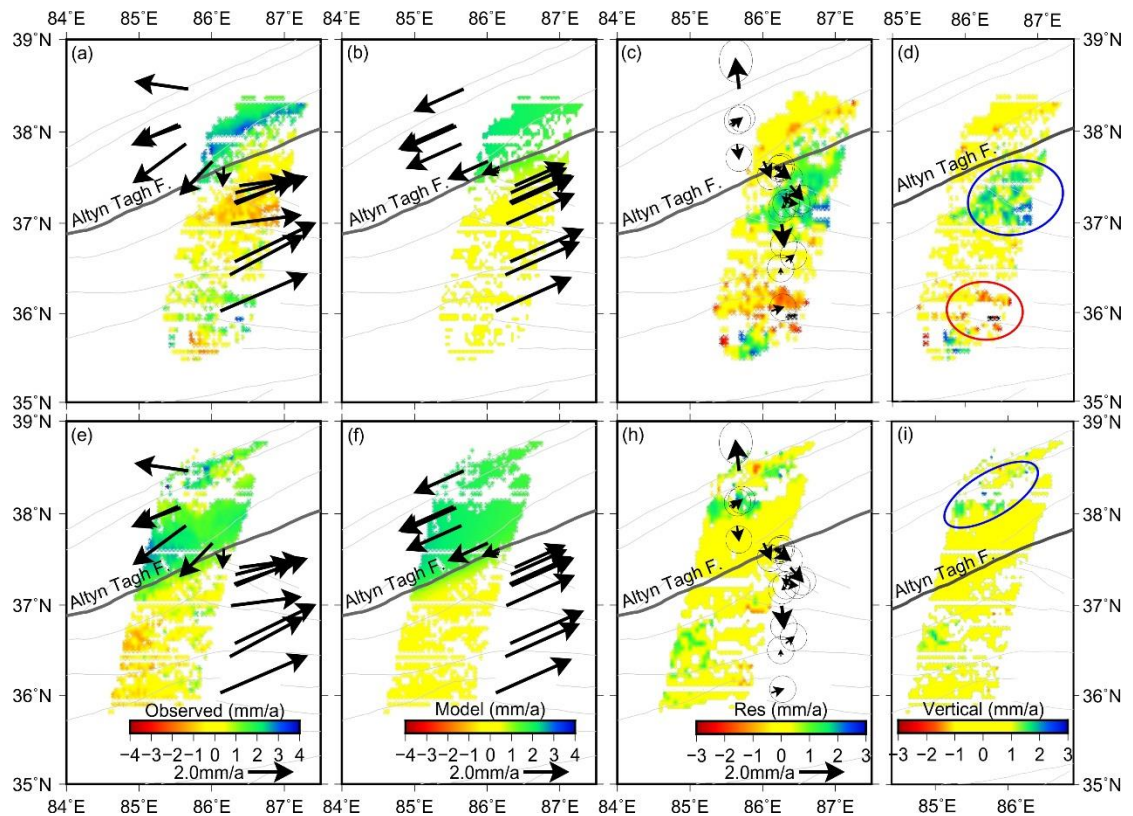


Figure 3.8. Comparison between data and model from the Bayesian inversion. (a) and (e) are the observed GPS and InSAR data (T348 in the upper panel and T119 in the lower panel). (b) and (f) are the model predictions. (c) and (h) are the residuals between observation and prediction. (d) and (i) are the vertical displacements from the InSAR and GPS, the color bar has been modified to mask out points with values smaller than its uncertainties (1.0 mm/a). Red and blue ellipses show the approximate location of

the localized subsidence and uplift regions.

There are also two regions with apparent uplift, one of which located 25-70 km to the south of the Altyn Tagh fault, overlapping the Qiman Shan (Figure 3.1 and Figure 3.8d). Daout et al. (2018) interpreted the velocity changes associated with the slight change of azimuth of the western Altyn Tagh fault and its connection with the Qiman Shan and eastern Kunlun Shan thrusts. They propose a south dipping thrust, north of the Qiman Shan, should be responsible for the vertical deformation. However, only slightly crustal shortening (<1 mm/a) and shear deformation (~ 0.2 mm/a) are observed in our GPS profile across the apparent uplift region, which could not account for the vertical uplift (1.5-2 mm/a) by a dipping thrust. Whether the surface uplift is controlled by regional faults or activities of the upper crust remains unknown. Detailed field tectonic investigations could help to verify potentially active faults. Another region with apparent uplift deformation located north of the Altyn Tagh fault, south of the Cherchen fault (Figure 3.8i). Daout et al. (2018) interpreted the low velocity gradient by introducing a shallow flat décollement ending in a steeper ramp in the north of the Altyn Tagh fault. Their model predicts 0.7 mm/a crustal shortening rate between the Altyn Tagh fault and the Cherchen fault, which account only half of the uplift rate (~ 1.5 mm/a). Besides, our GPS fault-perpendicular velocities show a roughly 0-1 mm/a tension rate between AT12 and I036 (50-80 km), suggesting normal faulting for the ramp, which is contradictory to the model of Daout et al. (2018). Consequently, we suggest that either the uplift region is related to the regional unmapped faults or activities of the upper crust. Our results highlight the complexity of three-dimensional crustal deformation in the northwestern Tibetan Plateau.

In conclusion, the above analyses indicate that the crustal deformation in the northwestern Tibetan Plateau is a combination of strike-slip faulting, localized crustal shearing, shortening, subsidence and uplift. Our current study calls for additional GPS stations, multiple InSAR observations and detailed field investigations to better delineate the crustal deformation of the northwestern Tibetan Plateau.

3.6. Conclusions

We combine two tracks of interseismic InSAR data with an improved GPS velocity data across the western Altyn Tagh fault. The geodetic data are consistent after masking out the (InSAR) points in localized crustal deformation regions. We correct for the block rotation contributions to the fault-parallel geodetic velocities, this has enabled us to robustly estimate the slip rate and locking depth of the western Altyn Tagh fault using a simple 2-D elastic dislocation model. A best fit is obtained with a left-lateral strike-slip rate of 8.1 ± 0.4 mm/a and locking depth of 15.1 ± 3.4 km. Our result implies that previous studies (2-D model results) have overestimated the slip rate of the western Altyn Tagh fault up to 36% and a relatively slow slip deficit accumulation rate is found. Moreover, our results show three regions with localized vertical deformation, of which two apparent uplift regions and one subsidence region, reinforcing the importance of accounting for the vertical deformation during the interseismic InSAR data interpretations.

We also show no apparent asymmetric interseismic velocities across the western Altyn Tagh fault, ruling out the requirement of lateral variations in elastic strength and/or dislocation shift with respect to the fault trace. The three-dimensional velocity field derived from quantitative comparison of the GPS and InSAR suggests that the crustal deformation in the northwestern Tibetan Plateau is a combination of strike-slip faulting, localized crustal shearing and shortening. It further suggests that vertical motion is not directly controlled by crustal fault activity.

Acknowledgments

We are grateful to all our colleagues who participated in the GPS fieldwork. We deeply thank Simon Daout and his co-workers for sharing the InSAR results. We are also grateful to Jiankun He, in the Institute of Tibetan Plateau Research, Chinese Academy of Sciences, who shared the GPS data acquired in 2009–2011 across the western Altyn Tagh fault. CMONOC GPS data were provided by the National Earthquake Infrastructure Service, China Earthquake Administration. This work was supported by the National Natural Science Foundation of China (Grant No. 41631073, 41461164002). Yanchuan Li was financially supported by the China Earthquake Administration and the China Scholarship Council. All figures were generated using the Generic Mapping Tools (GMT) software (Wessel et al., 2013). GPS velocity data are accessible in the published paper (<https://doi.org/10.1029/2018JB015814>).

3.7. References

- Avouac, J. P., Tapponnier, P., 1993. Kinematic model of active deformation in central Asia. *Geophys. Res. Lett.*, 20(10), 895-898.
- Bendick, R., Bilham, R., Freymueller, J., Larson, K., Yin, G., 2000. Geodetic evidence for a low slip rate in the Altyn Tagh fault system. *Nature*, 404(6773), 69.
- Blewitt, G., Lavallée, D., 2002. Effect of annual signals on geodetic velocity. *J. Geoph. Res.*, 107(B7), ETG 9-1-ETG 9-11.
- Burchfiel, B. C., Quidong, D., Molnar, P., Royden, L., Yipeng, W., Peizhen, Z., Weiqi, Z., 1989. Intracrustal detachment within zones of continental deformation. *Geology*, 17(8), 748-752.
- Chéry, J. 2008. Geodetic strain across the San Andreas Fault reflects elastic plate thickness variations (rather than fault slip rate). *Earth Planet. Sci. Lett.*, 269(3), 352-365.
- Cowgill, E. 2007. Impact of riser reconstructions on estimation of secular variation in rates of strike-slip faulting: Revisiting the Cherchen River site along the Altyn Tagh Fault, NW China. *Earth Planet. Sci. Lett.*, 254, 239-255.
- Cowgill, E., Gold, R. D., Xuanhua, C., Xiao-Feng, W., Arrowsmith, J. R., Southon, J., 2009. Low Quaternary slip rate reconciles geodetic and geologic rates along the Altyn Tagh fault, northwestern Tibet. *Geology*, 37(7), 647-650.
- Daout, S., Doin, M. P., Peltzer, G., Lasserre, C., Socquet, A., Volat, M., Sudhaus, H., 2018. Strain partitioning and present-day fault kinematics in NW Tibet from Envisat SAR interferometry. *J. Geoph. Res.*, 123(3), 2462-2483.
- Elliott, J. R., Biggs, J., Parsons, B., Wright, T. J., 2008. InSAR slip rate determination on the Altyn Tagh Fault, northern Tibet, in the presence of topographically correlated atmospheric delays. *Geophys. Res. Lett.*, 35(12), L12309.
- England, P., Molnar, P., 1997. Active deformation of Asia: from kinematics to dynamics. *Science*, 278(5338), 647-650.
- Fialko, Y. 2006. Interseismic strain accumulation and the earthquake potential on the southern San Andreas Fault system. *Nature*, 441(7096), 968-971.
- Gold, R. D., Cowgill, E., Arrowsmith, J. R., Gosse, J., Chen, X., Wang, X., 2009. Riser diachroneity, lateral erosion, and uncertainty in rates of strike-slip faulting: A case study from Tuzidun along the Altyn Tagh Fault, NW China. *J. Geophys. Res.*, 114(B4), B04401.
- He, J., Vernant, P., Chéry, J., Wang, W., Lu, S., Ku, W., Xia, W., Bilham, R., 2013. Nailing down the slip rate of the Altyn Tagh fault. *Geophys. Res. Lett.*, 40(20), 5382-5386.
- Herring, T. A. 2003. MATLAB Tools for viewing GPS velocities and time series. *GPS Solut.*, 7(3), 194-199.
- Houseman, G., England, P., 1993. Crustal thickening versus lateral expulsion in the Indian-Asian continental collision. *J. Geophys. Res.*, 98(B7), 12233-12249.
- Jolivet, R., Cattin, R., Chamot-Rooke, N., Lasserre, C., Peltzer, G., 2008. Thin-plate modeling of interseismic deformation and asymmetry across the Altyn Tagh fault zone. *Geophys. Res. Lett.*, 35(2), L02309.
- Kreemer, C., Blewitt, G., Klein, E. C., 2014. A geodetic plate motion and Global Strain Rate Model. *Geochem. Geophys. Geosyst.*, 15(10), 3849-3889.
- Lasserre, C., CavaliÈ, O., Peltzer, G., Socquet, A., Doin, M.-P., Sun, J., Xu, X., Shen, Z.-K., Wang,

- Q., Gaudemer, Y., 2007. Interseismic deformation across the Altyn Tagh and Haiyuan faults at the northern edge of the Tibetan plateau, measured by space geodesy, *Geophys. Res. Abstr.*, 9, 10,102.
- Le Pichon, X., Kreemer, C., Chamot-Rooke, N., 2005. Asymmetry in elastic properties and the evolution of large continental strike-slip faults. *J. Geophys. Res.*, 110(B3), B03405.
- Li, Y., Shan, X., Qu, C., Liu, Y., Han, N., 2018. Crustal deformation of the AltynTagh fault based on GPS. *J. Geophys. Res.*, 123.
- Meade, B. J., Hager, B. H., McClusky, S. C., Reilinger, R. E., Ergintav, S., Lenk, O., Barka, A., Ozener, H., 2002. Estimates of seismic potential in the Marmara Sea region from block models of secular deformation constrained by Global Positioning System measurements. *Bull. Seismol. Soc. Am.*, 92(1), 208-215.
- Mériaux, A. S., Ryerson, F. J., Tapponnier, P., Van der Woerd, J., Finkel, R. C., Xu, X., Xu, Z., Caffee, M. W., 2004. Rapid slip along the central Altyn Tagh Fault: morphochronologic evidence from Cherchen He and Sulamu Tagh. *J. Geophys. Res.*, 109, B06401.
- Mériaux, A. S., Tapponnier, P., Ryerson, F. J., Xu, X., King, G., Van der Woerd, J., Finkel, R. C., Li, H., Xu, Z., Chen, W., 2005. The Aksay segment of the northern Altyn Tagh fault: Tectonic geomorphology, landscape evolution, and Holocene slip rate. *J. Geophys. Res.*, 110, B04404.
- Mériaux, A. S., Van Der Woerd, J., Tapponnier, P., Ryerson, F. J., Finkel, R. C., Lasserre, C., Xu, X., 2012. The Pingding segment of the Altyn Tagh Fault (91°E): Holocene slip-rate determination from cosmogenic radionuclide dating of offset fluvial terraces. *J. Geophys. Res.*, 117(B9).
- Minson, S. E., Simons, M., Beck, J. L., 2013. Bayesian inversion for finite fault earthquake source models I - Theory and algorithm. *Geophys. J. Int.*, 194(3), 1701-1726.
- Molnar, P., Burchfiel, B. C., K'uangyi, L., Ziyun, Z., 1987. Geomorphic evidence for active faulting in the Altyn Tagh and northern Tibet and qualitative estimates of its contribution to the convergence of India and Eurasia. *Geology*, 15(3), 249-253.
- Molnar, P., Tapponnier, P., 1975. Cenozoic tectonics of Asia: Effects of a continental collision. *Science*, 189, 419-426.
- Molnar, P., Tapponnier, P., 1977. The collision between India and Eurasia. *Scientific American*, 236(4), 30-41.
- Peltzer, G., Tapponnier, P., Armijo, R., 1989. Magnitude of late Quaternary left-lateral displacements along the north edge of Tibet. *Science*, 246, 1285.
- Puysségur, B., Michel, R., Avouac, J. P., 2007. Tropospheric phase delay in interferometric synthetic aperture radar estimated from meteorological model and multispectral imagery. *J. Geophys. Res.*, 112, B05419.
- Reilinger, R., et al. 2006. GPS constraints on continental deformation in the Africa-Arabia-Eurasia continental collision zone and implications for the dynamics of plate interactions. *J. Geophys. Res.*, 111, B05411.
- Rosen, P. A., Hensley, S., Peltzer, G., Simons, M., 2004. Updated repeat orbit interferometry package released. *Eos, Transactions American Geophysical Union*, 85(5), 47-47.
- Savage, J. C. 2006. Dislocation pileup as a representation of strain accumulation on a strike-slip fault. *J. Geophys. Res.*, 111(B4), 170-176.
- Savage, J. C., Burford, R. O., 1973. Geodetic determination of relative plate motion in central California. *J. Geophys. Res.*, 78(5), 832-845.
- Savage, J. C., Gan, W., Prescott, W. H., Svarc, J. L., 2004. Strain accumulation across the Coast

- Ranges at the latitude of San Francisco, 1994-2000. *J. Geophys. Res.*, 109, B03413.
- Shen, Z. K., Wang, M., Li, Y., Jackson, D. D., Yin, A., Dong, D., Fang, P., 2001. Crustal deformation along the Altyn Tagh fault system, western China, from GPS. *J. Geophys. Res.*, 106, 30607-30621.
- Tapponnier, P., Zhiqin, X., Roger, F., Meyer, B., Arnaud, N., Wittlinger, G., Jingsui, Y., 2001. Oblique stepwise rise and growth of the Tibet Plateau. *Science*, 294(5547), 1671-1677.
- Vernant, P. 2015. What can we learn from 20 years of interseismic GPS measurements across strike-slip faults?. *Tectonophysics*, 644, 22-39.
- Wallace, K., Yin, G., Bilham, R., 2004. Inescapable slow slip on the Altyn Tagh fault. *Geophys. Res. Lett.*, 31(9).
- Wang, W., Qiao, X., Yang, S., Wang, D., 2017. Present-day velocity field and block kinematics of Tibetan Plateau from GPS measurements. *Geophys. J. Int.*, 208(2), 1088-1102.
- Wessel, P., Smith, W. H., Scharroo, R., Luis, J., Wobbe, F., 2013. Generic mapping tools: Improved version released. *Eos Transactions American Geophysical Union*, 94(45), 409-410.
- Wright, T. J., Parsons, B., England, P. C., Fielding, E. J., 2004a. InSAR observations of low slip rates on the major faults of western Tibet. *Science*, 305(5681), 236-239.
- Wright, T. J., Parsons, B. E., Lu, Z. 2004b. Toward mapping surface deformation in three dimensions using InSAR. *Geophys. Res. Lett.*, 31(1), L01607.
- Xiao, Q., Yu, G., Liu-Zeng, J., Oskin, M. E., Shao, G., 2017. Structure and geometry of the Aksay restraining double bend along the Altyn Tagh Fault, northern Tibet, imaged using magnetotelluric method. *Geophys. Res. Lett.*, 44(9), 4090-4097.
- Yin, A., Harrison, T. M., 2000. Geologic evolution of the Himalayan-Tibetan orogen. *Ann. Rev. Earth Pl. Sc.*, 28(1), 211-280.
- Yin, A., Rumelhart, P. E., Butler, R., Cowgill, E., Harrison, T. M., Foster, D. A., Ingersoll, R.V., Zhang, Q., Zhou, X., Wang, X., Hanson, A., Raza, A., 2002. Tectonic history of the Altyn Tagh fault system in northern Tibet inferred from Cenozoic sedimentation. *Geol. Soc. Am Bull*, 114(10), 1257-1295.
- Zhang, L., Unsworth, M., Jin, S., Wei, W., Ye, G., Jones, A. G., Jing, J., Dong, H., Xie, C., Pape, F. L., Vozar, J., 2015. Structure of the Central Altyn Tagh Fault revealed by magnetotelluric data: New insights into the structure of the northern margin of the India-Asia collision. *Earth Planet. Sci. Lett.*, 415, 67-79.
- Zhang, P. Z., Molnar, P., Xu, X., 2007. Late Quaternary and present-day rates of slip along the Altyn Tagh Fault, northern margin of the Tibetan Plateau. *Tectonics*, 26(5), 1-8.
- Zhang, P. Z., Shen, Z., Wang, M., Gan, W., Bürgmann, R., Molnar, P., Wang, Q., Niu, Z., Sun, J., Wu, J., Sun, H., You, X., 2004. Continuous deformation of the Tibetan Plateau from Global Positioning System data. *Geology*, 32(9), 809-812.
- Zheng, G., Wang, H., Wright, T. J., Lou, Y., Zhang, R., Zhang, W., Shi, C., Huang, J., Wei, N., 2017. Crustal deformation in the India-Eurasia collision zone from 25 years of GPS measurements. *J. Geophys. Res.*, 122(11), 9290-9312.
- Zhu, S., Xu, C., Wen, Y., Liu, Y., 2016. Interseismic deformation of the Altyn Tagh fault determined by interferometric synthetic aperture radar (InSAR) measurements. *Remote Sens.*, 8(3), 233.

Chapter 4· Surface creep on the Haiyuan fault system, northeastern Tibet, constrained from GPS and InSAR

The work in this chapter is a further extension my previous work (*Li, Y., Shan, X., Qu, C., Zhang, Y., Song, X., Jiang, Y., Zhang, G., J-M, Nocquet., Gong, W., Gan, W., Wang, C., 2017. Elastic block and strain modeling of GPS data around the Haiyuan-Liupanshan fault, northeastern Tibetan Plateau. Journal of Asian Earth Sciences, 150, 87-97*). In my previous work, I used GPS data only to invert for the interseismic fault coupling (ISC) along the Haiyuan fault system. It suffers from a low spatial resolution close to the fault and failed to capture any creep signal. To improve the ISC resolution, InSAR data is needed.

In this chapter, I use GPS and InSAR data to study the interseismic fault deformation along the Haiyuan fault system, northeastern Tibetan Plateau. Similar to the structure of the previous chapter, I first introduce the GPS and InSAR data that are used. Then, I present comparison methods and results of the GPS, InSAR and leveling data. I use both 2D and 3D kinematic models to investigate shallow creep along the fault system. In the discussion section, I present arguments on the mechanisms of shallow creep, the correspondence between present-day fault deformation and historical earthquakes, and implications for earthquake scenarios along the fault system.

The work is still in process, and I present in this chapter the results of the first stage.

4.1. Abstract

We analyze Global Positioning System (GPS) data (1999–2017) combined with Interferometric Synthetic Aperture Radar (InSAR) data (2003–2010) in northeastern Tibet to investigate the interseismic deformation along the Haiyuan fault system. The comparison between GPS, Leveling and InSAR Line Of Sight (LOS) rates show discrepancies at a few mm/a level, reflecting long-wavelength systematic errors or vertical deformation in InSAR and levelling data. We solve this problem by combining GPS with high-pass filtered InSAR data to produce a continuous LOS rate map around the Haiyuan fault system. Our geodetic data reveals three creeping segments separating four locked asperities. We confirm previous studies showing surface creep on the Laohushan fault ($\sim 103.6^{\circ}\text{E}$ – 103.9°E). We further identify 3–5 mm/a surface creep along a 10 km long segment for the western Haiyuan fault (HYW, $\sim 104.2^{\circ}\text{E}$ – 104.3°E) and 2–4 mm/a surface creep along a 43 km long segment for the eastern Haiyuan (HYE, $\sim 105.3^{\circ}\text{E}$ – 105.7°E) segments. Both present-day creeping segments are located along the surface rupture trace from the M \sim 8 1920 earthquake and they experienced 3 m and 3 to 10 m of co-seismic offsets respectively. This observation suggests that either the M \sim 8 1920 earthquake was able to cross pre-existing creeping segments or that large earthquakes show heterogeneous relocking, with creep lasting decades along some parts of the rupture.

4.2. Introduction

In a simple view, faults are locked over the entire seismogenic zone during the interseismic phase, eventually slip fast during earthquakes (e.g., Reid, 1910). However, during the last decade, high spatial resolution observations highlighted that some continental faults exhibit a dual mechanical behavior, where locked segments coexist with section where slip occurs aseismically and steadily in the seismogenic zone of the fault. Creeping faults are thought to limit the ability of the fault to generate major earthquakes (e.g., Avouac, 2015; Harris, 2017). Indeed, when the rate of aseismic creep is equal or larger than the relative motion of surrounding blocks, little or no elastic strain accumulates on the fault. Examples of this behavior are the Greenville fault in California (e.g., Lienkaemper et al., 2013), the Chaman fault in Pakistan and Afghanistan (e.g., Barnhart, 2016) and the Laohushan fault in northeastern Tibet (e.g., Jolivet et al., 2012, 2013). Oppositely, when the fault segment slips at a creep rate lower than the tectonic loading rate, slip deficit accumulates. In that latter case, many examples show that earthquakes can still occur, such as the central San Andreas fault (e.g., Lyons and Sandwell, 2003; Moore and Rymer, 2007; Ryder and Bürgmann, 2008; Gratier et al., 2011; Lindsey et al., 2014; Jolivet et al., 2015), the Hayward and Calaveras faults (e.g., Bürgmann et al., 2000; Chaussard et al., 2015), the Imperial fault (e.g., Lyons et al., 2002; Bilham et al., 2004; Lindsey and Fialko, 2016), the North Anatolian fault (e.g., Cakir et al., 2005; Karabacak et al., 2011; Bilham et al., 2016) and the Longitudinal Valley fault (e.g., Lee et al., 2003; Rau et al., 2007; Chen et al., 2008; Thomas et al., 2014). Furthermore, aseismic creep could be the triggering factor for small to moderate-size earthquakes, such as the two creep-driven earthquakes (M_i 4.6–4.7 in 2016–2017) on the Laohushan fault (Jolivet et al., 2013). Aseismic creep could also impede the propagation of the earthquake rupture, as it has been proposed for the 2017 Mw 6.5 Ormoc earthquake on the creeping segment of the Philippine fault (Yang et al., 2018). Thus, identifying and quantifying the spatial distribution, rates, and depths of aseismic slip is essential to propose scenarios of future ruptures, estimate the seismic potential of a fault and more generally for understanding the physics of earthquake (e.g., Bürgmann et al., 2000; Cetin et al., 2014). Here, we focus on the interseismic behavior of Haiyuan fault system, northeastern Tibetan Plateau, where creep has been previously identified along the Laohushan fault (Cavalié et al., 2008) (Figure 4.1).

The ~1000-km-long, active, left-lateral strike-slip Haiyuan fault system is one of a main structure in the northeastern Tibetan Plateau that accommodates the eastward motion of Tibet (e.g., Gaudemer et al., 1995; Tapponnier et al., 2001; Figure 4.1). From west to east, it consists of the Lenglongling fault, the Jinqianghe fault, the Maomaoshan fault, the Laohushan fault and the Haiyuan fault (note the differences of Haiyuan fault system and Haiyuan fault). The Haiyuan fault is further segmented into western (HYW), middle (HYM) and eastern (HYE) segments. The remaining faults constitute the Tianzhu seismic gap, where no M 7+ earthquakes have been recorded over the past few centuries despite clear geomorphic evidence of Holocene large earthquakes (Gaudemer et al., 1995; Liu-Zeng et al., 2007; Figure 4.1). Two M 8+ earthquakes occurred along

the Haiyuan fault system during the last century. The 1920 M~8.0 earthquake generated ~240 km of surface ruptures, with a maximum slip of ~10 m at its center, on the Haiyuan fault (Deng et al., 1986; Zhang et al., 1987).

Global Positioning System (GPS) and Interferometric Synthetic Aperture Radar (InSAR) have been extensively used along the Haiyuan fault system to quantify its interseismic deformation. Depending on the data used and inversion results, the slip rates were estimated to be between 5 and 10 mm/a (e.g., Gan et al., 2007; Cavalié et al., 2008; Jolivet et al., 2012, 2013; Daout et al., 2016; Li et al., 2016, 2017, 2018). Recent studies highlight along strike changes of locking depth from 2 to 22 km depth (Li et al., 2017; Song et al., 2019), with a 35 km-long creeping segment at the eastern end of the Laohushan fault (hereafter referred to the Laohushan creep segment; Cavalié et al., 2008; Jolivet et al., 2012; Daout et al., 2016).

Despite these extensive studies, interseismic fault coupling (ISC) along the rupture of the M~8 1920-ruptured Haiyuan fault earthquake remains poorly constrained. A first-order fault locking on the Haiyuan fault system derived from GPS data only has been proposed in Li et al. (2017), but their study suffers from a low spatial resolution close to the fault and failed to capture any creep signal. InSAR data certainly provide a way to constrain the ISC with dense near fault observation. However, one open question in using InSAR is to evaluate and separate vertical deformation that has could map into the Light Of Sight (LOS). Indeed, vertical deformation across the Haiyuan fault system might exist in the InSAR displacements, which would bias the creep-related interpretations. A limiting factor of InSAR is that an interferogram only measures one component of the surface deformation. Consequently, previous studies assume the InSAR displacements as fault-parallel and horizontal (Cavalié et al., 2008; Jolivet et al., 2012, 2013; Song et al., 2019). Such an assumption is valid only if there is no/negligible vertical deformation. However, long-term leveling measurements (1970–2012) have reported ~1–2 mm/a vertical velocity across the Haiyuan fault system despite of a spatial resolution to the levelling profiles (Figure B.1; Hao et al., 2014). In the case of descending Environmental Satellite (Envisat; incidence angle of 23° and azimuth of 193°) that adopted by previous studies (Cavalié et al., 2008; Jolivet et al., 2012, 2013; Daout et al., 2016; Song et al., 2019), $d_{LOS} = [d_N, d_E, d_U] \cdot [-0.094, 0.391, 0.916]^T$. The inference is that the LOS displacement is twice more sensitive to vertical deformation than horizontal. Considering the non-negligible vertical crustal deformation in northeastern Tibet (Hao et al., 2014), more careful work should be conducted in terms of interseismic InSAR LOS map interpretation.

The physical mechanism of shallow creep along the Laohushan fault remains controversial. Jolivet et al. (2013) reported that the creep rate scales logarithmically with the friction coefficient, in agreement with the rate-and-state friction law in a rate strengthening regime. On the other hand, Chen et al. (2018) proposed that the current creep motion may be transient due to afterslip following either the moderate 2000 Jingtai Mw 5.5 earthquake or in response to the great 1920 M~8 Haiyuan earthquake (Figure 4.1). To distinguish between the two mechanisms, more investigation is needed.

It would also be interesting to explore if any potential creeping segments exist along the 1920-ruptured Haiyuan fault, similarly as we observe along the ruptured North Anatolian Fault (e.g., Cakir et al., 2005; Karabacak et al., 2011; Bilham et al., 2016) or the Hayward Fault (e.g., Bürgmann et al., 2000; Chaussard et al., 2015).

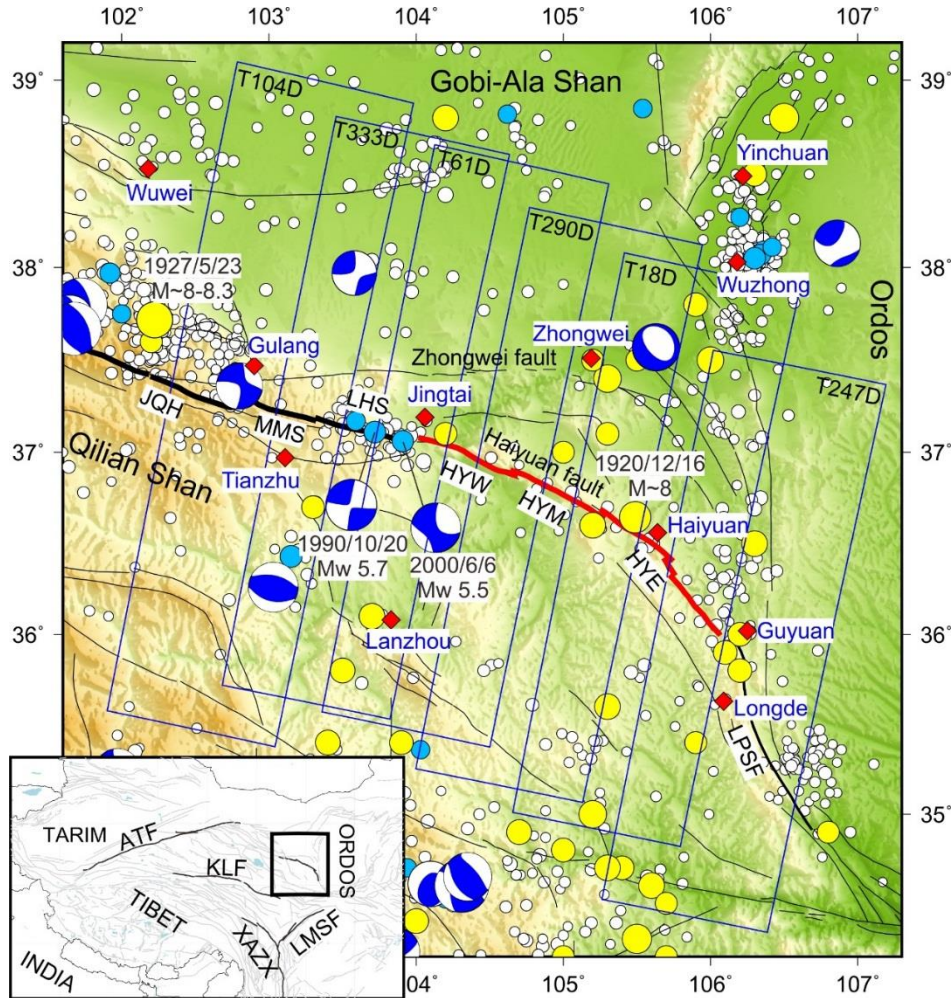


Figure 4.1. Regional tectonic map of the northeastern Tibetan Plateau. Bold red lines correspond to surface ruptures during the 1920 Haiyuan earthquake (Zhang et al., 1987). Bold black lines represent the Tianzhu seismic gap (Gaudemer et al., 1995). Thin black solid lines indicate regional major faults. Thin white circles represent earthquakes with magnitude smaller than 5.0 from the year 1970 to 2017 from China Earthquake Administration (<http://data.earthquake.cn/>). Light blue circles correspond to earthquakes with magnitude equal or greater than 5.0 between 1920 and 2017 from United States Geological Survey (USGS). Yellow circles represent historical earthquakes with magnitudes larger than 6.0 between 780 BC and 1967. Blue focal mechanism solutions ($M_w \geq 5.5$, 1976–2018) come from Global Centroid Moment Tensor (GCMT). Red diamonds show the location of main cities in northeastern Tibet. The blue polygons show the coverage of InSAR data used in this study. The inset map shows the study area. JQH: Jinqianghe fault, MMS: Maomaoshan fault, LHS: Laohushan fault, HYW: Western Haiyuan fault, HYM: Middle Haiyuan fault, HYE: Eastern Haiyuan fault, LPSF: Liupanshan fault; ATF: Altyn Tagh fault; KLF: Kunlun fault; XSHF: Xianshuihe fault; LMSF: Longmenshan fault.

To address the above issues, we use geodetic data composed of new/dense GPS velocity solution (1998–2017), long-term leveling velocity solution (1970–2012; [Hao et al., 2014](#)), and Envisat ASAR LOS map (2003–2010; [Song et al., 2019](#)) acquired along six tracks across the Haiyuan fault system. We first combined the GPS horizontal velocities and InSAR LOS displacements to investigate any creep segments along the fault system and to recover more realistic fault creep rates. We then inverted the geodetic data in order to model the spatially variable fault coupling and thus explore the potential correlation between present-day fault deformation and historical earthquake ruptures. Finally, we combined geodetic and seismic observations and modeled fault coupling to infer the physical mechanisms of the shallow creep and earthquake cycles along the Haiyuan fault system.

4.3. Geodetic data

4.3.1. GPS data and processing

The GPS data come from two sources: ① the majority comes from the Crustal Movement Observation Network of China (CMONOC I/II), including 24 continuous stations from 2010 to 2017 (of which 2 sites started to operate from 1999), 164 campaign-mode stations (conducted 5 to 10 campaigns between 1999 and 2017); ② 14 newly-built campaign-mode stations across the Haiyuan fault, near the Haiyuan County (Figure 4.2). These sites were installed in 2013 and measured every year (2013–2017) during summer in order to reduce potential biases induced by seasonal variations. We used Trimble NetR9 and Topcon NetG5 receivers with choke ring antennas to perform continuous observations of no less than 72 hours per site during each campaign.

The GAMIT/GLOBK 10.6 software (Herring et al., 2016) was used to process the GPS data. Raw pseudo-range and phase observations were first processed together with 20 International GNSS Service (IGS) stations, which are distributed around mainland China, to obtain daily loosely-constrained station coordinates and the satellite orbits parameters. We employed IGS precise orbits and earth orientation parameters, absolute antenna phase center calibrations, and the Finite Element Solution (FES) 2004 ocean tide-loading model during daily data processing (Lyard et al., 2006). The position time series of each site was carefully inspected to detect and remove outliers by using the GPS time series analysis software, PYACS (Nocquet and Trong, in preparation). Then, the daily solutions were transformed into the International Terrestrial Reference Frame 2014 (ITRF 2014) by estimating 7 transformation parameters (orientation, translation, and scale) using the 20 IGS stations. Finally, the GPS site velocities were transformed into a Eurasia-fixed reference frame using the Euler vector for Eurasia (Altamimi et al., 2017; Figure 4.2a). The least squares fitting results in an average velocity uncertainty of 0.4 mm/a. To avoid underestimation, we reweighted our sites velocity uncertainties by multiplying the standard deviations with a scale factor between the average uncertainty in Kreemer et al. (2014) and ours. The factors are 2.6 and 2.5 for the east and north components respectively, leading to uncertainties of in order of 1.0 mm/a (1-sigma).

During the GPS data span (1999–2017), several destructive earthquakes occurred in and around mainland China, including the 2001 Mw 7.8 Kokoxili earthquake, the 2008 Mw 7.9 Wenchuan earthquake and the 2011 Mw 9.0 Tohoku (Japan) earthquake. Among them, the Wenchuan earthquake and the Tohoku earthquake produced obvious coseismic deformation in northeastern Tibet (e.g., Wang et al., 2011). Therefore, we added offset parameters to the GPS position time series to correct for those coseismic deformations. Our study region is more than 500 km away from the epicenter of the Wenchuan earthquake, which generated postseismic displacements within a ~200 km area around the surface ruptures (e.g., Huang et al., 2014; Diao et al., 2018). Therefore, we did not consider the postseismic transients of the Wenchuan earthquake in our GPS data processing.

Processing results of positions and velocities relative to the stable Eurasia for all stations used in this study are presented in the supplementary material.

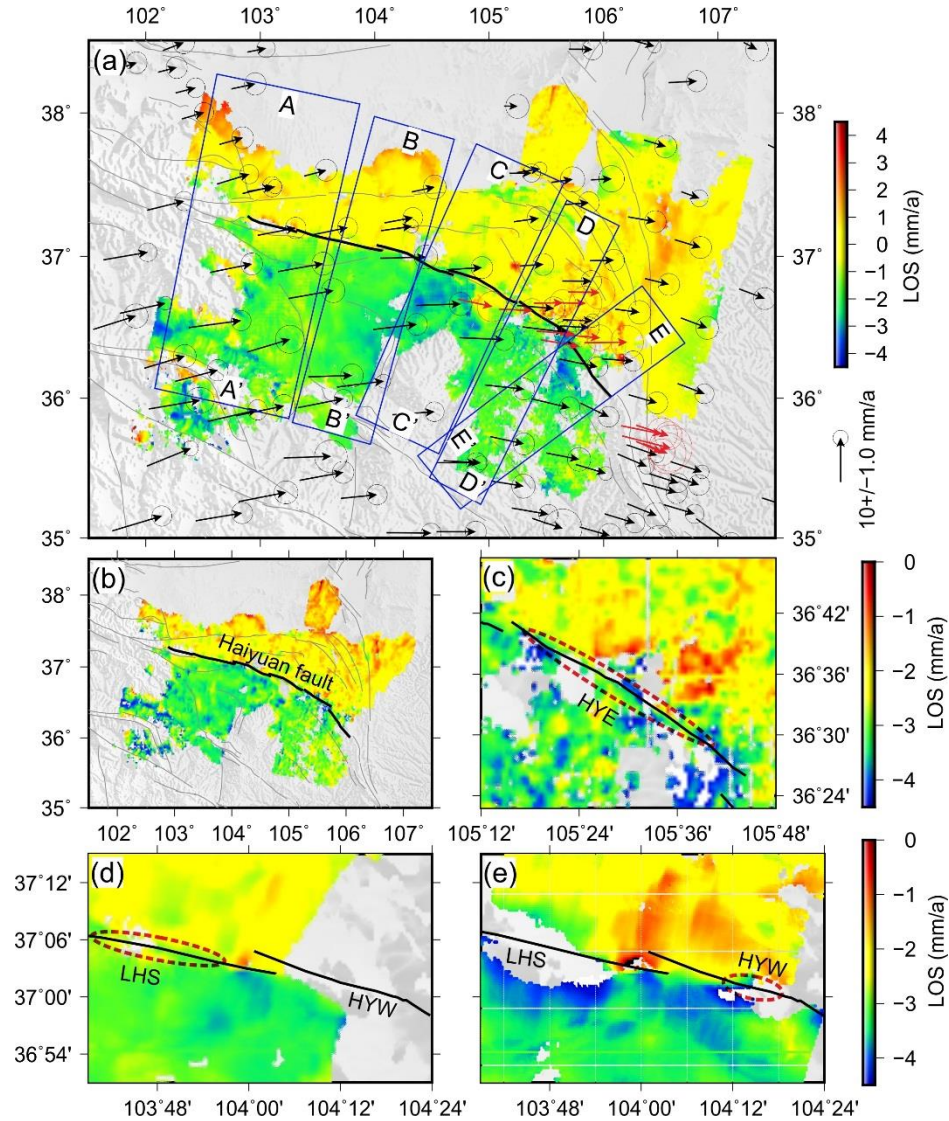


Figure 4.2. InSAR displacements and GPS velocity field in the northeastern Tibet. (a) GPS velocities with respect to the stable Eurasian plate. Arrows in red represent newly-built station velocities. Error ellipses indicate the 95% confidence levels. Blue rectangles indicate the location of GPS velocity profiles in Figure 4. Background color represent the observed InSAR displacements. (b) The InSAR displacements from the remove-restore method. (c) Enlarged view of the InSAR displacements across the HYE. (d) and (e) show the InSAR displacements across the LHS and HYW. Red dotted ellipses outline the shallow creep segments.

4.3.2. InSAR data

The six tracks of descending Envisat SAR strip-map images, spanning from 2003 to 2010, were processed by Song et al. (2019). They used the ROI_PAC software to compute interferograms (Rosen et al., 2004). During the data processing, atmospheric corrections are crucial for retrieving small ground displacements of a few millimeters per year across the Haiyuan fault system.

Tropospheric delays can be considered as the sum of a contribution of turbulent delays and a contribution from delay in a stratified troposphere. Turbulent delays are mostly spatially random and uncorrelated from one acquisition to the next. Thus, they are removed efficiently by stacking independent interferograms. Moreover, Song et al. (2019) used independent atmospheric data from the European Centre for Medium-Range Weather Forecasts (ECMWF) to simulate and correct for the stratified atmospheric delays. Subsequently, a ramp simulating any orbital linear residues was fitted and removed for each interferogram. Finally, stacking all interferograms allowed to infer the LOS rate map (Figure 4.2b).

The final LOS rate map includes contributions from horizontal and vertical deformation, and also non-tectonic spatially correlated noises. As in this study we focus on tectonics deformation, we masked InSAR data located in regions with obvious subsidence, which are related to groundwater extraction or coal mining. In the next section, we evaluate the consistency of the data sets in order to combine GPS and InSAR data.

4.3.3. Geodetic data comparison and combination

As a preliminary step, we evaluate the consistency between GPS, Levelling results (Hao et al., 2014) with InSAR LOS rate maps (Song et al., 2019). Three different approaches were used:

(1) InSAR versus 2D-GPS+leveling. Long-term leveling velocity solution comes from Hao et al. (2014), which allows to add a vertical component to the horizontal GPS velocity. The leveling benchmarks were measured according to first-order levelling standards, and a total of 2 to 7 campaigns were conducted during the period of 1970–2012. The linear rate (adjustment) was estimated under a regional reference frame, which was realized by nine GPS stations with occupations spanning 1998–2008. We show the leveling vertical velocity solution of the northeastern Tibet in Figure B.1. In practice, we first selected the leveling sites located in a 5-km radius from the GPS stations, and took leveling-derived velocity to simulate the vertical velocity of the GPS site. We then projected the 3D velocity into the InSAR LOS according to local incidence angles at each GPS sites. The InSAR data, which are located within a 1-km radius around the GPS sites, are averaged and used for comparison with the GPS+leveling projection.

(2) InSAR versus 3D-GPS. We do not estimate the GPS vertical velocities in our data processing that is because most of GPS sites were measured in campaign-mode. We instead used the GPS velocity solution (horizontal+vertical) of Liang et al. (2013) to test this approach (Figure B.2). In Liang et al.'s solution, we selected GPS sites with both horizontal and vertical velocities. Similar to the above scheme, we first projected the 3D GPS velocities into the InSAR LOS using local incidence angles, and then compare with the observed InSAR LOS values.

(3) InSAR combined with 2D-GPS. We used the remove-filter-restore method proposed by Wei et al. (2010). The basic idea of this method is to combine the long wavelength horizontal

displacements from GPS with short wavelength displacements (horizontal+potential vertical) from InSAR, and produce a LOS rate map that is free of long wavelength correlated noise, such as orbital residuals. Such method ensures that the InSAR velocities agree with the GPS at the longest wavelengths, while preserving the short-wavelength features (e.g., creeping signals) that make the InSAR contribution valuable in the near field of the fault. For our case, we want to combine 2D GPS velocity (horizontal) with the InSAR short wavelength deformation. We first removed an interpolated map of the LOS horizontal GPS velocities from the observed InSAR data, then high-pass filtered the residuals at 50 km wavelength (determined by the average spacing of GPS sites), and finally added the result back to the interpolated GPS velocity map. We used GMT *gpsgridded* approach (Sandwell and Wessel, 2016) to interpolate the GPS velocity. The final restored LOS velocity map is under the same reference frame with GPS horizontal velocity. That approach not only removes bias in the InSAR data but also potential long-wavelength vertical rates in the original InSAR LOS rate map. Small scales vertical rates might still be present in the restored InSAR LOS rate map.

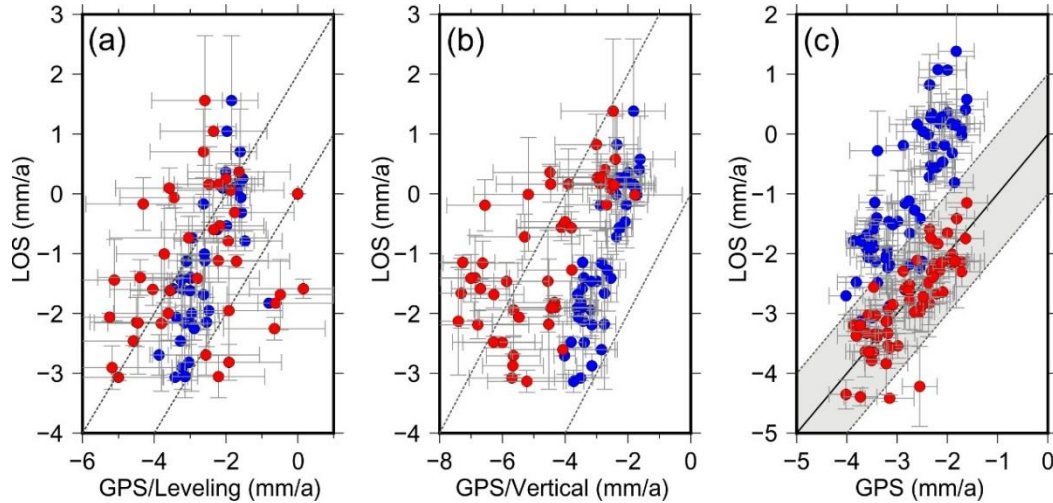


Figure 4.3. Comparisons between different geodetic dataset. (a) Observed InSAR LOS values versus observed GPS horizontal velocities projected to LOS (blue error bars). Observed InSAR LOS values versus the ‘GPS horizontal + leveling vertical’ projected to LOS (red error bars). (b) Blue error bars represent observed InSAR LOS values versus GPS horizontal velocities projected to LOS (Liang et al., 2013). Red error bars represent the observed InSAR LOS values versus ‘GPS horizontal + GPS vertical’ projected to LOS (Liang et al., 2013). (c) Blue error bars indicate observed InSAR LOS values versus observed GPS horizontal velocities projected to LOS. Red error bars represent the restored InSAR LOS values versus observed GPS horizontal velocities projected to LOS.

Results of the three approaches are shown in Figure 4.3. We see that the LOS projection of horizontal GPS velocities deviate significantly from observed InSAR LOS (Root Mean Square [RMS] of 1.9 mm/a). This indicates that systematic vertical deformation or orbital residuals exist in the InSAR LOS displacements, where the former is most likely the dominant factor. Figure 4.3a shows that adding the leveling-derived vertical velocities to form 2D GPS velocities then projected along the LOS leads to higher dispersion between GPS and InSAR (RMS=3.9 mm/a). The

discrepancy might be due to several factors: orbital residuals in InSAR, temporal variations in vertical rates over the past few decades as GPS (1999–2017), leveling (1970–2012) and InSAR (2003–2010) covers different periods, systematic errors in levelling data, or some combinations of the above factors. A similar disagreement between GPS and InSAR is also observed when using the velocity solution of [Liang et al., 2013](#) (RMS=2.3 mm/a; Figure 4.3b). The increase of scattering suggests that this originates in highly scattered GPS vertical rates.

Because of these results, the remove-filter-restore method that enforces 2D-GPS and InSAR consistency seems to be a reasonable approach (Figure 4.3c). That approach provides an overall consistency between GPS and InSAR LOS rate map at the 0.5 mm/a.

The above results indicate either complicated vertical crustal deformation in northeastern Tibet, and/or complex error structure in InSAR. Whatever, they highlight the significance to account for the vertical deformation signals in the observed InSAR LOS map. While not perfect, the restored LOS rate map is then used in our following models.

4.4. Modeling strategy

4.4.1. Interseismic horizontal GPS velocities

To investigate surface shallow creep along the Haiyuan fault system, we first analyze results along five profiles perpendicular to the faults. Profiles were selected according to the fault segmentation and GPS sites distribution, and we projected the GPS velocities into the local fault-parallel component (Figure 4.2a). We fitted a simple 2-D elastic dislocation model (Savage and Burford, 1973) to the fault parallel velocities (V_{par}) (Eq. (4-1)) for profile AA', BB', CC' and EE', to solve for slip rate (S) and locking depth (d_l). For profile DD', we also solved for the creep rate (C) and creep depth (d_2) (Eq. (4-2)) (Weertman and Weertman, 1964; Segall, 2010).

$$V_{par}(x) = \frac{S}{\pi} \tan^{-1} \left(\frac{x}{d_1} \right) + x \vartheta_{rot} + a \quad (4-1)$$

$$V_{par}(x) = \frac{S}{\pi} \tan^{-1} \left(\frac{x}{d_1} \right) + \frac{C}{\pi} \tan^{-1} \left(\frac{d_2}{x} \right) + x \vartheta_{rot} + a \quad (4-2)$$

where a is a constant, x is the perpendicular distance to the fault, and ϑ_{rot} corrects for the rotation of the Lanzhou block (south of the Haiyuan fault system) and the Alaxian block (north of the Haiyuan fault system) in the Eurasia-fixed reference frame. ϑ_{rot} is calculated for each profile by assuming that the pole of rotation is fixed at the location reported by Wang et al. (2017). A Bayesian approach was used to derive the posterior probability density function (PDF) of the model parameters (Minson et al., 2013; Nocquet, 2018), $p(\mathbf{m}|\mathbf{d})$ is defined as: $p(\mathbf{m}|\mathbf{d}) \sim p(\mathbf{m}) \exp [(\mathbf{d} - \mathbf{p})^T \mathbf{C}^{-1} (\mathbf{d} - \mathbf{p})]$, with \mathbf{d} and \mathbf{p} vectors containing the observations and model predictions, \mathbf{C}^{-1} the inverse of the covariance matrix of the data, and $p(\mathbf{m})$ the prior PDF of the model parameters. We used uniform prior distributions and took the covariance matrix as a diagonal matrix using the GPS data uncertainties. Results presented below were derived from a total of 100,000 sampling from a Markov chain using the PyMC software (Patil et al., 2010).

4.4.2. Combined GPS-InSAR inversion

In a second time, we used the restored LOS velocity data to improve the spatial resolution of the surface shallow creep along the Haiyuan fault system. We calculate the 'creep rate' based on the difference in fault-parallel velocity on each side of the fault. The velocities are taken in small boxes crossing the fault (1 km normal to the fault and 2 km along the strike). If the fault segment is creeping, the LOS data will show a step across the fault and thus the 'creep rate' should be larger than 0. Alternatively, if the fault segment is locked in surface, the LOS data will be a smoothed curve across the fault, and the 'creep rate' should be around 0 within the confidence level (e.g., Tong et al., 2018).

Apart from the surface shallow creep along the fault system, we are also interested in the interseismic coupling on the fault plane. We used the TDEFNODE program to fit the surface

geodetic data (horizontal GPS velocities and restored LOS velocities). This method assumes that the observed geodetic velocity are a result of block rotation, permanent strain rate within blocks and fault locking ([McCaffrey, 2009](#)). Interseismic backslip is applied along faults to solve for the fault coupling coefficient, a unitless parameter between 0 (fully creeping) and 1 (fully locked). The elastic block model is similar to our previous study ([Li et al., 2017](#)), except that we adopted four elastic blocks in this study (Figure B.3), and set vertical geometry for the Haiyuan fault system (patch size of 5 km along strike and 1 km along dip). Moreover, we did not introduce smoothing factors in the model to avoid smoothed fault coupling that might smear and hides some creep signals. Weight for GPS and InSAR data was set to be equal. We refer the reader to our previous study for detailed block modeling information ([Li et al., 2017](#)).

4.5. Results

4.5.1. GPS velocity profile fitting

GPS velocity profile modelling results are shown in Figure 4.4. We obtained far-field relative motion ranging of 5.4 ± 1.1 decreasing eastward to 2.7 ± 1.2 mm/a., consistently with previous studies (e.g., Li et al., 2009; Li et al., 2017). The PDF distribution highlights two features: the far field relative motion is resolved at 1 mm/a level, whereas the fault locking depths are marginally resolved due to sparse distribution of GPS sites near the fault. Despite that, GPS velocities (AA', CC', EE') seem to confirm the fault segments are locked to surface. The DD' profile shows an obvious velocity offset (~ 2 mm/a) across the eastern Haiyuan fault, near the Haiyuan County. Two GPS sites, on both sides of the fault, are only 1 km from the fault; consequently, we interpret the velocity offset as reflecting shallow creep along this segment. The creep rate is estimated to be 2.2 ± 1.8 mm/a, accounting for $\sim 55\%$ of the relative far field motion. Note that the BB' profile cross the Laohushan creep segment that was previously reported (Cavalié et al., 2008; Jolivet et al., 2012, 2013; Daout et al., 2016), our GPS network is too sparse to capture such signal.

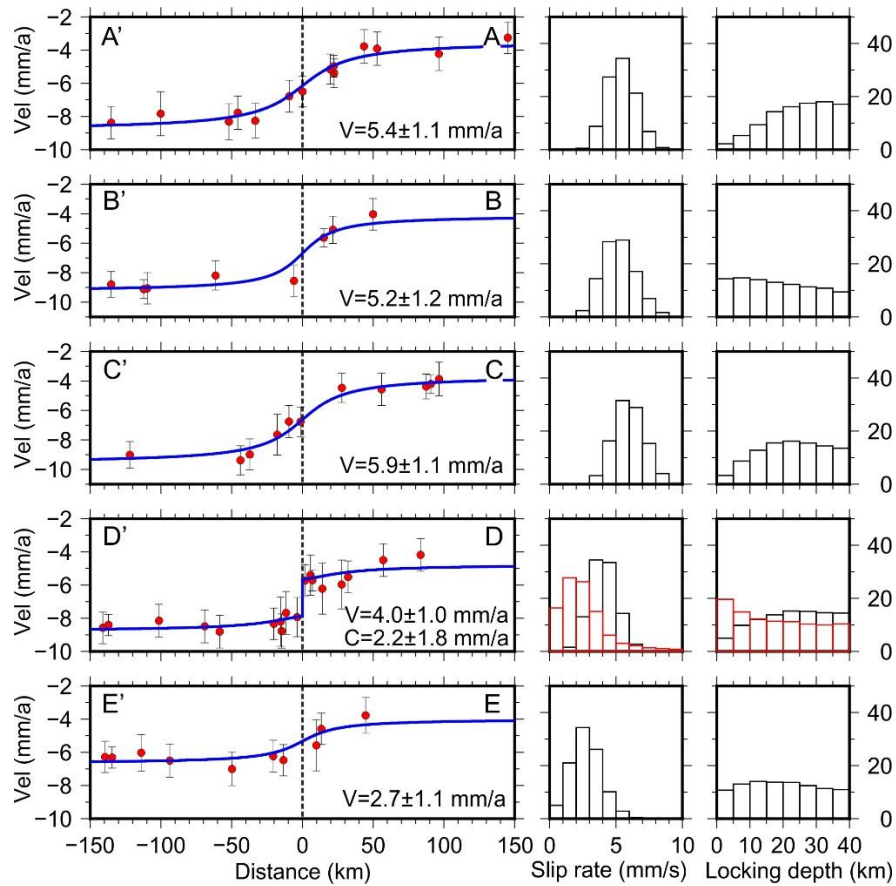


Figure 4.4. AA'-EE' show the observed and 2D model prediction for fault-parallel GPS velocities across the Haiyuan fault. Right panels show the posterior probability density function (PDF) of the model parameters. Red histograms represent the PDF of creep depth and creep rate.

4.5.2. Fault creep from the restored InSAR

The ‘creep rate’ results, calculated based on the difference of fault-parallel velocity (restored LOS rate map) on opposite sides of the Haiyuan fault system, are shown in Figure 4.5b. Creep rate results show 4 main features: ① a ~30 km-long shallow creep segment (~103.6°E–103.9°E) along the eastern Laohushan fault, with a rate of ~2–5 mm/a (Figure 4.5b, Figure 4.2d); ② significant velocity offsets across the junction of Laohushan fault and the western Haiyuan fault (~104°E), that are not confidently interpreted as shallow creep owing to the existence of the Jingtai pull-apart basin (Figure 4.5a, 4.5b); ③ the apparent velocity offsets across the western Haiyuan fault (~104.2°E–104.3°E), with shallow creep rates of ~3–5 mm/a and extend 10 km along strike (Figure 4.5b). We note a local subsidence zone located ~3–7 km south of the fault (Figure 4.2e), but it do not affect our result; ④ the ~1–3 mm/a velocity offsets across the eastern Haiyuan fault along a 43 km-long segment (~105.3°E–105.7°E; Figure 4.2c; Figure 4.5b), which we also interpret as shallow creep and in agreement with the horizontal fault-parallel GPS velocities (Figure 4.4-DD’).

In short, our results confirms the pre-identified creep segment on the Laohushan fault; moreover, we identify two additional creep segments along the Haiyuan fault, with creep rates ranging from 1 to 5 mm/a.

4.5.3. Block modeling of the GPS and restored InSAR

The block model results are shown in Figure 4.5b, 4.5d. The Haiyuan fault system is dominated by the left-lateral strike-slip motion estimated at 4–5 mm/a and decreasing eastwards (Figure 4.5b; Figure B.4). Fault normal slip rates were estimated at 0–0.5 mm/a (Figure B.4), which take less than 10% of the fault motion. The estimated slip rates are consistent with both geological (e.g., Li et al., 2009) and geodetic (e.g., Li et al., 2017, 2018) studies. Our geodetic data inversion highlights a highly heterogeneous fault coupling along the fault system, where low coupling values are found along several segments (Figure 4.5d). There are four potential locked asperities separated by three shallow locked (creep) segments: ① the asperity on the Laohushan fault, with a width of at least 50 km and locking depth of approximate 20 km; ② the HYW asperity is locked to ~15 km, extending ~40 km laterally; ③ the HYM asperity, which is more superficial (the locking depth is less than 10 km but it extends ~70 km along fault strike); ④ finally, the HYE asperity presents a high coupling patch between 5 and 25 km at depth, and extends laterally along ~40 km. We show the block internal strain rates and GPS residuals in Figure B.3 and Figure B.5 respectively. Further discussions of the shallow creep and locked asperities are present below.

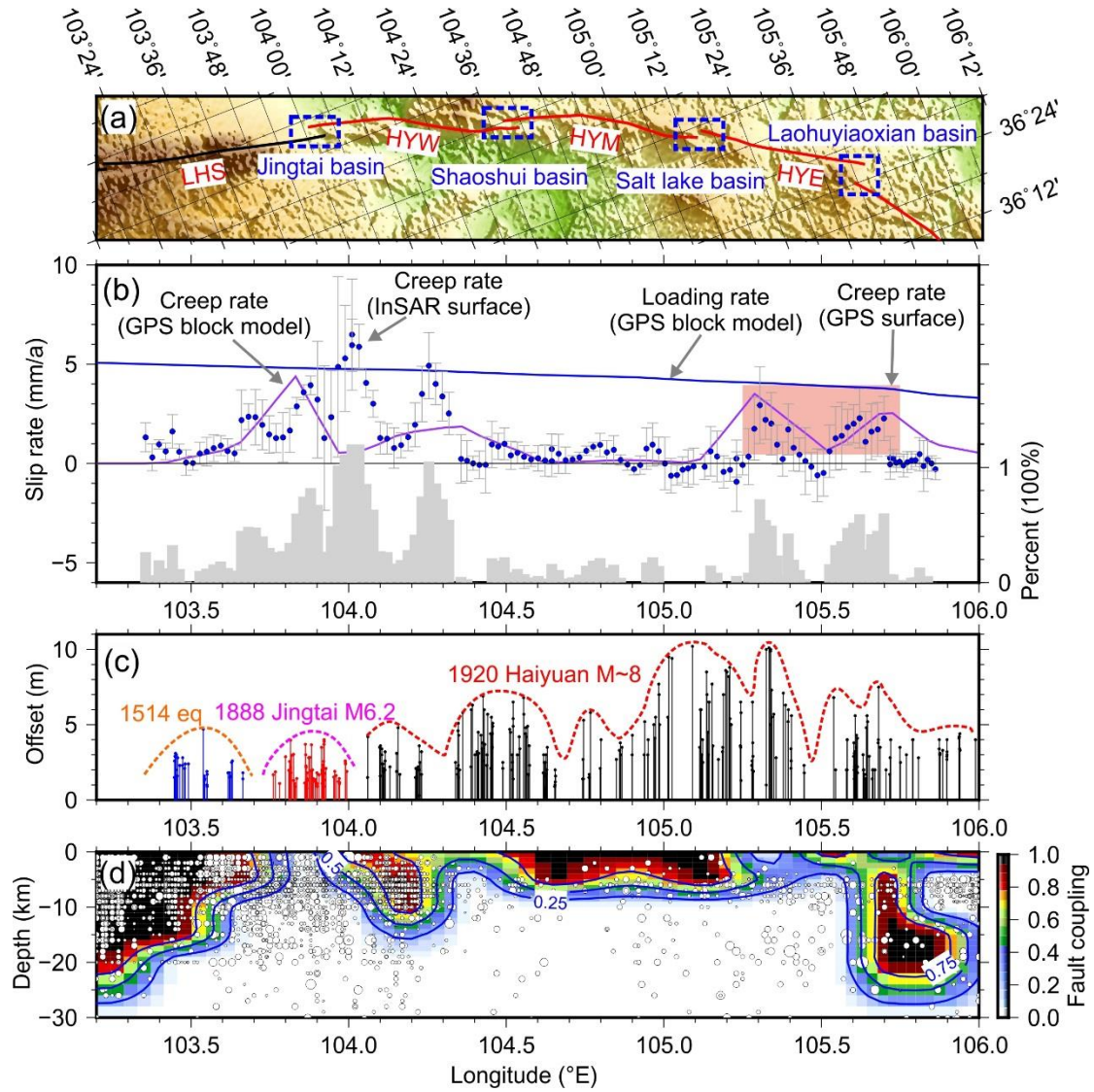


Figure 4.5. (a) Tectonic map across the Haiyuan fault. Blue dotted rectangles show the pull-apart basins along the fault. (b) ‘Creep rate’ along the Haiyuan fault. Error bars in blue represent the calculated ‘creep rate’ from the restored InSAR data. Light red background show the inverted creep rate from fault-parallel GPS velocities. The blue line corresponds to the block model-predicted fault slip rate, and the purple line show the fault creep rate from our block model. Gray histogram shows the creep rate (InSAR surface) as a percentage of the far-field loading rate (GPS block model). (c) Black, red, and blue vertical lines represent coseismic offset across the Haiyuan fault induced by the 1920, 1888, and 1514 earthquakes, respectively. Dotted lines indicate the approximate displacements pattern. (d) Fault coupling along the Haiyuan fault. White dots indicate microseism ($M \geq 2$) from 1965 to 2019 (<http://data.earthquake.cn/>). Blue lines show fault coupling contours.

4.6. Discussions

4.6.1. Shallow creep segments along the Laohushan fault

The Laohushan creep segment has been intensely studied by time-series stacking InSAR observations (e.g., Cavalié et al., 2008; Jolivet et al., 2012, 2013; Daout et al., 2016). Cavalié et al. (2008) first reported shallow creep along the Laohushan fault using European Remote Sensing (ERS) SAR data spanning 1993–1998. Their results show fault slip rate of 5 mm/a beneath 15 km, and creep rate of 11 mm/a between 2 and 7 km. Subsequently, Jolivet et al. (2012, 2013) used the Envisat SAR data (2003–2009 period) to show that the Laohushan fault creeps at a mean rate of 5 ± 1 mm/a (maximum rate of 8 ± 2 mm/a) and concentrated between 5 and 15 km depth, and extending 35 km laterally. Recently, Daout et al. (2016) obtained similar results by processing SAR data spanning the 2001–2011 period; they found a fault loading rate of 5.6 mm/a and a creep rate of 4.6 mm/a between 0.5 km and 24 km depth. Our results show minor differences with those above in creep rate, creeping depth and length. Indeed, the ~ 2 –5 mm/a creep rate (from our result; Figure 4.5b) is consistent with Jolivet et al. (2012, 2013) and Daout et al. (2016), but smaller than that of Cavalié et al. (2008). A difference is that in our results, creep occurs almost along the whole seismogenic zone (0–30 km) (Figure 4.5d), whereas only partial of the seismogenic zone is creeping in results of Cavalié et al. (2008) and Jolivet et al. (2012, 2013). Finally, results find shallow creep segment extends ~ 30 km laterally in our results (Figure 4.5b), a length slightly shorter than reported by Jolivet et al. (2012).

The apparent velocity offset across the junction of Laohushan fault and the western Haiyuan fault ($\sim 104^\circ\text{E}$; Figure 4.5b) is most probably related to the subsidence of the Jingtai pull-apart basin (Institute of Geology, State Seismological Bureau, 1990). Consequently, we do not interpret the velocity offsets as related to shallow fault creep. Note that we have masked the InSAR points located within the Jingtai basin in our block model inversion.

4.6.2. Mechanism of shallow fault creep along the Laohushan fault

Two mechanisms have been proposed to explain the Laohushan creep. Jolivet et al. (2013) proposed that the fault creep is reflects a velocity strengthening regime at shallow depths along the fault. Therefore, they suggested that the creeping segment may act as a persistent barrier to earthquake propagation. On the other hand, Chen et al. (2018) proposed that the shallow creep along the Laohushan fault might be the afterslip following the 2000 Jingtai Mw 5.5 earthquake and/or in response to the 1920 M \sim 8 Haiyuan earthquake rupture, and would thus reflect a transient behavior.

Our results show creep accounts for ~ 40 –80% of the loading rate (Figure 4.5b). Thus, the remaining slip deficit might be released partially by the continuous ruptures of small asperities indicated by a high density of small earthquakes (Figure 4.5d) with occasional moderate-size events

as the 1888 M 6.2 earthquake and the 2000 Mw 5.5 earthquake might be such cases. Besides, paleoearthquake investigation identified at least two earthquakes (the first one occurred in 143 or 374 A.D., and the second one in 1902 A.D.) that ruptured the whole Laohushan fault (Liu-Zeng et al., 2007; Chen et al., 2018). This observation suggests that the Laohushan creeping segment experienced seismic ruptures and hence did not act systematically as a persistent barrier as it has been suggested (Jolivet et al., 2013).

Considering as Chen et al. (2018) suggest that surface creep is mostly afterslip following the 2000 Mw 5.5 earthquake is unlikely. Indeed, InSAR observations during the 1993–1998 period reported the existence of shallow creep at a rate (~ 11 mm/a; Cavalié et al., 2008) even larger than during the 2003–2011 period (~ 5 – 8 mm/a; Jolivet et al., 2012, 2013; Daout et al., 2016).

Limited by the observation time span, we cannot rule out the possibilities that the Laohushan creep been activated by the 1920 M ~ 8 Haiyuan earthquake that occurred immediately to the east of it, or related to the afterslip of the 1920 event.

4.6.3. The correlation between fault creep and the M ~ 8 1920 Haiyuan earthquake

Our results identify segments with shallow creep on HYW ($\sim 104.2^\circ\text{E}$ – 104.3°E) and HYE ($\sim 105.3^\circ\text{E}$ – 105.7°E ; Figure 4.5b), independently in InSAR and block modelling results. InSAR rates show steep gradient across HYW and HYE (Figure 4.2c, 4.2e), implying creep motion in the seismogenic zone, while coupling inversion find surface slip rate being about half of the relative far field motion (Figure 4.5d). Along HYW, we note differences between the InSAR-derived creep rate and the block model-derived creep rate (Figure 4.5b). This discrepancy could be due to the block model that might smear and mask some more localized creep signals. Along HYE, both GPS and InSAR velocities show apparent gradient with a value of 1–3 mm/a (Figure 4.2c; Figure 4.4–DD'), which is larger than the geodetic velocity uncertainties. Consequently, we can rule out that the velocity gradient is reflecting noise in the data.

In order to investigate the mechanisms of shallow fault creeps on the Haiyuan fault and to discuss their roles in earthquake ruptures, Figure 4.5c shows the coseismic surface offsets associated with the 1920 M ~ 8 Haiyuan earthquake (Ren et al., 2016). We first notice that pull-apart basins (Figure 4.5a) correspond well to segments with relatively small coseismic surface offsets, which is expected. Besides, we notice that HYW creep segment ($\sim 104.2^\circ\text{E}$ – 104.3°E) shows a correlation with lower coseismic surface offset. Despite the HYE creep segment ($\sim 105.3^\circ\text{E}$ – 105.7°E) only partially overlaps a small coseismic offset segment ($\sim 105.4^\circ\text{E}$ – 105.6°E), coseismic offsets decreased drastically across the creeping segment. Although not a strict correspondence, the above comparison seems to show that there might be a correlation between present-day shallow creep and the 1920 Haiyuan earthquake.

Nonetheless, both present-day creeping segments are located along the surface rupture trace

from the M~8 1920 earthquake. They experienced large coseismic surface offset with 3 m for the HYW and 3 to 10 m for the HYE respectively. This observation suggests that either the M~8 1920 earthquake was able to cross pre-existing creeping segments or that large earthquakes show heterogeneous relocking, with creep lasting decades along some parts of the rupture. In the following, I discuss the two alternative views.

Considering the shallow creeps (HYW, HYE) as being the long-lasting afterslip of the 1920 M~8 Haiyuan earthquake. We present a simple calculation of the coseismic slip deficit to argue the inference. The basic idea is that coseismic slip of the M~8 1920 Haiyuan did not change dramatically over a short distance (or on one segment). Along the fault distance, the 1920 earthquake resulted in average coseismic offsets of ~2.6 m, ~2.0 m and ~3.6 m in 104.1°E–104.2°E, 104.2°E–104.3°E and 104.3°E–104.4°E respectively (Figure 4.5c), thus leaving ~1.1 m coseismic surface slip deficit on the HYW creep segment. Similarly, we got average coseismic offsets of ~5.1 m, ~2.9 m and ~3.1 m in 105.2°E–105.3°E, 105.3°E–105.7°E and 105.7°E–105.8°E respectively (Figure 4.5c), and calculated ~1.2 m coseismic surface slip deficit on the HYE creep segment. Previous studies show 3–18% reduction in slip near the surface due to shallow slip deficit for strike-slip earthquakes ($M_w > 7$; e.g., Xu et al., 2016). Take the maximum, we expect ~1.3 m and ~1.4 m coseismic slip deficit on the HYW and HYE creep segments respectively. We consider is it possible for afterslip releasing such amount of slip deficit. We note that among well documented strike-slip earthquakes, the Mw 7.6 1999 Chi-Chi earthquake released maximum slip of 0.5 m in the 15 months following the main shock (e.g., Yu et al., 2003). The Mw 6 2004 Parkfield earthquake generated afterslips with magnitudes 0.1–0.15 m in the first 2 years (e.g., Freed, 2007). Perfettini and Avouac (2007) show as much as 1.4 m afterslip on the fault plane 6 years after the Mw 7.3 1992 Landers earthquake. More surprisingly, up to 2–3.8 m of afterslip was inferred during 6.5 years following the 1999 Izmit-Düzce earthquake sequence ($M=7.4$ and $M=7.2$; Ergintav et al., 2009). Consequently, we consider our above hypothesis is possible.

Here, the most intriguing issue is what kind of mechanism controls the afterslip lasting for about 100 years. Published studies show that the afterslip induced by the 1944 Mw 7.4 Bolu/Gerede earthquake on the Ismetpasa segment, North Anatolian Fault, continued probably up to 50–70 year after the earthquake (e.g., Cakir et al., 2005; Ozener et al., 2013; Cetin et al., 2014). For our case, it might be the frictional nature results in the postseismic afterslip on the Haiyuan fault has much longer decay time than the afterslips following regular earthquakes.

Alternatively, we consider the shallow creeps (HYW, HYE) being persistent, meanwhile, allowing earthquake rupture to propagate and generate surface offsets. Indeed, both laboratory experiments (Kohli et al., 2011) and numerical simulations (Weng and Ampuero, 2019) show that aseismic creep switch to seismic fault behavior is possible (Harris, 2017). In this case, we note that ~1 m and ~1.7 m coseismic offset decrease after the rupture (1920 Haiyuan earthquake) propagated though the HYW and HYE creep segments respectively (Figure 4.5c), this might attribute to the

fact that creeping regions could absorb/reduce rupture energy.

Currently, limited by observational data, we are not able to distinguish between the above two hypotheses. More geodetic observations, with long sequence and high spatial resolution, are needed in the future. Meanwhile, we know little about the creep mechanisms. Previous studies (e.g., [Avouac, 2015](#); [Harris, 2017](#)) have shown that frictional resistance of specific rock types, chemical reactions, dilation of dry rocks, elevated pore pressure, elevated temperatures, fault geometry, or combinations of these factors are responsible for fault creep. But those factors have been rarely studied along the Haiyuan fault system.

4.6.4. Earthquake scenarios along the Haiyuan fault system

In this section, we focus on the implication of present-day fault coupling for future earthquake scenarios along the Haiyuan fault system. We first calculate the seismic moment accumulated at the identified asperities. Figure 4.5d shows the fault coupling inferred from our block model and the microseismicity that occurred between 1965 and 2019, selected within 20 km on either side of the Haiyuan fault system. We note that most of the microseismicity occurs around the transition zone between locked and freely slipping regions, suggesting that the microseismicity is triggered by the higher slip rate gradient (e.g., [Stevens and Avouac, 2015](#)). However, we also observe high microseismicity activity on the Laohushan fault and the western Haiyuan fault that are highly locked patches. This implies that either the high coupling ratio is an overestimation or the coupling ratios of these segments are increasing to higher values.

Assuming that present-day fault coupling is representative of the locking pattern of the fault system since the 1920 M~8 Haiyuan earthquake, we estimate the seismic moment accumulation rates of 2.36×10^{16} N·m/a, 1.27×10^{16} N·m/a, 9.14×10^{15} N·m/a and 2.03×10^{16} N·m/a along the Laoshushan, HYW, HYM, and HYE fault segments, respectively. If we consider that the 1092 large earthquake ($M > 8$; [Liu-Zeng et al., 2007](#)), which might have ruptured the whole Haiyuan fault system, reset all the elastic strain on the Laohushan fault and assuming a M_w 6.0–6.5 for the 1514 earthquake, we find a total cumulated seismic moments of 1.56×10^{19} – 2.08×10^{19} N·m on the Laohushan fault. This implies potential seismic hazard M_w 6.8–6.9 on the Laohushan fault. Similarly, if we consider that the 1920 M~8 Haiyuan earthquake released all elastic strain on the Haiyuan fault, we calculate the moment deficit of 1.25×10^{18} N·m, 9.05×10^{17} N·m and 2.0×10^{18} N·m on the HYW, HYM and HYE, corresponding to earthquakes of M_w 6.0, M_w 5.9 and M_w 6.2 respectively. The seismic potential might be overestimated, as the fault coupling changes over time. Despite this limitation, the current results emphasize a moderate seismic hazard on the eastern Haiyuan fault (the Haiyuan County is nearby) even just 100 years after the 1920 M~8 Haiyuan earthquake.

As discussed above, shallow creep segments and/or pull-apart basins along the Haiyuan fault system are likely acting as barriers for earthquake rupture propagation. Consequently, the present-

day fault coupling highlights potential segmentation or partial failure of future earthquakes on the Haiyuan fault system. Specifically, the Haiyuan fault could host earthquakes with magnitude M_w ranging from 5.9 to 6.3 depending on whether asperities break alone or as a single event. Actually, paleoseismology studies have reported moderate earthquakes ($M \sim 6-7$) along the Haiyuan fault, and suggested that the Haiyuan fault did not always break as one large multi-segment rupture event (e.g., [Liu-Zeng et al., 2015](#)). Should we assume the three asperities (HYW, HYM and HYE) are fully locked down to 15 km, they are capable of generating earthquakes with magnitudes about M_w 7.3–7.7 every thousand years. The 1920 Haiyuan $M \sim 8$ earthquake, which broke multiple segments, might be such a large but rare event that occurred on the fault. This raises more challenges for paleoseismology and geomorphology studies, especially in identifying and distinguishing the surface ruptures and offsets induced by moderate-small earthquakes; and in turn, bring more uncertainties in assessing earthquake hazard and determining earthquake recurrence (e.g., [Liu-Zeng et al., 2007](#)).

4.7. Conclusions

We processed the GPS data (CMONOC+14 new GPS benchmarks) measured in 1999–2017 in northeastern Tibet. Complemented by the leveling measurements (1970–2012) and the LOS ground velocity map derived from six tracks of descending Envisat/ASAR (2003–2010), we obtained a dense interseismic velocity field in northeastern Tibet. Comparisons between GPS, InSAR and Leveling highlight either long-wavelength systematic errors or vertical deformation in InSAR and levelling data. As a best choice, we combined horizontal GPS with high-pass filtered InSAR data to obtain a continuous LOS rate map around the Haiyuan fault system.

GPS and the combined LOS rate map show three creeping segments separating four locked asperities along the Haiyuan fault system. The previously identified Laohushan segment ($\sim 103.6^{\circ}\text{E}$ – 103.9°E) creeps at a rate of ~ 2 – 5 mm/a and extends ~ 30 km long. Two additional creep segments (HYW and HYE) were identified, both ruptured in the $M \sim 8$ 1920 Haiyuan earthquake. The HYW ($\sim 104.2^{\circ}\text{E}$ – 104.3°E) creeps at a rate of 3 – 5 mm/a, limiting to 10 km along the fault strike. The HYE ($\sim 105.3^{\circ}\text{E}$ – 105.7°E) creeps at 2 – 4 mm/a and extends 43 km long laterally. Up to 3 m and 3 – 10 m surface rupture along the HYW and HYE creep segments respectively suggest that the creeps either be the long-lasting afterslip of the $M \sim 8$ 1920 Haiyuan earthquake, or persistent creep. The former case implies heterogeneous relocking on the Haiyuan fault. The latter case suggests that large rupture can cross previously existing creeping segments.

In calculating the seismic moment deficit along the Haiyuan fault system, we show that the Laohushan fault is capable of an M_w 6.8 – 6.9 earthquake even though its easternmost is creeping. The Haiyuan fault could generate an M_w 5.9 – 6.3 earthquake depending on whether asperities break as isolated seismic events or cooperate to produce a larger rupture. Present-day fault coupling along the Haiyuan fault system highlights segmentation or partial failure of the fault during earthquakes.

Acknowledgements

We are grateful to all colleagues who participated in the GPS stations construction and measurements. Thanks to all the postgraduates who engaged in the fieldwork over the past few years. CMONOC GPS data are provided by the National Earthquake Infrastructure Service, China Earthquake Administration. This work is supported by the National Natural Science Foundation of China (Grant No. 41631073). Yanchuan Li was financially supported by the China Earthquake Administration and the China Scholarship Council. Figures were generated using the Generic Mapping Tools (GMT) software ([Wessel et al, 2013](#)). Data supporting the conclusions of this study are presented in the supplementary material.

4.8. References

- Altamimi, Z., Métivier, L., Rebischung, P., Rouby, H., Collilieux, X., 2017. ITRF2014 plate motion model. *Geophys. J. Int.* 209, 1906–1912.
- Avouac, J. P., 2015. From geodetic imaging of seismic and aseismic fault slip to dynamic modeling of the seismic cycle. *Annu. Rev. Earth Pl. Sc.* 43, 233–271.
- Barnhart, W. D., 2016. Fault creep rates of the Chaman fault (Afghanistan and Pakistan) inferred from InSAR. *J. Geophys. Res., Solid Earth* 122, 372–386.
- Bilham, R., Ozener, H., Mencin, D., Dogru, A., Ergintav, S., Cakir, Z., Aytun, A., Aktug, B., Yilmaz, O., Johnson, W., Mattioli, G., 2016. Surface creep on the North Anatolian fault at Ismetpasa, Turkey, 1944–2016. *J. Geophys. Res., Solid Earth* 121, 7409–7431.
- Bilham, R., Suszek, N., Pinkney, S., 2004. California creepmeters. *Seismol. Res. Lett.* 75(4), 481–492.
- Bürgmann, R., Schmidt, D., Nadeau, R. M., d'Alessio, M., Fielding, E., Manaker, D., McEvilly, T. V., Murray, M. H., 2000. Earthquake potential along the northern Hayward fault, California. *Science* 289, 1178–1182.
- Cakir, Z., Akoglu, A. M., Belabbes, S., Ergintav, S., Meghraoui, M., 2005. Creeping along the Ismetpasa section of the North Anatolian fault (Western Turkey): Rate and extent from InSAR. *Earth Planet. Sci. Lett.* 238, 225–234.
- Cavalié, O., Lasserre, C., Doin, M. P., Peltzer, G., Sun, J., Xu, X., Shen, Z. -K., 2008. Measurement of interseismic strain across the Haiyuan fault (Gansu, China), by InSAR. *Earth Planet. Sci. Lett.* 275, 246–257.
- Cetin, E., Cakir, Z., Meghraoui, M., Ergintav, S., Akoglu, A. M., 2014. Extent and distribution of aseismic slip on the Ismetpaşa segment of the North Anatolian Fault (Turkey) from Persistent Scatterer InSAR. *Geochem. Geophys. Geosy.* 15, 2883–2894.
- Chaussard, E., Bürgmann, R., Fattahi, H., Johnson, C. W., Nadeau, R., Taira, T., Johanson, I., 2015. Interseismic coupling and refined earthquake potential on the Hayward-Calaveras fault zone. *J. Geophys. Res., Solid Earth* 120(12), 8570–8590.
- Chen, K. H., Nadeau, R. M., Rau, R. J., 2008. Characteristic repeating earthquakes in an arc-continent collision boundary zone: The Chihshang fault of eastern Taiwan. *Earth Planet. Sci. Lett.* 276, 262–272.
- Chen, T., Liu-Zeng, J., Shao, Y., Zhang, P., Oskin, M. E., Lei, Q., Li, Z., 2018. Geomorphic offsets along the creeping Laohu Shan section of the Haiyuan fault, northern Tibetan Plateau. *Geosphere* 14, 1165–1186.
- Daout, S., Jolivet, R., Lasserre, C., Doin, M. P., Barbot, S., Tapponnier, P., Peltzer, G., Socquet, A., Sun, J., 2016. Along-strike variations of the partitioning of convergence across the Haiyuan fault system detected by InSAR. *Geophys. J. Int.* 205, 536–547.
- Deng, Q., Chen, S., Song, F., Zhu, S., Wang, Y., Zhang, W., Jiao, D., Burchfiel, B., Molnar, P., Royden, L., Zhang, P., 1986. Variations in the geometry and amount of slip on the Haiyuan (Nanxihaushan) fault zone, China, and the surface rupture of the 1920 Haiyuan earthquake. *Earthquake Source Mechanics, Geophys. Monogr. Ser.* 37, 169–182.
- Diao, F., Wang, R., Wang, Y., Xiong, X., Walter, T. R., 2018. Fault behavior and lower crustal rheology inferred from the first seven years of postseismic GPS data after the 2008 Wenchuan

- earthquake. *Earth Planet. Sci. Lett.* 495, 202–212.
- Ergintav, S., McClusky, S., Hearn, E., Reilinger, R., Cakmak, R., Herring, T., Ozener, H., Lenk, O., Tari, E., 2009. Seven years of postseismic deformation following the 1999, M=7.4 and M=7.2, Izmit-Düzce, Turkey earthquake sequence, *J. Geophys. Res., Solid Earth* 114, B07403.
- Freed, A. M., 2007. Afterslip (and only afterslip) following the 2004 Parkfield, California, earthquake. *Geophys. Res. Lett.* 34, L06312.
- Gan, W., Zhang, P., Shen, Z. K., Niu, Z., Wang, M., Wan, Y., Zhou, D., Cheng, J., 2007. Present-day crustal motion within the Tibetan Plateau inferred from GPS measurements. *J. Geophys. Res., Solid Earth* 112.
- Gaudemer, Y., Tapponnier, P., Meyer, B., Peltzer, G., Guo, S., Chen, Z., Dai, H., & Cifuentes, I., 1995. Partitioning of crustal slip between linked, active faults in the eastern Qilian Shan, and evidence for a major seismic gap, the 'Tianzhu gap', on the western Haiyuan Fault, Gansu (China). *Geophys. J. Int.* 120, 599–645.
- Gratier, J. P., Richard, J., Renard, F., Mittempergher, S., Doan, M. L., Di Toro, G., Hadizadeh, J., Boullier, A. M., 2011. Aseismic sliding of active faults by pressure solution creep: Evidence from the San Andreas Fault Observatory at Depth. *Geology* 39, 1131–1134.
- Hao, M., Wang, Q., Shen, Z., Cui, D., Ji, L., Li, Y., Qin, S., 2014. Present day crustal vertical movement inferred from precise leveling data in eastern margin of Tibetan Plateau. *Tectonophysics* 632, 281–292.
- Harris, R. A., 2017. Large earthquakes and creeping faults. *Rev. Geophys.* 55, 169–198.
- Herring, T. A., R. W. King, M. A. Floyd, S. C. McCluskey., 2016. Introduction to GAMIT/GLOBK, Release 10.6, Massachusetts Institute of Technology, http://geoweb.mit.edu/~simon/gtgt/Intro_GG.pdf
- Huang, M. H., Bürgmann, R., Freed, A. M., 2014. Probing the lithospheric rheology across the eastern margin of the Tibetan Plateau. *Earth Planet. Sci. Lett.* 396, 88–96.
- Institute of Geology, State Seismological Bureau, 1990. The Haiyuan Active Fault, *Seismol. Press*, Beijing.
- Jolivet, R., Lasserre, C., Doin, M. P., Guillaso, S., Peltzer, G., Dailu, R., Sun, J., Shen, Z. -K., Xu, X., 2012. Shallow creep on the Haiyuan fault (Gansu, China) revealed by SAR interferometry. *J. Geophys. Res., Solid Earth* 117.
- Jolivet, R., Lasserre, C., Doin, M. P., Peltzer, G., Avouac, J. P., Sun, J., Dailu, R., 2013. Spatio-temporal evolution of aseismic slip along the Haiyuan fault, China: Implications for fault frictional properties. *Earth Planet. Sci. Lett.* 377, 23–33.
- Jolivet, R., Simons, M., Agram, P. S., Duputel, Z., Shen, Z. -K., 2015. Aseismic slip and seismogenic coupling along the central San Andreas Fault. *Geophys. Res. Lett.* 42, 297–306.
- Karabacak, V., Altunel, E., Cakir, Z., 2011. Monitoring aseismic surface creep along the North Anatolian Fault (Turkey) using ground-based LIDAR. *Earth Planet. Sci. Lett.* 304, 64–70.
- Kohli, A. H., D. L. Goldsby, G. Hirth, T. Tullis, 2011. Flash weakening of serpentinite at near-seismic slip rates. *J. Geophys. Res.* 116, B03202.
- Kreemer, C., Blewitt, G., Klein, E. C., 2014. A geodetic plate motion and Global Strain Rate Model. *Geochem. Geophys. Geosy.* 15, 3849–3889.
- Lee, J. C., Angelier, J., Chu, H. T., Hu, J. C., Jeng, F. S., Rau, R. J., 2003. Active fault creep variations at Chihshang, Taiwan, revealed by creep meter monitoring, 1998–2001. *J. Geophys. Res., Solid Earth* 108.

- Li, C., Zhang, P. Z., Yin, J., Min, W., 2009. Late Quaternary left-lateral slip rate of the Haiyuan fault, northeastern margin of the Tibetan Plateau. *Tectonics* 28, TC5010.
- Li, Y., Liu, M., Wang, Q., Cui, D., 2018. Present-day crustal deformation and strain transfer in northeastern Tibetan Plateau. *Earth Planet. Sci. Lett.* 487, 79–189.
- Li, Y., Shan, X., Qu, C., Wang, Z., 2016. Fault locking and slip rate deficit of the Haiyuan-Liupanshan fault zone in the northeastern margin of the Tibetan Plateau. *J. Geod.* 102, 47–57.
- Li, Y., Shan, X., Qu, C., Zhang, Y., Song, X., Jiang, Y., Zhang, G., Nocquet, J. M., Gong, W., Gan, W., Wang, C., 2017. Elastic block and strain modeling of GPS data around the Haiyuan-Liupanshan fault, northeastern Tibetan Plateau. *J. Asian Earth Sci.* 150, 87–97.
- Liang, S., Gan, W., Shen, C., Xiao, G., Liu, J., Chen, W., Ding, X., Zhou, D., 2013. Three-dimensional velocity field of present-day crustal motion of the Tibetan Plateau derived from GPS measurements. *J. Geophys. Res., Solid Earth* 118, 5722–5732.
- Lienkaemper, J. J., Barry, G. R., Smith, F. E., Mello, J. D., McFarland, F. S., 2013. The Greenville fault: preliminary estimates of its long-term creep rate and seismic potential. *Bull. Seismol. Soc. Am.* 103, 2729–2738.
- Lindsey, E. O., Fialko, Y., 2016. Geodetic constraints on frictional properties and earthquake hazard in the Imperial Valley, Southern California. *J. Geophys. Res., Solid Earth* 121, 1097–1113.
- Lindsey, E. O., Fialko, Y., Bock, Y., Sandwell, D. T., Bilham, R., 2014. Localized and distributed creep along the southern San Andreas Fault. *J. Geophys. Res., Solid Earth* 119, 7909–7922.
- Liu-Zeng, J., Klinger, Y., Xu, X., Lasserre, C., Chen, G., Chen, W., Tapponnier, P., Zhang, B., 2007. Millennial recurrence of large earthquakes on the Haiyuan fault near Songshan, Gansu Province, China. *Bull. Seismol. Soc. Am.* 97, 14–34.
- Liu-Zeng, J., Shao, Y., Klinger, Y., Xie, K., Yuan, D., Lei, Z., 2015. Variability in magnitude of paleoearthquakes revealed by trenching and historical records, along the Haiyuan Fault, China. *J. Geophys. Res., Solid Earth* 120, 8304–8333.
- Lyard, F., Lefevre, F., Letellier, T., Francis, O., 2006. Modelling the global ocean tides: modern insights from FES2004. *Ocean Dynam.* 56, 394–415.
- Lyons, S. N., Bock, Y., Sandwell, D. T., 2002. Creep along the Imperial Fault, southern California, from GPS measurements. *J. Geophys. Res., Solid Earth* 107.
- Lyons, S., Sandwell, D., 2003. Fault creep along the southern San Andreas from interferometric synthetic aperture radar, permanent scatterers, and stacking. *J. Geophys. Res., Solid Earth* 108.
- McCaffrey, R., 2009. Time-dependent inversion of three-component continuous GPS for steady and transient sources in northern Cascadia. *Geophys. Res. Lett.* 36, L07304.
- Minson, S. E., Simons, M., Beck, J. L., 2013. Bayesian inversion for finite fault earthquake source models I—Theory and algorithm. *Geophys. J. Int.* 194, 1701–1726.
- Moore, D. E., Rymer, M. J., 2007. Talc-bearing serpentinite and the creeping section of the San Andreas Fault. *Nature* 448, 795.
- Nocquet, J.M., 2018. Stochastic static fault slip inversion from geodetic data with non-negativity and bound constraints. *Geophys. J. Int.* 214, 366–385.
- Ozener, H., Dogru, A., Turgut, B., 2013. Quantifying aseismic creep on the Ismetpasa segment of the North Anatolian Fault Zone (Turkey) by 6 years of GPS observations. *J. Geodyn.* 67, 72–77.
- Patil, A., Huard, D., Fonnesbeck, C. J., 2010. PyMC: Bayesian stochastic modelling in Python. *J. Stat. Softw.* 35, 1.

- Perfettini, H., and Avouac, J.-P., 2007. Modeling afterslip and aftershocks following the 1992 Landers earthquake, *J. Geophys. Res., Solid Earth* 112, B07409.
- Rau, R. J., Chen, K. H., Ching, K. E., 2007. Repeating earthquakes and seismic potential along the northern Longitudinal Valley fault of eastern Taiwan. *Geophys. Res. Lett.* 34.
- Reid, H. F., 1910. On mass movements in tectonic earthquakes and the depth of the focus. *Beitragen Geophys.* 10, 318–351.
- Ren, Z., Zhang, Z., Chen, T., Yan, S., Yin, J., Zhang, P., Zheng, W., Zhang, H., Li, C., 2016. Clustering of offsets on the Haiyuan fault and their relationship to paleoearthquakes. *Bulletin* 128, 3–18.
- Rosen, P. A., Hensley, S., Peltzer, G., Simons, M., 2004. Updated repeat orbit interferometry package released. *Eos, Transactions American Geophysical Union* 85, 47–47.
- Ryder, I., Bürgmann, R., 2008. Spatial variations in slip deficit on the central San Andreas fault from InSAR. *Geophys. J. Int.* 175, 837–852.
- Sandwell, D. T., Wessel, P. 2016. Interpolation of 2-D vector data using constraints from elasticity. *Geophys. Res. Lett.* 43, 10–703.
- Savage, J. C., Burford, R. O., 1973. Geodetic determination of relative plate motion in central California. *J. Geophys. Res.* 78, 832–845.
- Segall, P., 2010. *Earthquake and Volcano Deformation*, Princeton Univ. Press, Princeton, N. J
- Song, X., Jiang, Y., Shan, X., Gong, W., Qu, C., 2019. A fine velocity and strain rate field of present-day crustal motion of the northeastern Tibetan Plateau inverted jointly by InSAR and GPS. *Remote Sens.* 11, 435.
- Stevens, V. L., Avouac, J. P., 2015. Interseismic coupling on the main Himalayan thrust. *Geophys. Res. Lett.* 42, 5828–5837.
- Tapponnier, P., Zhiqin, X., Roger, F., Meyer, B., Arnaud, N., Wittlinger, G., Yang, J., 2001. Oblique stepwise rise and growth of the Tibet Plateau. *Science* 294, 1671–1677.
- Thomas, M. Y., Avouac, J. P., Champenois, J., Lee, J. C., Kuo, L. C., 2014. Spatiotemporal evolution of seismic and aseismic slip on the Longitudinal Valley Fault, Taiwan. *J. Geophys. Res., Solid Earth* 119, 5114–5139.
- Tong, X., Sandwell, D. T., Schmidt, D. A., 2018. Surface creep rate and moment accumulation rate along the Aceh segment of the Sumatran fault from L-band ALOS-1/PALSAR-1 observations. *Geophys. Res. Lett.* 45, 3404–3412.
- Wang, M., Li, Q., Wang, F., Zhang, R., Wang, Y., Shi, H., Zhang, P., Shen, Z., 2011. Far-field coseismic displacements associated with the 2011 Tohoku-oki earthquake in Japan observed by Global Positioning System. *Chinese Sci. Bull.* 56, 2419–2424.
- Wang, W., Qiao, X., Yang, S., Wang, D., 2017. Present-day velocity field and block kinematics of Tibetan Plateau from GPS measurements. *Geophys. J. Int.* 208, 1088–1102.
- Weertman, J., J. R. Weertman., 1964. *Elementary Dislocation Theory*, 213 pp., MacMillan, New York.
- Wei, M., Sandwell, D., Smith-Konter, B., 2010. Optimal combination of InSAR and GPS for measuring interseismic crustal deformation. *Adv. Space Res.* 46, 236–249.
- Weng, H., & Ampuero, J.-P., 2019. The dynamics of elongated earthquake ruptures. *J. Geophys. Res., Solid Earth* 124, 8584–8610.
- Wessel, P., Smith, W. H., Scharroo, R., Luis, J., Wobbe, F., 2013. Generic mapping tools: improved version released. *Eos, Transactions American Geophysical Union* 94, 409–410.

- Xu, X., Tong, X., Sandwell, D. T., Milliner, C. W., Dolan, J. F., Hollingsworth, J., Leprince, S., Ayoub, F., 2016. Refining the shallow slip deficit. *Geophys. J. Int.* 204, 1867–1886.
- Yang, Y., Tsai, M., Hu, J., Aurelio, M. A., Hashimoto, M., Escudero, J. A. P., Su, Z., Chen, Q., 2018. Coseismic slip deficit of the 2017 Mw 6.5 Ormoc earthquake that occurred along a creeping segment and geothermal field of the Philippine Fault. *Geophys. Res. Lett.* 45, 2659–2668.
- Yu, S. B., Hsu, Y. J., Kuo, L. C., Chen, H. Y., Liu, C. C., 2003. GPS measurement of postseismic deformation following the 1999 Chi-Chi, Taiwan, earthquake. *J. Geophys. Res., Solid Earth* 108, 2520.
- Zhang, W., Jiao, D., Zhang, P., Molnar, P., Burchfield, B. C., Deng, Q., Wang, Y., Song, F., 1987. Displacement along the Haiyuan fault associated with the great 1920 Haiyuan, China, earthquake. *Bull. Seismol. Soc. Am.* 77, 117–131.

Chapter 5· Heterogeneous interseismic coupling along the Xianshuihe-Xiaojiang fault system, eastern Tibet

This chapter focuses on the interseismic fault deformation along one major fault system in the eastern Tibetan Plateau, the Xianshuihe-Anninghe-Zemuhe-Xiaojiang (XAZX) fault system. I use multi-temporal GPS and InSAR to map the interseismic faulting behavior along this fault system. I start with introductions of the GPS and InSAR data, then I present the modeling method and results. In the discussion part, I address the seismogenic coupling and moment budget along the fault system, and the implications in terms of seismic hazards and earthquake cycle. Finally, I present arguments on the shallow creep characteristics along the Xianshuihe fault.

The work in this chapter has been submitted to *Earth and Planetary Science Letters*.

5.1. Abstract

The ~1400 km-long Xianshuihe-Xiaojiang fault system (XXFS) is one of the large strike-slip faults that cuts the eastern Tibet and further extends in the highly populated Sichuan and Yunnan provinces in southern China. Available historical records attest that the fault has regularly hosted $M > 7.5$ earthquakes during the last six centuries, making this fault one of the most seismically active in China and one of the potentially most damaging one. Here, we use Global Positioning System (GPS) velocity solutions and Interferometric Synthetic Aperture Radar (InSAR) results to quantify the interseismic coupling along the XXFS and its change through time. An elastic block model confirms predominantly left-lateral strike slip motion with slip rates of 7–11 mm/a along the XXFS. South of $\sim 29.5^\circ\text{N}$, high interseismic coupling is found down to 20 km-depth along the 240 km-long Anninghe-Zemuhe fault. A second 130 km-long segment, highly coupled down to 10–15 km-depth, is identified along the northern Xiaojiang fault. North of 30.2°N , the Xianshuihe fault appears to be predominantly creeping. However, the previously observed shallow creep observed during 4 decades after the 1973 $M 7.6$ Luhuo earthquake has ended ([Allen et al., 1991](#), [Zhang et al., 2018a](#)), possibly marking the initial state of one new earthquake cycle and progressive relocking of the fault. Farther south along the Xianshuihe fault, we identify a ~30 km-long creep section (latitude $\sim 30.2^\circ\text{N}$ – 30.4°N) overlapping the Kangding-Bamei segment, whose creep rates show a transient behavior with a creep rate of 7.4 ± 2.4 mm/a during the 1999–2007 period, 9.0 ± 2.0 mm/a for the 1999–2014 and 7.3 ± 1.5 mm/a in 2015–2018. Position time series from four GPS sites confirm an increase in creep rate during the 2008–2014 period that we tentatively attribute to the Coulomb stress failure increment induced by the 2008 $M_w 7.9$ Wenchuan earthquake that ruptured 200 km north of it. The 2014 $M_w 5.9$ Kangding earthquake occurred along the creeping segment at the end of the period of accelerated creep. Finally, the moment released by historical earthquakes and the moment accumulation derived from interseismic fault coupling model were quantitatively compared to obtain moment balance on the fault plane. The moment balance highlights that along the Anninghe, Zemuhe and Xiaojiang faults, moment deficits for $M > 7$ earthquakes has now accumulated.

5.2. Introduction

The left-lateral strike-slip Xianshuihe fault is one of the large strike-slip faults cutting through the eastern Tibetan Plateau and contributing to the eastward motion of Tibet (e.g., [Tapponnier and Molnar, 1977](#); [Allen et al., 1991](#); [Tapponnier et al., 2001](#)). The Xianshuihe fault extends over several hundreds of kilometers farther east outside the Tibetan Plateau along the Anninghe, Zemuhe and Xiaojiang segments in the Sichuan and Yunnan provinces, where the fault finally merges with the Red River fault (Figure 5.1). The 1400 km-long Xianshuihe-Xiaojiang fault system (XXFS) has been one of the most seismically active faults in mainland China. The fault benefits from a detailed history of past earthquakes for the last three centuries (e.g., [Larson et al., 1999](#); [Deng et al., 2014](#); [Wen et al., 2008a](#)). During that period, macro-seismic intensities based on historical records indicate more than 35 earthquakes with magnitude estimated to be larger than 6. Additional historical records dating back to the XIVth century indicate that each of the four main segments have hosted at least one large $M > 7.5$ earthquake and the largest event occurred in 1833 along the Xiaojiang fault in Yunnan with a proposed magnitude of 8.0. According to the earthquake history summarized by Wen et al. (2008a), the Xianshuihe segment in the eastern Tibetan Plateau hosted regular large events with $M > 7.5$ earthquakes in 1327, 1786, 1816, 1955 and 1973 (Figure 5.1).

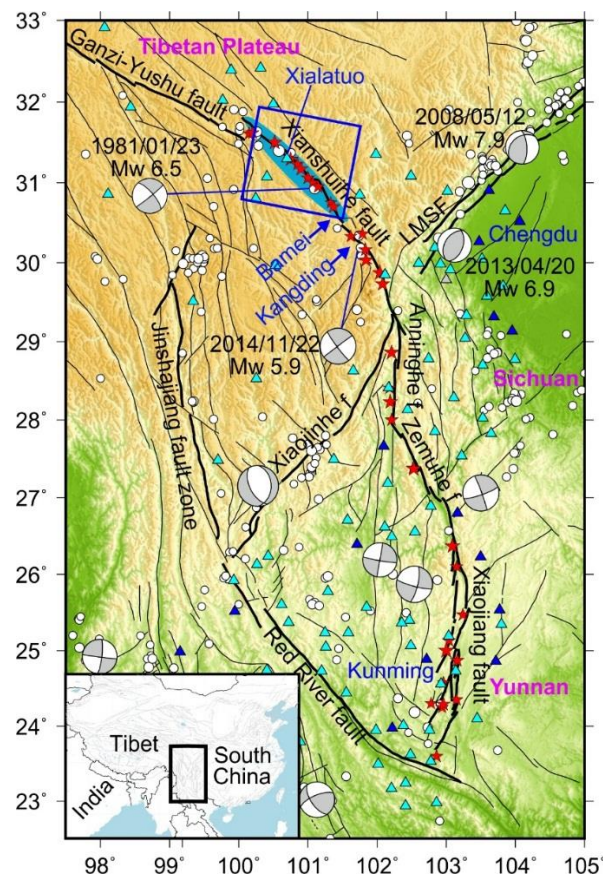


Figure 5.1. Regional tectonic map of the eastern Tibetan Plateau. Bold black lines correspond to the Xiaoshuihe-Anninghe-Zemuhe-Xiaojiang fault system (XXFS). Thin black lines indicate active faults ([Deng et al., 2003](#)). Gray focal mechanism solutions ($M_w > 6$, 1976–2015) come from the Global

Centroid Moment Tensor (GCMT). Thin white circles represent earthquakes ($M_w > 5$, 1960–2015) from the United States Geological Survey (USGS). Red stars mark the epicenters of historical earthquakes ($M > 6$; Wen et al., 2008a). Triangles show the locations and populations of cities (cyan: < 0.5 million; blue: > 0.5 million). Blue rectangle shows the InSAR coverage. Cyan ellipse indicates creeping segments proposed by Allen et al. (1991) and Zhang et al. (2018a). LMSF denotes the Longmenshan fault. The inset map shows the study area.

Since the 1973 M 7.6 Luhuo earthquake, the XXFS has been relatively silent with only two earthquakes with moment magnitude of 6.5 (1981) and 5.9 (2014) that occurred along the northwestern segments. Several studies assessed the short-term seismic potential along XXFS. Ran et al. (2008) and Wen et al. (2008a) show that for the Xianshuihe fault, from the Kangding County to Bamei town (hereafter refer to the Kangding-Bamei segment) and for the Anninghe fault, the time elapsed since the last large earthquake is close to the average earthquake recurrence time derived from paleoseismology studies. Interseismic fault coupling inversion of GPS velocity solution for the 1999–2013 period also find that the Kangding-Bamei segment and the Anninghe fault are very close to the time of rupture for a characteristic earthquakes (Jiang et al., 2015). Since the region crossed by the XXFS hosts a dense population of more than 50 million, assessing the seismic potential of the XXFS is a major issue in a rapidly developing area in China.

The Xianshuihe fault further allowed to study the fault behavior following the large M 7.6 Luhuo earthquake. From an analysis of short-baseline (~ 130 m) geodetic resurvey data (1976–1984), Allen et al. (1991) found up to ~ 6 mm/a of surface creep at Xialatuo site (longitude 100.75°E and latitude 31.28°N ; Figure 5.1) along the Luhuo earthquake surface rupture. Recently, Zhang et al. (2018a) reprocessed the short-baseline and short-leveling arrays data (1976–2014) at seven sites along the Xianshuihe fault between latitudes $\sim 30.5^\circ\text{N}$ and 31.6°N , and reported an average creep rates of 1.3–3.5 mm/a during the observation span, decaying through time at a logarithmic rate. However, Wang et al. (2009) interpreted the fault segment between $\sim 31^\circ\text{N}$ and 31.8°N along the Xianshuihe fault be locked to a depth of 3–6 km by processing the ERS-1/2 and Envisat SAR data for the 1996–2008 period. These different results may reflect a progressive relocking of the segment ruptured during the Luhuo earthquake.

In this study, we first derive GPS velocity solutions for eastern Tibet, spanning three different periods 1999–2007, 1999–2014 and 2015–2018, whose density is almost twice that of previous studies (e.g., Jiang et al., 2015; Zhao et al., 2015; Zheng et al., 2017). Then, using elastic block modeling (McCaffrey et al., 2007), we estimate the spatial distribution of interseismic fault coupling (ISC) along the XXFS. Using the available earthquake history, we derive balances of moment accumulation vs release and discuss the implications in terms of seismic potential. We also identify a ~ 30 km-long creeping segment on the Xianshuihe fault, which does not overlap and is located south of the creep area described in Allen et al. (1991) and Zhang et al. (2018a). We investigate the temporal variations in creep rate and its implication for the fault behavior.

5.3. Data and model

5.3.1. GPS data processing

We use three different GPS velocity solutions spanning the 1999–2007, 1999–2014 and 2015–2018 respectively to investigate the potential time variations of coupling and slip rate along the XXFS:

(1) The 1999–2007 GPS velocity solution, which is used in section 4.2 and 4.3 for cross-fault velocity profiles, is derived from Zhang et al. (2013). This solution represents interseismic velocities for eastern Tibet before the 2008 Mw 7.9 Wenchuan earthquake.

(2) The 1999–2014 GPS velocity solution, used as constraints for block model in section 3, consists of two parts: (a) The Crustal Movement Observation Network of China and the Tectonic (CMONOC I/II) GPS data were acquired between 1999 and 2014, including a total of 300 sites in the study area (244 campaign and 56 continuous stations); these data were processed by Wang et al. (2017) (see Wang et al., 2017 for details; Text C.1). (b) The Sichuan GNSS/GPS Network of the Sichuan Earthquake Bureau and the Sichuan Surveying and Mapping Bureau, including 177 new sites that were occupied between 2004 and 2014. These GPS observations were processed by Rui and Stamps (2016) (see Rui and Stamps, 2016 for details; Text C.1). The two GPS velocity solutions were originally referenced to different frames. We combine them into a single consistent solution by solving for an Euler vector, which minimize the velocity residuals between common sites. We chose the Wang et al. (2017) solution as the master solution and rotated the Rui and Stamps (2016) solution onto it. We selected a total of 197 common sites and the Root Mean Square (RMS) of the velocity residuals was 0.86 mm/a. We averaged the velocities for the co-located sites; the final GPS site velocities under the South China reference frame are shown in Figure 5.2.

(3) The 2015–2018 GPS velocity solution, which is also used in section 4.2 and 4.3 for cross-fault velocity profiles, was derived from our own processing of CMONOC GPS data in the study area. Following the GPS data processing strategies of Li et al. (2018), we obtained the geodetic velocity field in eastern Tibet and China in a Eurasia-fixed reference frame (Altamimi et al., 2011). In August 8, 2017, a Mw 6.5 earthquake struck the Jiuzhaigou County (epicenter 103.861°E, 33.198°N), about 350 km away from XXFS. During our data processing, we corrected the coseismic offsets for GPS stations located within 150 km from the epicenter. Considering that the magnitude of the earthquake is relatively small and that there were no continuous GPS stations near the epicenter (within 50 km), we ignored the postseismic transients in our GPS velocity solution.

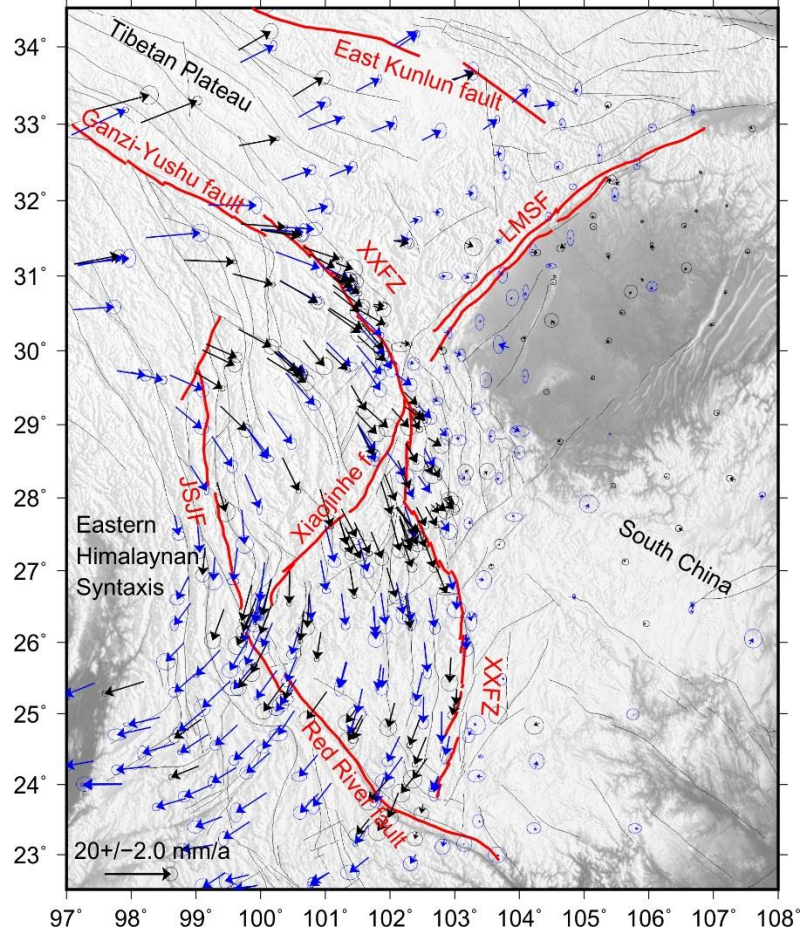


Figure 5.2. Global Positioning System (GPS) velocity fields (1998–2014) with respect to the South China block. Error ellipses show 68% confidence levels. Arrows in blue represent the velocity solution from Wang et al. (2017); arrows in black represent the velocity solution from Rui and Stamps (2016). Gray lines correspond to active faults.

5.3.2. GPS data modeling

We evaluate time variations of slip rate at specific locations along the fault using two-dimensional buried dislocation models. The 2-D elastic dislocation model (Weertman and Weertman, 1964; Segall, 2010) fits the fault parallel velocities (V_{par}) and solve for a slip rate (S), a locking depth (d_1), a creep rate (c) from the surface to depth (d_2):

$$V_{par}(x) = \frac{S}{\pi} \tan^{-1} \left[\frac{x}{d_1} \right] + \frac{c}{\pi} \tan^{-1} \left[\frac{d_2}{x} \right] + a \quad (1)$$

where a is a constant and x is the distance from the fault. We use a Bayesian approach to derive posterior probability density functions (PDF) of the model parameters (e.g. Minson et al., 2013; Nocquet, 2018), $p(\mathbf{m}|\mathbf{d})$ is defined as: $p(\mathbf{m}|\mathbf{d}) \sim p(\mathbf{m}) \exp [(\mathbf{d} - \mathbf{p})^T C^{-1} (\mathbf{d} - \mathbf{p})]$, where \mathbf{d} and \mathbf{p} are vectors containing the observations and model predictions, C^{-1} is the inverse of the data covariance matrix, and $p(\mathbf{m})$ is the prior PDF of the model parameters. We used uniform prior distributions and took the covariance matrix as a diagonal matrix using the GPS data uncertainties. Results presented below were derived from a total of 50,000 sampling from a Markov chain

implemented in the PyMC Python package (Patil et al., 2010).

We also use the elastic block modelling implemented in DEFNODE package (McCaffrey et al., 2007) to obtain a regional kinematic model. We simultaneously solve for block rotations rate, strain rate within blocks, and the spatial distribution interseismic coupling (ISC) along block-bounding faults. We show the detailed modeling strategies in Figure C.1 and Text C.2.

We assess the spatial resolution of our ISC model by performing checkerboard tests with increasing size of individual elements from 20 to 70 km (Figure C.2). The results show that lateral variations of 20 km are recovered all along the fault above a depth of ~ 10 km, whereas poorer resolution is found below a depth of ~ 10 km. However, compared with previous studies (Jiang et al., 2015), our denser GPS network provides better spatial resolution.

5.3.3. InSAR data and processing

We compile interseismic InSAR LOS (Line of Sight) rate (data span: 13 December 2014 to 26 November 2016; Figure 5.3a) from Zhang et al. (2018b) covering the Xianshuihe fault between $\sim 30.5^\circ\text{N}$ and 31.6°N . We adopt the remove-filter-restore approach proposed by Wei et al. (2010) to integrate GPS (1999–2014) and InSAR. Then using the integration (Figure 5.3b) to calculate the ‘surface creep rates’ along the Xianshuihe fault. The detailed strategies are present in Text C.3.

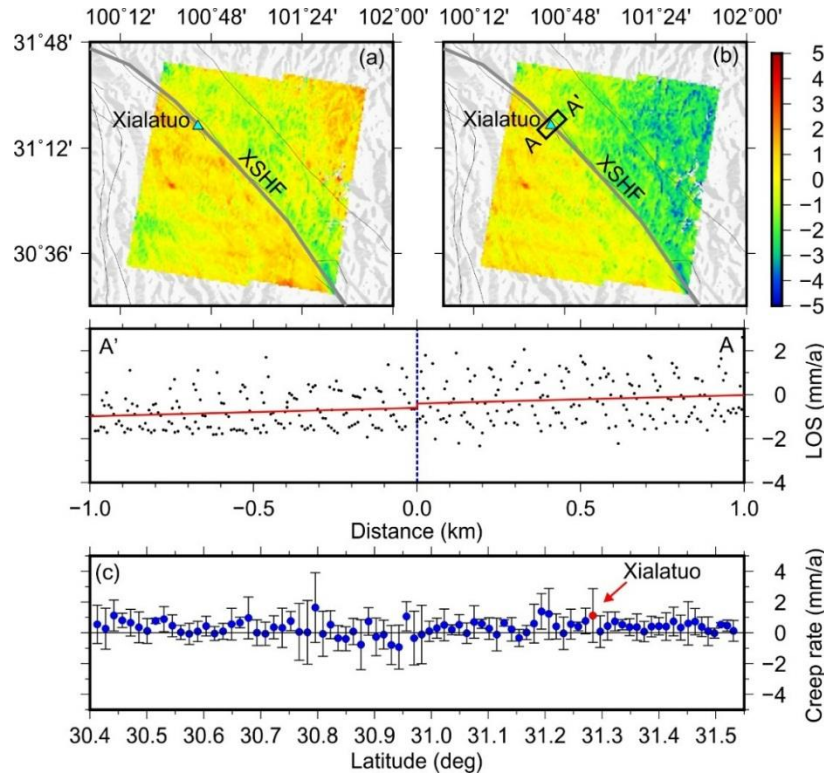


Figure 5.3. (a) InSAR LOS rate map across the Xianshuihe fault from Zhang et al. (2018b). (b) High-pass filtered InSAR LOS rate map across the Xianshuihe fault. Black rectangles show the locations of velocity profile across the Xialatuo site, with Line of Sight (LOS) velocities below. Red lines are linear

fitting. (c) Along fault variations of creep rates for the Xianshuihe fault. The blue error bars represent 1σ uncertainties.

5.4. Interseismic coupling results

We obtained the angular velocities, internal strain parameters of each block, and ISC along the block bounding faults in our best fitting model ($\chi_n^2 = 2.7$; GPS velocity residuals are shown in Figure C.1). The angular velocities were used to calculate the slip rate along the XXFS (Figure 5.4). The XXFS is dominated by left-lateral strike-slip motion with the fastest rates of 10–11 mm/a found along the northwesternmost segment of the Xianshuihe fault, progressively decreasing to 7 mm/a along the Anninghe, Zemuhe and Xiaojiang faults. These estimates are consistent with both geological (~9–10 mm/a; e.g., Yan and Lin, 2017; Bai et al., 2018) and previous geodetic (~7–13 mm/a; e.g., Shen et al., 2005; Loveless and Meade, 2011; Wang et al., 2017) results. Our ISC model highlights two opposite behaviors. From latitude 32°N to latitude 30°N, the Xianshuihe fault appears to be predominantly creeping, while the Anninghe, Zemuhe and Xiaojiang faults show significant coupling. In the detail, high coupling occurs along three locked regions hereafter referred as A1, A2, and A3 (A is an abbreviation for Asperity), separated by narrow segments of shallower (~5 km depth) or weaker coupling (Figure 5.4). Asperity A1 located along the southernmost part of the Xiaojiang fault appears to be locked down to ~20 km depth. However, since this location corresponds to the edge of the model, we cannot rule out the possibility of boundary effects and will not interpret this pattern in the following discussion. Asperity A2 along the Xiaojiang fault is confined to ~10 km depth but spans ~130 km along strike. The largest asperity A3 is found to be locked down to ~20 km and extends laterally over ~240 km along the Anninghe and Zemuhe faults. According to our checkerboard tests (Figure C.2), A2 and A3 are robust features, each extends hundreds of kilometers.

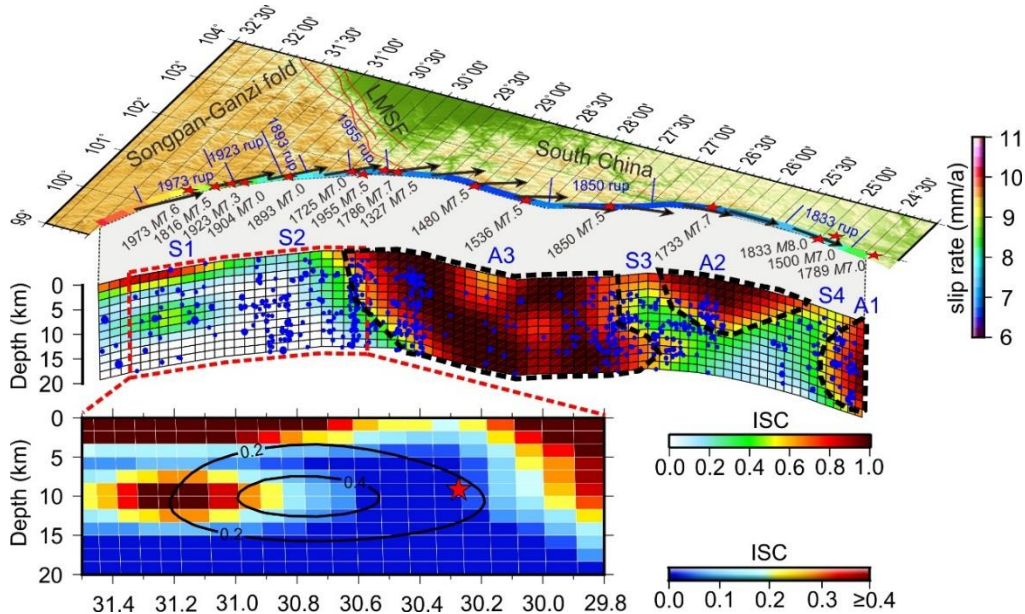


Figure 4. Fault slip and interseismic fault coupling (ISC) along the Xianshuihe-Anninghe-Zemuhe-Xiaojiang fault system (XXFS). (Upper panel) Estimated total magnitude of fault slip rate along the XXFS is shown with color, with black arrows indicates direction. Red stars denote locations of historical earthquakes. The approximate location of the surface ruptures come from Wen et al. (2008a). (Middle

panel) ISC distribution on the XXFS plane. Blue dots indicate epicenters of microseismicity (1970–2015), for which data come from the China Earthquake Data Center (<http://data.earthquake.cn>). Thick black dotted lines outline the asperities, which are named as A1, A2 and A3 respectively. (Lower panel) Enlarged view of the ISC distribution on the Xianshuihe fault. The red star represents the epicenter of the 2014 Mw 5.9 Kangding earthquake, and the black circle outlines the coseismic slip contour (Jiang et al., 2015).

Additional remarkable features of the fault coupling are the shallow locking depth found along several segments (hereafter refer to S1, S2, S3 and S4; S is an abbreviation for Segment; Figure 5.4). S1 is located along the northwestern segment of the Xianshuihe fault between latitude 30.4°N to 32°N, with a very shallow locking depth of 2–3 km. It overlaps the segment experiencing surface creep found by Allen et al. (1991) and Zhang et al. (2018a). Adjacent to S1, the S2 segments extends ~30 km along the Xianshuihe fault between latitude 30.2°N to 30.4°N and overlaps the Kangding-Bamei segment. ISCs along S2 are estimated to be smaller than 20%, possibly reflecting creep reaching the surface. From our block model, the surface creep rate is estimated to be ~7.5 mm/a, comparable with the estimated long-term slip rate (7.9 ± 1.6 mm/a). S3 and S4 are short segments separating the locked asperities A1–A2 and A2–A3 respectively, with fault locking depths in the range of ~2–5 km.

We show the block internal strain rates and GPS residuals in Figure C.1; block rotation and strain rate parameters are provided as Supplementary Material. The principal strain rates are 7.4/0.04, 3.3/8.0, 1.0/3.9, 2.4/10.1 (compressive/tensile in nanostrain per year) for the South Yunnan block, the North Yunnan block, the Longmenshan block, and the Bayanha block respectively. These strain rate values highlight submillimeter per year internal deformation at the scale of the blocks in eastern Tibet. GPS velocity residuals follow a Gaussian distribution, are spatially randomly distributed without systematic misfits and are within their uncertainties. This indicates that no significant signal has been left out by the model and show a reasonable consistency between observations and model.

5.5. Discussion

Our results show highly heterogeneous fault locking along the XXFS. The difference of present-day slip mode might reflect different friction properties or show a behavior at different stages of an earthquake cycle. Given the relatively complete historical earthquake records for the past centuries and the fact that the time elapsed since the last large earthquake is different from one segment to another, the present ISC result provides an opportunity to explore the fault behavior at different stages of the earthquake cycle. In the following sections, we use the ISC results to quantitatively calculate moment budget along the different segments and infer areas with a higher probability of future seismic ruptures. Finally, we discuss the shallow creep detected along the Xianshuihe fault in the context of the earthquake sequence, and evaluate its decadal and more recent temporal variations.

5.5.1. Fault behavior and moment budget along the XXFS

5.5.1.1. Overall characteristics

We first evaluate the overall reliability of our fault coupling, its consistency or differences with the results of previous studies. Our block model results highlight four fault segments (S1, S2, S3 and S4) with shallow fault locking depth and two highly locked potentially seismogenic asperities (A2 and A3) along the XXFS (Figure 5.4). Although consistent with previous results at the first order ([Jiang et al., 2015](#); [Zhao et al., 2015](#)), our model has a better spatial resolution and identifies a newly creeping segment (latitude 30.2°N–30.4°N; S2) along the Xianshuihe fault. As an external verification, Figure 5.4 shows the fault coupling together with the background seismicity. Earthquakes from the China Earthquake Data Center catalogue were selected from within 15 km width on either side of the XXFS from January 1970 to November 2014. Despite the uncertainty of location especially for their depths, most of these minor earthquakes appear to occur around the transition zone between locked and slipping segments. This observation is consistent with the view that slip gradient induce larger shear stress rate than locked or slipping area. The correspondence of seismicity and the edge of the locked zones has been observed on the main Himalayan thrust for instance ([Stevens and Avouac, 2015](#)).

In the next section, we take the opportunity of the available earthquake history to quantitatively assess the seismic moment budget on main segments, that we then use to quantify the seismic potential. Our calculation, to some extent, relies on the completeness and reliability of the historical earthquake catalogue. Despite some inherent limitations, the long history of written records in the relatively densely populated Sichuan and Yunnan regions makes it among the best fault to attempt to calculate a seismic moment budget over time. It's unlikely that large earthquakes ($M > 7$) would have been missed. As a check, we calculate the frequency-magnitude plot of earthquakes for the

whole XXFS. We find a Gutenberg-Richter (Gutenberg and Richter, 1944) distribution of earthquakes with a b -value of 1.01 for earthquakes with magnitude larger than 6.5 (Figure 5.5), suggesting that the earthquake catalogue is complete above this magnitude. Below M 6.5, Figure 5.5 indicate that the frequency of moderate-size earthquakes is underestimated. Owing to their small magnitudes and limited moment release, they do not affect significantly the moment budget.

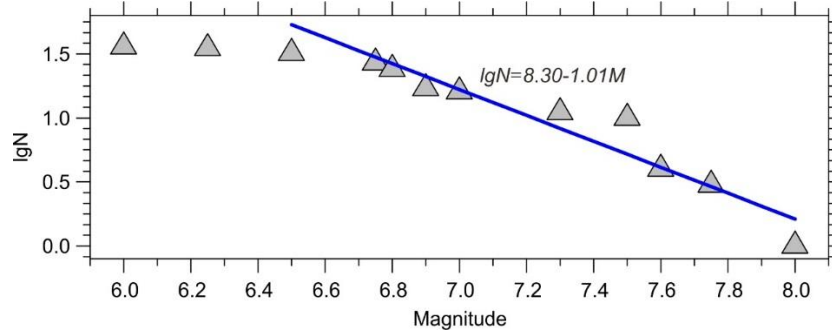


Figure 5.5. Gutenberg-Richter law showing the relation between the frequency and magnitude for earthquakes in 1937–2015 along the XXFS. Blue line represent the linear fitting for earthquakes with magnitudes larger than 6.5.

5.5.1.2. Northern Xianshuihe fault

The ISC result shows significant lateral variations along the Xianshuihe fault (Figure 5.4). Guided by the historical earthquakes (Figure 5.6), we divide the Xianshuihe fault into 2 sub-segments Sa1 & Sa2. Sa1 is located north of the Bamei town and encompasses lowly-locked segment S1 (Figure 5.4). Sa2 from Bamei town to Shimian County, encompasses the creeping segment S2 and part of Asperity A3 (Figure 5.4).

Along segment Sa1, at least 12 earthquakes with magnitudes larger than 6 occurred during the past 300 years (Figure 5.6). The present-day fault locking depth of 2–3 km indicates that the fault is predominantly creeping at depth and is at odd with the earthquake history. Segment Sa1 has been last ruptured in 1893 (M 7) for the southern part, 1923 (M 7.3) and 1981 (Mw 6.9) for the central part and in 1967 (M 6.8) and 1973 (M 7.6) for the northern part. For the latter segment, shallow creep has been observed from short baseline geodetic measurements since 1976 (Allen et al., 1991, Zhang et al., 2018a). Figure 5.7 summarizes these measurements. It shows that surface creep following the 1973 M 7.6 Luhuo earthquake lasted more than 4 decades after the earthquake, with a logarithmic decay of creep rate through time, indicating a progressive relocking of the fault at shallow depth. Maximum creep is observed along the southern part of the 1973 earthquake rupture and to a lesser extent in the northern part, whereas the central part had much little motion if any. Surface creep was also documented south of the 1973 rupture segment after the 1981 M 6.9 earthquake. Along the 1893 earthquake rupture trace, short-baseline measurements do not show significant surface creep. However, our ISC model finds a still weak coupling with an average coupling coefficient of ~20–40% in that area (Figure 5.4, 5.6e).

To go one step further, we compare the rate of moment accumulation predicted by our model to the moment released in large earthquakes. Taking a length of 205 km and an elastic shear modulus of 30 GPa, our model indicates an accumulation rate of moment deficit rate at 4.68×10^{17} N·m/a. The amount of moment released by earthquakes since 1700 is 7.26×10^{20} N·m, corresponding to ~1500 years of moment accumulated at the present-day rate with no earthquakes. There is clearly a discrepancy here, which originates from either an abnormally high frequency of earthquakes during the last three centuries or a too weak amount of present-day accumulation moment rate that would then not be representative of the longer term average fault coupling. As a point of comparison, if we assume the 205 km-long fault to be entirely locked down to 15–20 km depth, a moment accumulation rate of $9.23\text{--}12.3 \times 10^{17}$ N·m/a ($10 \text{ mm/a} \times 15\text{--}20 \text{ km} \times 205 \text{ km} \times 30 \text{ GPa}$) leads to a moment deficit of $6.03\text{--}8.04 \times 10^{20}$ N·m over the 1327–1981 period, a value fully consistent with the moment released by earthquakes over the same period.

Together with the transient creep from short baseline geodesy, this calculation supports the view that at the scale of several centuries, the northern Xianshuihe fault is locked and that the current behavior represent a transient behavior, progressively moving towards a relocking of the fault and initiating a new super cycle.

This interpretation raises several questions. First, afterslip here appears to be long lasting compared to previous results, which indicate decay-time of a few years. Here, accelerated surface creep lasted several decades after the 1973 and 1981 earthquakes and our ISC model indicate that aseismic slip still prevails at depth even for the segment ruptured in 1893. The Xianshuihe case of long-lasting afterslip might not be so uncommon however. For instance, the afterslip following the 2004 Mw 6.0 Parkfield strike-slip earthquake lasted ~6–12 years (e.g., [Lienkaemper and McFarland, 2017](#)). The 1944 (Mw 7.2) and 1951 (Mw 6.9) strike-slip earthquakes along the North Anatolian Fault generated afterslip continuing during at least 20 years, probably up to 50–70 year, on the Ismetpasa segment, where is still creeping nowadays (e.g., [Cakir et al., 2005](#); [Ozener et al., 2013](#); [Cetin et al., 2014](#); [Bilham et al., 2016](#)). Second, although the lack of coseismic slip models for previous earthquakes and the resolution of our model both prevent to document the spatial relationship between rupture and long lasting afterslip, our result still indicates that on average from 20 km depth to the surface, the fault should be slipping. This certainly encompasses areas that were locked before the earthquake and seismically ruptured. So, the observation here suggests that progressive slow relocking is taking place and ruptured area did not relocked immediately after the seismic rupture. Lasting several decades, this slow process of progressive relocking is not short with respect to the average recurrence time between successive earthquakes.

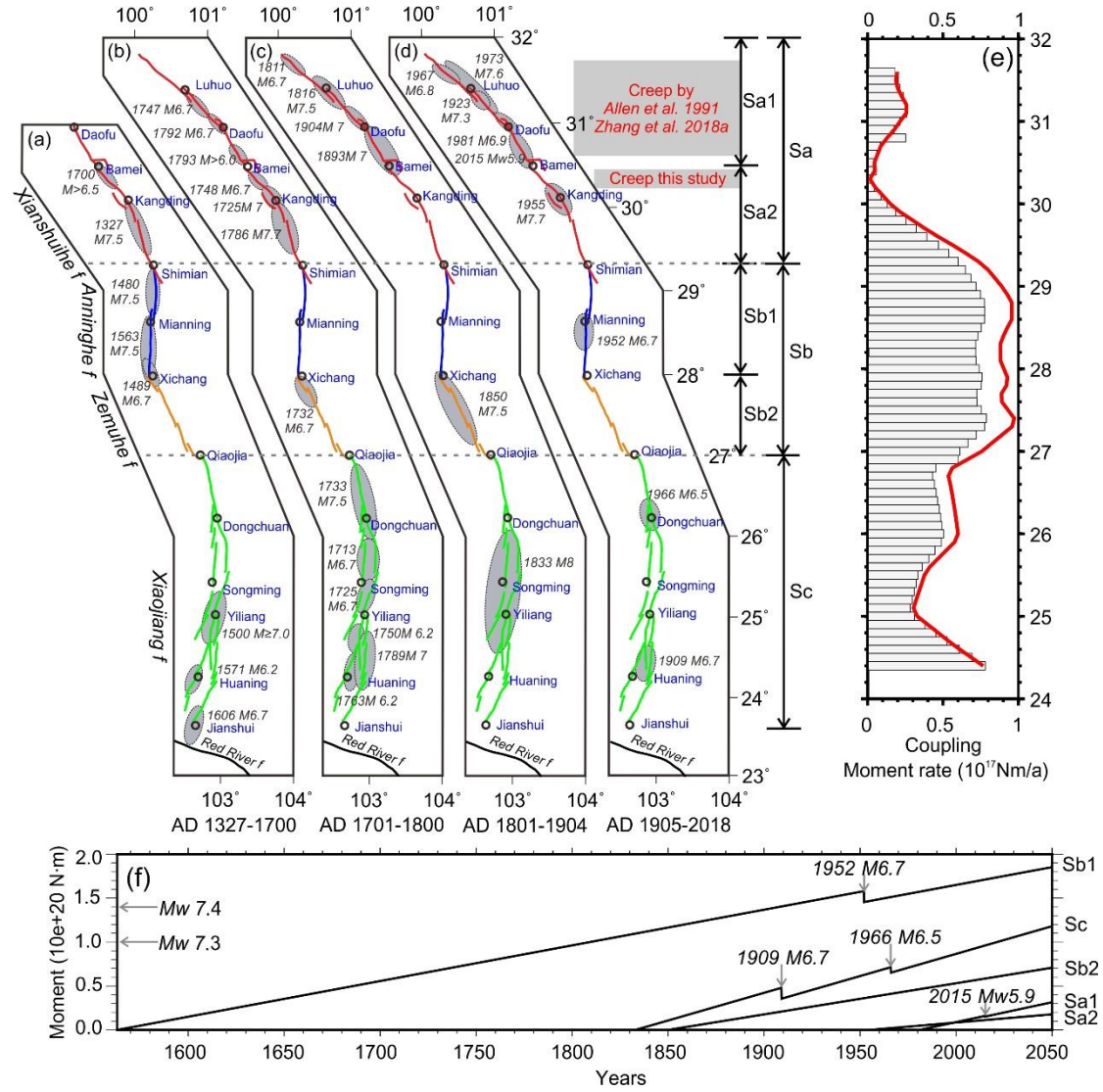


Figure 6. (a–d) Maps for four historical periods of relative severely damaged areas of 36 $M > 6$ earthquakes along the XXFS (modified from Wen et al. 2008a). Gray ellipses relative severely damaged areas of earthquakes with date and magnitude indicated. The red, blue, yellow and green lines correspond to the Xianshuihe fault, the Zemuhe fault, the Anninghe fault and the Xiaojiang fault respectively. (e) Red line corresponds to the vertical averaged coupling coefficients above 20 km depth. Grey histograms represent cumulative seismic moments every 0.2° bin. (f) Cumulative moment deficit corrected from large earthquakes moment released since 1563.

5.5.1.3. Southern Xianshuihe fault

Along the segment Sa2, our ISC result shows two opposite behaviors, with almost full decoupling (locking coefficient of $< 20\%$) along the Bamei-Kangding segment (i.e., S2 in Figure 5.4), and a transition towards full coupling down to ~ 10 – 20 km depth along the Kangding-Shimian segment (Figure 5.4, 5.6e). Our results show discrepancies with previous results from Jiang et al. (2015), who reported 60–100% locking along the Bamei-Kangding segment and a shallow fault locking depth of 0–10 km along the Kangding-Shimian segment. The discrepancies attribute to different

models and model resolutions along this segment (Sa2). Our checkerboard tests indicate a fairly good resolution along this segment (Figure C.2).

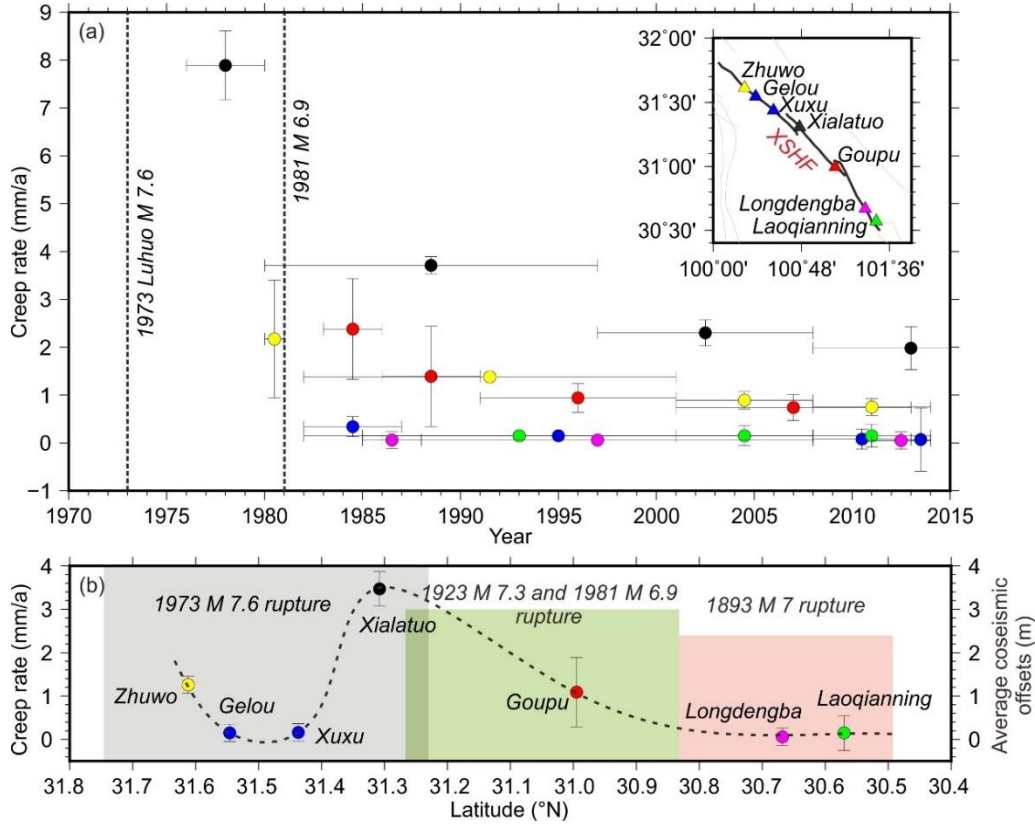


Figure 5.7. (a) Surface creep rate from short baseline measurements as a function of time along the rupture area of the 1973 Mw 7.6 Luhuo earthquake. Dot color show the measurements at different sites, whose location and color code are shown in the inset. Vertical dotted lines represent the date of earthquakes. Vertical error bars show 3- σ uncertainty, while horizontal error bar show the period used to estimate the surface creep rate. (b) Error bars show the average surface creep rate during the whole observation period. Dotted line indicates the overall shape of the creep distribution along the fault. Background color corresponds to the average surface offset of each earthquake (Papadimitriou et al., 2004).

We show in section 4.2 additional results for the Bamei-Kanding segment showing that this segment is also experiencing surface creep. South of it, the Kangding-Shimian segment hosted an M 7.7 earthquake in 1955. Unlike the Sa1 segment, this segment appears to be now in a state of full coupling. In addition to the 1955 M 7.7 earthquake, this segment experienced large earthquakes in 1327 (M 7.5) and in 1786 (M 7.7; Figure 5.6). Such magnitudes are consistent with a full rupture of its 165 km length, according to the earthquake scaling relationships (Wells and Coppersmith, 1994). This allows to test whether the moment released in earthquakes over 7 centuries is consistent with the present day geodetically derived model. Our model provides an accumulation rate of moment deficit rate at 1.87×10^{17} N·m/a, equivalent to a total moment of 1.17×10^{20} N·m between 1327 and 1955. This amount is less than 15% of the released moment through earthquakes (8.41×10^{20} N·m) during the same period. Now considering that this fault segment is 100% coupled down to 15–20

km, the accumulation rate of moment deficit is $5.57\text{--}7.43 \times 10^{17}$ N·m/a, resulting in a moment of $3.50\text{--}4.66 \times 10^{20}$ N·m for the 1327–1955 period. Such values are 70–90% of the moment release in earthquakes and can be considered as being consistent to a first order, given the uncertainty for magnitudes of historical earthquakes.

This result suggests that the present-day rate of moment deficit accumulation is also somehow transient along this segment. More specifically, the newly creeping section identified here along the Bamei-Kanding segment is probably also a transient feature and we show in section 4.2 that it also undergoes slip rate variation at the time scale of a few years. Combining the results for both Sa1 & Sa2 segment, the Xianshuihe fault appears to be in a transient state following a rich sequence of earthquakes for the last three centuries, and then initiating a new cycle of progressive increasing locking. Overall, given the past sequence of earthquakes and the still low rate of moment deficit accumulation, the seismic potential appears weaker than for the other segments of the XXFS. For the most locked area, if we assume the 1955 M 7.7 to have reset all the previously accumulated elastic strain along the segment, the current moment available for an earthquake is Mw 6.7.

5.5.1.3. Anninghe-Zemuhe fault

The Anninghe-Zemuhe fault involves the main coupled part of the XXFS system (asperity A3), where full locking down to depth ~20 km-depth along a 240 km-long segment is obtained from our block model (Figure 5.4, 5.6e). The history of earthquakes shows that the northern segment from Shimian to Xichang towns did not experienced any large earthquake for more than 4 centuries (last $M > 7$ earthquake occurred in 1563), while the southern segment last ruptured on 1732. A roughly slip deficit of 2–4 m is thus expected along the Anninghe-Zemuhe fault, corresponding to high potential of earthquake hazard, that is consistent with the seismic gap proposed by [Wen et al. \(2008b\)](#).

The northern segment (Sb1) has a length 150-km able to host a magnitude 7.6 earthquake according scaling laws ([Wells and Coppersmith, 1994](#)). For our moment balance, we therefore assume the 1563 M 7.5 earthquake reset all the accumulated moment for this segment. Under this assumption, we find a geodetic total moment deficit of 1.85×10^{20} N·m for the 1563–2050 period at an accumulation rate of 4.06×10^{17} N·m/a from our block model. This amount is equivalent to an Mw 7.5 earthquake if released in a single event (Figure 5.6f).

Along the southern segment Sb2, with reference to the scaling relationship between earthquake magnitude and rupture length ([Wells and Coppersmith, 1994](#)), the 130 km-long segment could host an Mw 7.5 earthquake. We consider that the 1850 M 7.5 earthquake as our starting date for the moment balance assessment. Our model predicts a moment deficit accumulation rate of 3.54×10^{17} N·m/a. By 2050, this amount leads to a moment of 7.08×10^{19} N·m (Mw 7.2) available for an earthquake (Figure 5.6f).

In overall, the Anninghe-Zemuhe shows a much larger seismic potential than the Xianshuihe fault.

5.5.1.4. Xiaojiang fault

The southern part of the XXFS fault shows along strike varying ISC with a highly ~180 km-long locked segment (A2 in Figure 5.4) terminating at both ends by relatively narrow shallowly locked segments (S3 and S4 in Figure 5.4). High locking close to the southern tip of the XXFS is also imaged but with a lower resolution due to possible side effects at the merging of the Xiaojiang fault with the Red River fault (A1 in Figure 5.4).

From the past history of earthquakes dating back to the XVIth century, we do not observe a clear segmentation of earthquakes with the one suggested by our ISC models. Indeed, segments S3 and S4 were at least partially ruptured in the 1733 M 7.5 and 1833 M 8 earthquakes respectively. Given the time elapsed since these earthquakes, shallow locking here probably reflects long term frictional variations along the Xiaojiang fault rather than transient creep following large earthquakes. Here, for the moment budget calculation, we assume that the 1833 M 8 earthquake released all elastic strain along the Xiaojiang fault. At the estimated moment deficit rate from our GPS model, we find an equivalent single event with moment magnitude of 7.4 period to be required in 2050 to balance the accumulated moment since 1833 (Figure 5.6f).

5.5.1.5. Seismic potential along XXFS

Earthquake rupture length-magnitude scaling relationships (Wells and Coppersmith, 1994) indicate maximum magnitude will be Mw 8.1, Mw 7.6 and Mw 7.5 along the Xiaojiang fault (Sc), the Anninghe fault (Sb1) and the Zemuhe fault (Sb2), respectively. Comparing with the accumulated moment (Figure 5.6f), the above calculation indicates that the Anninghe and Zemuhe faults are quite mature and possess a higher seismic potential. Our results agree with previous studies (e.g., Ran et al., 2008; Wen et al., 2008a; Jiang et al., 2015). Besides, we also find that the Xiaojiang fault has a relatively high seismic potential with an accumulated moment deficit allowing for an $M > 7$ earthquake to happen.

In the northern part, the Kangding-Bamei segment between latitude ~30.0°N–30.5°N, has been interpreted to be very close to rupture from both paleoseismological investigations (e.g., Ran et al., 2008; Wen et al., 2008a) and geodetic inversions (e.g., Jiang et al., 2015). However, our block model results indicate that this segment has very shallow fault locking depths (0–5 km), and includes a creeping segment (S2; Figure 5.4) between latitude ~30.2°N–30.4°N. This suggests that large earthquakes are unlikely along this part of the fault system.

5.5.2. Shallow creep along the Xianshuihe fault

Moment budget along the Xianshuihe fault suggest that the shallow creep documented along several segments of the fault is transient at the scale of the earthquake cycle. Here, we focus on shorter time scale variation of the creep. Recently, Zhang et al. (2018a) collected and processed the short-baseline and short-leveling data (1976–2014) measured at seven sites along the Xianshuihe fault (Figure 5.7). They proposed that spatio-temporal variations in surface creep rates occur between latitudes $\sim 30.5^\circ\text{N}$ and 31.6°N . In Figure 5.8a, we summarize existing estimates of the creep rate at Xialatuo site as a function of time together with our estimates from our GPS study and InSAR analysis. The rate of creep appears to have exponentially decay with time since the 1973 M 7.6 Luhuo earthquake from ~ 8 mm/a to ~ 2 mm/a or less. Extrapolated to the date of the earthquake, the surface creep rate is 12 mm/a, barely exceeding the loading rate due to the relative velocity of the two blocks separated by the Xianshuihe fault. This result is surprising since afterslip induced by co-seismic stress increment appear to be at least several times the relative block velocity.

Modern geodesy observations, to some extent, show discrepancies with repeated short-baseline measurements results for the latest period (Zhang et al., 2008a). For instance, Wang et al. (2009) reported that the fault segment between $\sim 31.0^\circ\text{N}$ and 31.8°N along the Xianshuihe fault be locked to a depth of 3–6 km by processing SAR data acquired in 1996–2008. Our block model results also show a shallow yet apparent fault locking depth (2–3 km) along this fault segment (Figure 5.4). To provide another independent reference for the existence of creep segment as well as the creep rate, we fitted a simple 2-D elastic dislocation model to the fault parallel GPS velocities across the Xialatuo site (Figure 5.8b–d; fault normal GPS velocities are shown in Figure C.3). The curve fitting results in a creep rate of 1.5 ± 1.2 mm/a for the 1999–2007 period, 0.5 ± 2.8 mm/a for the 1999–2014 and 0.2 ± 0.4 mm/a for the 2015–2018 period. These results suggest that creep rates at Xialatuo sites ended during the 2010–2018 period. To further investigate if there is any creep signal along the Xianshuihe fault segments between $\sim 30.5^\circ\text{N}$ and $\sim 31.6^\circ\text{N}$, we adopted the InSAR data (2014–2016; Figure 5.3b) across the fault and calculated the ‘creep rates’ on the fault. The result (Figure 5.3c, 5.8a) also shows no apparent creeping signal. Space geodetic creep results (0–1.5 mm/a) are smaller than obtained by ground short-baseline measurements results (2–3 mm/a, Zhang et al., 2018a) in 1996–2018. The above discrepancies might be explained in two ways. Either, the discrepancies reflect the different datasets and the temporal scale. As predicted by the exponential function (Figure 5.8a), the average creep rate in 1996–2008 is ~ 2 mm/a, which is at the same precision level with geodetic observations (i.e., GPS and InSAR), thus, the creep signal is hardly detected or probably be ignored. Such case suggests that the fault is progressively relocking, being at the end of postseismic phase, and initiating of a new cycle. Alternatively, the surface creep might have ended before 1996, after the 1973 M 7.6 Luhuo earthquake; the creeping results derived from short-baseline measurements are limited by their spatial coverage (baseline length < 300 m), thus the observations are probably related to a shattered or damaged fault zone in the shallow sediments (e.g., Hamiel et al., 2018). Such interpretation implies that the Xianshuihe fault experienced postseismic deformation in a period shorter than proposed by Zhang et al. (2018a). In summary, despite these

subtle differences between our results and Zhang et al. (2018a), both show that shallow creep along the Xianshuihe fault ($\sim 30.5^\circ\text{N}$ – 31.6°N) is afterslip during the years following the 1973 and 1981 earthquakes, and is at present in a state of progressive relocking of the shallow part of the fault.

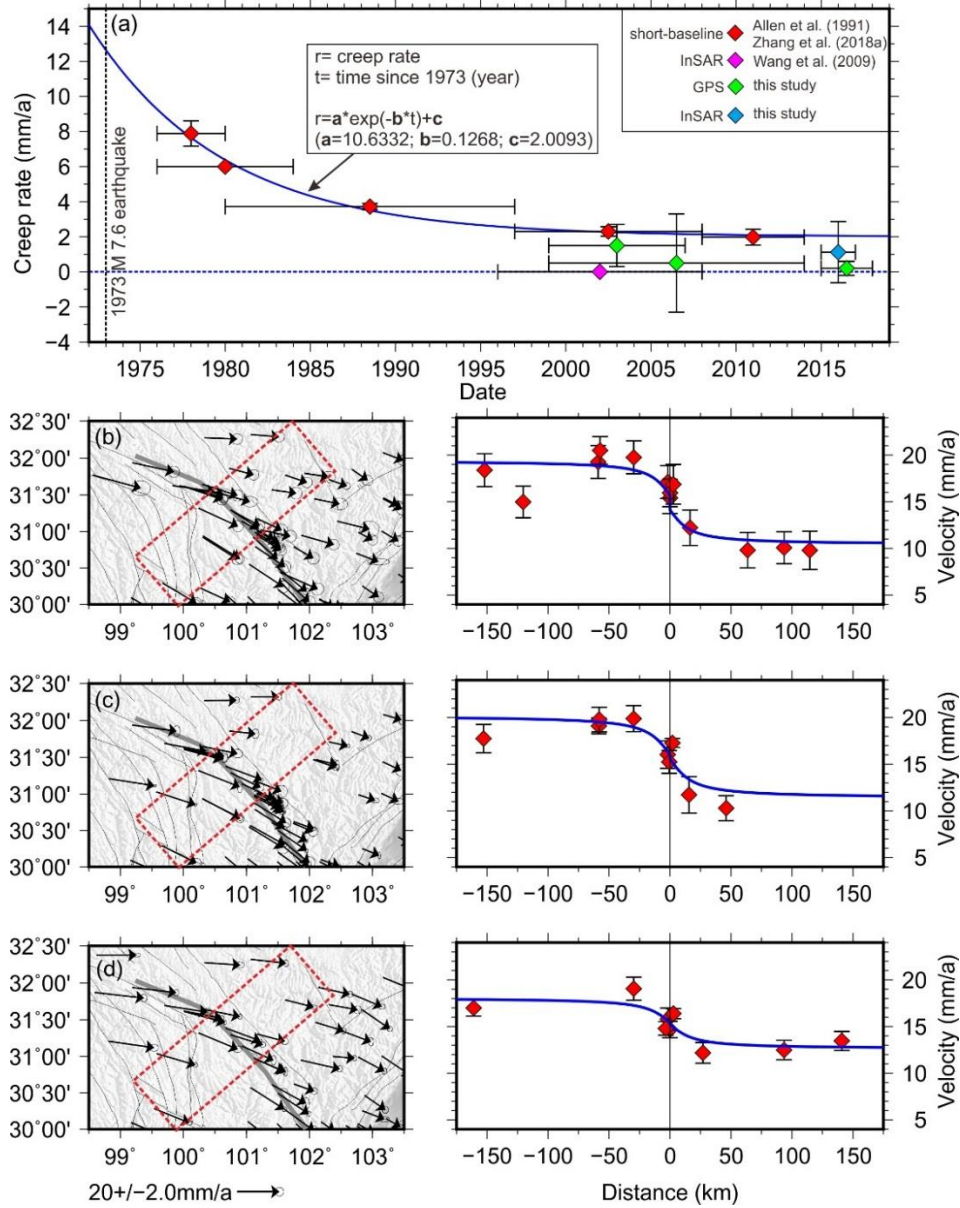


Figure 5.8. (a) Fault creep rate at the Xialatuo site as a function of time. Blue solid line is the fitting of short-baseline results. Error bars show 1- σ uncertainty. (b) GPS velocity solution in 1999–2007 and corresponding fault parallel velocities across the Xialatuo site, with its locations shown in red rectangles in the left panel. Blue solid line represent the best fitting curve. (c) and (d) are GPS velocity solutions in 1999–2014 and 2015–2018 respectively.

The other creep segment highlighted by our GPS results lies in $\sim 30.2^\circ\text{N}$ – 30.4°N along the Bamei-Kangding segment, which extends ~ 30 km-long (Figure 5.4). To provide independent reference for the existence of creep segment as well as the creep rate, we also fitted 2-D elastic dislocation model to the fault parallel GPS velocities (Figure 5.9a). Results show sharp, yet continuously gradient across the fault for AA' and CC' north and south of the creeping section,

indicating locked fault segments with locking depths of 5.9 ± 2.1 km and 7.1 ± 4.3 km respectively. The estimated values overlap with the 2–3 km fault locking depth from our block model. However, for profile BB' crossing our proposed creep segment, GPS velocities show apparent offset across the fault, indicating creeping fault segment. The creep rate is estimated to be 9.0 ± 2.0 mm/a (Posterior marginal Probability Density Functions [PDFs] are shown in Figure C.5); this is larger than the result from the block model (~ 7.5 mm/a) but similar to the estimated far-field loading rate (8.8 ± 1.0 mm/a).

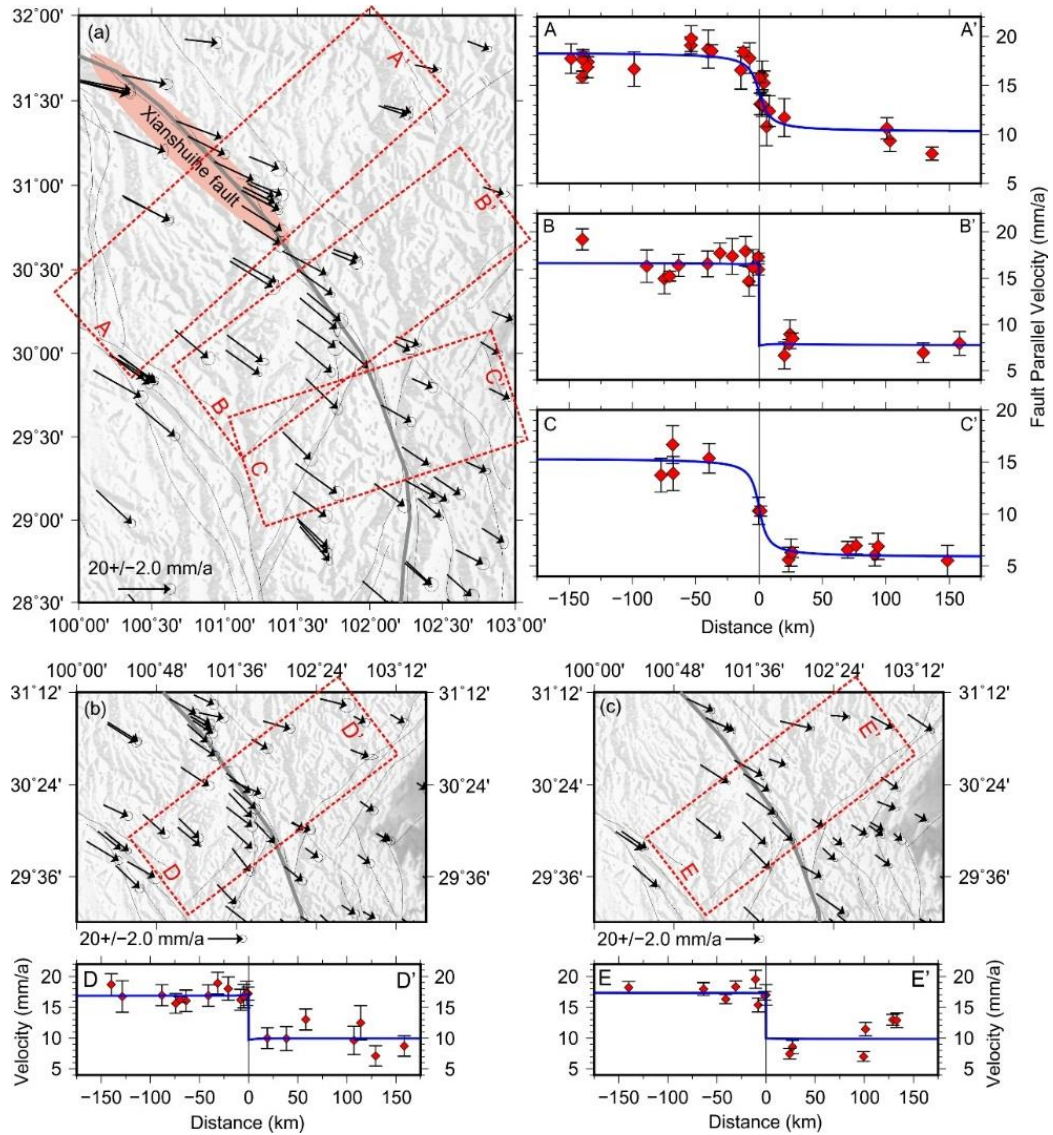


Figure 5.9. (a) (Left panel) Enlarged map of GPS velocity fields (1998–2014) across the Xianshuihe fault, with error ellipses show 68% confidence levels; orange ellipse indicates creeping segments proposed by [Allen et al. \(1991\)](#) and [Zhang et al. \(2018a\)](#); (Right panel) observed and calculated fault-parallel velocities across the Xianshuihe fault, with its locations shown in red rectangles in the left panel. Red diamonds with 1σ uncertainty error bars show the fault-parallel velocity components of GPS data. Blue solid lines represent best fitting curves. (b) Enlarged map of GPS velocity fields (1998–2007) across the Xianshuihe fault, the observed and calculated fault-parallel velocities across the fault are shown below. (c) Enlarged map of GPS velocity fields (2015–2018) across the Xianshuihe fault, the observed

and calculated fault-parallel velocities across the fault are shown below.

One intriguing issue here is whether the shallow creep ($\sim 30.2^{\circ}\text{N}$ – 30.4°N) is a permanent or long-term or also shows a time-decaying rate as found for the northwestern Xianshuihe fault. Paleoseismological investigations identified 17 earthquake with magnitudes greater than 6.0 along the Xianshuihe fault during the past 700 years (Figure 5.4, 5.6). 16 of them terminated on either sides of the creeping segment. Only the 1748 M 6.7 earthquake appears to have occurred at the creeping segment. Such medium earthquake is unlikely to produce afterslip after 270 years. The above evidence suggests the fault creep to be long-existed. Modern microseismicity show cluster beneath the creeping segment, indicating abundant ruptures of small-sized asperities. The 22 November, 2014 Mw 5.9 Kangding earthquake ruptured slightly north on the creeping segment at 10 km depth (Figure 5.4). Consequently, it is likely that the creep segment have been one barrier for large earthquakes ($M > 7$), with potential slip deficit released by ruptures of medium-small-sized asperities, and both the 1748 M 6.7 earthquake and the 2014 Mw 5.9 earthquake might be such cases.

Another possibility is that shallow creep on this segment has been activated as a propagation of the afterslip along the northwestern Xianshuihe. Such inference requires observational evidences at least prior to the 1981 M 6.9 earthquake, we will try to collect available data in our future work.

5.5.3. Temporal variation in creep rate along the Xianshuihe fault ($\sim 30.2^{\circ}\text{N}$ – 30.4°N)

We further investigate if temporal variation in surface creep rate along the Xianshuihe fault ($\sim 30.2^{\circ}\text{N}$ – 30.4°N) could be detected in our data. We first fitted 2-D elastic dislocation model to the fault parallel GPS velocities (1999–2007; Figure 5.9b; fault normal GPS velocities are shown in Figure C.4) and found a creep rate of 7.4 ± 2.4 mm/a, smaller than the averaged creep rate (9.0 ± 2.0 mm/a) during the 1999–2014 period (Figure 5.9a, 5.10a) but consistent with the ~ 7.5 mm/a estimation by block model. This comparison in turn implies that the creep rate during the 2008–2014 period should be larger than 9.0 mm/a. We also fitted the fault parallel GPS velocities between 2015 and 2018 (Figure 5.9c), the result shows an average creep rate of 7.3 ± 1.5 mm/a, which is compatible with that in 1999–2007. The above results therefore indicate an increase in creep rate for the 2008–2014 period, hence is transient (Figure 5.10a). To provide independent reference for the temporal variations in creep rate, we fitted the linear velocities for four GPS sites that observed in 1999–2015 and that are adjacent to the creep segment in different time bin (Figure 5.10c). The results show an obvious velocity acceleration (2008–2014) in the fault parallel direction, especially for sites H066 and H079, which are ~ 8 km to the fault. Moreover, time series of H067 and JB35 (~ 220 km away from the Wenchuan earthquake surface rupture) indicates that the postseismic transients of the 2008 Mw 7.8 Wenchuan earthquake had scarcely effects on the velocity (2008–2014), strengthening our conclusion that the temporal variations in GPS sites velocities are most likely related to the shallow creep rate acceleration. Although the few GPS campaigns does not

allow us to determine the full time behavior of displacement, we note that the velocity change is consistent with an onset following the 2008 Mw 7.9 Wenchuan earthquake.

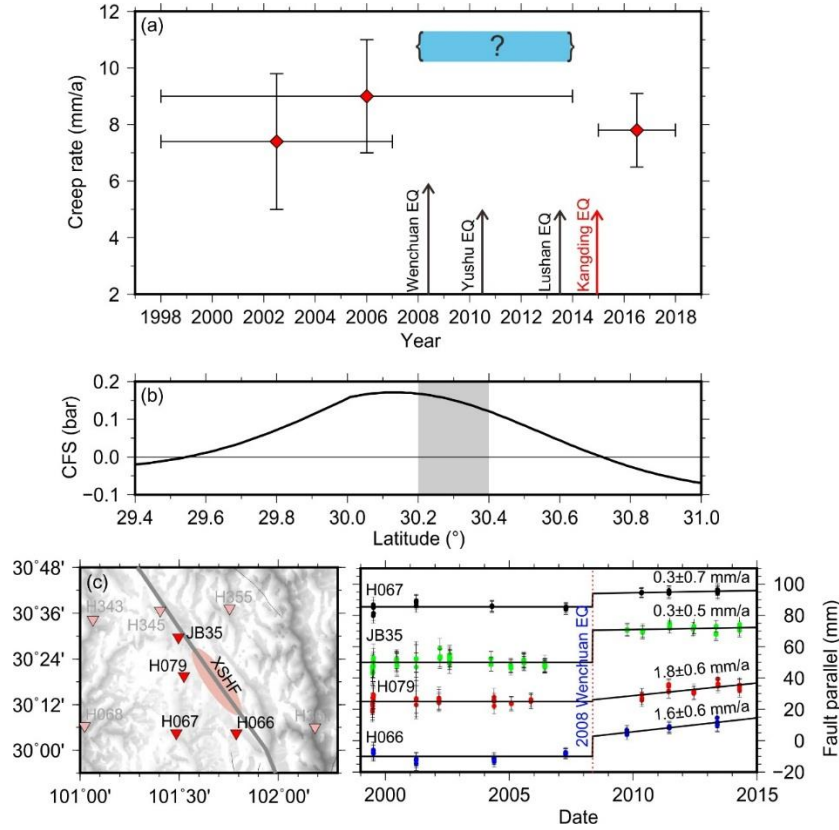


Figure 5.10. (a) Creep rate along the Xianshuihe fault as a function of time. Black (red) arrows show the time of large earthquake in eastern Tibet. Light green rectangle indicates the inferred creep rate in 2008–2014. (b) Coulomb failure stress (CFS) on the Xianshuihe caused by the 2008 Mw 7.9 Wenchuan, 2010 Mw 6.8 Yushu earthquake and the 2013 Mw 6.5 Lushan earthquake. The stress state was in 2013 (Shan et al., 2013). Orange ellipse indicates the proposed creep segment. (c) GPS sites distribution along the Xianshuihe fault, and time series of the fault parallel component in 1999–2015.

We attribute the temporal variation in creep rate to stress perturbations from nearby large earthquakes, i.e., the 2008 Mw 7.9 Wenchuan earthquake, the 2010 Mw 6.8 Yushu earthquake and the 2013 Mw 6.5 Lushan earthquake, which occurred in eastern Tibet between 2008 and 2014 and overlap the creep rate acceleration period. We show the Coulomb failure stress changes (Δ CFS) due to those earthquakes (co- and post-seismic stress; mostly induced by the 2008 Wenchuan Mw 7.9 earthquake) in Figure 5.10b (Shan et al., 2013); it is obvious that positive Δ CFS along the creep segment ($\sim 30.2^\circ\text{N}$ – 30.4°N), implying that the stress changes may have effects on the Xianshuihe fault creep rate (e.g., Xu et al., 2018).

Another intriguing issue is the 2014 Mw 5.9 Kangding earthquake, which occurred along the creep segment and just after the increase of creep rate. Although the relationship between the earthquake and creep on the Xianshuihe fault remains to be understood, there have been evidences on other continental faults that shallow fault creep rate acceleration could trigger medium-small

earthquakes, such as along the Haiyuan fault (e.g., [Jolivet et al., 2012](#)). Moreover, by comparing the coseismic slip of the 2014 Mw 5.9 Kangding earthquake with our preferred fault coupling derived from block model (Figure 5.4), we note that the earthquake ruptured at least part of creep regions, although data resolution does not allow to better constrain the creep distribution at depth.

5.6. Conclusions

In this study, we present a detailed description of the crustal deformation along the XXFS, which is one of the most seismically active and potentially most damaging one in China. Firstly, using the GPS velocity solution (1999–2014) for eastern Tibet and the elastic block model, we obtained left-lateral slip rates of 7–11 mm/a, decreasing with strike, along the fault system. In the northern part of the XXFS from latitude 32°N to latitude 30°N, the Xianshuihe fault appears to be predominantly creeping, whereas the Anninghe, Zemuhe and Xiaojiang faults show significant coupling.

Shallow creep appears to be long-lasting afterslip following the large (M 7.6 in 1973) and moderate-size (M 6.9 in 1981) earthquakes. Several arguments also indicates that relatively weak coupling further south also contain a transient contribution arousing from past earthquakes in 1955 and even 1893. This view is further supported by surface creep rate decaying through time and possibly having stopped during the last years, therefore starting a new cycle of increasing slip deficit accumulation.

We further identify that the Kangding-Bamei segment includes a ~30 km-long creeping section (latitude 30.2°N to 30.4°N) and find that creep rate accelerated during the 2008–2014 period, possibly as a result of stress increments induced by surrounding large earthquakes and among them the 2008 Mw 7.9 Wenchuan earthquake. Finally, quantitative calculation of moment budget highlights relatively high seismic potential on the Anninghe, Zemuhe and Xiaojiang faults, where the elastic strain deficit could be balanced by Mw 7.5, Mw 7.2 and Mw 7.4 earthquakes respectively.

Acknowledgments

We are grateful to all colleagues who constructed the GPS network and collected GPS measurements. Parts of the GPS sites velocities were derived from published papers (doi: 10.1016/j.tecto.2012.08.006 and doi: 10.1002/2016JB012839). Robert McCaffrey shared the block model program (www.web.pdx.edu/~mccaf/defnode.html). The GPS time series data were provided by GNSS Data Product Service Platform of China Earthquake Administration (<http://www.cgps.ac.cn>). The authors thank Guoyan Jiang for kindly sharing the coseismic slip result of the 2014 Mw 5.9 Kangding earthquake. We also show our thanks to Bin Shan for sharing the Coulomb failure stress result on the Xianshuihe fault, to Lei Zhang for sharing the InSAR result. This work was supported by the National Natural Science Foundation of China (grant number 41631073). Yanchuan Li was financially supported by the China Scholarship Council and the China Earthquake Administration. All figures were generated using the Generic Mapping Tools (GMT) software ([Wessel et al., 2013](#)).

5.7. References

- Allen, C. R., Zhuoli, L., Hong, Q., Xueze, W., Huawei, Z., Weishi, H., 1991. Field study of a highly active fault zone: The Xianshuihe fault of southwestern China. *Geol. Soc. Am. Bull.* 103 (9), 1178–1199.
- Altamimi, Z., Métivier, L., Collilieux, X., 2012. ITRF2008 plate motion model. *J. Geophys. Res., Solid Earth* 117, B07402.
- Bai, M., Chevalier, M. L., Pan, J., Replumaz, A., Leloup, P. H., Métois, M., Li, H., 2018. Southeastward increase of the late Quaternary slip-rate of the Xianshuihe fault, eastern Tibet: geodynamic and seismic hazard implications. *Earth Planet. Sci. Lett.* 485, 19–31.
- Bilham, R., Ozener, H., Mencin, D., Dogru, A., Ergintav, S., Cakir, Z., Aytun, A., Aktug, B., Yilmaz, O., Johnson, W., Mattioli, G., 2016. Surface creep on the North Anatolian fault at Ismetpasa, Turkey, 1944–2016. *J. Geophys. Res., Solid Earth* 121 (10), 7409–7431.
- Cakir, Z., Akoglu, A. M., Belabbes, S., Ergintav, S., Meghraoui, M., 2005. Creeping along the Ismetpasa section of the North Anatolian fault (Western Turkey): Rate and extent from InSAR. *Earth Planet. Sci. Lett.* 238 (1–2), 225–234.
- Cetin, E., Cakir, Z., Meghraoui, M., Ergintav, S., Akoglu, A. M., 2014. Extent and distribution of aseismic slip on the Ismetpaşa segment of the North Anatolian Fault (Turkey) from Persistent Scatterer InSAR. *Geochem. Geophys. Geosy.* 15 (7), 2883–2894.
- Deng, Q., Cheng, S., Ma, J., Du, P., 2014. Seismic activities and earthquake potential in the Tibetan Plateau. *Chinese J. Geophys.* 57 (7), 2025–2042.
- Deng, Q., Zhang, P., Ran, Y., Yang, X., Min, W., Chu, Q., 2003. Basic characteristics of active tectonics of China. *Sci. China. Ser. D.* 46, 356–372.
- Gutenberg, B., Richter, C. F., 1944. Frequency of earthquakes in California. *Bull. Seismol. Soc. Am.* 34 (4), 185–188.
- Hamiel, Y., Piatibratova, O., Mizrahi, Y., Nahmias, Y., Sagy, A., 2018. Crustal Deformation across the Jericho Valley section of the Dead Sea fault as resolved by detailed field and geodetic observations. *Geophys. Res. Lett.* 45 (7), 3043–3050.
- Jiang, G., Xu, X., Chen, G., Liu, Y., Fukahata, Y., Wang, H., Yu, G., Tan, X., Xu, C., 2015. Geodetic imaging of potential seismogenic asperities on the Xianshuihe-Anninghe-Zemuhe fault system, southwest China, with a new 3-D viscoelastic interseismic coupling model. *J. Geophys. Res., Solid Earth* 120 (3), 1855–1873.
- Jolivet, R., Lasserre, C., Doin, M. P., Guillaso, S., Peltzer, G., Dailu, R., Sun, J., Shen, Z.-K., Xu, X., 2012. Shallow creep on the Haiyuan fault (Gansu, China) revealed by SAR interferometry. *J. Geophys. Res., Solid Earth* 117, B06401.
- Larson, K. M., Bürgmann, R., Bilham, R., Freymueller, J. T., 1999. Kinematics of the India-Eurasia collision zone from GPS measurements. *J. Geophys. Res., Solid Earth* 104 (B1), 1077–1093.
- Li, Y., Shan, X., Qu, C., Liu, Y., Han, N., 2018. Crustal deformation of the Altyn Tagh fault based on GPS. *J. Geophys. Res., Solid Earth* 123 (11), 10309–10322.
- Lienkaemper, J. J., McFarland, F. S., 2017. Long-term afterslip of the 2004 M 6.0 Parkfield, California, earthquake—Implications for forecasting amount and duration of afterslip on other major creeping faults. *Bull. Seismol. Soc. Am.* 107 (3), 1082–1093.
- Loveless, J. P., Meade, B. J., 2011. Partitioning of localized and diffuse deformation in the Tibetan Plateau from joint inversions of geologic and geodetic observations. *Earth Planet. Sci. Lett.* 303

- (1–2), 11–24.
- McCaffrey, R., Qamar, A. I., King, R. W., Wells, R., Khazaradze, G., Williams, C. A., Stevens, C. W., Vollick, J. J., Zwick, P. C., 2007. Fault locking, block rotation and crustal deformation in the Pacific Northwest. *Geophys. J. Int.* 169 (3), 1315–1340.
- Minson, S. E., Simons, M., Beck, J. L., 2013. Bayesian inversion for finite fault earthquake source models I—Theory and algorithm. *Geophys. J. Int.* 194 (3), 1701–1726.
- Nocquet, J. M., 2018. Stochastic static fault slip inversion from geodetic data with non-negativity and bound constraints. *Geophys. J. Int.* 214 (1), 366–385.
- Nocquet, J. M., Jarrin, P., Vallée, M., Mothes, P. A., Grandin, R., Rolandone, F., Jarrin, P., Cisneros, D., Alvarado, A., Audin, L., Bondoux, F., 2017. Supercycle at the Ecuadorian subduction zone revealed after the 2016 Pedernales earthquake. *Nat. Geosci.* 10 (2), 145–149.
- Ozener, H., Dogru, A., Turgut, B., 2013. Quantifying aseismic creep on the Ismetpasa segment of the North Anatolian Fault Zone (Turkey) by 6 years of GPS observations. *J. Geodyn.* 67, 72–77.
- Papadimitriou, E., Wen, X., Karakostas, V., Jin, X., 2004. Earthquake triggering along the Xianshuihe fault zone of western Sichuan, China. *Pure Appl. Geophys.* 161 (8), 1683–707.
- Patil, A., Huard, D., Fonnesbeck, C. J., 2010. PyMC: Bayesian stochastic modelling in Python. *J. Stat. Softw.* 35 (4), 1–81.
- Ran, Y., Chen, L., Cheng, J., Gong, H., 2008. Late Quaternary surface deformation and rupture behavior of strong earthquake on the segment north of Mianning of the Anninghe fault. *Sci. China. Ser. D.* 51 (9), 1224–1237.
- Rui, X., Stamps, D. S., 2016. Present-day kinematics of the eastern Tibetan Plateau and Sichuan Basin: Implications for lower crustal rheology. *J. Geophys. Res., Solid Earth* 121 (5), 3846–3866.
- Segall, P., 2010. *Earthquake and Volcano Deformation*, Princeton Univ. Press, Princeton, N. J.
- Shan, B., Xiong, X., Zheng, Y., Jin, B., Liu, C., Xie, Z., Hsu, H., 2013. Stress changes on major faults caused by 2013 Lushan earthquake and its relationship with 2008 Wenchuan earthquake. *Sci. China. Ser. D.* 56 (7), 1169–1176.
- Shen, Z. K., Lü, J., Wang, M., Bürgmann, R., 2005. Contemporary crustal deformation around the southeast borderland of the Tibetan Plateau. *J. Geophys. Res., Solid Earth* 110, B11409.
- Stevens, V. L., Avouac, J. P., 2015. Interseismic coupling on the main Himalayan thrust. *Geophys. Res. Lett.* 42 (14), 5828–5837.
- Tapponnier, P., Molnar, P., 1977. Active faulting and tectonics in China. *J. Geophys. Res., Solid Earth* 82 (20), 2905–2930.
- Tapponnier, P., Zhiqin, X., Roger, F., Meyer, B., Arnaud, N., Wittlinger, G., Yang, J., 2001. Oblique stepwise rise and growth of the Tibet Plateau. *Science* 294(5547), 1671–1677.
- Wang, H., Wright, T. J., Biggs, J., 2009. Interseismic slip rate of the northwestern Xianshuihe fault from InSAR data. *Geophys. Res. Lett.* 36, L03302.
- Wang, W., Qiao, X., Yang, S., Wang, D., 2017. Present-day velocity field and block kinematics of Tibetan Plateau from GPS measurements. *Geophys. J. Int.* 208(2), 1088–1102.
- Weertman, J., J. R. Weertman., 1964. *Elementary Dislocation Theory*, 213 pp., MacMillan, New York.
- Wei, M., Sandwell, D., Smith-Konter, B., 2010. Optimal combination of InSAR and GPS for measuring interseismic crustal deformation. *Adv. Space Res.* 46 (2), 236–249.
- Wells, D. L., Coppersmith, K. J., 1994. New empirical relationships among magnitude, rupture length, rupture width, rupture area, and surface displacement. *Bull. Seismol. Soc. Am.* 84 (4),

- 974–1002.
- Wen, X., Ma, S., Xu, X., He, Y., 2008a. Historical pattern and behavior of earthquake ruptures along the eastern boundary of the Sichuan-Yunnan faulted-block, southwestern China. *Phys. Earth Planet. Inter.* 168 (1–2), 16–36.
- Wen, X., Fan, J., Yi, G., Deng, Y., Long, F., 2008b. A seismic gap on the Anninghe fault in western Sichuan, China. *Sci. China. Ser. D.* 51 (10), 1375–1387.
- Wessel, P., Smith, W. H., Scharroo, R., Luis, J., Wobbe, F., 2013. Generic Mapping Tools: improved version released. *Eos Trans. AGU* 94 (45), 409–410.
- Xu, X., Ward, L. A., Jiang, J., Smith-Konter, B., Tymofeyeva, E., Lindsey, E. O., Sylvester, A., Sandwell, D., 2018. Surface creep rate of the southern San Andreas fault modulated by stress perturbations from nearby large events. *Geophys. Res. Lett.* 45 (19), 10–259.
- Yan, B., Lin, A., 2017. Holocene activity and paleoseismicity of the Selaha Fault, southeastern segment of the strike-slip Xianshuihe Fault Zone, Tibetan Plateau. *Tectonophysics* 694, 302–318.
- Zhang, J., Wen, X. Z., Cao, J. L., Yan, W., Yang, Y. L., Su, Q., 2018a. Surface creep and slip-behavior segmentation along the northwestern Xianshuihe fault zone of southwestern China determined from decades of fault-crossing short-baseline and short-level surveys. *Tectonophysics*, 722, 356–372.
- Zhang, L., Cao, D., Zhang, J., Sui, L., 2018b. Interseismic fault movement of Xianshuihe Fault Zone based on across-fault deformation data and InSAR. *Pure Appl. Geophys.* 176 (2) 649–667.
- Zhang, Z., McCaffrey, R., Zhang, P., 2013. Relative motion across the eastern Tibetan Plateau: Contributions from faulting, internal strain and rotation rates. *Tectonophysics* 584, 240–256.
- Zhao, J., Jiang, Z., Niu, A., Liu, J., Wu, Y., Wei, W., Liu, X., Yan, W., 2015. Study on dynamic characteristics of fault locking and fault slip deficit in the eastern boundary of the Sichuan-Yunnan rhombic block. *Chinese J. Geophys.* 58(3), 872–885.
- Zheng, G., Wang, H., Wright, T. J., Lou, Y., Zhang, R., Zhang, W., Shi, C., Huang, J., Wei, N., 2017. Crustal deformation in the India-Eurasia collision zone from 25 years of GPS measurements. *J. Geophys. Res., Solid Earth* 122(11), 9290–9312.

Chapter 6· Discussions and conclusions

In this concluding chapter, I summarize what we learned from the fault behavior and their seismic potential in the Tibetan Plateau. I discuss the importance of fault creeping along the Haiyuan fault system and the Xianshuihe fault, and rephrase it in the context of creeping observations worldwide. Then, I present short comments on the geodetic data and their current level of confidence. Finally, I finish by discussing the limitations and future works.

6.1. Fault coupling and seismic potential

From the perspective of elastic rebound (Davison, 1901), the slip deficit accumulated on the locked (coupled) patch will be eventually released in a large earthquake or several small earthquakes. The inference is that, to some extent, we could evaluate future earthquake potential or derive rupture scenarios from interseismic locking distribution (e.g., Yang et al., 2019).

Over the last 30 years, benefiting from a wealth of new geodetic observation data, the interseismic fault coupling on crustal faults have been derived systematically. Among them, the Japan subduction zone (e.g., Loveless and Meade, 2010), the Sumatra subduction zone (e.g., Chlieh et al., 2008), the Andes subduction zone (e.g., Nocquet et al., 2014), the North Anatolian Fault (e.g., Bulut et al., 2019), the San Andreas Fault (e.g., Jolivet et al., 2015), and the Main Himalayan Thrust (e.g., Stevens and Avouac, 2015) have all been studied. The relationship between high coupling and earthquake is, to some extent, easier to test and verify in subduction zone; this is mainly because fast convergence rate lead to short earthquake reoccurrence time and frequent earthquakes; what's more, because shallow dip allows a good resolution of interseismic coupling map, at least for the downdip part (e.g., Kaneko et al., 2010; Perfettini and Avouac, 2014; Nocquet et al., 2017). For instance, Nocquet et al. (2017) show that the 2016 Mw 7.8 Pedernales earthquake ruptured two patches on the Ecuador subduction plate interface that were locked prior to the earthquake. Using the GPS data, Loveless and Meade (2011) show that the coseismic rupture extent for the March 11, 2011 Mw 9.0 earthquake Tohoku-oki earthquake may be spatially correlated (0.26 ± 0.05 to 0.82 ± 0.05) with a region estimated to be partially to fully coupled during the interseismic period preceding the event, though there is substantial variation in the estimated distribution and magnitude of coseismic slip. Compared to well-studied subduction zones, despite intensive studies focused on the fault deformation using geodetic measurements (i.e., GPS and InSAR) in the Tibetan Plateau, the interseismic fault coupling on main crustal faults are largely understudied. For instance, incomplete knowledge of the fault deformation along the Longmenshan fault led us to ignore the seismic potential for an Mw 7.9 (2008 Wenchuan) earthquake that actually occurred (Zhang, 2013).

This work, at least contribute to improve the knowledge along three major strike-slip faults in China, the Altyn Tagh fault, the Xianshuihe-Xiaojiang fault system and the Haiyuan fault system. My results show that the majority of the Altyn Tagh fault is locked, whereas only certain segments of the Xianshuihe-Xiaojiang fault system and the Haiyuan fault system are locked. Benefiting from the intensive geomorphology and paleoearthquake studies and abundant geodetic observations along the latter two fault systems, I identify locked segments corresponding to either 'seismic gap' or fault portions with historical earthquake elapsed for centuries, implying high seismic potential on these segments. More specifically, the Laohushan segment on the Haiyuan fault system and the Anninghe-Zemuhe fault on the Xianshuihe-Xiaojiang fault system seem to ready for a large earthquake to happen in the next decades. However, although large portions of the Altyn Tagh fault

appear locked, limited by the sparse GPS station coverage across the fault and incomplete knowledge of the rupture histories, I prefer to regard the coupling result as a first-order behavior. My quantitative calculation of the seismic moment deficit along the Altyn Tagh fault provide us with, at least, a sense of rupture potential. More geodetic observations and geological investigations are needed across the Altyn Tagh fault. Moreover, we learn from the limited case studies that the interseismic fault coupling along crustal faults in Tibet is highly heterogeneous, implying heterogeneous interseismic deformation behaviors and thus seismic potential. The interseismic fault coupling results in my work could provide reference to earthquake studies, guidance to the construction of high-rate GNSS stations aiming at Earthquake Early Warning, and useful information to disaster relief related departments.

We need to keep in mind that the fault coupling result in my study represents only a part of the seismic potential of the whole Tibetan Plateau. My studies also suffer from limitations, as I only focus on three main crustal faults in Tibet. There are other crustal faults that are understudied, such as the Longmenshan fault system and the Kunlun fault. Both faults hosted large earthquakes a few years ago, i.e., the 2001 Mw 7.8 Kokoxili earthquake on the Kunlun fault and the 2008 Mw 7.9 Wenchuan earthquake on the Longmenshan fault, investigating into the fault coupling could provide us with information about the onset of relocking and rupture area. Moreover, not all destructive earthquakes occur on known faults. Actually, quite a few moderate size earthquakes occurred in unexpected locations, like the 2013 Mw 6.9 Lushan earthquake, the 2015 Mw 6.5 Pishan earthquake and the 2017 Mw 6.5 Jiuzhaigou earthquake. All these events ruptured unmapped faults. Furthermore, there are cases of earthquakes occur on secondary faults in Tibet, such as the 1997 Mw 7.6 Manyi earthquake on the ~200 km-long Manyi fault and the 2016 Mw 6.6 Muji earthquake on the ~100 km-long Muji fault. To some extent, investigating the interseismic deformation along these unmapped and secondary faults is a real challenge for us. Currently, the CMONOC GPS network covering Tibet is still suffering from a limited spatial resolution. InSAR might bring new contribution but is largely affected by atmospheric errors and loss of coherence. Knowledge of rupture history along crustal faults is still limited, and the modeling of the complicated faults in Tibet needs a new generation of dynamic models, possibly incorporating strength variations and strain-weakening mechanisms. All these factors limit us in deriving an accurate fault-locking-map of the Tibetan Plateau.

6.2. What we learn about the shallow fault creep in Tibet

In my studies, one most important contribution is that I found two additional shallow creeping segments along the Haiyuan fault and one creeping segment on the Xianshuihe fault. Creeping faults have been discovered more than 50 years ago in the central part of California, i.e., the San Andreas Fault (e.g., [Louderback, 1942](#); [Steinbrugge et al., 1960](#); [Tocher, 1960](#); [Whitten and Claire, 1960](#)). In Tibet, shallow fault creep was first reported by [Allen et al. \(1991\)](#) along the Xianshuihe fault and [Cavalié et al. \(2008\)](#) along the Haiyuan fault. My results complement previous studies, yet raising questions regarding the creep mechanism, implications for earthquake cycle.

6.2.1. Interseismic fault creep on crustal faults in Tibet

My results show that the Altyn Tagh fault is locked to the surface (Chapter 3), implying no surface creep along the fault. Here, considering the fact that I used sparsely distributed GPS sites in my inversion, my results do not necessarily rule out the possibility that shallow creep exists along the Altyn Tagh fault. Recently, [Xu and Zhu \(2019\)](#) used InSAR data spanning 1996-2017 to investigate the interseismic fault deformation across the western Altyn Tagh fault (longitude 83°E-86°E), their results show surface creep rate of ~2.0 mm/a with a creep extending at 1.0–2.0 km depth. However, cautions should be paid regarding their modeling method; instead of analyzing the creep signal using data near the fault surface (several kilometers), they conducted cross-fault profiles extending 100 km long and tens of kilometers wide, and fitted the data using a buried infinite screw dislocation ([Segall, 2010](#)). Such a simple modeling method would bring large uncertainties to their results. Figure 6.1 shows one example from [Xu and Zhu \(2019\)](#).

It is obvious that no significant LOS rate gradient is found across the Altyn Tagh fault; besides, the simple arctangent curve fitting would mathematically produce the ‘creep rate’ result, which is worth considering regarding its physical meaning. Thus, it’s dangerous to interpret shallow creeps exist along the Altyn Tagh fault. With reference to what I did (Chapter 4 and Chapter 5), I propose that more careful works should be done.

Surface fault creep has long been identified. Creeping faults have been observed in the USA, Mexico, Italy, Turkey, Israel, Afghanistan, Pakistan, mainland China, Taiwan, the Philippines, and Japan. With the advance of high resolution space geodetic observations, it is now possible to map surface creeps in great detail. Figure 6.2 shows the known creeping fault world-wide. Table 6.1 summaries key point about these creeping faults (from [Harris, 2017](#)). There are quite a few similarities and differences between the creeping faults in Tibet and other creeping faults world-wide.

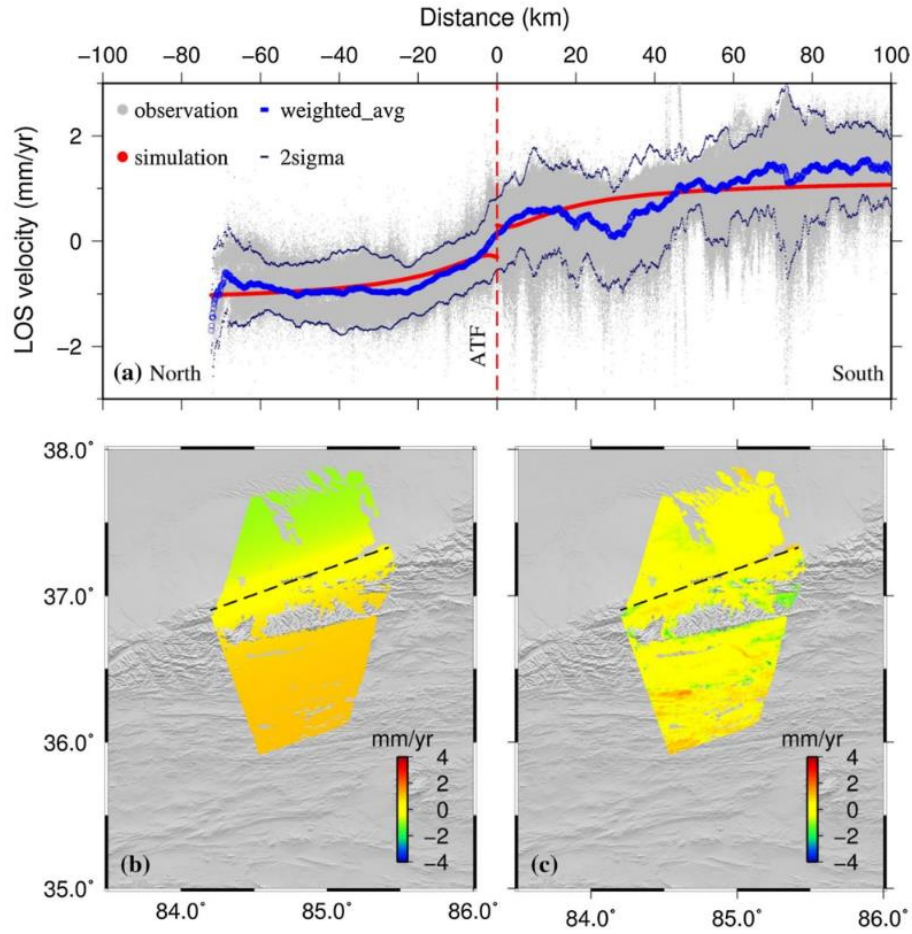


Figure 6.1. (a) Profiles and weighted average profile (dark blue line) with the 2σ deviation (light blue line) for the ENVISAT data. All the points shown on the left are projected onto the profile as gray dots. The red line denotes the best-fitting model with a slip rate of 7.4 mm/year and a locking depth of 18.0 km. (b) Simulation map generated from the best-fitting model values. (c) Residuals between the modeling and observation results. From Xu and Zhu (2019).



Figure 6.2. A global view of the locations of many of the world's well-documented shallow continental creeping faults (circles). Key: Flt = fault, FZ = Fault Zone. From Harris (2017).

Table 6.1. Well-documented shallow continental creeping faults (update from [Harris, 2017](#))

Fault Name	Fault Type*	Creep Length†	Creep Depth†	Fault Base†	Creep Rate/Deep Rate	Creep Mechanism
San Andreas fault, creeping section	S	100	0–20	20	0.8–0.9	Talc-bearing serpentinite, chlorite-smectite clay minerals, pressure solution creep
San Andreas fault, southern section	S	50	0–3	12	0.2	Water saturated sediments
Hayward and Calaveras Faults	S	185	0–7	12	0.3–0.6	Serpentinite, hydrothermal fluids
Rodgers Creek Fault	S	25	0–6	10	0.3–0.4	Fault geometry
Bartlett Springs Fault	S	85	0–5	13	0.5	Antigorite serpentinite
Greenville Fault	S	20	0–14	15	0.8–1.0	Mineralogy, smooth fault geometry, heat flow
Green Valley Fault	S	75	0–8	14	0.4–0.6	Mineralogy, smooth fault geometry, Heat flow
Maacama Fault	S	110	0–5	9	0.4–0.5	Mineralogy, smooth fault geometry, heat flow
Superstition Hills Fault	S	20	0–4	6	0.2–0.8	Elevated pore pressures in unconsolidated sediments
Imperial Fault	S	20	0–4	6	0.2–0.3	Elevated pore fluid pressure in the sediments
Alto Tiberina Fault	N	30	>4	4	0.9	Phyllosilicate-minerals CO ₂ -rich hydrous fluids decrease fault friction, Fluid overpressures
North Anatolian fault, Ismetpasa region	S	100	0–5	15	0.3	Serpentinite, downward circulation of meteoritic fluids, limestone and pressure solution creep
North Anatolian fault, Destek region	S				0.3–0.4	
Dead Sea Fault, Jordan Valley section	S	40	0–1.5	10	0.6	Thick salt layers, high heat flow
Chaman Fault, southern and central sections	S	125 (340)	0–?	<1	?–1.0	Ophiolite, serpentinite bodies
Philippine Fault	S	600			0.3–1.0	Low rock strength, high hydrothermal flow
Xianshuihe Fault	S				0.4–0.6	
Haiyuan Fault, Lao Hu Shan segment	S	35	5–15	20	1	Frictional properties
Longitudinal Valley Fault	R	75	0–26	26	0.8–0.9	Lichi Melange Pressure solution creep
Atotsugawa Fault	S				<0.1	Graphite

* S=Strike-slip, N=Normal, R=Reverse; † in kilometers.

Similarities:

(1) Shallow creeps occur along large-scale strike-slip faults in Tibet. Except for the Alto Tiberina Fault (normal) and the Longitudinal Valley Fault (thrust/reverse), the remaining well-documented shallow continental creeping faults are strike slip faults. In Tibet, both the Haiyuan fault and the Xianshuihe fault are large-scale strike-slip faults, where shallow creeps occur. There are other strike-slip faults, such as the Altyn Tagh fault, where shallow fault creeping might exist but needs further study. The strike-slip Kunlun fault, similar to the Haiyuan fault and the Xianshuihe fault, has repeated ruptures, might also be one candidate. Besides, by analyzing the rocks in the fault surface, the Guanxian-Anxian Fault (the frontal fault of the Longmen Shan thrust belt) was proposed to be creeping at long-term at shallow depths and locked at greater depths (He et al., 2018); such an inference needs more evidence from creepmeter measurements, alignment array measurements, repeating earthquakes, and/or satellite geodetic measurements (GPS and InSAR). Although there is no firm evidence, creeping seems to easier be seen/observed along strike-slip faults.

(2) Slip deficit occur along the creeping segments. As seen from Table 6.1, almost all creeping faults have slip deficit, that is, the ratio of creep rate to loading rate is less than 100%. My results along the Haiyuan fault system show that shallow creep segments release around 20–100% of the loading rate, implying slip deficit accumulation on the fault plane and the ability of rupture. In the discussion section of Chapter 4, I present arguments about the rupture characters on the creeping segments along the Haiyuan fault system. In the study on the Xianshuihe fault (Chapter 5), despite my results show the creep rate account for 109% of the loading rate, considering its transient behavior, I could not rule out the possibility that slip deficit accumulate on the fault plane. This suggests that the potential slip deficit on the creeping segment could be released by ruptures of medium-small-sized asperities. Both the 1748 M 6.7 earthquake and the 2014 Mw 5.9 earthquake, occurred on the creeping segment of the Xianshuihe fault, might be such cases. The above arguments suggest regular earthquakes could occur on the creeping segments. I present more arguments in the next section. Actually, Harris and Abrahamson (2014) investigated the ground motions from the 11 largest well-recorded earthquakes (M 5.0–6.7) on shallow creeping faults in the San Andreas Fault system; they found that the peak ground motions generated by the creeping fault earthquakes are similar to the peak ground motions generated by earthquakes on locked faults.

Differences:

(1) Surface creep along the Haiyuan fault and the Xianshuihe fault are relatively short in length. Three creeping segments along the Haiyuan fault system have lengths of 10–43 km, and only a 35 km-long segment of the Xianshuihe fault is creeping. Despite the majority of the Xianshuihe fault appears to be loosely coupled, we are prone to regard the mild fault coupling as associated with the long-term afterslip of the 1973 M 7.6 Luho earthquake (Chapter 5). Globally, the Philippine Fault has creep length of 600 km, 100 km-long segment of the North Anatolian fault is creeping, and the creeping segments along the San Andreas Fault system have lengths ranging from 20 to 185 km.

(2) Surface creeps along the Haiyuan fault and the Xianshuihe fault extend to the bottom of the seismogenic portion. This means that no locked patches exist on the creeping segments, as we show in Chapter 4 and Chapter 5. We note that, currently, creeps along the creeping section of the San Andreas Fault and the Longitudinal Valley Fault were reported to extend to the bottom of the seismogenic portion, whereas other creeping faults (segments) extend 15-90% of the seismogenic depth (Table 6.1).

(3) The mechanism of shallow creep along the Haiyuan fault system and the Xianshuihe fault system has yet to be understood. As shown in Table 6.1, a range of physical and chemical processes have been proposed to explain the occurrence of fault creep, including the frictional resistance of specific rock types, chemical reactions, dilation of dry rocks, elevated pore pressure, elevated temperatures, fault geometry, or combinations of these factors. Along the Haiyuan fault system (Chapter 4), we propose the creeps to be related to fault frictional properties. Along the Xianshuihe fault (Chapter 5), we suggest the creep might be activated by postseismic deformation induced by previous earthquakes, or activated by stress (e.g., Coulomb failure stress) perturbations from preceding earthquakes, or related to tectonic loading. Here, I have to stress that a large range of factors that might cause the shallow creep along the Haiyuan fault system and the Xianshuihe fault system still remains to be understood. Our above hypotheses need more detailed geological and geomorphological investigations in the future.

(4) Transient creep behaviors along the Haiyuan fault system and the Xianshuihe fault system. Along the Laohushan fault (Haiyuan fault system), Jolivet et al. (2013) used InSAR data to map the spatio-temporal evolution of shallow creep and reported that the creep rate accelerated in 2007; the transient behaviors were coeval with the largest earthquakes ($M \sim 4-5$). Along the Xianshuihe fault, my results (Chapter 5) also show an increase in creep rate during the 2008–2014 period that might related to the Coulomb failure stress increment induced by the 2008 Mw 7.9 Wenchuan earthquake. What is interesting is the 2014 Mw 5.9 Kangding earthquake occurred along the creeping segment at the end of the period of accelerated creep. Published studies show transient creep behaviors have been observed along the Ismetpasa segment of the North Anatolian Fault, the Parkfield region of the San Andreas Fault and the Hayward fault. Although I am not sure if other creeping faults have the transient behavior, it seems to be a common feature.

In general, still too little is known about the spatial distribution of creep along the Haiyuan fault and the Xianshuihe fault, the physical mechanisms of the fault creep, and the role of creep in major ruptures, to draw conclusions of a predictive nature.

6.2.2. Very long-term creep/afterslip on crustal faults in Tibet

Among the creep mechanisms that I proposed for the creeps on the Haiyuan fault system and the Xianshuihe fault, postseismic afterslip following a large earthquake might be one candidate. However, the classic view hold that that afterslips only lasts a few years after the mainshock. Thus,

the question is whether it is possible for afterslips lasting for several decades (46 years for the Xianshuihe fault and 98 years for the Haiyuan fault). In that case, what mechanism does control such a long-lasting aseismic slip? The case of the North Anatolian Fault might help to understand these questions.

There is a hypothesis that the observed long-lasting (10–100 years) fault creep is a continuation of postseismic fault slip, which is perhaps then loaded by other, deeper relaxation processes in the Earth's lower crust and upper mantle. Cakir et al. (2012) suggested this hypothesis for the Izmit section of the North Anatolian Fault, and Cakir et al. (2005) and Cetin et al. (2014) discussed this hypothesis for the Ismetpasa section that is hundreds of kilometers to the east, on the same fault. However, new ideas do not agree with the above hypothesis. Bilham et al. (2016) showed that although there may indeed be some long-lasting effects from the 1944 magnitude 7.4 earthquake, most of the creep along the Ismetpasa section of the North Anatolian Fault that is observed today is due to tectonic loading. Similarly, Hussain et al. (2016) showed that the actual postseismic creep rate for the Izmit section of the North Anatolian Fault is much slower than that originally inferred by Cakir et al. (2012) and that this slower postseismic creep rate is consistent with a creep rate that decays with time following a large earthquake.

I propose that long-lasting afterslip is possible. As I showed for the creep rate at the Xialatuo site on the Xianshuihe fault, it is quite obvious that the observed surface creep was associated with the afterslip of the 1973 M 7.6 Luhuo earthquake (Chapter 5). Despite we are not sure about the mechanism of the creep that we identified along the Bamei-Kangding segment, currently, we have no reason to rule out that creep was activated by the afterslip of the 1973 M 7.6 Luhuo earthquake or related to the event. Actually, there have been studies showing that earthquakes could trigger fault creep. The 2014 Napa, California, earthquake, a magnitude 6.0 event northeast of San Francisco, triggered sizable postseismic fault slip (creep) in a fault zone that lacked notable (>2 mm/a) preevent fault creep (Lienkaemper et al., 2016). The recent 2019 Ridgecrest, California Earthquake sequence (Mw 6.4 and Mw 7.1) triggered aseismic slip along 20–25 km of the central Garlock fault (Barnhart et al., 2019); as of now, no study has been published to investigate its temporal variations. Along the Haiyuan fault, comparisons between creep-distribution and historical earthquake ruptures indicate that the observed surface creep might be related to the 1920 M~8 Haiyuan earthquake (Chapter 4). The long-lasting afterslip, as an alternative, gives a reasonable explanation for the current datasets. I suggest that fault frictional properties might be the mechanism controlling the long-lasting aseismic slip. That means, the aseismic slip on the Haiyuan fault might has much longer decay time than the afterslips following regular earthquakes.

6.2.3. The role of shallow creeping in seismic behavior

I have discussed in Chapter 4 and Chapter 5 regarding the implications of interseismic creep and afterslip on the earthquake occurrence and rupture location. Here, I address two issues: are regular

earthquakes occur on creeping segments? Could coseismic rupture propagate through creeping segments; in other words, could creeping segments act as permanent barriers?

Although it is generally thought that a large earthquake would not occur on a creeping fault section, it has been observed that medium earthquakes occur on shallow creeping faults, such as the M 5.0-6.6 earthquakes (1966-2007) recorded on shallow creeping faults in the San Andreas Fault system (Harris and Abrahamson, 2014). It is also recognized that small earthquakes occur at the boundaries between creeping and locked parts of faults (Stevens and Avouac, 2015). Harris (2017) argue that *“it appears that well-recorded creeping fault earthquakes of up to magnitude 6.6 that have occurred in shallow continental regions produce similar fault-surface rupture areas and similar peak ground shaking as their locked fault counterparts of the same earthquake magnitude. The behavior of much larger earthquakes on shallow creeping continental faults is less well known, because there is a dearth of comprehensive observations”*. I acknowledge that, at least for now, we could not rule out the possibility that large earthquakes could occur on creeping faults. But I think this possibility is relatively small. The study of Wei et al. (2013) may provide us with some clues. In a study of creep events on two California faults, Wei et al. (2013) propose that the frictional behavior of the crustal layers may be a complex depth-dependent layering of aseismic (velocity-strengthening) and seismic (velocity-weakening). That is to say, even creeping regions of faults have locked patches sprinkled among them, and thus ensuring earthquake nucleation and rupture propagation. From my perspective, it is relatively easier for small locked patches rupture and results in medium-small earthquakes; whereas producing a large earthquake requires the cooperation of several asperities, which needs complex rate-weakening and kinematic triggering processes. Here, what is intriguing is that we hardly see locked patches sprinkled in creeping regions (from kinematic inversions), that is probably indicates geodesy observations (even high spatial resolution InSAR) have limited resolution in depth. Studying repeated earthquakes on creeping segments may be a way to verify the above hypothesis. Also note, in Chapter 4 and Chapter 5, I propose little seismic potential on the creeping segments along the Haiyuan fault system and the Xianshuihe fault. This inference is based on observational data and inversion results, and is not contradictory to the point I am discussing.

Hypothesis has been proposed that earthquakes nucleate in a locked part of a fault and propagate into or through a creeping part of a fault. Such an inference has been confirmed in higher fault slip rate (above 0.1 m/s) rotary shear laboratory experiments on serpentinite (Kohli et al., 2011). Continuing on this theme, McLaskey and Kilgore (2013) observed on laboratory experiments that small earthquakes may occur solely due to a high stressing rate (regardless of creeping fault or locked fault). Such an inference might also applies to larger earthquakes. Consistent with these studies, Weng and Ampuero (2019) conducted numerical simulations to earthquake rupture and concluded that the energy release rate of a long steady state rupture depends on rupture width, stress drop, and shear modulus, and is independent of propagation distance and rupture speed. The inference is that earthquake rupture through a creeping fault segment cannot be ruled out on the

physical grounds of the present model.

In general, the above discussions suggest that earthquakes could occur on and propagate through a creeping part of a fault. My studies on the relationship between historical ruptures and shallow creeps on the Haiyuan fault system and the Xianshuihe fault are consistent with this view. Therefore, although I suggest small seismic potential on the creeping faults in my studies, we cannot completely discard that earthquakes might happen on the creeping segments in the future.

6.3. What we learn about the geodetic data

In this section, I stress the lessons that we learned from comparing and incorporating different source of geodetic data (GPS, InSAR and Leveling).

The vertical deformation in the observed InSAR LOS displacements could not be ignored. In previous studies, a conventional practice was to ignore the vertical deformation in InSAR, which might lead to erroneous conclusions. An example showing the contribution of vertical deformation in InSAR is presented in Chapter 2. In Tibet, the convergence between the Indian plate and the Eurasian plate is accommodated by crustal shortening, thickening and lateral extrusion, thus inevitably causes vertical deformation. For instance, leveling results show that the eastern and northeastern Tibet have a vertical velocity of up to ~ 6 mm/a relative to the stable Sichuan Basin (Hao et al., 2014). Unfortunately, so far, kinematic models (e.g., block model, fault dislocation model) could not effectively incorporate vertical deformation. As an option, as I show in Chapter 4 and Chapter 5, the remove-filter-restore method could separate long wavelength vertical deformation from the observed InSAR LOS ratemap, despite short wave length vertical deformation might still be preserved. To sum up, I propose that a preprocessing of the observed InSAR data is needed before further interpreting.

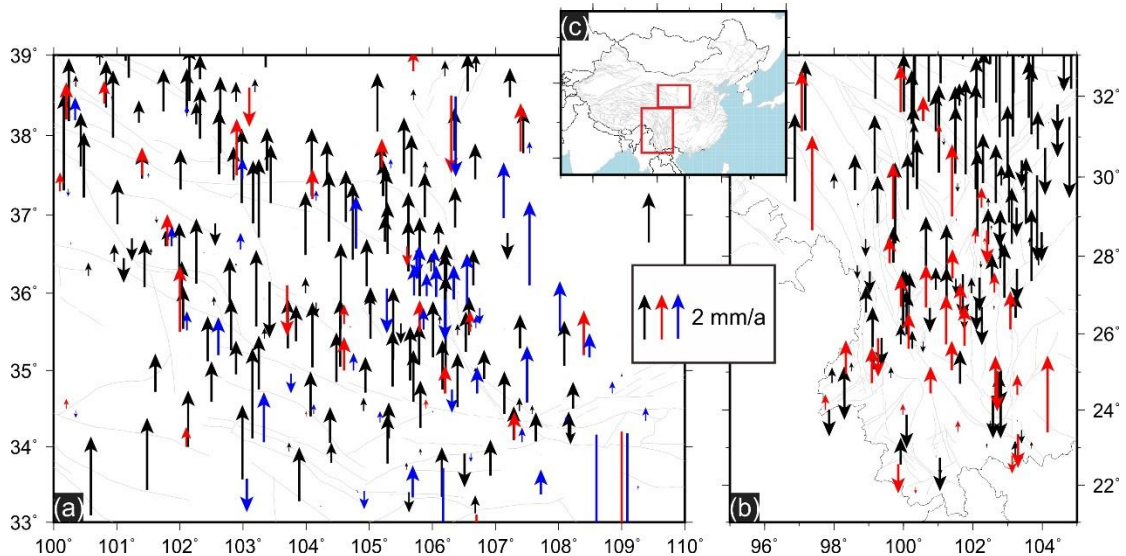


Figure 6.3. Comparison of GPS vertical velocities from different studies. (a) The black arrows show GPS vertical velocities from Liang et al. (2013), red arrows show GPS vertical velocities from Pan et al. (2018), and blue arrows represent GPS vertical velocities from Su et al. (2019). (b) The black arrows show GPS vertical velocities from Liang et al. (2013), red arrows show GPS vertical velocities from Hao et al. (2016). The regions are outlined in (c). GPS vertical velocities are in the ITRF 2008.

The vertical GPS velocity in Tibet should be used with caution. I show in Chapter 4 that the conventional nontectonic deformation corrections (especially for campaign-mode GPS sites) in GPS vertical velocity estimation, such as atmospheric loading and surface water loading (Liang et al.,

2013), are insufficient to derive a reliable tectonic vertical velocity solution. Actually, different studies have significantly different vertical velocities even for the same continuous GPS stations. I show the published results in Figure 6.3. It is obvious that different GPS vertical velocity solutions differ significantly. Currently, we could not determine which solution is more reliable; my study stresses the need for a uniformed GPS vertical velocity solution of the Tibetan Plateau.

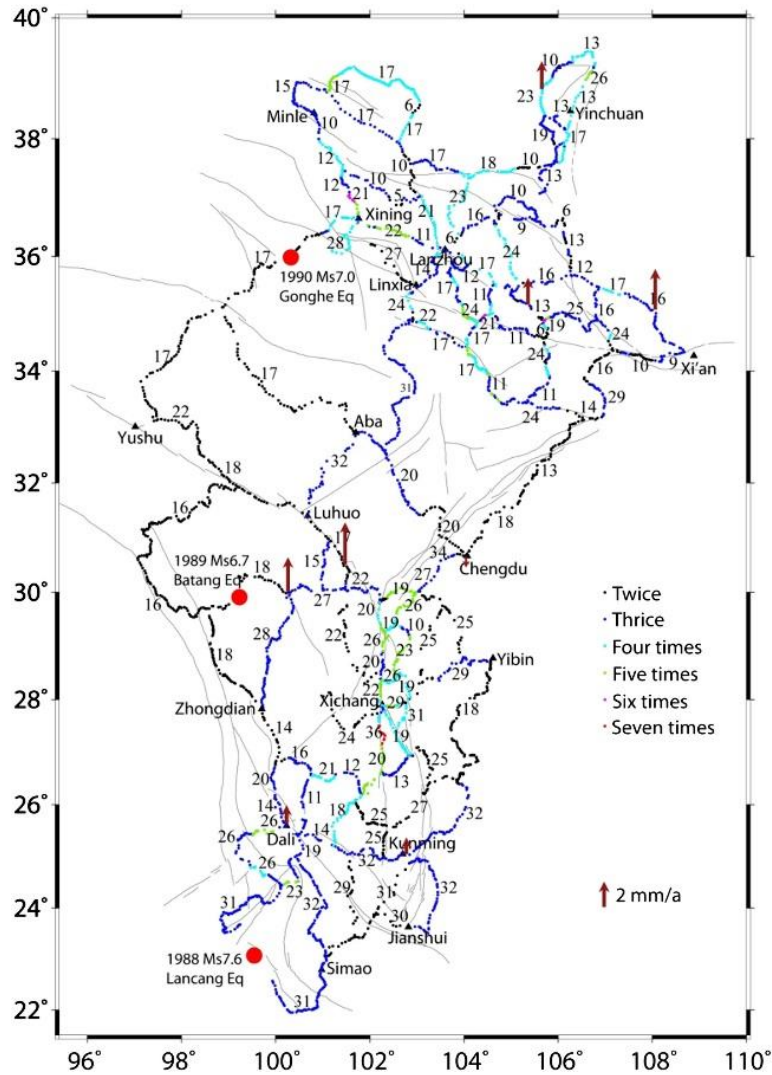


Figure 6.4. Map showing leveling routes and their surveying time spans. The dots show the locations of the leveling benchmarks, whose colors denote the number of survey epochs. The numbers next to the routes indicate the duration years between the first and last observations. The red solid circles denote the three earthquakes which contaminated the leveling measurements. Figure from Hao et al. (2014).

The long-term leveling vertical velocity solution (1970-2012) should also be used with caution. In Chapter 4, I also stress the inconsistency between Leveling and GPS/InSAR. There are several factors controlling the reliability of the leveling velocity solution: coseismic/postseismic contribution, route of the leveling measurements, time-varying vertical deformation, and systematic errors. Figure 6.4 shows the leveling routes and their surveying time spans in Tibet (Hao et al., 2014). During the 1970-2012 period, several earthquakes ($M_s \geq 6$) occurred adjacent to the route of the

leveling measurements ([Hao et al., 2014](#)), limited by the data observations of coseismic and postseismic deformation, source models of these earthquakes were inaccurate. Therefore, it is risky to adopt simple source models to account for the contributions from these earthquakes. The route of the leveling measurements also play a part. Basically, the leveling route is along the roads and villages, and thus inevitably affected by human factors, such as groundwater pumping. Time-varying vertical deformation, such as annual cycle nontectonic loading, may also contribute to the uncertainty of the leveling velocity solution (campaigns of only 2–7 times); despite we generally regard both vertical and horizontal deformation are linear, the influence of nonlinear factors, especially in vertical, is significant and cannot be excluded. Furthermore, systematic error is an inherent problem with leveling measurements (e.g., [Reilinger and Brown, 1981](#)). While various instrumental and procedural modifications designed to enhance leveling precision have been introduced over the years, the basic measurement system has remained virtually unchanged since the mid-nineteenth century. The physical source(s) of systematic errors remain poorly understood, yet topography dependent errors are an exceptionally troublesome type for leveling. Other varieties of systematic error also contribute, such as the large, long baseline accumulations of error ([Vanicek et al., 1980](#)).

6.4. Future work

Summarizing what we found and discussed regarding the crustal deformation along the Altyn Tagh fault, the Haiyuan fault system and the Xianshuihe-Xiaojiang fault system, I propose further works for future.

First of all, large scale SAR data crossing the Altyn Tagh fault, the Xianshuihe-Xiaojiang fault system and the Longmenshan fault could be processed. As I show in Figure 1.8, a large portion of the Altyn Tagh fault remain unmapped by InSAR; furthermore, whether shallow creeping exists along the fault is unclear, thus leaving more uncertainties and possibilities in interpreting earthquake cycles on the fault. Similar to the Altyn Tagh fault, the majority of the Xianshuihe-Xiaojiang fault system has been unmapped by InSAR; despite dense GPS stations have been deployed across the fault system, we still have a limited ability in addressing the creeping behaviors on the Kangding-Bamei segment, and thus unclear about its relationship with major earthquakes. To further investigate the role of shallow creep in earthquake rupture, the Longmenshan fault system provides a rare opportunity, because of the occurrence of the 2008 Mw 7.9 Wenchuan earthquake. The Guanxian-Anxian fault zone, the frontal fault of the Longmen Shan thrust belt, was reported to be creeping at shallow depths and locked at greater depths. During the Wenchuan earthquake, the shallow creeping section of the Guanxian-Anxian fault ruptured seismically accommodating 4 m of seismic slip, however, a much larger amount of slip was accommodated by the Yingxiu-Beichuan fault (up to 11 m; [He et al., 2018](#)). To verify the above inference, geodetic observations (i.e., InSAR) crossing the fault zone prior to the 2008 Wenchuan earthquake are needed.

A second perspective is to investigate the temporal creep/afterslip behaviors on the Haiyuan fault system and the Xianshuihe fault. One certain question is to know whether the creep on the Haiyuan fault and the Xianshuihe fault are long-term or the afterslip of preceding earthquakes. Geodetic observations spanning tens of years could help. Thanks to the accumulation of SAR data (e.g., ENVISAT and ERS) from the late 90s and the open access of the Sentinel SAR data, we could address the above issues. This is a good hint for further study.

Third, more accurate nontectonic corrections are needed when processing GPS data for the vertical velocities. Currently, surface mass changes (usually derived from GRACE data) and seasonal oscillations (polynomial fitting) are the two main corrections when deriving the vertical GPS sites velocities. However, several other factors contribute the uncertainty of vertical velocity (especially on campaign-mode stations), i.e., the relation between GPS station and denudated surface, truncation errors in computing GRACE loading effect, non-strict annual and semi-annual variations, among others. We expect more efforts will be made in GPS data processing.

Last, as noticed in my studies, kinematic models incorporating vertical deformation are needed. Currently, we are still not sure about the role of vertical deformation in the crustal deformation of

the Tibetan Plateau, thus resulting in vague understandings of the crustal deformation mechanisms, such as lithosphere extrusion model and continuum model, especially in determining the existence of lower crustal flow.

For sure, we will get a long way to solve the above issues. I expect with the development of the discipline, more and more people could participate in the study of earth science.

6.5. References

- Allen, C. R., Zhuoli, L., Hong, Q., Xueze, W., Huawei, Z., & Weishi, H. (1991). Field study of a highly active fault zone: The Xianshuihe fault of southwestern China. *Geological Society of America Bulletin*, 103(9), 1178-1199.
- Barnhart, W. D., Hayes, G. P., & Gold, R. D. (2019). The July 2019 Ridgecrest, California earthquake sequence: kinematics of slip and stressing in cross-fault ruptures. *Geophysical Research Letters*, 46.
- Bilham, R., Ozener, H., Mencin, D., Dogru, A., Ergintav, S., Cakir, Z., ... & Mattioli, G. (2016). Surface creep on the North Anatolian fault at Ismetpasa, Turkey, 1944–2016. *Journal of Geophysical Research: Solid Earth*, 121(10), 7409-7431.
- Bulut, F., Aktuğ, B., Yaltırak, C., Doğru, A., & Özener, H. (2019). Magnitudes of future large earthquakes near Istanbul quantified from 1500 years of historical earthquakes, present-day microseismicity and GPS slip rates. *Tectonophysics*, 764, 77-87.
- Cakir, Z., Akoglu, A. M., Belabbes, S., Ergintav, S., & Meghraoui, M. (2005). Creeping along the Ismetpasa section of the North Anatolian fault (Western Turkey): Rate and extent from InSAR. *Earth and Planetary Science Letters*, 238(1-2), 225-234.
- Cakir, Z., Ergintav, S., Özener, H., Dogan, U., Akoglu, A. M., Meghraoui, M., & Reilinger, R. (2012). Onset of aseismic creep on major strike-slip faults. *Geology*, 40(12), 1115-1118.
- Cavalié, O., Lasserre, C., Doin, M. P., Peltzer, G., Sun, J., Xu, X., & Shen, Z. K. (2008). Measurement of interseismic strain across the Haiyuan fault (Gansu, China), by InSAR. *Earth and Planetary Science Letters*, 275(3-4), 246-257.
- Cetin, E., Cakir, Z., Meghraoui, M., Ergintav, S., & Akoglu, A. M. (2014). Extent and distribution of aseismic slip on the Ismetpaşa segment of the North Anatolian Fault (Turkey) from Persistent Scatterer InSAR. *Geochemistry, Geophysics, Geosystems*, 15(7), 2883-2894.
- Chlieh, M., Avouac, J. P., Sieh, K., Natawidjaja, D. H., & Galetzka, J. (2008). Heterogeneous coupling of the Sumatran megathrust constrained by geodetic and paleogeodetic measurements. *Journal of Geophysical Research: Solid Earth*, 113(B5).
- Davison, C. (1901). The Great Japanese Earthquake of October 28, 1891. *The Geographical Journal*, 17(6), 635-655.
- Hao, M., Freymueller, J. T., Wang, Q., Cui, D., & Qin, S. (2016). Vertical crustal movement around the southeastern Tibetan Plateau constrained by GPS and GRACE data. *Earth and Planetary Science Letters*, 437, 1-8.
- Hao, M., Wang, Q., Shen, Z., Cui, D., Ji, L., Li, Y., & Qin, S. (2014). Present day crustal vertical movement inferred from precise leveling data in eastern margin of Tibetan Plateau. *Tectonophysics*, 632, 281-292.
- Harris, R. A. (2017). Large earthquakes and creeping faults. *Reviews of Geophysics*, 55(1), 169-198.
- Harris, R. A., & Abrahamson, N. A. (2014). Strong ground motions generated by earthquakes on creeping faults. *Geophysical Research Letters*, 41(11), 3870-3875.
- He, X. L., Li, H. B., Wang, H., Zhang, L., Xu, Z. Q., & Si, J. L. (2018). Creeping along the Guanxian-Anxian fault of the 2008 Mw 7.9 Wenchuan earthquake in the Longmen Shan, China. *Tectonics*, 37(7), 2124-2141.

- Hussain, E., Wright, T. J., Walters, R. J., Bekaert, D., Hooper, A., & Houseman, G. A. (2016). Geodetic observations of postseismic creep in the decade after the 1999 Izmit earthquake, Turkey: Implications for a shallow slip deficit. *Journal of Geophysical Research: Solid Earth*, 121(4), 2980-3001.
- Jolivet, R., Simons, M., Agram, P. S., Duputel, Z., & Shen, Z. K. (2015). Aseismic slip and seismogenic coupling along the central San Andreas Fault. *Geophysical Research Letters*, 42(2), 297-306.
- Kaneko, Y., Avouac, J. P., & Lapusta, N. (2010). Towards inferring earthquake patterns from geodetic observations of interseismic coupling. *Nature Geoscience*, 3(5), 363.
- Liang, S., Gan, W., Shen, C., Xiao, G., Liu, J., Chen, W., ... & Zhou, D. (2013). Three-dimensional velocity field of present - day crustal motion of the Tibetan Plateau derived from GPS measurements. *Journal of Geophysical Research: Solid Earth*, 118(10), 5722-5732.
- Lienkaemper, J. J., S. B. DeLong, C. J. Domrose, & C. M. Rosa (2016), Afterslip behavior following the M6.0, 2014 South Napa earthquake with implications for afterslip forecasting on other seismogenic faults, *Seismological Research Letter*, 87(3), 609–619
- Louderback, G. D. (1942). Faults and earthquakes. *Bulletin of the Seismological Society of America*, 32(4), 305-330.
- Loveless, J. P., & Meade, B. J. (2010). Geodetic imaging of plate motions, slip rates, and partitioning of deformation in Japan. *Journal of Geophysical Research: Solid Earth*, 115(B2).
- Loveless, J. P., & Meade, B. J. (2011). Spatial correlation of interseismic coupling and coseismic rupture extent of the 2011 Mw=9.0 Tohoku-oki earthquake. *Geophysical Research Letters*, 38(17).
- McLaskey, G. C., & Kilgore, B. D. (2013). Foreshocks during the nucleation of stick - slip instability. *Journal of Geophysical Research: Solid Earth*, 118(6), 2982-2997.
- Nocquet, J. M., Jarrin, P., Vallée, M., Mothes, P. A., Grandin, R., Rolandone, F., ... & Régnier, M. (2017). Supercycle at the Ecuadorian subduction zone revealed after the 2016 Pedernales earthquake. *Nature Geoscience*, 10(2), 145.
- Nocquet, J. M., Villegas-Lanza, J. C., Chlieh, M., Mothes, P. A., Rolandone, F., Jarrin, P., ... & Martin, X. (2014). Motion of continental slivers and creeping subduction in the northern Andes. *Nature Geoscience*, 7(4), 287.
- Pan, Y., Shen, W. B., Shum, C. K., & Chen, R. (2018). Spatially varying surface seasonal oscillations and 3-D crustal deformation of the Tibetan Plateau derived from GPS and GRACE data. *Earth and Planetary Science Letters*, 502, 12-22.
- Reilinger, R. and Brown, L. (2013). Neotectonic Deformation, Near-Surface Movements and Systematic Errors in U.S. Releveling Measurements: Implications for Earthquake Prediction. In *Earthquake Prediction* (eds D.W. Simpson and P.G. Richards).
- Segall, P. (2010). *Earthquake and volcano deformation*. Princeton University Press.
- Steinbrugge, K. V., Zacher, E. G., Tocher, D., Whitten, C. A., & Claire, C. N. (1960). Creep on the San Andreas Fault. *Bulletin of the Seismological Society of America*, 50(3), 389-415.
- Stevens, V. L., & Avouac, J. P. (2015). Interseismic coupling on the main Himalayan thrust. *Geophysical Research Letters*, 42(14), 5828-5837.
- Su, X., Yao, L., Wu, W., Meng, G., Su, L., Xiong, R., & Hong, S. (2019). Crustal deformation on the northeastern margin of the Tibetan plateau from continuous GPS observations. *Remote Sensing*, 11(1), 34.

- Tocher, D. (1960). Creep on the San Andreas fault-Creep rate and related measurements at Vineyard, California. *Bulletin of the Seismological Society of America*, 50, 394-404.
- Vanicek, P., Castle, R. O., & Balazs, E. I. (1980). Geodetic leveling and its applications. *Reviews of Geophysics*, 18(2), 505-524.
- Wei, M., Kaneko, Y., Liu, Y., & McGuire, J. J. (2013). Episodic fault creep events in California controlled by shallow frictional heterogeneity. *Nature Geoscience*, 6(7), 566.
- Weng, H., & Ampuero, J. P. (2019). The Dynamics of Elongated Earthquake Ruptures. *Journal of Geophysical Research: Solid Earth*, 124, 8584– 8610.
- Whitten, C. A. (1960). Analysis of geodetic measurements along the San Andreas Fault. *Bulletin of the Seismological Society of America*, 50, 404-415.
- Xu, C., & Zhu, S. (2019). Temporal and spatial movement characteristics of the Altyn Tagh fault inferred from 21 years of InSAR observations. *Journal of Geodesy*, 1-14.
- Yang, H., Yao, S., He, B., Newman, A. V., & Weng, H. (2019). Deriving rupture scenarios from interseismic locking distributions along the subduction megathrust. *Journal of Geophysical Research: Solid Earth*, 124, 10376-10392.
- Zhang, P. Z. (2013). Beware of slowly slipping faults. *Nature Geoscience*, 6(5), 323.

Appendix A-Appendix for Chapter 3

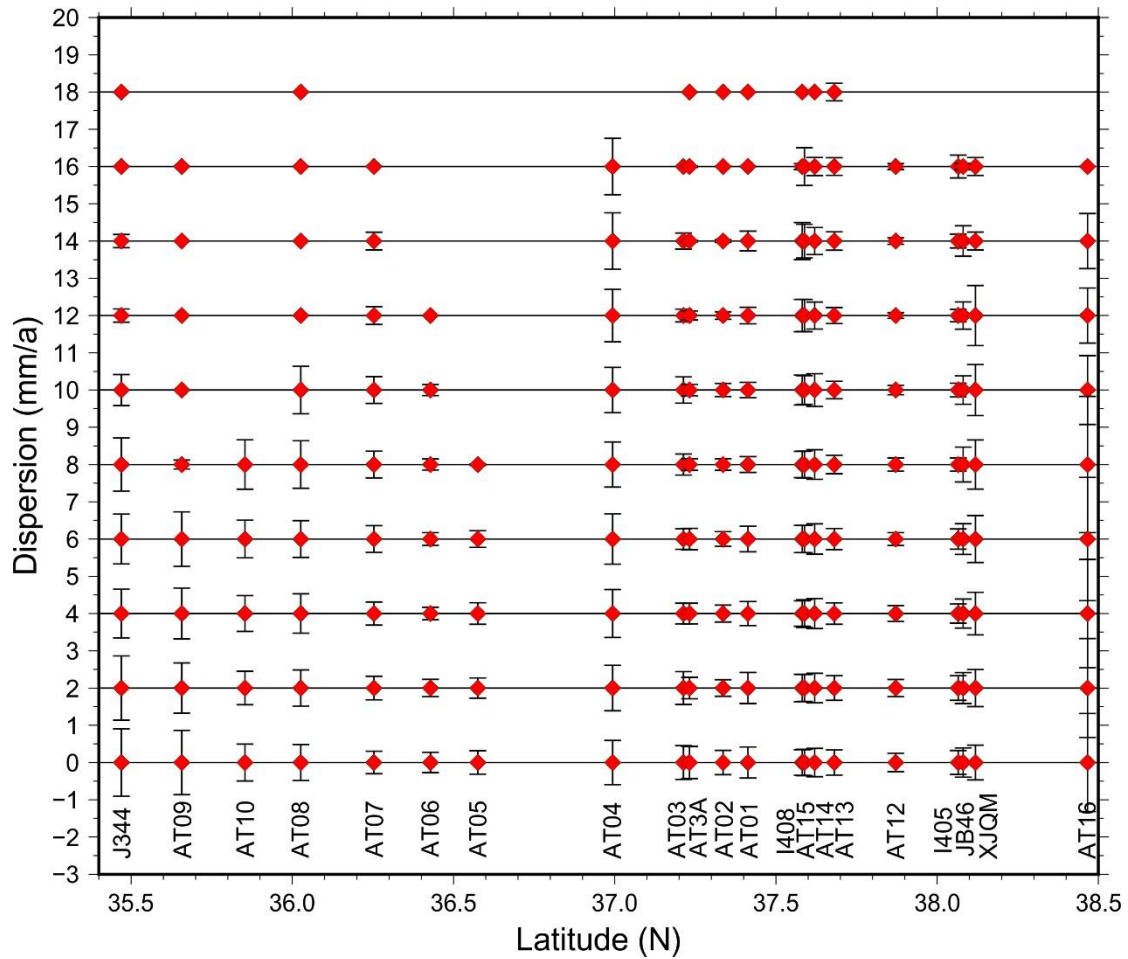


Figure A.1. From top to bottom, standard deviations (represented by error bar length) of InSAR data, near the GPS sites, within a radius from 1km to 10km.

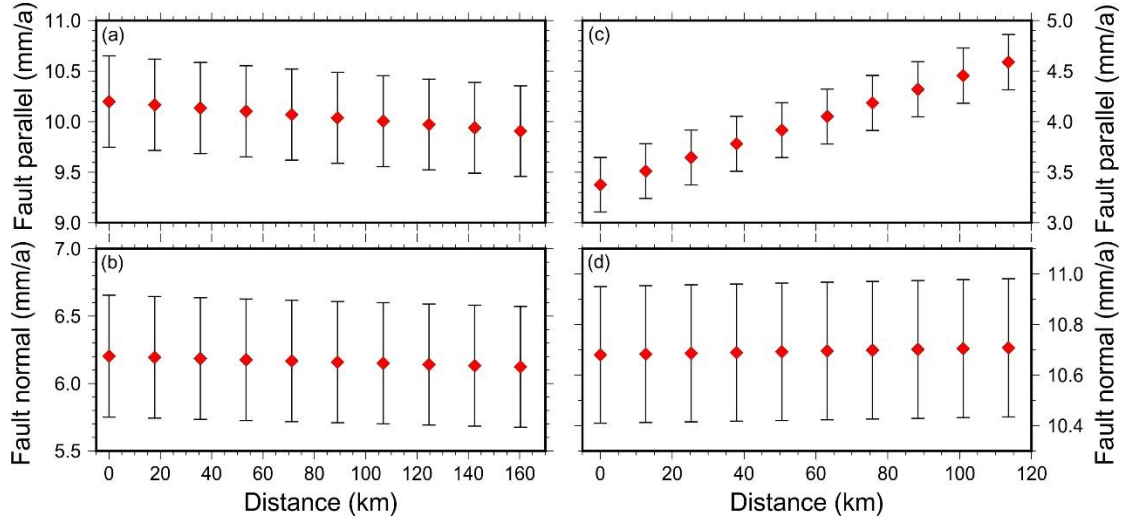


Figure A.2. Fault-parallel and fault-perpendicular components from block rotation. (a) and (b) are the forward model results in the south of the Altyn Tagh fault; (c) and (d) are the results in the north of the Altyn Tagh fault.

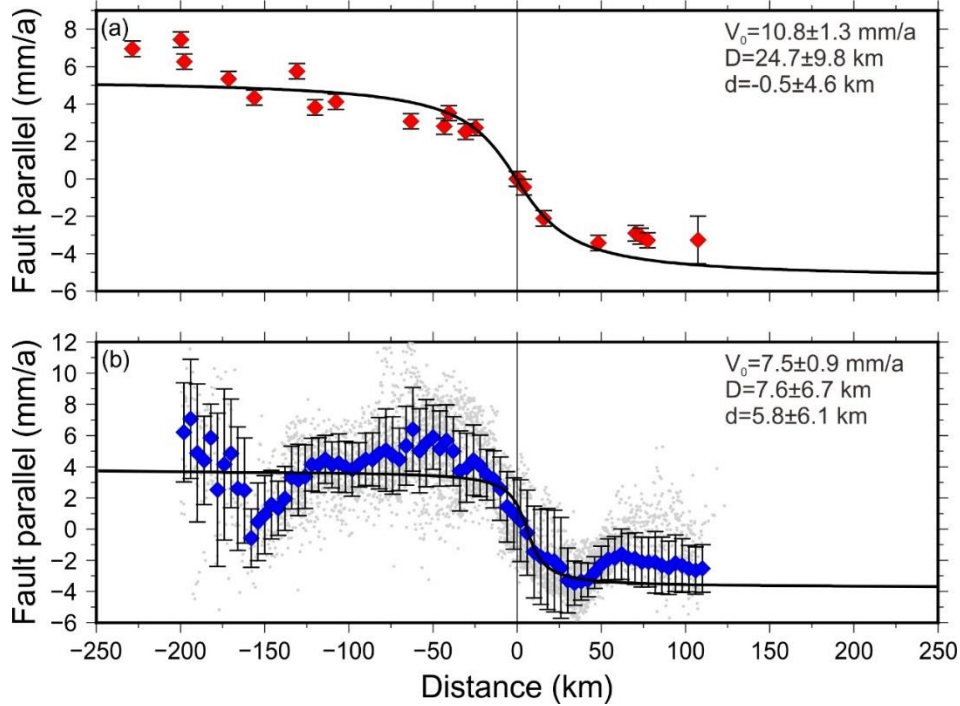


Figure A.3. Observed and calculated fault-parallel velocities across the western Altyn Tagh fault. Red and blue diamonds with 1σ uncertainty error bars show the fault-parallel velocity component of the GPS and InSAR respectively. Black solid lines represent best fitting curves for (a) GPS data only, (b) InSAR data only. The velocity of each InSAR data point is calculated using the median rates and their standard deviation of all the pixels (gray dots) within a 4-km-wide bin along the profile. The parameters of the best-fit results are show in each sub graph.

This appears as the Supplementary materials in Li et al. (2018).

Table A.1. Block strain rate and rotation parameters

Block strain rates (nanostrain/yr)

S#	Block	Long.	Lat.	E _{xx}	E _{yy}	E _{xy}	S _{xx}	S _{yy}	S _{xy}	C _{xx-yy}	C _{xx-xy}	C _{yy-xy}
1	TMBK	86.9730	39.6530	0.0000	0.0000	0.0000	0.0000	0.0000	0.0000	0.0000	0.0000	0.0000
2	QDBK	92.6170	37.1490	-0.4800	-15.4700	-6.3300	0.3200	0.9400	0.5900	0.0000	0.0000	0.0000
3	QLBK	98.8660	38.9370	-2.7000	-9.2800	-10.6400	1.3800	1.8400	1.2100	0.0000	0.0000	0.0000
4	TIBK	79.2960	36.0490	-7.4700	-46.2900	-11.2900	9.8800	17.4700	10.3100	0.0000	0.0001	0.0000
5	ALBK	100.2190	41.5920	0.0000	0.0000	0.0000	0.0000	0.0000	0.0000	0.0000	0.0000	0.0000
6	TSBK	83.7510	42.2060	-0.4600	-21.4400	5.2800	0.2100	0.7800	0.3800	0.0000	0.0000	0.0000
7	PABK	72.3320	37.3460	-10.2400	-21.9300	-8.8500	7.5300	4.7100	4.6300	0.0000	0.0000	0.0000

Block principal strain rates (nanostrain/yr)

S#	Blok	Long.	Lat.	E1	SigE1	E2	SigE2	A1	SigA1
1	TMBK	86.9730	39.6530	0.0000	0.0000	0.0000	0.0000	0.0000	0.0000
2	QDBK	92.6170	37.1490	-17.7800	0.9200	1.8300	0.4900	20.0900	1.6400
3	QLBK	98.8660	38.9370	-17.1300	1.7100	5.1500	1.5900	36.4100	2.9400
4	TIBK	79.2960	36.0490	-49.3400	16.1800	-4.4300	10.4900	15.0900	13.3900
5	ALBK	100.2190	41.5920	0.0000	0.0000	0.0000	0.0000	0.0000	0.0000
6	TSBK	83.7510	42.2060	-22.6900	0.7700	0.8000	0.2700	-13.3500	0.9500
7	PABK	72.3320	37.3460	-26.6900	5.4900	-5.4800	6.7000	28.2900	11.3600

Block residual principal strain rates (ns/yr) and rotations (nanoradians/yr)

Block	E1	SigE1	E2	SigE2	A1	SigA1	Rot	SigRot
TMBK	-1.49	0.33	-0.22	0.18	-26.48	8.87	-0.71	0.17
QDBK	-0.96	0.26	6.18	0.82	-95.38	3.57	-3.79	0.44
QLBK	-5.05	1.27	0.74	1.37	-130.00	7.45	-2.31	1.02

Appendix A

TIBK	7.97	18.76	28.48	21.31	-55.19	29.03	0.40	16.68
ALBK	-5.50	0.70	3.74	0.70	42.90	2.18	-2.50	0.51
TSBK	-0.90	0.38	2.94	0.52	-125.24	4.70	-1.20	0.32
PABK	1.94	4.67	45.51	7.51	-17.89	6.05	-2.10	4.43

Rotation of blocks relative to reference frame

Name	Wx	Wy	Wz	Sx	Sy	Sz	Sxy	Sxz	Syz
TMBK	0.0470	-0.4895	-0.4135	0.0031	0.0155	0.0134	0.0000	0.0000	0.0002
QDBK	0.0921	-0.2615	-0.1405	0.0035	0.0327	0.0253	-0.0001	-0.0001	0.0008
QLBK	-0.0222	0.2045	0.1864	0.0091	0.0549	0.0460	-0.0005	-0.0004	0.0025
TIBK	-0.0669	-1.0379	-0.8085	0.1078	0.5581	0.4053	0.0600	0.0436	0.2262
ALBK	0.0000	0.0000	0.0000	0.0000	0.0000	0.0000	0.0000	0.0000	0.0000
TSBK	0.0557	-0.1085	-0.0947	0.0033	0.0220	0.0201	0.0000	0.0000	0.0004
PABK	0.1457	-0.2717	-0.2031	0.0453	0.2038	0.1646	0.0090	0.0073	0.0332

Rotation of blocks relative to reference frame

Name	Lon.	Lat.	Omega	SigOm	E _{max}	E _{min}	Az	
TMBK	95.4806	40.0562	-0.6425	0.0206	0.2800	0.1300	96.9400	6.5600
QDBK	109.4061	26.8650	-0.3108	0.0397	3.0700	0.5600	134.2600	17.5200
QLBK	96.1967	42.1858	0.2776	0.0720	1.3600	0.4500	317.3400	3.8300
TIBK	86.3135	37.8606	-1.3173	0.6939	4.6900	0.3100	249.9600	5.9000
ALBK	180.0000	0.0000	0.0000	0.0000	0.0000	0.0000	90.0000	82.3500
TSBK	117.1697	37.8486	-0.1544	0.0280	5.7000	0.5200	111.6700	25.8600
PABK	118.2036	33.3814	-0.3692	0.2225	30.2100	4.0100	110.3800	37.3400

Abbreviation of block names: TMBK: Tarim; QDBK: Qaidam; QLBK: Qilian; TIBK: Tianshuihai; ALBK: Alashan (the reference); TSBK: Tien Shan; PABK: Pamir

Appendix B-Appendix for Chapter 4

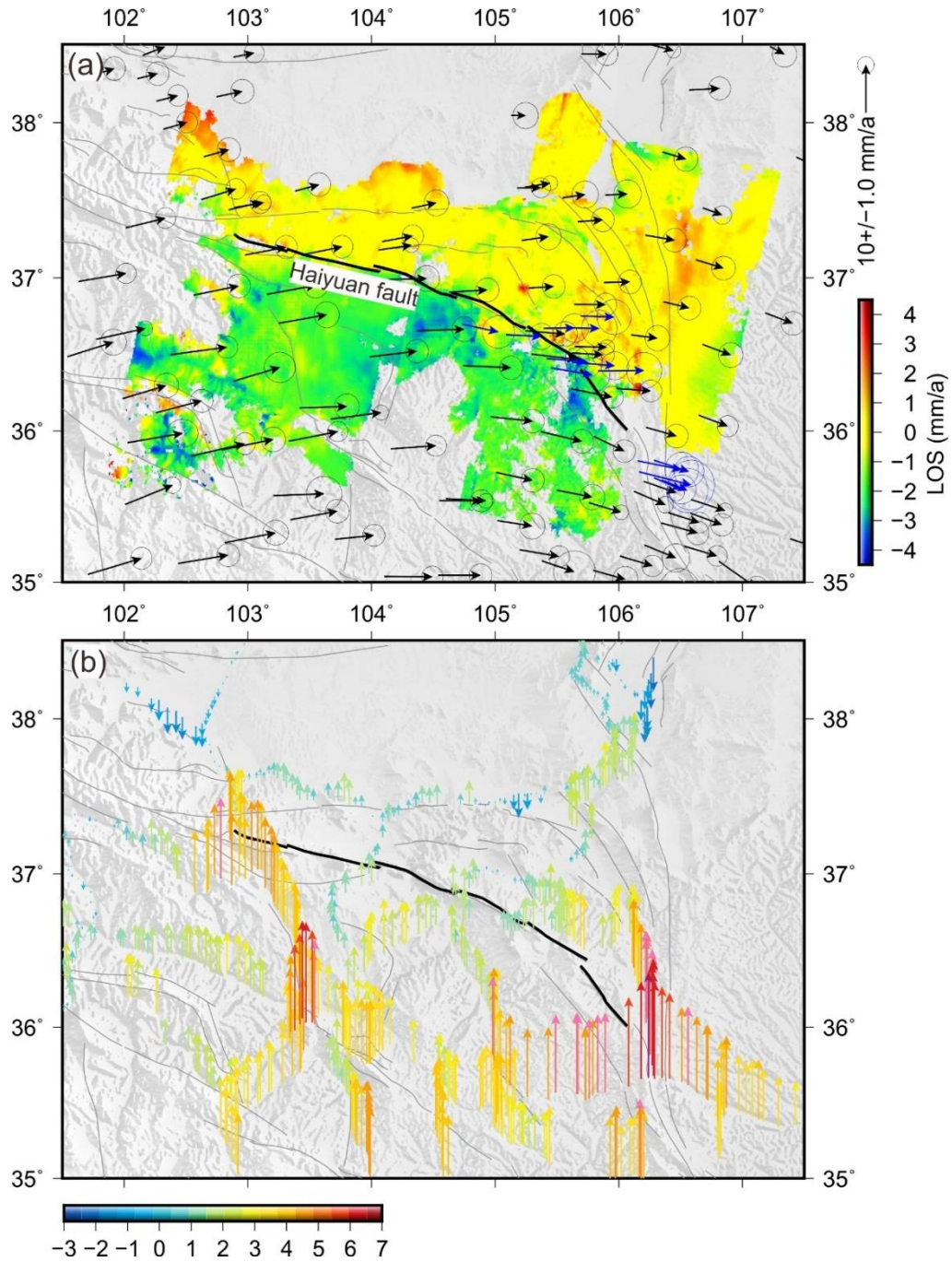


Figure B.1. (a) Observed InSAR displacements and GPS velocity field in the northeastern Tibet. (b) Vertical velocity field from leveling measurements (Hao et al., 2014).

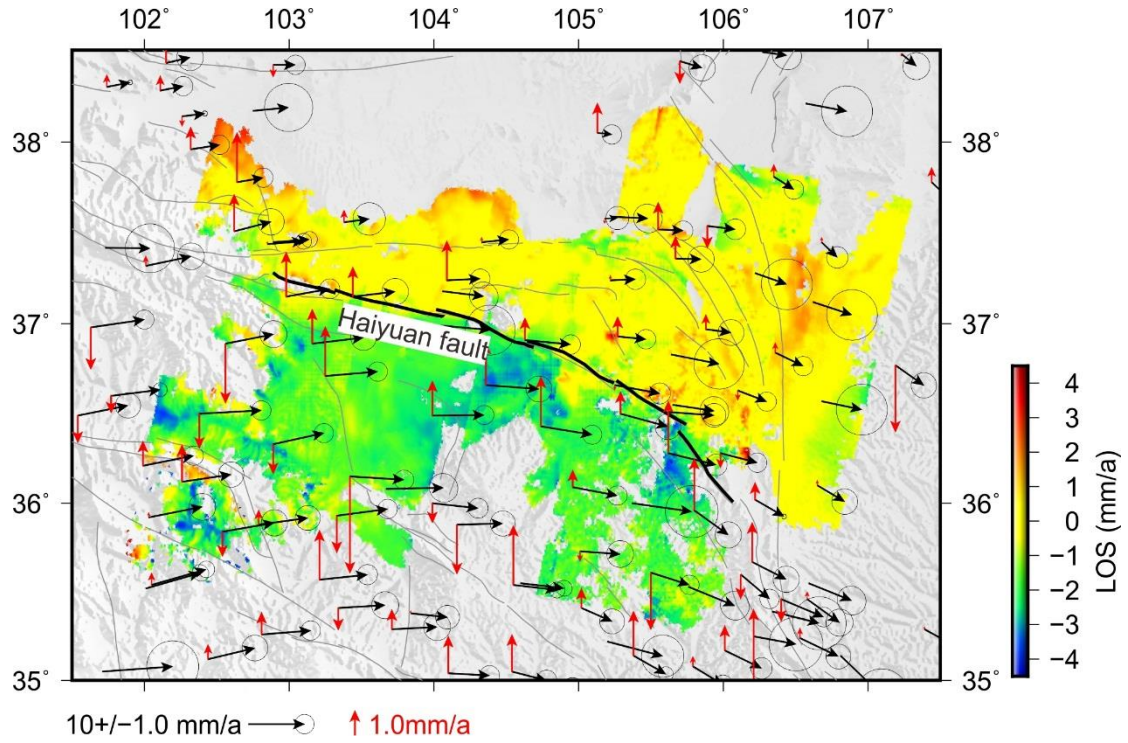


Figure B.2. Observed InSAR displacements and three dimensional GPS velocity field in the northeastern Tibet (Liang et al., 2013).

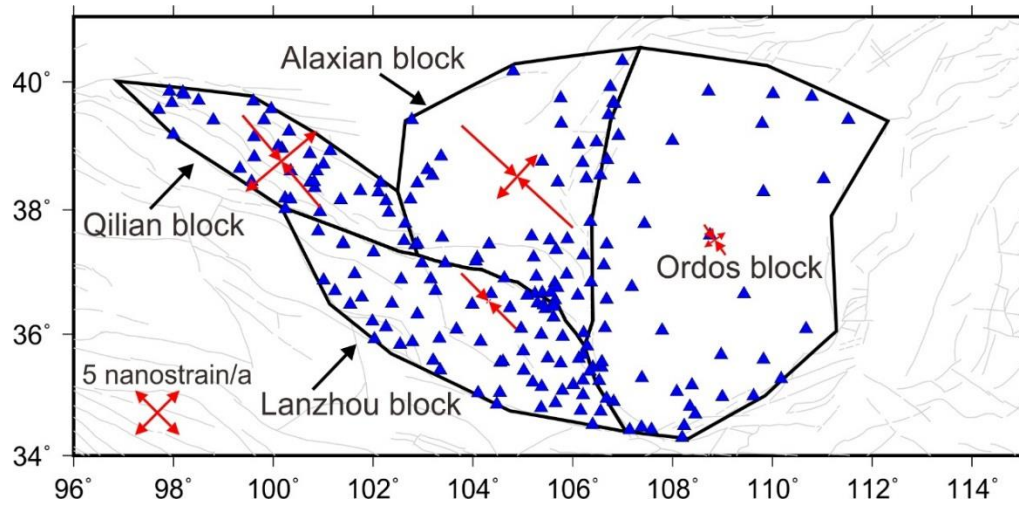


Figure B.3. Blocks used in this study. Bold black lines represent block boundaries. Blue triangles show the position GPS sites. Red arrows show the inverted block internal strain rates.

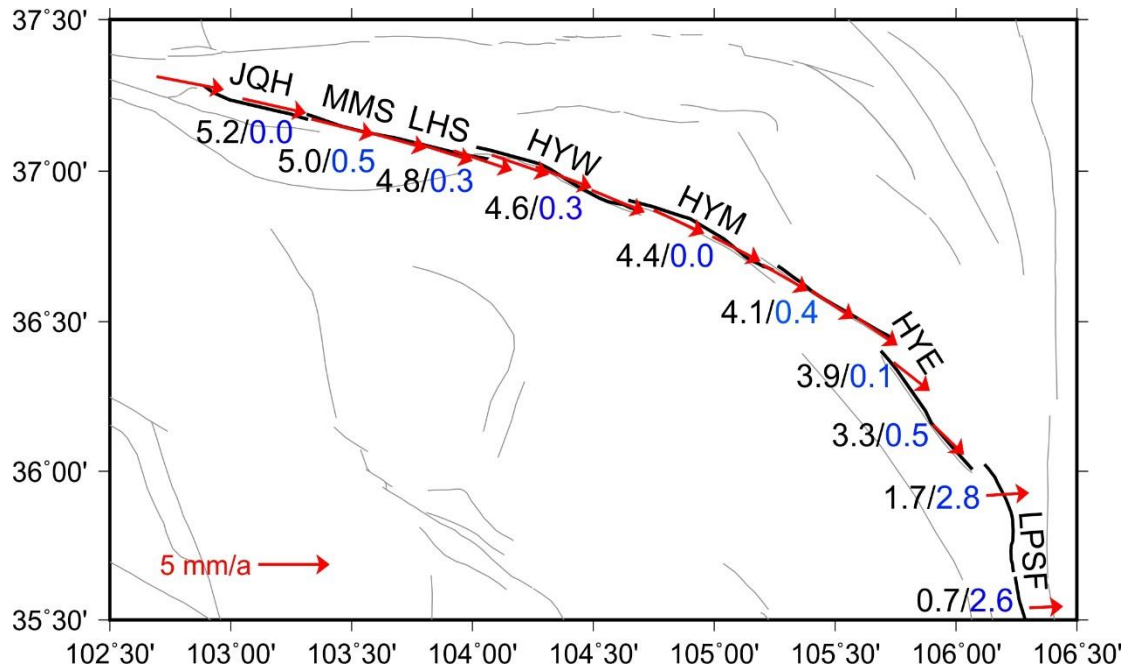


Figure B.4. Inverted fault slip rates along the Haiyuan fault. Black numbers represent strike-slip rates, and blue numbers represent thrust slip rates. Red arrows show the Lanzhou block motion relative to the Alaxian block.

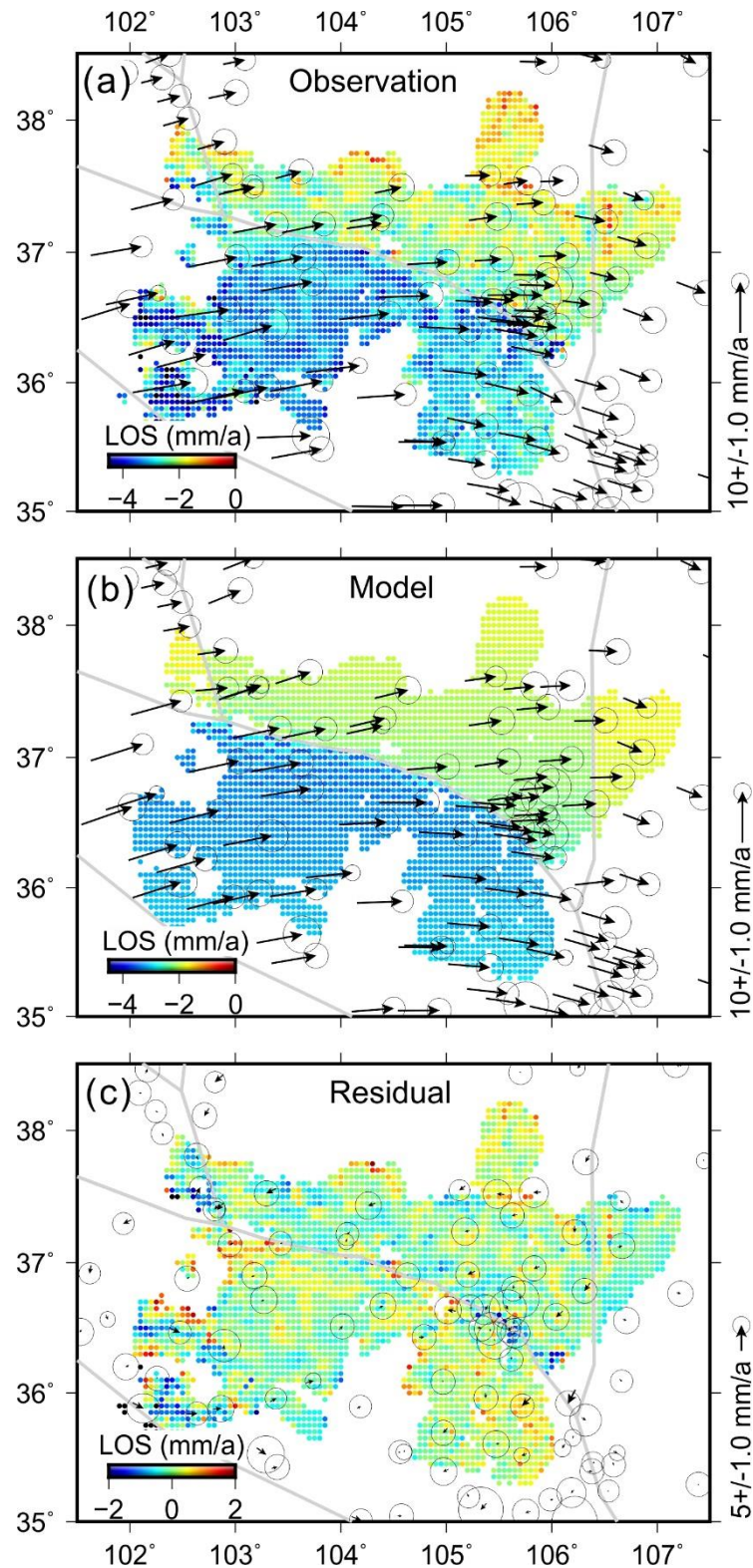


Figure B.5. (a) The observed GPS velocities and InSAR displacements. (b) Block model predictions. (c) Residuals. Gray lines represent block boundaries. Error ellipses indicate the 95% confidence levels.

Appendix C-Appendix for Chapter 5

Text C.1.

GPS data processing

Wang et al. (2017) used the Bernese 5.0 GPS software (Dach et al., 2007) to process the CMONOC GPS data. During data processing, they corrected coseismic offsets for GPS stations affected by large earthquakes that in and around mainland China between 1998 and 2015, such as the 2001 Mw 7.8 Kokoxili earthquake, the 2008 Mw 7.9 Wenchuan earthquake and the 2011 Mw 9.0 Tohoku, Japan earthquake. For the postseismic perturbations of large events, they removed the post-earthquake data of near-field stations.

Rui and Stamps (2016) used the GAMIT/GLOBK 10.4 software (Herring et al., 2010) to process the Sichuan GNSS/GPS Network GPS data. They also corrected the coseismic offsets for GPS stations. In addition, they evaluated time series (11 continuous GNSS/GPS stations) for postseismic transients following the 2008 Mw 7.9 Wenchuan earthquake and the 2013 Mw 6.9 Lushan earthquake, and solved for relaxation times and amplitudes of transients. The time series showed unresolvable postseismic transients 9 months after the Wenchuan earthquake; consequently, they removed 9 months of data after both events for their final velocity solution. In summary, we regard the above GPS solutions represent interseismic velocities in 1999–2014.

Text C.2.

GPS data modeling

We use the elastic block modelling implemented in DEFNODE package (McCaffrey et al., 2007) to obtain a regional kinematic model. In the model, faults are represented by a set of 3-D nodes defining the fault surface and the ISC at each node is estimated during the inversion. The fault surface between the fault nodes is divided into patches of 10 km length along strike and 1.7 km along dip. A bilinear interpolation is applied to obtain the ISC for each rectangle. We minimized data misfit, defined by the reduced chi-squared statistic (χ_n^2):

$$\chi_n^2 = \sum_1^n \left(\frac{\gamma_i}{\sigma_i} \right)^2 / (n - m) \quad (1)$$

where n is the number of observations, m is the number of free parameters, γ_i is the residuals (observed minus calculated velocities), and σ_i is the data uncertainty for observation i .

Following previous studies (e.g., Loveless and Meade, 2011; Wang et al., 2017; Figure C.1), we divide the eastern Tibetan Plateau into five tectonic blocks: the South China block, the Longmenshan block, the Bayanha block, the North Yunnan block, and the South Yunnan block. Block boundaries follow the surface traces of major active faults. The South China block is assumed to be rigid and we solve internal strains for the Longmenshan block, the Bayanha block, the North Yunnan block and the South Yunnan block respectively. In the model, the Longmenshan fault was modeled to be listric in shape, consistent with the geometry proposed in previous studies (Thompson et al., 2015). As in previous studies (e.g., Allen et al., 1991; Deng et al., 2003; Jiang et al., 2015; Wen et al., 2008), we model the XXFS as a 80° southwestward dipping fault while other block bounding faults are taken vertical (89.9°). In order to account for the elastic contribution of locked faults surrounding the XXFS, we first solve for the mean fault locking depth for all of the block bounding faults using a grid search method (between 0.1 and 30 km with a step of 1 km). The optimal result providing the minimum misfit is 20 km. Therefore, a uniform fault locking depth of 20 km was used for the block bounding faults, except for the Longmenshan fault to be consistent with previous studies and the XXFS, where ISCs are estimated parameters in the inversion.

Text C.3.**InSAR data processing**

In order to make InSAR and GPS consistent, we adopt the remove-filter-restore approach proposed by Wei et al. (2010). We first remove an interpolated map of the horizontal GPS velocities from the InSAR data set, then high-pass filter the obtained residual LOS rate map with a cut-off distance of 50 km, and finally add the result back to the GPS velocity map. Such procedure ensures that the InSAR velocities agree with the GPS at the longest wavelengths, while preserving the short-wavelength features that make the InSAR contribution valuable in the near field of the Xianshuihe fault. The corrected data set is shown in Figure 3b. We calculate the ‘surface creep rates’ as the difference in fault-parallel velocity averaged in 1 km normal and 2 km along the strike bins on opposite sides of the fault (e.g., Tong et al., 2018; Xu et al., 2018). If the fault segment is creeping, the ‘creep rate’ should be larger than 0, and if the fault segment is coupled at the surface, the ‘creep rate’ should be around 0 within its confidence level.

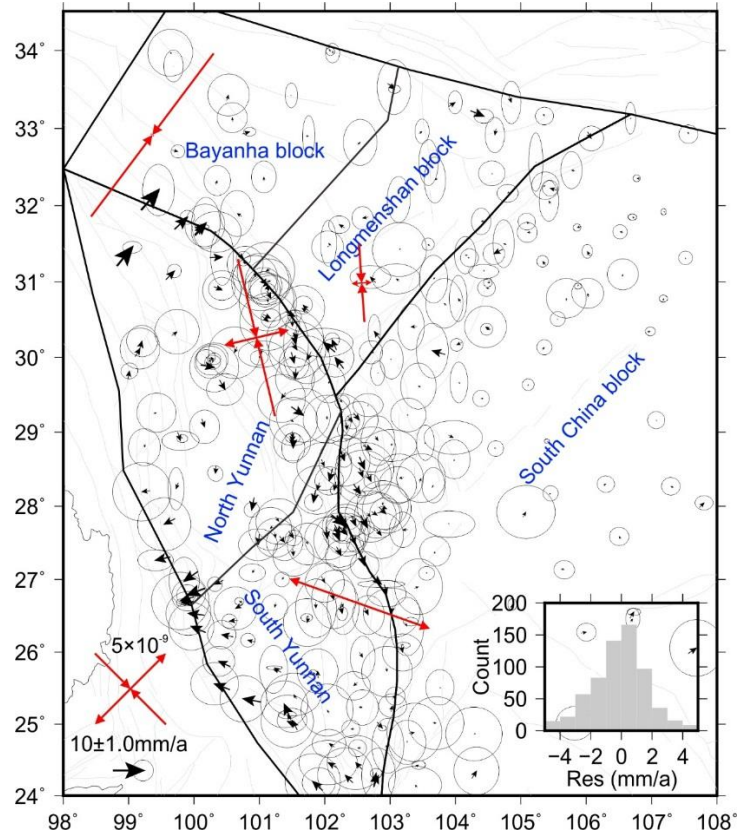


Figure C.1. Global Positioning System (GPS) velocity residuals associated with the block kinematic model and their statistical histogram. Error ellipses indicate the 95% confidence levels. Black lines represent the block boundaries. Red arrows show principal strain rate.

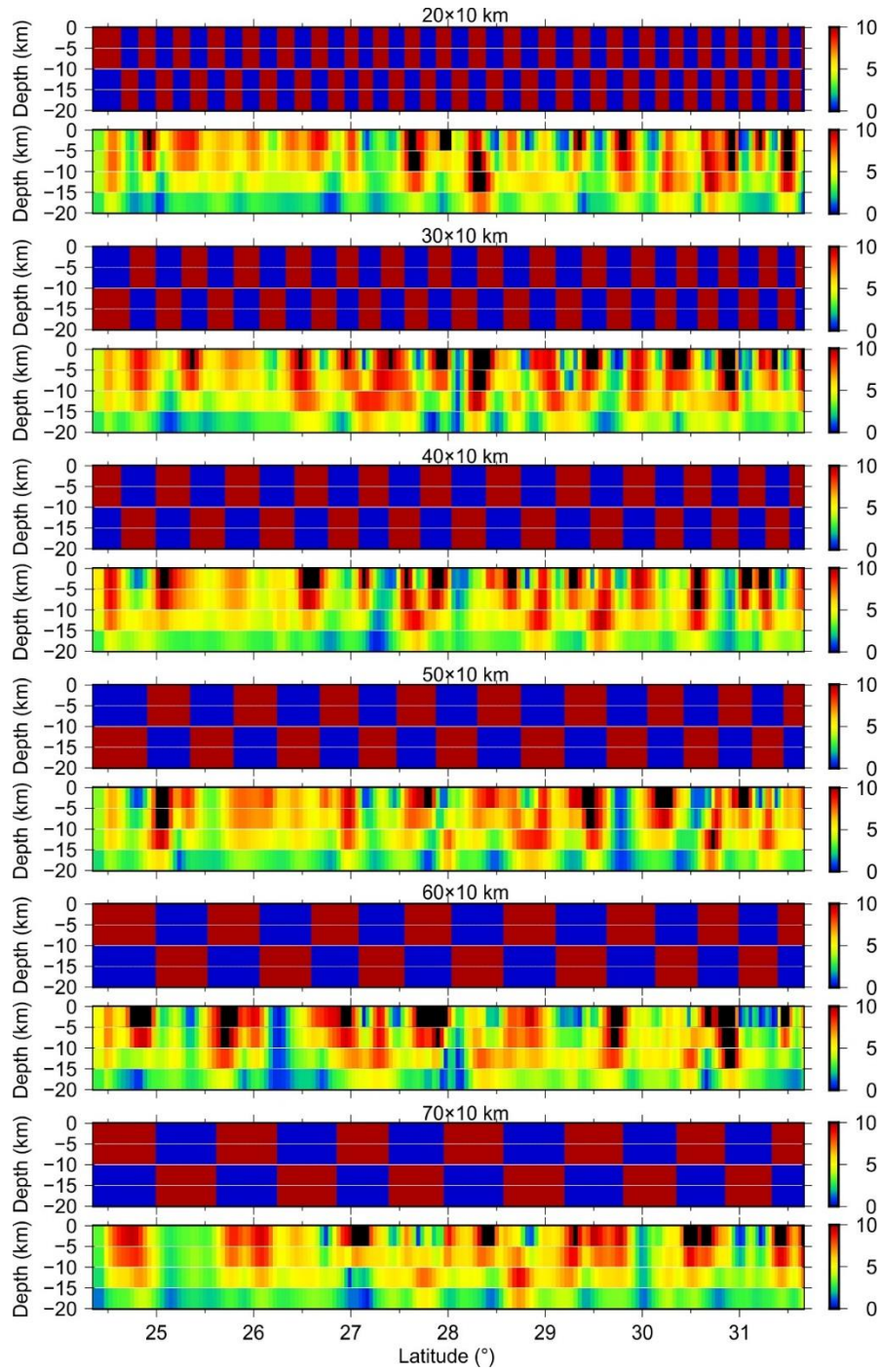


Figure C.2. Resolution test, with increasing checkerboard lengths, for interseismic fault coupling on the XXFS.

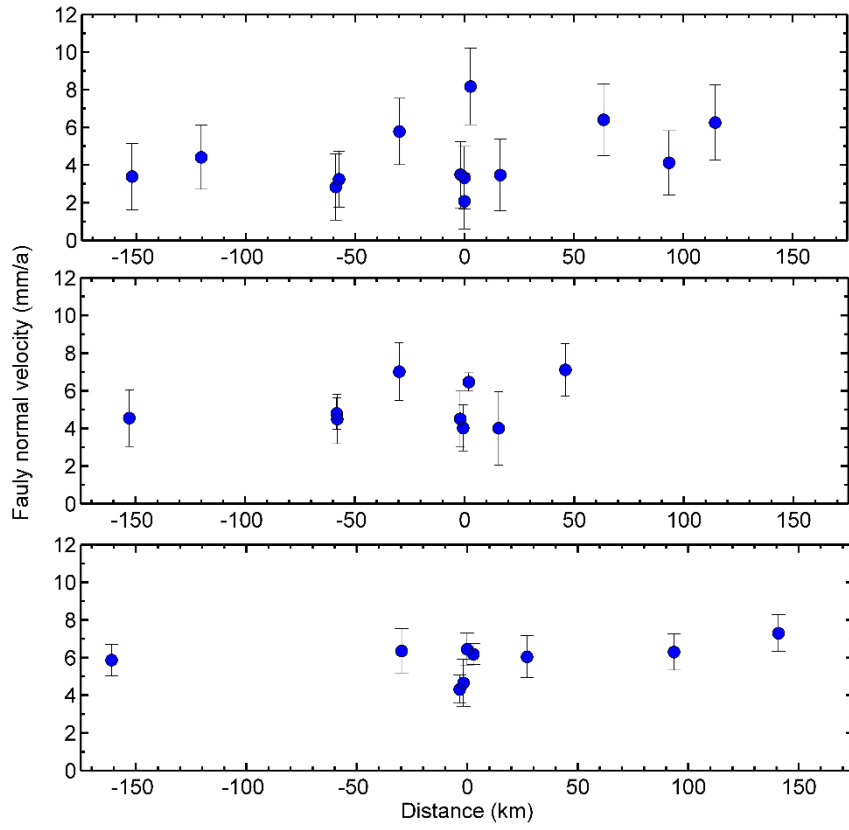


Figure S3. Fault normal GPS velocities. From top to bottom, subfigures correspond to (b), (c) and (d) in Figure 5.8.

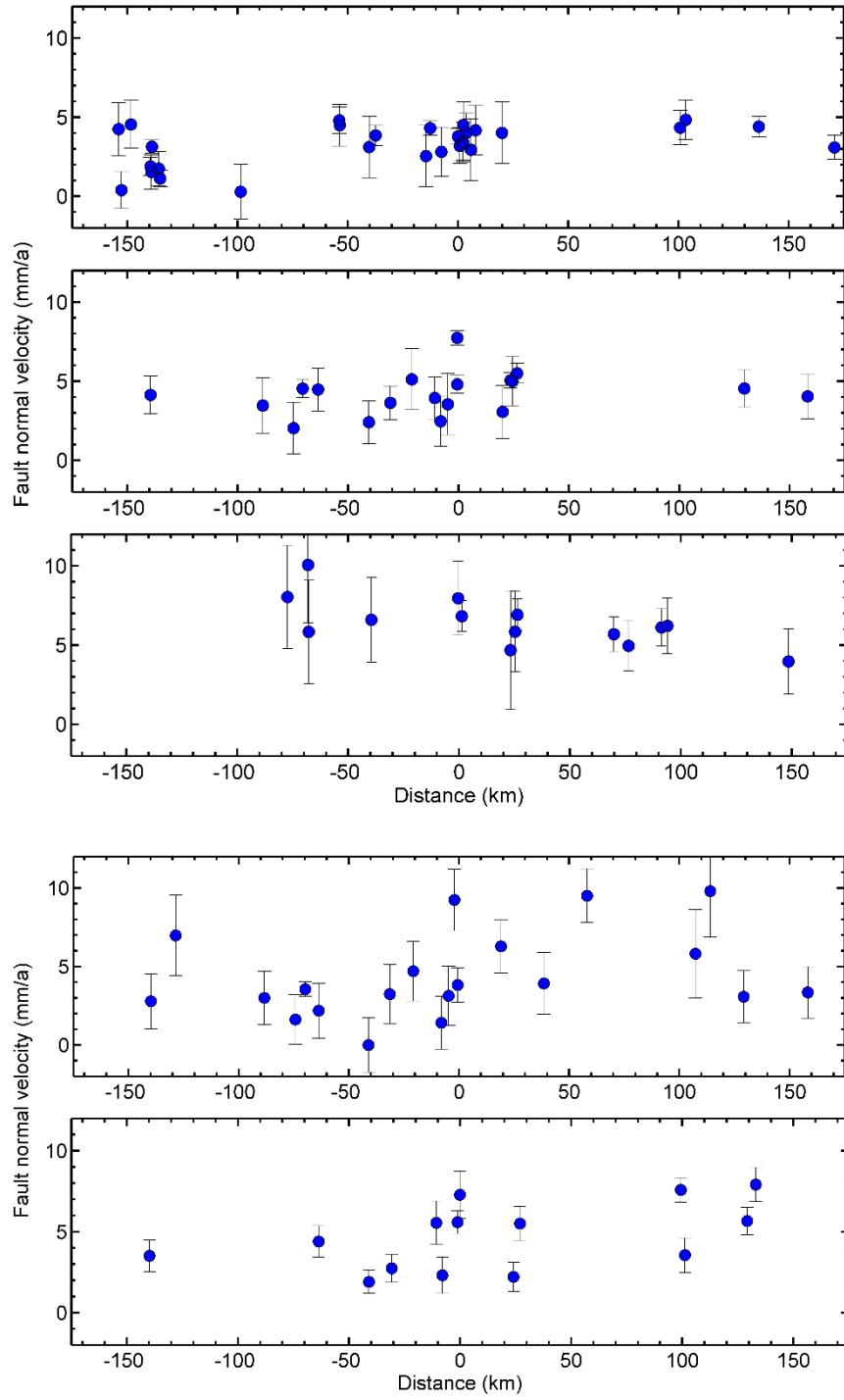


Figure S4. Fault normal GPS velocities. From top to bottom, subfigures correspond to GPS profiles AA', BB', CC', DD' and EE' in Figure 5.9.

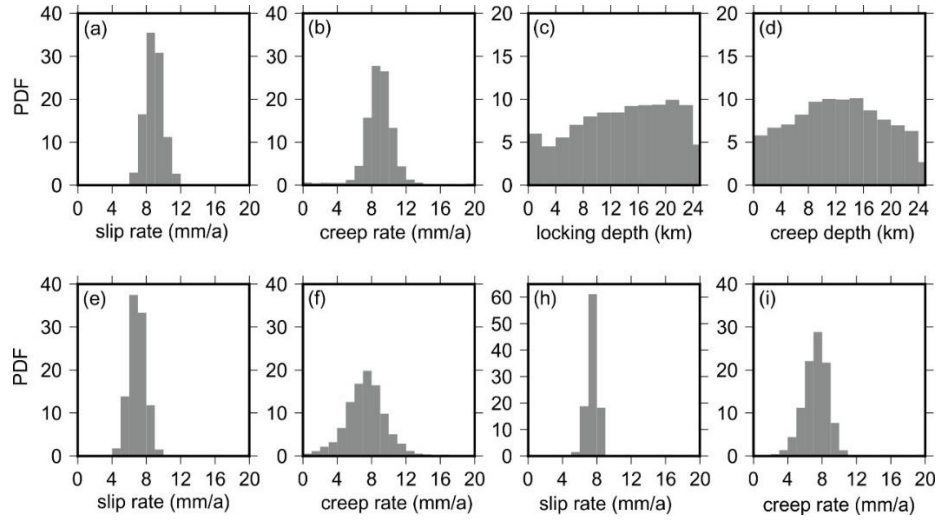


Figure C.5. Posterior marginal Probability Density Functions (PDFs) of: (a-d) GPS velocities in 1998-2014, (e-f) GPS velocities in 1998-2007 and (h-i) GPS velocities in 2015-2018.

Table C.1. Block rotation poles

Block name	Longitude (°)	Latitude (°)	Rotation rate (Ma/a)
Bayanha	280.672±0.070	-29.107±0.377	2.248±0.250
Longmenshan	279.401±1.030	-18.347±4.593	0.425±0.146
North Yunnan	250.369±12.033	12.936±17.468	0.238±0.068
South Yunnan	269.704±2.076	-19.138±1.359	0.550±0.094
South China	113.938±0.294	47.298±0.498	0.165±0.004

Table C.2. Block internal strain rates

Block name	Longitude (°)	Latitude (°)	Compressive (nanostrain/a)	Tensile (nanostrain/a)	Azimuth angle (°)
Bayanha	99.362	32.917	2.376E-10	-1.015E-08	36.9212
Longmenshan	102.565	30.986	1.008E-09	-3.887E-09	-3.9980
North Yunnan	100.956	30.264	3.316E-09	-8.018E-09	-13.2690
South Yunnan	102.534	26.668	7.426E-09	-3.897E-11	19.5465
